

Development of a Novel Finite Volume Methodology for Multi-Dimensional Fuel Performance Applications

Présentée le 9 juillet 2021

Faculté des sciences de base
Laboratoire de physique des réacteurs et de comportement des systèmes
Programme doctoral en énergie

pour l'obtention du grade de Docteur ès Sciences

par

Alessandro SCOLARO

Acceptée sur proposition du jury

Dr S.-R. Cherkaoui, président du jury
Prof. A. Pautz, Dr I. D. Clifford, directeurs de thèse
Dr P. Van Uffelen, rapporteur
Prof. G. Pastore, rapporteur
Prof. H. M. Prasser, rapporteur

Acknowledgements

This thesis is not *just* the result of four years of hard work but is the most recent chapter of a journey that began seven years ago with my arrival in Switzerland. Many people have contributed to this work by providing inspiration, confrontation, support or simply by being there when I needed them, and I wish to thank them sincerely.

I want to start by acknowledging Prof. Alessandro Di Maio from the University of Palermo, my hometown. He is a fantastic teacher and mentor. His passion has ignited in me the interest for nuclear engineering and his advice has driven me to pursue a PhD in this field. I will always be grateful to him.

I wish to thank the EPFL and the ETHZ for accepting my application to the Nuclear Engineering master program. Those two years have passed in a blink, filled with long hours of study, unforgettable experiences, and with friends from all over the world. Most importantly, those two years have been my gateway to this beautiful country and to this city that I fell in love with. I wish to thank all the Professors and members of the teaching staff of the Nuclear Engineering master program. Among them, I am particularly honored to have been a student of Prof. Horst-Michael Prasser and Prof. Andreas Pautz and I wish to thank them for their ability to teach nuclear engineering with brilliant and entertaining lectures.

A crucial moment in my personal and professional growth has been my stay at Nagra, first as an intern, then as a freshly graduated nuclear engineer before starting my PhD. I will always be grateful to my ex-supervisor and friend Ben Volmert for seeing something in me, for his sincerity, for his extreme generosity and for his relentless belief in my capabilities. I wish to thank also all the friends that I have made during my time in Aargau, in particular Benoit Soubelet and Stathis Vlasopoulos, and I hope to visit them more often in the future. A special thanks goes to Valentyn Bykov for his continuous support despite the distance, for all our passionate discussions and for the tech advices. Naturally, a second special thanks goes to Ahmed Shama, for sharing *that* apartment and for not burning the kitchen, in the end.

Four years of PhD can be tough if they are not alleviated by the presence of colleagues and friends. I have always been surrounded by exceptional people and these last years have not been any less. Thank you, Daniel Siefman and Fanny Vitullo, for the laughs, for the beers at Sat and for the special bond that only sharing the office with someone can create; thank you, Stefan Radman, for your sense of humor, for being my computational companion during these last four years and for the weekly discussions that have given so many unrecognized contributions to this work; thank

you, Oskari Pakari, for teaching me how to appreciate the simple nice things in life, for being an affectionate friend, and for spotting me on the bench; thanks also to Edoardo Brunetto, for having helped tremendously in shaping this work in the few months since your arrival. And thank you Giorgio Rossi with all my heart, you are one of the most generous and sincere friends that I have.

I wish to thank also Mathieu Hursin, Vincent Lamirand, Tom Mager, Pavel Frajtag and all the other members of the laboratory for creating an always interesting and dynamic working environment. I am especially grateful to the students that have contributed to this work: thank you, Audrey Giancesello and Yves Robert, your work has been greatly appreciated.

Finding your own path in a large undefined project like a PhD might be a daunting task. I have been extremely lucky, as I could not hope to have better mentors to guide me through. I am grateful once again to Prof. Pautz for agreeing to be my thesis director and for the important role he has played in guiding me during this last seven years.

I owe so much to Ivor Clifford and Carlo Fiorina. They are two of the most knowledgeable person I have ever met. In their different ways they have taught me most of the things I know about nuclear reactors, numerical methods, and science in general. I sincerely believe that if this thesis is any good it is mostly because of the excellent supervision I received. With Carlo I had also the opportunity to live in the same city and share more than just a professional relationship. I do not consider him *only* a supervisor, but a mentor, a role model, and a close friend.

I am grateful also to my mentors at JRC, Paul Van Uffelen and Arndt Schubert, for welcoming me in their team during my brief but very productive stay in Karlsruhe. They have shown me the joy that comes from genuine scientific collaboration. I might not miss that small studio in Karlstrasse, but I certainly miss those engaging coffee breaks!

As a PhD student and member of the LRS at EPFL, I had the luck to travel around the world, visit new places, exchange ideas with other researchers. Among all the interesting people I have met in these years, I wish to thank Prof. Giovanni Pastore from the University of Tennessee and Dr. Clément Introini from CEA Cadarache for the interest they have shown in my work and for the many words of support and appreciation.

Moving to my hometown, I wish to thank my old pals, my friends of a lifetime: Alessandro Crupi, Filippo Mauro, Gianluca Chiaramonte, Gianluca Gucciardi, and Luca Dragotto. Thank you, because despite the distance and the years, when we are together it feels like we have just graduated from high school. Thank you for remaining who you are through all these years. I particularly want to thank you, Guccio, for accepting to be my best man and giving me the honor to be yours.

I also wish to thank my colleagues and friends from what now appears to be in retrospect almost an alternative reality: Aldo Orlando, Carla D'Amico, Ciccio Giovenco, Giulio Sanseverino and Andrea Pecoraro, but also Alessandro Sorrentino, and Nicolino and Pasquale Di Matteo. I might regret some of my initial university choices, but I would redo it all just to have the chance to meet you along the way.

I wish to thank my parents, Pippo and Antonietta. They are an example of human dignity and humility that I try to follow every day. They have supported me always, without asking anything in return. Thanks also to my sister Laura for her always too high opinion of me and thanks to my parents-in-law Rosalia and Angelo for their unconditional love and support.

But the biggest thank you goes to the person who has shared every important moment with me over the past 14 years, the person I had the privilege to marry during this PhD. Thank you, Rosa, you know the best and the worst version of me. Thanks for putting up with my long hours and accepting me as I am. And thanks for Fujiko, when I see you with her, I know how lucky I am. You are the main reason why I am here, celebrating this beautiful milestone.

Lausanne, 27th April 2021

Abstract

Fuel performance codes are an essential tool for ensuring the safe and economic operation of nuclear reactors. Traditionally, these codes have been developed following a simple 1.5-D modelling approach, where the fuel behavior is simplified by assuming axisymmetric and plain strain conditions and where phenomenological correlations are largely privileged over the use of accurate physical and mathematical models. However, in recent decades the advent of modern high-performance computing has awakened a growing interest towards higher-fidelity tools with multi-dimensional and multi-physics capabilities. The main development efforts have been carried out employing the popular finite element method, while the alternative approach offered by the finite volume method has not been explored by the fuel performance community.

Interested in the potential of this numerical scheme for fuel analysis and multi-physics applications, this PhD thesis aims to develop a finite volume methodology and associated software for the high-fidelity analysis of fuel behavior. As a result, a novel finite volume fuel performance code named OFFBEAT is developed. The code is based on the open-source C++ library OpenFOAM and it is envisioned as a multi-dimensional, readily-available and flexible tool, which is straightforward to extend and modify, and open to multi-physics simulations.

The thesis presents the development strategy of OFFBEAT, discussing the numerical framework, the treatment of the gap as well as the structure of the code with its main models and overall solution scheme. In this context, a novel contact methodology is developed that introduces a semi-implicit discretization of the contact stresses, improving the convergence properties of many contact scenarios. To test the robustness and accuracy of the code, extensive efforts are carried out to verify and validate OFFBEAT against numerical benchmark and experimental data.

The novel methodology is applied to the 3-D analysis of the effect of eccentricity on fuel disc irradiation test campaigns performed in the past in the Halden Boiling Water Reactor and characterized by rods with large gap and high conductive fuel. This represents an interesting example of how multi-dimensional capabilities can be used to study separate-effect tests, which are becoming increasingly more relevant in nuclear fuel research and are often characterized by unconventional features.

Additionally, the thesis describes a set of methodologies and tools that complement OFFBEAT enabling its interaction with other codes relevant for the fuel performance community. First, a coupling between OFFBEAT and the Monte Carlo neutron transport code Serpent2 is developed to allow one to obtain a higher-fidelity solution for the neutron flux and for the fuel isotopic composition. This is particularly relevant for fuel rod configurations outside of the range of application of traditional simplified neutronics models such as for new fuel types, experimental reactors, or fuel

rods with strong absorbers. Second, a coupling strategy is developed and implemented between the legacy code TRANSURANUS and OFFBEAT. Taking advantage of the strength of both codes, the main aim is to use a validated and fast 1.5-D code to simulate the base irradiation and set accurate initial conditions for a multi-dimensional transient performed with OFFBEAT.

In conclusion, this thesis shows that the finite volume method offers a viable alternative to the finite element method for the analysis of complex multi-dimensional fuel performance scenarios. Despite the validation and verification base should be extended to include multi-dimensional cases, the extensive testing efforts indicate that the methodology established in this thesis complemented by appropriate gap heat transfer and contact procedures can provide accurate results in line with those obtained by other codes. Acceleration techniques might be introduced in the future to overcome the unavoidable instabilities deriving from the stiffness and non-linearity of the gap behavior, but the use of relaxation factors and adaptive time steps is already an effective solution to reach convergence without excessively compromising the computational time expected from a higher-fidelity tool. The thesis also shows how the novel methodology and more in general multi-dimensional codes can complement traditional fuel behavior analysis by assisting in the design and interpretation of separate effect tests or by offering new modeling opportunities through the coupling with a legacy code. Finally, the coupling with the Serpent2 neutron transport code offers an interesting example of how high-fidelity tools can overcome the limitation of traditional 1-D models by interacting with separate solvers dedicated to a single physics.

Keywords

Nuclear; Fuel performance; Solid-mechanics; Heat transfer; Finite volume; OpenFOAM; C++; Contact; Verification; Validation; Fuel eccentricity; Separate effect tests; Multi-physics; Coupling

Résumé

Les codes de performance simulant le comportement sous irradiation du combustible sont des outils essentiels pour garantir le fonctionnement sûr et économique des réacteurs nucléaires. Traditionnellement, ces codes ont été développés suivant une approche de modélisation 1.5-D, qui simplifie le modèle en faisant l'approximation d'un comportement axisymétrique pour les déformations ; et qui privilège l'utilisation de corrélations empiriques par rapport à l'utilisation de modèles physiques et mathématiques.

Cependant, ces dernières années, l'augmentation de la puissance de calcul a permis de considérer le développement d'outils numériques de haute-fidélité, dotés de capacités multi-dimensionnelles et multi-physiques. A ce jour, les majorités des codes multidimensionnels utilisent la méthode des élément finis. L'approche alternative présentée par la méthode des volumes finis n'a pas été explorée par la communauté.

Intéressée par le potentiel de ce schéma numérique, la présente thèse vise à développer un code base sur la méthode de volumes finis pour la modélisation haute-fidélité et multi-physique du comportement des combustibles nucléaire sous irradiation. Ce code est nommé OFFBEAT. Il est basé sur la librairie open-source pour C++ OpenFOAM et il est envisagé comme un outil multi-dimensionnel, flexible, facile à modifier et permettant de réaliser des simulations multi-physiques.

La thèse présente la stratégie de développement d'OFFBEAT, et discute les méthodes numériques employées, le traitement du gap ainsi que la structure du code avec ses principaux modèles et son schéma de calcul. Plus spécifiquement, un nouveau modèle de contact pastille gaine est développé. Ce modèle introduit une discrétisation semi-implicite des forces de contact et améliore les propriétés de convergence du code pour nombreux scénarios d'intérêt. Pour tester la robustesse et la fiabilité du code, OFFBEAT est vérifié et validé par rapport à des données numériques et expérimentales.

La nouvelle méthodologie est appliquée à l'analyse 3-D de deux campagnes expérimentales d'irradiation des disques de combustible, en se focalisant sur les problématiques d'excentricité et leurs effets sur le comportement du combustible. Les deux campagnes, effectuées dans le REB à Halden, étaient caractérisées par des grands gaps et par un combustible à haute conductivité. Cette étude démontre comment les capacités multidimensionnelles (2-D et 3-D) peuvent être utilisées pour étudier les expériences sur le separate effect tests, qui ont souvent des caractéristiques non conventionnelles.

La thèse décrit également un ensemble de méthodologies et d'outils qui complètent OFFBEAT et permettent son interaction avec d'autres codes pertinents pour l'analyse multiphysique du com-

bustible sous irradiation. Un premier couplage est développé entre OFFBEAT et le code de transport de neutrons Monte Carlo Serpent2 pour obtenir un flux de neutrons et une composition du combustible plus précises. Ceci est particulièrement utile pour la modélisation de combustibles exotiques comme par exemple les nouveaux types de combustibles, celui des réacteurs expérimentaux ou des crayons contenant des absorbants neutroniques. Le comportement des combustibles ne peut pas être étudié avec des modèles neutroniques traditionnels et simplifiés. De plus, une stratégie de couplage est développée entre le code TRANSURANUS et OFFBEAT. L'objectif principal est d'utiliser un code 1.5-D, validé et rapide, pour simuler l'irradiation de base et définir des conditions initiales précises pour un transitoire multi-dimensionnel réalisé avec OFFBEAT.

En conclusion, cette thèse montre que la méthode des volumes finis offre une alternative viable à la méthode des éléments finis pour l'analyse haute-fidélité du combustible nucléaire. Bien que la validation doive être étendue pour inclure des cas multi-dimensionnels. Les tests réalisés pendant la thèse indiquent que la méthodologie établie, complétée par des procédures de transfert de chaleur et de contact appropriées, peut fournir des résultats précis conformes à ceux obtenus par autres codes. Des techniques d'accélération pourraient être introduites pour surmonter les instabilités liées à la modélisation du gap. L'utilisation de facteurs de relaxation et de pas de temps adaptatifs sont déjà des solutions efficaces pour atteindre la convergence sans augmenter le temps de calcul de façon significative. La thèse montre également comment les codes multi-dimensionnels peuvent contribuer à la conception et à l'interprétation des separate effect test, et comment ils peuvent offrir de nouvelles opportunités de modélisation grâce au couplage avec un code traditionnel. Finalement, le couplage avec le code de transport de neutrons Serpent2 a démontré comment les outils haute-fidélités peuvent surmonter la limitation des modèles 1-D traditionnels en interagissant avec d'autres codes dédiés à une seule physique.

Mots-clés

Nucléaire; Combustible; Mécanique des solides; Analyse thermique; Volumes fini; OpenFOAM; C++; Contact; Vérification; Validation; Excentricité du combustible; Multi-physique; Couplage

Contents

Acknowledgements.....	i
Abstract	vi
Keywords.....	vii
Résumé.....	viii
Mots-clés	ix
List of Figures	xv
List of Tables	22
Chapter 1 Introduction.....	24
1.1 Thesis’s motivations and main aims	27
1.2 Strategy and thesis’s outline	27
Chapter 2 A short review of fuel behavior and fuel modeling	29
2.1 Nuclear fuel configuration in LWR	29
2.2 Fuel behavior during irradiation	31
2.3 Fuel modeling approaches	40
2.4 Main components of a fuel performance code	41
2.4.1 Thermal analysis	41
2.4.2 Stress analysis	43
2.4.3 Main phenomena affecting the gap size	44
2.4.4 Fission gas release	45
2.4.5 Neutronics analysis	46
2.4.6 Chemical analysis.....	47
2.4.7 Base irradiation vs. transient analysis	47
2.5 Conclusions	48
Chapter 3 Finite volume framework for fuel performance	49

3.1	Governing equations and constitutive relations.....	50
3.2	Discretization procedure.....	52
3.2.1	Domain.....	52
3.2.2	Temporal terms	53
3.2.3	Volume source terms.....	54
3.2.4	Heat flux and forces over internal faces.....	54
3.2.5	Heat flux and forces over boundary faces.....	57
3.2.6	Final form of the discretized equations.....	58
3.3	Multi-dimensional analysis	59
3.4	Conclusions	63
Chapter 4	Numerical developments	65
4.1	The gap and the AMI mapping algorithm	65
4.2	Gap heat transfer methodology.....	68
4.2.1	Issues with the thin gap approximation	68
4.2.2	Discretization of the gap heat fluxes	68
4.3	Contact methodology.....	71
4.3.1	Explicit contact based on the penalty method.....	72
4.3.2	Implicit contact with closed gap and conformal, orthogonal meshes	73
4.3.3	Frictional component	76
4.3.4	Correction for non-orthogonal boundaries and non-conformal meshes ...	77
4.3.5	Transition between open and closed gap	80
4.3.6	The sigmoid blending function	82
4.3.7	Implicit contact for boundaries with different geometry and orientation .	84
4.4	Conclusions	86
Chapter 5	The multi-dimensional fuel behavior code OFFBEAT	88
5.1	Software framework	88
5.2	Code structure and solution strategy	89
5.2.1	Solution strategy.....	90
5.2.2	Relaxation factors	94
5.3	Thermal sub-solver.....	95

5.4	Mechanical sub-solver	97
5.5	Gap model	99
5.6	Neutronics and burnup model	101
5.7	Fission gas release model	103
5.8	Material and behavioral models	104
5.8.1	UO ₂	104
5.8.2	Zircaloy	108
5.9	Rheology	110
5.9.1	Instantaneous and rate-dependent plasticity: mathematical model	110
5.9.2	Instantaneous plasticity model: Von Mises plasticity	112
5.9.3	Instantaneous plasticity model: numerical implementation	113
5.9.4	Zircaloy creep: Limbäck model	114
5.9.5	UO ₂ creep: MATPRO model	115
5.9.6	Time dependent creep: numerical implementation	116
5.10	Multi-physics and coupling options	117
5.11	Conclusions	119
Chapter 6	Verification, validation, and demonstration cases	121
6.1	Verification	122
6.1.1	Steady-state and transient temperature profile	122
6.1.2	Steady-state stress profile	124
6.1.3	Contact benchmarks: verification of implicit contact methodology	125
6.1.4	Contact benchmarks: 2-D punch test	129
6.1.5	Contact benchmarks: 3-D punch test with rounded edge	132
6.1.6	Plasticity benchmark	138
6.1.7	Creep benchmark	139
6.2	Validation	141
6.2.1	IFA-562.1	141
6.2.2	IFA-432	143
6.2.3	Super Ramp	144
6.2.4	Risoe AN3 and Risoe AN2	147

6.3	Multi-dimensional demonstration cases	149
6.3.1	RIA scenario with MPS defect.....	149
6.3.2	Constant irradiation with cladding ridges formation	153
6.4	Conclusions	159
Chapter 7	Effect of eccentricity on fuel disc irradiation.....	160
7.1	Effect of eccentricity during irradiation	161
7.2	Experimental campaigns	161
7.2.1	Test 1: the High Burnup Rim Project	162
7.2.2	Test 2: the fuel creep test.....	163
7.3	2-D analysis	165
7.3.1	Modeling approach and assumptions	165
7.3.2	Results and discussion	168
7.3.3	Parametric study on the gap heat transfer model	170
7.4	3-D analysis of eccentricity	171
7.4.1	Modeling approach and assumptions	171
7.4.2	Results.....	172
7.5	Conclusions	177
Chapter 8	Multi-physics and coupling options	179
8.1	Coupling with the Monte Carlo neutron transport code Serpent	180
8.1.1	Coupling strategy	181
8.1.2	PWR test case	183
8.1.3	Gd-doped BWR test case	187
8.1.4	Remarks and outlook.....	191
8.2	Coupling with TRANSURANUS.....	192
8.2.1	Coupling strategy	192
8.2.2	Risoe3 AN3 segment simulation setup.....	194
8.2.3	Verification against a stand-alone TRANSURANUS simulation	197
8.2.4	Results.....	199
8.2.5	Remarks and outlook.....	202
8.3	Conclusions	202

Chapter 9	Conclusions.....	205
9.1	Main outcomes and takeaways	205
9.2	Future Works.....	207
9.2.1	Thermo-mechanics framework and code structure.....	207
9.2.2	Gap heat transfer and contact methodologies	208
9.2.3	Validation.....	209
9.2.4	Possible code extensions.....	210
9.2.5	Separate effect studies	211
9.2.6	Coupling with Serpent	211
9.2.7	Coupling with TRANSURANUS	211
9.3	Closing remarks	212
References		213
Curriculum Vitae		226

List of Figures

Figure 1.1 – Scheme of a typical LWR fuel rod.	24
Figure 2.1 – Example of FAs for BWR and PWR. From [12].	31
Figure 2.2 – Typical temperature profile in a LWR rod under axisymmetric conditions. The maximum fuel temperature is significantly lower in the annular pellet compared to an equivalent solid pellet.	33
Figure 2.3 – UO_2 thermal conductivity as a function of temperature and burnup. The plot is obtained employing the MATPRO model [46].	34
Figure 2.4 – Typical radial power profile for LWR fuel at the Beginning Of Life (BOL) and at the End Of Life (EOL) according to the TUBRNP model [17]. The figure comes from [12]. The normalized power becomes progressively more peaked with burnup.	35
Figure 2.5 – On the left, hourglassing of fuel pellets and formation of ridges (bambooing) [50]. The colour map shows the distribution of the equivalent or von Mises stress. On the right, example of chamfered and dished pellet. .	36
Figure 2.6 – Axial (left) and horizontal cross section (right) from the post irradiation examination of a commercial LWR fuel pellet. From [12].	37
Figure 2.7 – Typical modeling of creep strains, divided into primary, secondary and tertiary creep.	38
Figure 2.8 – Example of relocation model. From FRAPCON 3.4 [61]. The gap closure is given as a function of linear heat rate and burnup. A saturation value is reached after $\sim 5 \text{ MWd/kgU}$	45
Figure 3.1 - Polyhedral cell or Control Volume (CV). From [33].	53
Figure 3.2 – Non-orthogonal correction vectors.	56
Figure 3.3 – 2-D block (top-left), 1-D slab (top-right) and r - θ case (bottom) with the use of empty boundary conditions.	60
Figure 3.4 – Example of use of wedge boundary conditions: a 3-D 5 pellet rodlet (on the left) is reduced to a 2-D r - z case (on the right).	61
Figure 3.5 – The combination of wedge and empty boundary conditions produces a 1-D radial slice (left). If several slices are stacked on top of each other, separated by empty boundary conditions, OFFBEAT can perform 1.5-D simulations.	62

Figure 4.1 - Non-conformal master and slave surfaces facing each other across the gap (left). The AMI mapping algorithm reconstructs a single virtual opposing slave cell for each face on the master side (right), and vice versa.....	67
Figure 4.2 – Circuit of thermal resistances between master cell-center and slave cell-center.	69
Figure 4.3 – Example of contact between master cell in Pm and slave cell in Ngs. The meshes are orthogonal and conformal.	74
Figure 4.4 – Non-orthogonal correction vectors for master cell in Pm and slave cell in Ngs. The meshes are supposed to be conformal.....	78
Figure 4.5 – Non-orthogonal correction for non-conformal boundaries. The AMI method introduces non-orthogonality even in the presence of orthogonal original boundaries.	80
Figure 4.6 – Non-orthogonal correction with open-gap. The owner face-center must be projected on the neighbor face to calculate the neighbor traction.81	
Figure 4.7 – Sigmoid blending function. The offset o and the half-width h are shown.....	83
Figure 4.8 – Effect of changing offset and half-width on the blending function curve.	83
Figure 4.9 – Boundaries with different orientation. The owner face-center (the master face-center in this example) is projected along the common normal \mathbf{n}_g^*	85
Figure 5.1 – Simplified class structure of OFFBEAT. The main dependencies are shown with arrows.	92
Figure 5.2 – Segregated solution scheme adopted for OFFBEAT.....	93
Figure 5.3 – Decomposition of the free volume into V_{gap} and V_{plenum} . The central hole volume V_{hole} present in some fuel designs is also included in the Figure.	100
Figure 5.4 – Typical modeling of plastic loading and unloading cycle. When the load is removed only the elastic component of the strain is recovered...	111
Figure 5.5 – Summary of main options for coupling and interaction considered in the development of OFFBEAT.....	119
Figure 6.1 – Analytic and numerical temperature profile for the steady-state case.	123

Figure 6.2 – Analytic and numerical temperature profile for the transient power ramp case with Dirichlet boundary condition (fixed temperature on the outside of the fuel pellet).	124
Figure 6.3 – Analytic and numerical stress profiles (radial and hoop) for the steady-state case.	125
Figure 6.4 – Bi-material cylinder, dimensions (left), load for case with uniform internal pressure (center) and load for case with outer tangential traction (right).	126
Figure 6.5 - Radial stress in bi-material cylinder with inner pressure p_i for various E_1/E_2 ratios.	128
Figure 6.6 - Hoop stress in bi-material cylinder with inner pressure p_i for various E_1/E_2 ratios.	128
Figure 6.7 - Shear stress in bi-material cylinder with tangential load τ for various E_1/E_2 ratios.	128
Figure 6.8 - Circumferential displacement in bi-material cylinder with tangential load τ for various E_1/E_2 ratios.	129
Figure 6.9 – Two-dimensional frictionless punch test: model (right) and mesh detail of the contact region (left).	130
Figure 6.10 – Two-dimensional punch test: contact stresses on the cylinder outer surface.	131
Figure 6.11 – Residuals against number of iterations for Case 3 on the finest mesh. Residuals are shown both for the implicit contact and penalty-method based boundary conditions.	132
Figure 6.12 – Punch test with rounded edge, 2-D wedge model: main dimensions (left) and detail of the finest mesh (Level 3) near the contact area (right).	133
Figure 6.13 – Punch test with rounded edge, axial displacement on the foundation top edge. On the left, the results obtained for the frictionless contact case. On the right, the results obtained with a friction coefficient equal to 0.1.	134
Figure 6.14 – Punch test with rounded edge, contact stress on the foundation top edge. On the left, the results obtained for the frictionless contact case. On the right, the results obtained with a friction coefficient equal to 0.1.	135
Figure 6.15 – Punch test with rounded edge, radial displacement on the foundation top edge. On the left, the results obtained for the frictionless contact case. On the right, the results obtained with a friction coefficient equal to 0.1.	135

Figure 6.16 – Punch test with rounded edge: three-dimensional computational model for the finest mesh refinement level.....	137
Figure 6.17 – Punch test with rounded edge: axial displacement on foundation top horizontal edge calculated with the most refined 3-D model. The reference solution calculated with Code Aster on a 2-D wedge model (and the respective implicit contact 2-D solution) are included in the graph.....	137
Figure 6.18 – Radial, tangential, and axial stresses for the plasticity benchmark case. Both the reference values and the results obtained with OFFBEAT are shown.....	139
Figure 6.19 – Predicted temperature against measured temperature for the lower cluster rods of the IFA-562.1. The burnup varies from 0 to ~10 MWd/kgU. Only the values of the lower TCs are reported in the graph.....	142
Figure 6.20 – Predicted temperature against measured temperature for the upper cluster rods of the IFA-562.1. The burnup varies from 0 to ~10 MWd/kgU. Only the values of the lower TCs are reported in the graph.....	143
Figure 6.21 – Predicted temperature against measured temperature for Rod 1, Rod 3 and Rod 5 of the IFA-432. The burnup varies from 0 to ~40 MWd/kgU.	144
Figure 6.22 – Plot comparing calculated and measured FGR fraction for PK and AN rods.	147
Figure 6.23 – Comparison between the FCT measured during the experiment and the FCT calculated by OFFBEAT for the Risoe3 AN3 segment.....	148
Figure 6.24 – Comparison between the FGR% measured during the experiment (from pressure transducer and from puncturing) and the one calculated with OFFBEAT for the Risoe3 AN3 segment.	149
Figure 6.25 – RIA scenario test case: 3-D model of short rodlet with 5 pellets and a missing pellet surface defect. The two detailed views on the right show the defective region as well as the mesh.	151
Figure 6.26 – Hoop stress (left) and equivalent or von Mises stress (right) distribution on the inner side of the cladding at $t = 35$ ms. The stress concentration on the area directly facing the defect can be observed. ...	152
Figure 6.27 – Cumulative plastic strain at the end of the transient (i.e. $t = 50$ s).	153
Figure 6.28 – Power history for the ridging test-case rodlet. The time axis is not to scale.....	154

Figure 6.29 – Axisymmetric model used for ridging test-case rodlet simulations. The pellets are attached through the land region. A detail of the computational mesh is visible on the right.	155
Figure 6.30 – Outward displacement of inner and outer cladding (left). Color plot of the von Mises or equivalent stress (Pa) for a segment section of the cladding (right). The geometry is warped using the displacement field multiplied 50 times.	156
Figure 6.31 – Von Mises or equivalent stress on the inner and outer surface of the cladding at the end of the 180 days of constant power irradiation. The results for both elastic and non-elastic cladding are shown.....	157
Figure 6.32 – Outward displacement of inner and outer cladding surfaces at the end of the simulation (with the rod in thermal equilibrium with the coolant). Permanent deformations due to creep following the ridges structure are visible for the second case.....	158
Figure 7.1 - General scheme of the HBRP experiment [149]. The Figure shows the target temperatures and burnups.....	163
Figure 7.2 – Axisymmetric model for the separate-effect rods with discs. A reduced stack with 5 fuel discs is used to characterize the temperature distribution surrounding the TC position. Due to symmetry, the numerical model corresponds to the area overlaid with the mesh grid.....	166
Figure 7.3 – Results of the axisymmetric simulations. Temperatures obtained with OFFBEAT are plotted against the corresponding TC measurements.	168
Figure 7.4 – Results of the parametric study on the gap heat transfer model. Temperatures obtained with OFFBEAT are plotted against the corresponding TC measurements.....	171
Figure 7.5 – Cross section of the 100% eccentricity model used for the stack S41 from the first campaign (left). Detail showing the 2-D temperature distribution on a horizontal slice at the center of the eccentric molybdenum disc (right).	172
Figure 7.6 – Results of 3-D analysis for Rod1 of test 2 with varying degrees of eccentricity. Fuel centerline temperatures obtained with OFFBEAT are plotted against irradiation time. The measurements from centerline TC are included in the graph.....	173
Figure 7.7 – Results of 3-D analysis for stack S11 from test 1 with varying degrees of eccentricity. Outer molybdenum temperatures obtained with OFFBEAT are plotted against irradiation time. The measurements from the TC are included in the graph.....	174

Figure 7.8 – Results of 3-D analysis for stack S41 from test 1 with varying degrees of eccentricity. Outer molybdenum temperatures obtained with OFFBEAT are plotted against irradiation time. The measurements from the TC are included in the graph.....	175
Figure 7.9 – Results of 3-D simulations with 0 and 100% eccentricity for the test 1 stacks. The calculated temperatures are plotted against the corresponding measurements.	176
Figure 7.10 – Impact of eccentricity against Biot number for the stacks from Test 1. The impact of eccentricity is measured as $\Delta T_{100\%}$, i.e. the average temperature difference between the simulations with 100% and those with 0% eccentricity.....	177
Figure 8.1 - Flowchart of the external coupling between OFFBEAT and Serpent	182
Figure 8.2 – PWR case Serpent model.....	184
Figure 8.3 – Comparison between the plutonium concentration evolutions calculated by TUBRNP and the OFFBEAT-Serpent coupling.....	185
Figure 8.4 – Comparison between the Pu^{239} radial concentration obtained with OFFBEAT/Serpent and TUBRNP at 5 MWd/kgHM (left) and 100 MWd/kgHM (right).	185
Figure 8.5 – Comparison between the U^{235} radial concentration obtained with OFFBEAT/Serpent and TUBRNP at 50 MWd/kgHM (left) and at 100 MWd/kgHM (right).	186
Figure 8.6 – Comparison between the normalized radial power profile obtained with OFFBEAT/Serpent and TUBRNP at 50 MWd/kgHM (left) and at 100 MWd/kgHM (right).	186
Figure 8.7 – BWR case Serpent model.....	188
Figure 8.8 – Comparison between the plutonium concentration evolutions with TUBRNP and the coupling for the Gd-doped BWR.....	189
Figure 8.9 – Comparison between the Pu^{239} radial concentration obtained with OFFBEAT/Serpent and TUBRNP for the Gd-doped rod at 5 MWd/kgHM (left) and at 100 MWd/kgHM (right).	189
Figure 8.10 – BWR case, comparison between OFFBEAT/Serpent and TUBRNP: the evolution of the Gd^{155} and Gd^{157} total concentration is shown on the left; the power peaking factor or normalized radial power profiles at 1, 3 and 10 MWd/kgHM is shown on the right.	190

Figure 8.11 – Comparison between the normalized radial power profile obtained with OFFBEAT/Serpent and TUBRNP at 100 MWd/kgHM for the BWR test case.	191
Figure 8.12 – Coupling scheme between TRANSURANUS and OFFBEAT. .	194
Figure 8.13 – Full (left) and bump test (right) irradiation history for the AN3 segment. The power is normalized to the bump test peak value.	195
Figure 8.14 – Three OFFBEAT models coupled to TRANSURANSUS for the study of the AN3 segment.	196
Figure 8.15 – Cladding permanent deformations at the end of the bump test. The rod atmosphere is not changed between base irradiation and bump test. The values are given as diametral variation with respect to the cold state at the start of the bump test as calculated by TRANSURANUS. The values obtained with the 1.5-D OFFBEAT model and with the TRANSURANUS standalone run are compared.	199
Figure 8.16 – Cladding permanent deformations at the end of the bump test. The values are given as diametral variation with respect to the cold state at the start of the bump test as calculated by TRANSURANUS. The values obtained with the three OFFBEAT models are compared with the experimental measurements.	200
Figure 8.17 – Cladding permanent deformations at the end of the bump test. The values are given as diametral variation with respect to the cold state at the start of the base irradiation. The isotropic cracking model is now switched off. The experimental measurements are included.	201

List of Tables

Table 6.1 – Dimensions and case properties for the steady-state verification case	123
Table 6.2 – Punch test with rounded edge: running times for the frictionless case on wedge geometry. The results are shown for each mesh refinement level (the number of cells and the number of faces is indicated) both for the implicit and penalty method.....	136
Table 6.3 – Punch test with rounded edge: running times for the frictionless case on 3-D geometry. The results are shown for each mesh refinement level (the number of cells and the number of faces is indicated) both for the implicit and penalty method.....	138
Table 6.4 – Plasticity verification case: stress components at the end of step 6.	139
Table 6.5 – Creep benchmark setup.....	140
Table 6.6 – Creep verification case: results compared against analytical solution [111].	140
Table 6.7 – Comparison between calculated and measured integral FGR for PK and AN rods.	146
Table 6.8 – Dimensions and specifics for the RIA scenario test case	150
Table 6.9 – Dimensions and specifics for the ridging test case	154
Table 7.1 - Dimension and design parameters of the HBRP rods [149]. ...	163
Table 7.2 - Dimension and design parameters of the fuel creep test rods [150].	164
Table 7.3 –Time-averaged quantities for the calculation of the Biot number for Test 1.....	177
Table 8.1 - PWR case characteristics	183
Table 8.2 - BWR case characteristics	188
Table 8.3 – Comparison against PIE data for two TRANSURANUS simulations of the AN3 segment. The first simulation employs the URGAS module while the second one employs the SCIANTIX module. The cladding deformations are severely underpredicted.....	197
Table 8.4 - Comparison against PIE data for a full-history TRANSURANUS simulations of the AN3 segment employing SCIANTIX as fission gas release module. The cladding creep model is multiplied by a factor of 2x to increase	

creep-down and obtain higher cladding deformations at the end of the base irradiation. 197

Table 8.5 – Comparison with the measured fission gas release fraction for the three coupled simulations. **Errore. Il segnalibro non è definito.**

Chapter 1

Introduction

The fuel used in nuclear reactors is exposed to severe thermomechanical conditions, an intense radiation field and a corrosive environment. Its response during reactor operation is the result of a complex set of heterogeneous phenomena taking place at different time and length scales, including heat transfer, contact, plasticity, creep, cracking, isotope transmutation and corrosion.

The analysis and simulation of fuel behavior is the main concern of the branch of nuclear engineering named *nuclear fuel modeling*. Fuel scientists and fuel modelers are often asked to assess the state of the nuclear fuel, accurately predicting the temperature and stress/strain distribution under specific irradiation conditions. Since an analytical treatment is made impossible by the sheer number of phenomena involved and by the high degree of interplay and non-linearity, the fuel modeling task takes advantage of specific software called *fuel performance* or *fuel behavior codes*.

After the first experiences in the late 1960s [1] with codes such as CYGRO [2] and COMETHE [3], several fuel performance codes have been developed in numerous institutes and laboratories around the world (an historical overview is provided by Van Uffelen et al. in appendix to their review article on fuel modeling [4]). As commercial Light Water Reactors (LWRs) constitute almost the totality of the currently operating reactor fleet [5], the main efforts have been focused on the pellet-in-cladding oxide fuel type used in these reactors. The scheme of a typical LWR rod is shown in Figure 1.1. Today, fuel performance codes are extensively used both in the nuclear industry and in research institutes for a variety of purposes. Representing a cheaper alternative to expensive fuel experiments (which nonetheless remain indispensable for validation and a deep understanding of fuel behavior), these codes have become an essential tool for ensuring the safe and economic operation of nuclear reactors and for a more efficient fuel design.

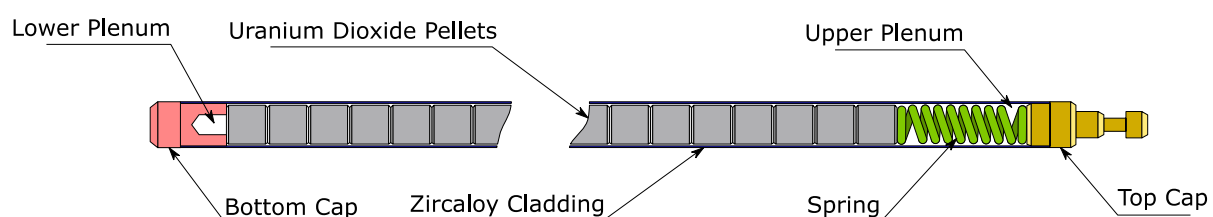


Figure 1.1 – Scheme of a typical LWR fuel rod.

Most of the fuel modeling software used today is *one-dimensional* (1-D), more precisely 1.5-D. That is, the fuel rod analysis is simplified by assuming axisymmetric conditions and axially subdividing the rod in few mechanically independent slices in plane strain. Axial coupling due to gap pressure and composition update is ensured by iterating the solution of the code over the slices. A non-comprehensive list of available codes includes the European fuel performance code TRANSURANUS developed at the JRC in Karlsruhe [6]; the FRAPCON/FRAPTRAN series developed by the NRC in the U.S. [7], [8]; the FEMAXI code developed by the JAEA in Japan [9]; and the ENIGMA code jointly developed by the BNFL and the CEBG in England [10]. As they are often the result of development efforts started decades ago, these codes are sometimes referred to as *legacy codes*.

The main reason behind the success of the 1-D approach is twofold. On the one hand, 1-D codes are simpler to program and have better performance than higher-dimensional counterparts: certainly, the modest computational power available in the early decades of fuel modeling made *two-dimensional* (2-D) and *three-dimensional* (3-D) simulations difficult or impossible to achieve. On the other hand, most of the data used in fuel performance codes for validation purposes or as input for the main behavioral models are intrinsically 1-D if not 0-D. Indeed, many of the models included for treating meso-scale or atomistic-scale processes that take place in the fuel rod are semi-empirical correlations often developed assuming a 1-D framework [11]. The experimental measurements used in validation campaigns are typically *integral results*, such as the fuel temperature at a single thermocouple location or the total fission gas released during irradiation. Finally, the intrinsically multi-dimensional aspects of the LWR fuel such as the pellet crack pattern are characterized by large uncertainties [12] and have been treated with simplified axisymmetric models to capture the average behavior of the rod.

In the last two decades, following the increase of computational power and the availability of High-Performance Computing (HPC), the fuel performance community has shown a growing interest towards the development of higher fidelity tools with multi-dimensional capabilities. This interest is demonstrated by international projects like the NEA PCMI benchmark [13] and by efforts like the development of BISON [14] at the INL, of DIONISIO [15] at CNEA, and of ALCYONE [16] at CEA, FRAMATOME and EDF.

As multi-dimensional data and models are still largely missing, one might question the added value of such endeavors. However, when envisioned as a support and not as a replacement for the traditional fuel behavior analysis, the modern higher fidelity tools provide interesting modeling opportunities and open new research avenues for fuel performance applications [11]. Despite the use of behavioral models derived from legacy codes, a multi-dimensional analysis allows one to capture phenomena which are simply out of reach for the classic 1-D approach. For example, a 2-D simulation with discrete modeling of single pellets can reproduce the formation of the so-called ridge pattern in the cladding. The stress concentration in the ridges is relevant for the study of pellet-cladding interaction and ultimately for assessing the integrity of the rod. A 3-D code enables the modeling of complex and poorly known phenomena such as the presence of a defective pellet, an

explicit cracking pattern as opposed to the use of a simplified isotropic cracking model, or an asymmetric heat exchange that might be relevant during an accident scenario. Although similar simulations might be challenging to conceive and interpret (how large should the defect be? how many cracks are realistic? what about their orientation?), their use can improve the understanding of very complex aspects of fuel behavior that limit the performance of LWR fuel rods and might suggest novel research directions for new studies or experiments.

Also, the limitations of current simplified 1-D models can be partly overcome by coupling the multi-dimensional fuel performance code with separate solvers for neutronics, thermal-hydraulics or other physics. For example, the coupling with a Monte Carlo neutron transport code provides a higher fidelity solution for the neutron flux and for the isotope transmutation in the fuel pellet if compared to traditional simplified neutronics models like TUBRNP [17]. Indeed, efforts have been carried out in various laboratories to integrate some of the most recent higher fidelity fuel analysis tools in a framework for multi-physics and multi-scale simulations [18] [19].

Finally, the combination of traditional analysis with 2-D or 3-D simulations could lead the fuel performance community either towards the development of newer behavioral models better suited for multi-dimensional applications or towards an improvement of the existing ones. This could be achieved, for example, by means of analysis of separate effect tests, which are often characterized by unconventional configurations and might allow the transfer of information from higher-dimensional studies to 1-D codes.

While less of a concern for legacy codes, the choice of the most appropriate numerical methodology becomes relevant with the advent of multi-dimensional tools. The higher-fidelity codes like BISON or ALCYONE that have been developed until now have employed the Finite Element Method (FEM). This follows a long tradition in Computational Solid Mechanics (CSM) and the example of well-known software like ANSYS [20] or COMSOL [21]. Despite the FEM representing a traditional choice for CSM, the Finite Volume Method (FVM) has also proven to be a viable alternative for CSM applications, beside representing a choice of reference for Computational Fluid Dynamics (CFD). Since the seminal work of Jasak and Weller [22] and that of Demirdžić [23], the FVM has been applied to a wide range of problems from welding [24], [25] and extrusion processes [26], to viscoelasticity [27], [28], contact mechanics [29], [30], dynamic fracture [31], crack propagation [32] and many others.

Additionally, the FVM is characterized by promising features for multi-physics applications. Its simple and conservative formulation based on control volume balances is considered beneficial in a complex environment requiring the collaboration of several experts and the handling of different physics. Relevant routines for multi-physics calculations such as the projection of fields between meshes are simplified when the underlying numerical scheme relies on conservative control volume balances. Also, the coupling with CFD would benefit from adopting the same discretization method [33] instead of following the alternative approach of using the FVM for fluid dynamics and the FEM for solid mechanics. Despite these interesting aspects relevant for fuel modeling and de-

spite the advancements of the last decades summarized in the comprehensive review of Cardiff [34], the FVM has not yet been explored by the fuel performance community.

1.1 Thesis's motivations and main aims

This PhD thesis moves from the growing interest of the fuel performance community towards multi-dimensional and multi-physics tools discussed in the previous paragraphs. The triggering event was a recent fuel failure that took place in a Swiss Nuclear Power Plant (NPP) and the extensive root cause analysis that was launched to identify potential new effects [35]. This highlighted the lack of a readily available tool for the study of complex multi-dimensional phenomena like the effect of asymmetric intra-pin power profiles and thick non-uniform oxide and/or crud layers on the fuel integrity.

At the same time, the thesis is motivated by the unexplored potential of the FVM for fuel behavior analysis, with the FVM representing a significant expertise in the laboratories at PSI and EPFL that are involved in this thesis work. Leveraging on this expertise, this thesis aims to develop a novel Finite Volume (FV) methodology for the analysis of complex multi-dimensional fuel behavior phenomena and investigate its potential role in the modern fuel performance landscape. The primary objective of the thesis is to demonstrate the feasibility of such methodology, validate its accuracy against experimental data and test its performance.

Serving the needs and trends of modern fuel modeling approaches, the new methodology is envisioned as a readily available and flexible tool, straightforward to extend and modify. Embedded in a modern CFD-like framework, the new tool is designed to be open to multi-physics simulations and to interact with other codes relevant to the community. For this reason, the thesis also sets out to create a first set of coupling tools that can complement the FV fuel performance methodology and help to expand further the frontier of fuel modeling.

1.2 Strategy and thesis's outline

To achieve the aims and objectives described in the previous section, a novel FV fuel performance code was developed in the framework of this thesis. The code is named **OpenFOAM Fuel BEhavior Analysis Tool** or OFFBEAT, and it is based on the C++ library OpenFOAM® [36], [37]. This well-known open-source library has been used already in the field of nuclear reactor modeling for neutronics [38], [39], thermal-hydraulics [40], [41] and for the creation of a multi-physics reactor simulation platform named Gen-Foam [42].

Building on the works of Jasak, Weller, Tuković and Cardiff, OFFBEAT is developed according to a cell-centered FV framework for total Lagrangian, small strain solid mechanics. This is combined with a framework for thermal analysis and with numerical developments concerning the treatment of the gap heat transfer and contact, based on a mapping algorithm that allows the use of independent non-conformal meshes for fuel and cladding. The code considers the temperature and burnup dependence of the material properties, and it can model fuel densification, relocation,

swelling, growth, fission gas release, creep, plasticity, and other relevant fuel behavior phenomena.

The development approach followed in this work is certainly not the only possible for a FV fuel performance code. For this reason, after the introductory Chapter 2 reviewing the basics of fuel behavior and fuel modeling, the development strategy is presented with a series of three chapters. First, the numerical structure that lays at the foundation of the code is outlined in Chapter 3 in terms of governing equations, constitutive relations, and discretization techniques. The mapping, gap heat transfer and contact methodologies are presented in Chapter 4. Finally, the structure of OFFBEAT with its main components and modules, and with its overall solution scheme is described in detail in Chapter 5.

To test the accuracy of the novel FV fuel performance methodology, the development of OFFBEAT proceeds in parallel with verification tests and validation campaigns. Additional 2-D and 3-D cases are created to test the capability of the code to capture relevant multi-dimensional features in simplified but realistic scenarios. These testing and validation efforts are summarized in Chapter 6.

The methodology developed in this thesis is then used to investigate the potential role of multi-dimensional codes in the modern fuel performance landscape. An interesting area of application is offered by separate effect experiments which are often characterized by intrinsic 2-D or 3-D features that cannot be captured with legacy codes. Also, they are small in scale if compared against commercial LWR rods so that the increase in computational cost due to a higher dimensional simulation becomes less of a burden. An example of this possible application is given in Chapter 7 where, in the framework of a collaboration with the JRC in Karlsruhe, two fuel disc irradiation campaigns performed in the past are selected because of their peculiar configuration characterized by a large gap and a high conductive fuel.

Two additional methodologies and associated tools are developed to extend the capabilities of OFFBEAT and are presented in Chapter 8. The first one enables the coupling with the Monte Carlo neutron transport code Serpent2 [43] allowing for a more accurate fuel power distribution in conditions that are outside the realm of application of the simplified 1-D models. This includes new fuel types, fuel with strong neutron absorbers like those used in some LWR, and unconventional configurations. The second developed coupling is between OFFBEAT and the legacy code TRANSURANUS. Taking advantage of the strength of both codes, the main aim is to use a well-established, validated, and fast 1-D code to simulate the base irradiation and set accurate initial conditions for a multi-dimensional transient performed with OFFBEAT. The final summary discussions, outlook and conclusions for this thesis outlined in Chapter 9.

Chapter 2

A short review of fuel behavior and fuel modeling

Although not concerned with the development of new experimental techniques or theoretical models for fuel behavior analysis, this PhD thesis is interested in extending the numerical capabilities within the fuel modeling community and it deals with the development of a novel fuel performance code. Therefore, this initial chapter provides a concise review of fuel behavior and fuel modeling as an introduction to the work done as part of the thesis. The chapter is aimed both at the engineer who is not familiar with nuclear fuel and is looking for a brief introduction with an outline of the main references, and at a more experienced audience who is looking for a quick revision. More comprehensive works on fuel behavior and fuel modeling can be found in the two articles by Van Uffelen et al. [4], [12], or in Olander's seminal book [44].

The first two sections of this chapter focus on a phenomenological description of the nuclear fuel. Section 2.1 outlines the typical geometrical and material arrangement of the nuclear fuel rod used in LWRs, while Section 2.2 describes the main phenomena characterizing the fuel behavior during irradiation. The last two sections shift the attention on fuel modeling, with Section 2.3 describing the main modeling approaches commonly followed in the field, and Section 2.4 giving an overview of the structure and main components of a typical fuel performance code.

2.1 Nuclear fuel configuration in LWR

The energy produced by a nuclear reactor derives from the **fission** reactions that take place inside the nuclear **fuel**, where atoms of uranium or heavier elements are continuously split by the neutrons that move inside the reactor. A tremendous amount of heat is released in the process, together with two lighter atoms called **fission products** and two (or three) neutrons. Although high energy or **fast** neutrons (> 10 keV) can be used to sustain the fission chain reaction, almost the totality of the reactor fleet currently operating around the world employs low energy (< 1 eV) or **thermal** neutrons to consume the so-called **fissile** atoms, i.e. fuel isotopes with a high probability of being fissioned by thermal neutrons. The most common fissile isotope used for energy generation is U^{235} , the only one found directly in nature; other fissile isotopes such as Pu^{239} or Pu^{241} are also used, but they must be produced in advance in a nuclear reactor, through a series of neutron **capture** reactions starting from U^{238} (the main constituent of natural uranium).

Water cooled reactors represent over 95% of the currently operating reactor fleet around the world [5]. The most common type is the Light Water Reactor (**LWR**), mainly in the form of Pressurized Water Reactor (**PWR**) or Boiling Water Reactor (**BWR**). In all commercial LWR designs, the fuel takes the form of small cylindrical **pellets** made of a ceramic material, with typical dimensions of ~ 1 cm in diameter and ~ 1 -2 cm in height. In the common Uranium OXide fuel type (**UOX**), the pellets are made of uranium dioxide (UO_2) with the uranium usually going through an **enrichment** stage [45] before being prepared by the fuel manufacturer. At the end of this process, the content of fissile isotope U^{235} is increased from the natural weight ratio of $\sim 0.7\%$ to a typical value ranging from 3 to 5%. Alternatively, in the Mixed Oxide fuel design (**MOX**), the pellets consist of a mixture of uranium and plutonium oxides (PuO_2), derived from the **reprocessing** of **spent** fuel previously used in another nuclear reactor.

The UO_2 or the $(\text{U,Pu})\text{O}_2$ oxides are first obtained as a fine powder, which is then cold pressed and finally sintered in a high temperature furnace to produce a pellet with $\sim 95\%$ theoretical density (TD). This is intentional and it is not a defect of the fabrication process. Indeed, a smaller amount of **porosity** (or a too dense fuel) would not be able to retain part of the gaseous atoms produced by the fission reactions, while a higher amount of porosity (or a lower density fuel) would affect the thermal conduction in the fuel. The production process also determines the **grain size** and the fuel **stoichiometry**. The latter is also referred to as **oxygen-to-metal ratio** (OM) and it is typically required to be closely equal to 2 as any deviation from this value has a significant effect on the fuel thermo-mechanical properties (particularly on its thermal conductivity).

Several fuel pellets, typically ~ 300 in commercial LWRs, are stacked on top of each other forming a column of ~ 3.5 m. The **fuel stack** or **fuel column** is encapsulated inside a slender metallic **cladding**, ~ 4 m in height. The cladding is made of Zircaloy, an alloy based on the element zirconium (Zr) chosen because of the good balance between its strength, corrosion resistance properties and low neutron capture cross section, i.e. its low probability of absorbing neutrons. Alloying elements such as oxygen, tin, iron, or niobium are added in different amounts according to the requirement of the specific Zircaloy produced, with the most common in the industry being the Zircaloy-2 for BWRs and the Zircaloy-4 for PWRs.

The cladding is *separated* from the pellets by a small **gap** of ~ 100 μm , and it is plugged and sealed at the two ends, forming the **fuel rod** already shown in Figure 1.1. The fuel rod constitutes the first barrier against the release of radioactive fuel material to the outer environment, thus its integrity is of primary importance for a safe operation of the nuclear reactor. Before being sealed with the **top cap**, the rod is pressurized with helium (He), which establishes a good thermal exchange due to its relatively high thermal conductivity, reaching an internal pressure of ~ 2 MPa in PWRs and ~ 3 bar in BWRs. The region between the end of the pellet stack and the rod top cap is called **plenum** and it provides additional room for the accumulation of the gaseous atoms produced by the fission reactions that manage to escape from the fuel matrix. The gas plenum also hosts a metal **spring** which limits the lateral movement of the pellet stack while allowing its axial expansion. Alumina (Al_2O_3) or natural uranium pellets are often used as **insulator** between the top of the fuel stack

and the plenum spring, as well as between the bottom pellet and the **lower end plug** or **bottom cap**.

The fuel rods are grouped together in bundles called **Fuel Assemblies** (FAs) submerged in the **coolant** fluid. Light or ordinary water (in particular, liquid water in PWRs and a mixture of water and steam in BWRs) is used in LWRs to remove the heat generated in the fuel and to produce steam and ultimately electricity. The cooling water also acts as **neutron moderator**, necessary to slow down the fast neutrons coming out of the fission process and sustain the chain reaction. The FAs can have different designs according to the reactor type, as shown in Figure 2.1 (from [12]) with two different examples for PWRs and BWRs. While the PWR FA design remains bare, the BWR FAs are encased within a metallic canister (not shown in the figure) that channels the flow of water through the assembly. The FAs are also equipped with additional components such as metallic spacer grids to fix the fuel rod positions, guide tubes, partial length rods, handles for moving the FA during refueling and loading operations, and inlet and outlet nozzles for the coolant. Finally, following the thermal-hydraulics and neutronics needs of the reactor design, the FAs are arranged in a specific configuration forming the reactor **core**.

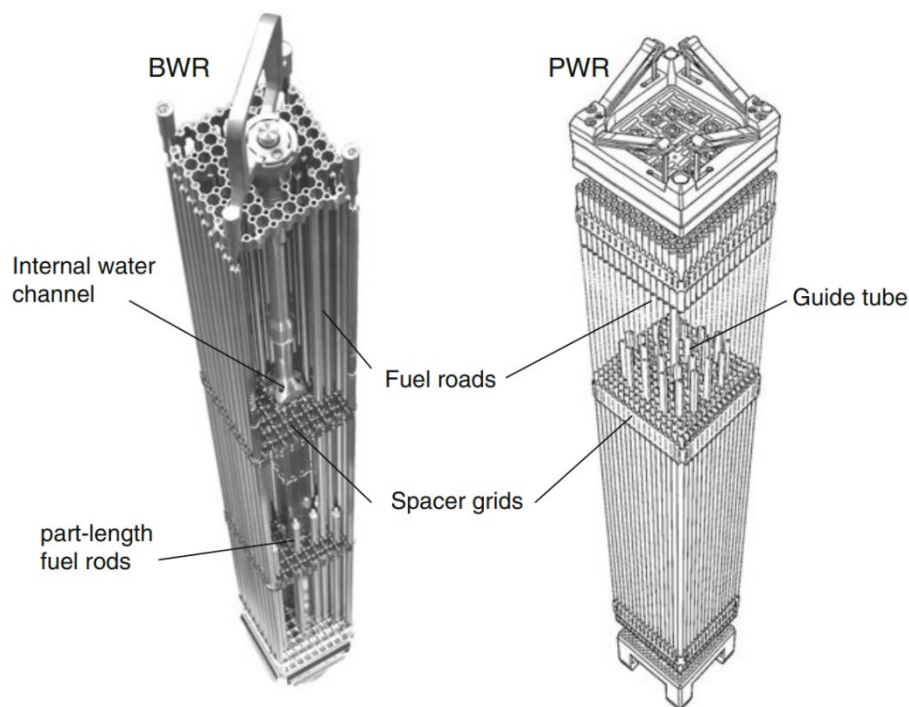


Figure 2.1 – Example of FAs for BWR and PWR. From [12].

2.2 Fuel behavior during irradiation

The thermo-mechanical behavior of the nuclear fuel rod during irradiation is influenced by a plethora of phenomena of different nature. The ability of the fuel pellet to dissipate the heat pro-

duced via fission is mainly affected by the degradation of the fuel thermal conductivity with burnup and by the formation of a radial power profile due to neutron flux self-shielding and non-uniform isotope transmutation. Thermal expansion, irradiation induced swelling and densification, relocation and cladding creep-down have the largest effect on the size of the gap width. This, together with the evolution of the gap gas composition due to fission gas release, determines the thermal exchange through the gap. The presence of thermal gradients in the fuel not only causes the pellet to crack leading to relocation but also changes its stress state influencing the retention of fission gases in the fuel matrix. Once the gap is closed during irradiation, the mechanical interaction between the expanding fuel and the cladding is complicated by the presence of micro-cracks, corrosion layers, bonding, ridges, and other aspects which might threaten the integrity of the rod.

The following paragraphs provide a short overview of the main phenomena affecting fuel behavior now quickly mentioned. As the focus is on standard operating conditions, phenomena that become relevant only during accident scenarios are not discussed.

Heat production and temperature profile: Most of the ~ 200 MeV released by the fission reaction appears in the form of kinetic energy of the two fission products. Flying out in opposite directions, these heavy charged particles come quickly to rest transferring their energy to the atoms in the UO_2 matrix. Consequently, the fuel pellet heats up and releases its thermal energy to the cladding (through the gap) and ultimately to the coolant. Considering axisymmetric conditions, the temperature distribution assumes the typical profile shown in Figure 2.2: a parabolic shape in the pellet with the maximum temperature reached at the pellet center, and a mostly logarithmic shape in the cladding. In certain fuel designs (as done for the Russian reactors VVER) the pellets include a **central hole**. An example of **annular** pellet is shown on the left of Figure 2.2 together with the traditional **full** or **solid pellet** design used in Western reactors. The presence of the central hole significantly decreases the maximum fuel temperature as the average distance between heat source and heat sink is reduced (naturally, the power density of the annular pellet must be increased to maintain the same total power of an equivalent solid pellet).

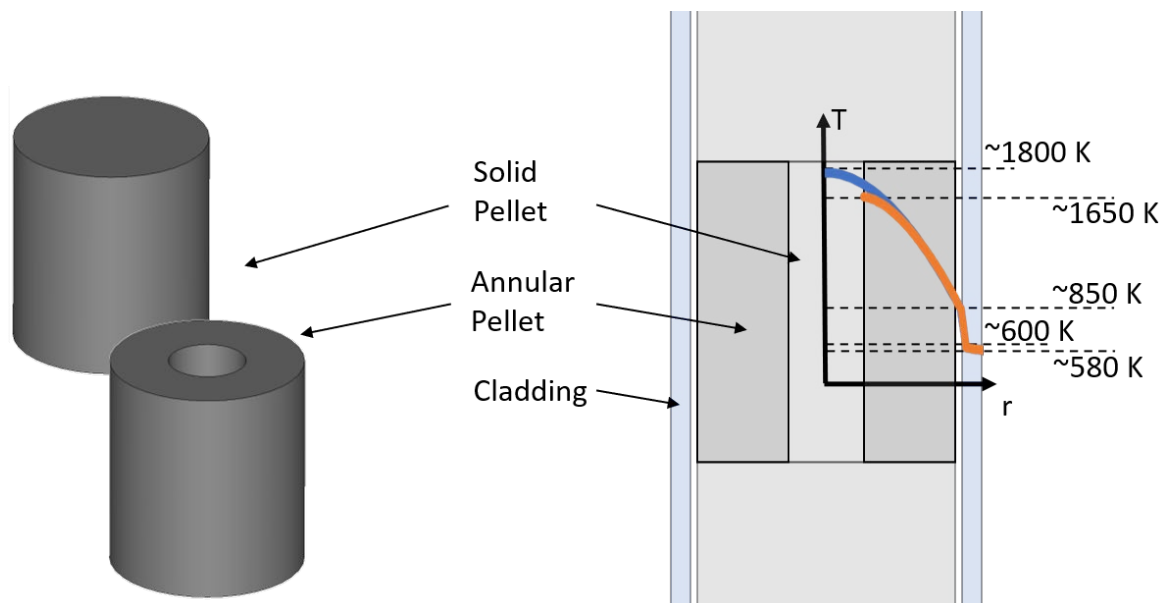


Figure 2.2 – Typical temperature profile in a LWR rod under axisymmetric conditions. The maximum fuel temperature is significantly lower in the annular pellet compared to an equivalent solid pellet.

Heat exchange with the coolant and heat conduction through the cladding: The temperature on the outer cladding wall is determined by the coolant thermal-hydraulics conditions such as velocity, flow regime and temperature, and by the total power produced in the fuel. In both PWRs and BWRs, the temperature jump between the coolant and the cladding remains quite small during normal operating conditions, as the flow of water (or of the mixture of water and steam) is designed to provide efficient cooling. As shown in Figure 2.2, the temperature difference across the cladding is also small, limited to some tens of degrees, due to the slender nature and the high conductivity ($\sim 15\text{--}20\text{ W/mK}$) of the Zircaloy tube.

Gap heat transfer: The temperature jump across the gap is typically in the range of a few hundred degrees, although its actual value varies significantly during the lifetime of the rod. In the first stages of irradiation, when the gap is partially open, the heat is transferred mainly via conduction through the gas, determined primarily by the gap width and the gap gas composition. A radiative component is also present, but it constitutes only a small fraction of the total gap heat transfer because of the limited surface temperatures. Over time, the gap size changes, affected by the complex interplay of phenomena outlined in this section. Also, the filling gas originally composed of pure He is progressively poisoned by the low-conductive gaseous atoms (Xe and Kr) that manage to escape from the fuel matrix. Eventually the gap closes, and at this stage a large fraction of heat is transferred via conduction through the points of contact.

Heat diffusion in the pellet: The heat generated in the fuel is removed via conduction, but the low **thermal conductivity** of the ceramic oxides results in relatively high temperatures and thermal gradients. The diffusion of heat in fresh UO_2 is a temperature-dependent phenomenon determined primarily by two mechanisms: the scattering of phonons by interaction with lattice imper-

fections or other phonons; and the excitation of free electrons. Below ~ 1500 K, the heat diffusion by phonons prevails, and the conductivity decreases as the fuel gets hotter as shown in Figure 2.3. After a minimum at ~ 2000 K, the excitation of free electrons becomes the dominant mechanism, and the conductivity starts to increase with the temperature. An important aspect to consider in the design of the reactor is the **degradation of the fuel thermal conductivity** during irradiation, also shown in Figure 2.3. This phenomenon is caused primarily by the accumulation of point defects created by the fission fragments knocking atoms out of their position in the crystal lattice, with the point defects acting as scattering center increasing phonon scattering. For the same reason, the thermal conductivity is also a function of the oxygen-to-metal ratio and of the content of PuO_2 (relevant mostly for MOX fuels) and neutron absorbers such as Gd_2O_3 present in the fuel matrix. Additionally, the conductivity is strongly affected by the pellet porosity as the pores are filled with gas and are poor heat conductors. Thus, the higher the porosity, the lower is the fuel's capacity to remove the heat generated by the fission reactions.

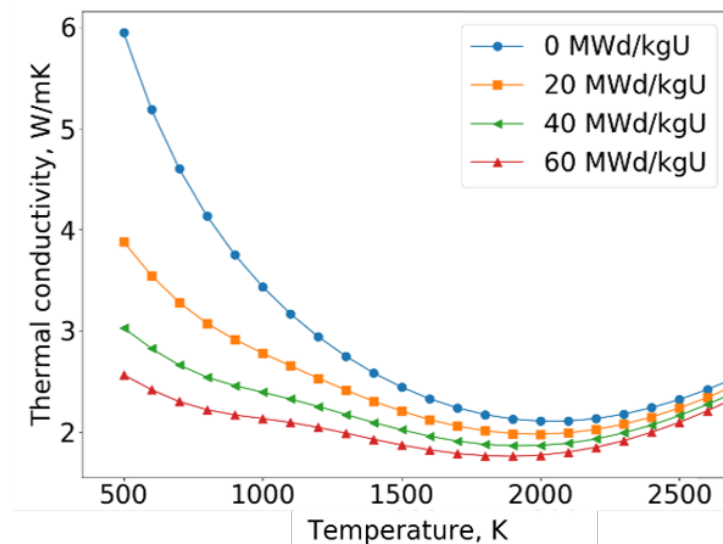


Figure 2.3 – UO_2 thermal conductivity as a function of temperature and burnup. The plot is obtained employing the MATPRO model [46].

Fuel isotopic evolution: During irradiation, the isotopic composition of the fuel changes: the fissile atoms are consumed by the fission reactions leading to the buildup of fission products; and the atoms of U^{238} are converted by progressive neutron capture reactions to higher actinides, including fissile isotopes such as Pu^{239} , Pu^{241} and Am^{241} . The speciation of the fuel and its stoichiometry are changed as well by the transmutation and buildup processes, potentially affecting the fuel thermo-mechanical properties like conductivity. The distribution of the fissile isotopes and the energy they generate via the fission reactions is not uniform across the pellet. Under axisymmetric conditions, a radial profile establishes with a characteristic **peak** at the pellet rim as shown for the normalized radial power density in Figure 2.4 (from [12]). At the beginning of irradiation, due to

the neutron flux spatial and energy **self-shielding** [12], [47]–[49], a large fraction of neutrons is absorbed in the outer region of the fuel causing a depression of the neutron flux in the central part of the pellet. Consequently, the heat generated by the fissile atoms follows the same moderately peaked profile. With time, the outer rim converts more U^{238} atoms to higher actinides compared to the inner portion of the pellet. This preferential buildup of fissile atoms in the pellet outer region makes the power and the isotopic profiles progressively more peaked with burnup.

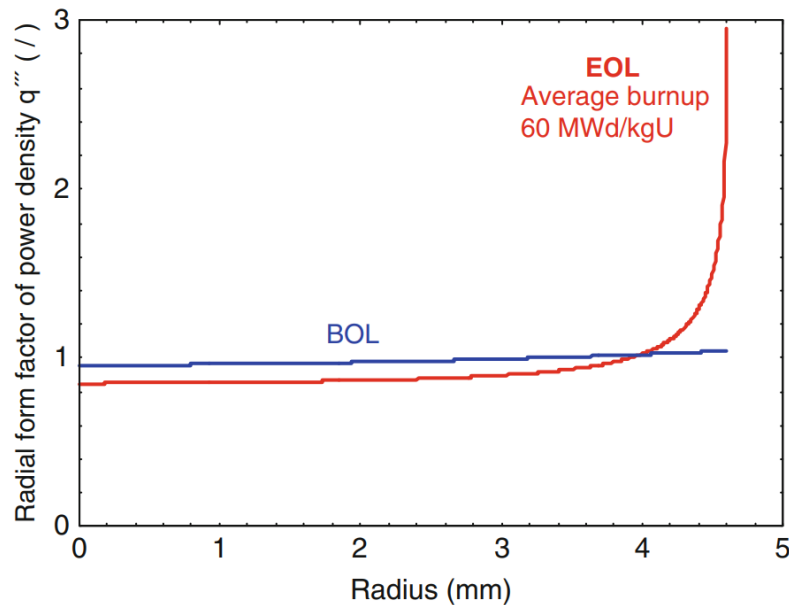


Figure 2.4 – Typical radial power profile for LWR fuel at the Beginning Of Life (BOL) and at the End Of Life (EOL) according to the TUBRNP model [17]. The figure comes from [12]. The normalized power becomes progressively more peaked with burnup.

Thermal expansion: As the pellet and the cladding heat up, they expand. The oxide fuel is exposed to higher temperature ranges and has a higher thermal expansion coefficient than the Zircaloy cladding, thus the net result is that the fuel expands more than the cladding, reducing the initial gap width. The presence of axial thermal gradients causes the pellet to assume the well-known **hourglass** shape shown on the left of Figure 2.5. When the gap is closed and the fuel touches the cladding, the outward pointing ends of the pellet might cause the formation of **ridges**. This phenomenon, often referred to as **bambooing**, might threaten the rod's integrity due to possible stress concentration. To anticipate and limit pellet hourglassing and cladding ridging, certain fuel designs use a **dished** and **chamfered** pellet (as shown on the right of Figure 2.5).

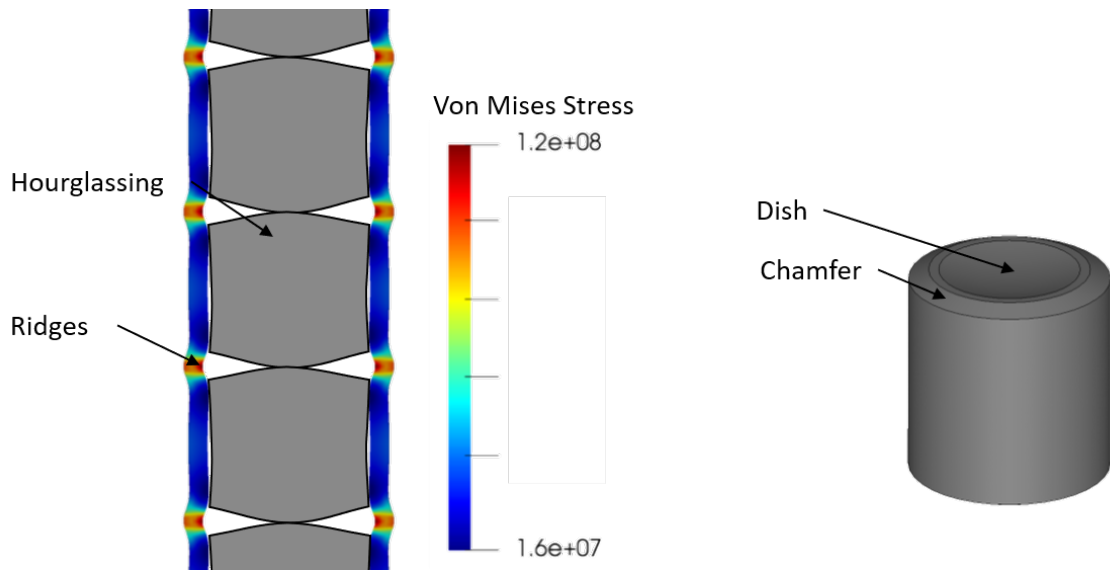


Figure 2.5 – On the left, hourglassing of fuel pellets and formation of ridges (bambooing) [50]. The colour map shows the distribution of the equivalent or von Mises stress. On the right, example of chamfered and dished pellet.

Cracking: Due to the presence of relatively high thermal gradients, the ceramic pellet experiences high tensile stresses and it starts to crack during the first ramp to power. As shown in the post irradiation picture of a commercial fuel pellet in Figure 2.6 (from [12]), the actual cracking pattern is impossible to predict and this stochastic nature poses serious obstacles to its modeling. Nevertheless, the importance of cracking in the evolution of fuel behavior cannot be understated. The presence of cracks changes the mechanical properties of the pellet as the cracked surfaces cannot resist tensile stresses in the direction perpendicular to the crack surface. The macroscopical thermal properties are changed as well since the space between cracks is now filled with gas. Additionally, the cracking causes the separation of **pellet fragments**. Given that they can expand more than the solid cylindrical pellet, the fragments move closer to the cladding under the effect of in-reactor vibrations. This phenomenon called **relocation** is the major factor contributing to the reduction of the average gap width in the early irradiation (apart from thermal expansion), but it is also the one subjected to the largest uncertainties due to its stochastic nature.

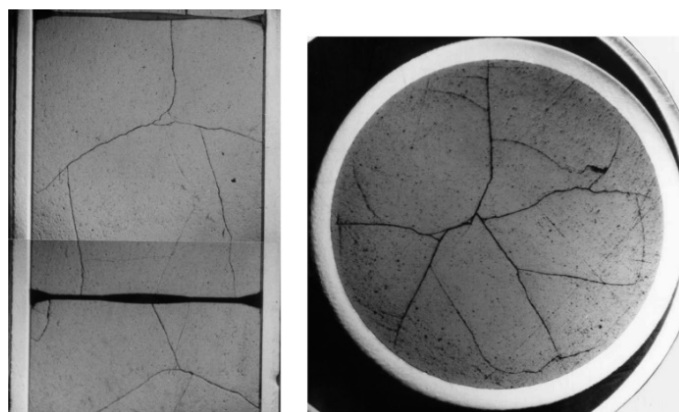


Figure 2.6 – Axial (left) and horizontal cross section (right) from the post irradiation examination of a commercial LWR fuel pellet. From [12].

Evolution of fuel porosity: After fabrication, the fuel pellets used in most commercial LWRs have a remaining porosity corresponding to $\sim 5\%$ of the TD. A portion of this initial porosity disappears during irradiation due to a process similar to sintering, assisted and enhanced by the interaction of the fuel pores with the fission fragments. This process is called **densification** and it causes the pellet to shrink and the gap size to increase. It is typical of the early stages of irradiation and it is saturated at a burnup of $\sim 3\text{--}5$ MWd/kg. The presence of high stresses induces an additional mechanism called **hot pressing** that contributes to the densification due to the reduction of pore size.

Swelling and fission gas release: The phenomenon of fuel swelling is the pellet volume increase due to the substitution of fissile atoms with the lighter isotopes produced by the fission reactions. The swelling is usually subdivided into a smaller contribution coming from the solid fission products and a more substantial component due to the gaseous fission products. The latter is strictly connected to the **fission gas release** (FGR), one of the most complex aspects of fuel behavior and an essential component of any fuel modeling effort [44]. Indeed, some of the fission reactions result in the production of gaseous atoms, most importantly Xe and Kr. These atoms are insoluble in the UO_2 matrix and they either remain in the grain potentially forming intra-granular bubbles that contribute to the **intra-granular swelling** or are released to the rod free volume. The main mechanism is the diffusion of single gas atoms from the fuel grain where they are produced toward the grain boundaries where they form large inter-granular bubbles. During a certain **incubation period** characterized by a limited amount of fission gas release, the grain boundary bubbles grow and coalesce. When the inter-connected network is large enough part of the fission gases accumulated on the grain surface can escape to the rod free volume and, as the conductivity of Xe and Kr is lower than that of He, the FGR tends to make the rod hotter. The bubbles retained on the grain boundary cause **inter-granular swelling** contributing to the reduction of the gap width and promoting pellet-cladding contact. The FGR is influenced by another phenomenon called **grain growth**, the increase of the average fuel grain size during irradiation. With larger grains, the gas atoms take longer to travel the now greater distance and reach the grain surface. At the same

time, the grain boundary sweeps some of the insoluble fission atoms from the fuel matrix and creates an additional channel for bringing the fission gases on the grain surface from where they can be released.

Creep: When a material is exposed for long periods of time to a stress below its yielding point and to high temperatures it starts to accumulate plastic strains, i.e. deformations that are not recovered once the load is removed. This phenomenon, called creep, is usually noticeable at temperatures starting from 30-50% of the melting point. Creep deformations are often divided in three stages as shown in Figure 2.7: In the first stage called **primary creep** the strain rate is relatively high, but it decreases with time; in the second stage called **secondary creep** the strain rate reaches its minimum value and stays constant; the third stage called **tertiary creep** is characterized by necking or cracking with the significant loss of strength quickly leading to failure. In a fuel rod, both cladding and fuel experience creep. In particular, the Zircaloy is known to exhibit considerable amounts of creep deformations promoted by the high stresses and the neutron fast flux (a phenomenon known as **irradiation-induced creep**). When the gap is open, under the influence of the outer coolant pressure, the cladding **creeps down** toward the fuel, significantly reducing the gap size and affecting the rod heat transfer. Once the gap is closed, the further expansion of the fuel pellets forces the cladding to creep outward.

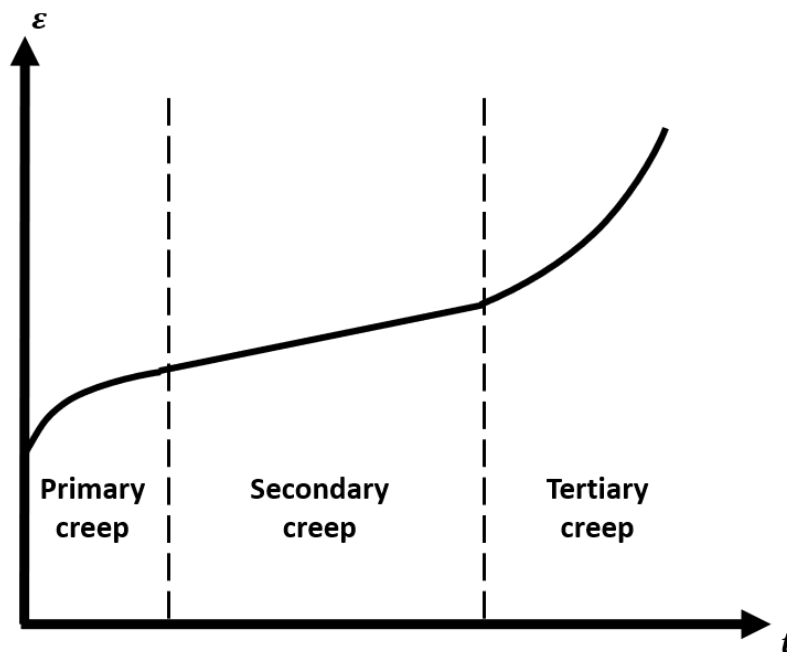


Figure 2.7 – Typical modeling of creep strains, divided into primary, secondary and tertiary creep.

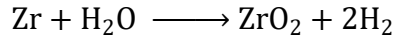
Irradiation growth: The Zr crystal at room temperature has a hexagonal close packed (hcp) structure. This **α phase** is completely substituted by a body centered cubic (bcc) or **β phase** only at

higher temperatures (~ 1140 K), although the exact transition temperature of the Zircaloy depends on the composition and on the fabrication process. The hcp structure of the α phase causes some of the material properties of Zircaloy to be slightly anisotropic, although this difference is often neglected by fuel performance codes. Additionally, during irradiation, with the Zircaloy mostly in the α phase, the point defects caused by the interaction between the fast neutrons and the atoms in the lattice present an anisotropic clustering. At the single Zr crystal level, this causes a volume conservative transformation with a contraction along the prismatic plane and an elongation along the basal plane. This phenomenon is called irradiation growth. Because the cladding tubes are formed in a way that makes the basal crystal planes preferentially oriented parallel to the axial direction, the overall effect is an axial elongation of the rod accompanied by a contraction along the radial direction. Irradiation growth is assumed to be additive to creep and its effect on the total length change of the cladding is small if compared to other phenomena.

Contact: With the combined contributions of thermal expansion, swelling, relocation and cladding creep down, the fuel-to-cladding gap closes relatively early during irradiation. This is the onset of a complex series of phenomena usually indicated under the term ***Pellet Cladding Mechanical Interaction*** or ***PCMI***. As contact stresses arise the rod's integrity is threatened, and the cladding might start to crack, for example due to stress concentration around the already mentioned ridges. Once in contact, fuel and cladding allow only a limited amount of relative sliding, depending on the characteristics of the two surfaces, and they might even chemically ***bond***. This usually translates into substantial friction forces that might cause the phenomenon of ***ratcheting***, with the pellets pulling the cladding upward. During rapid transients, if the cladding contact stresses rise quickly enough to surpass a certain yield limit, the cladding starts to accumulate plastic deformations that ultimately weaken it. This phenomenon is called ***rate-independent plasticity*** to differentiate it from time-dependent plastic phenomena such as creep, and it is relevant only when the time scale is too short for the creep to relax the stresses in the cladding. In-reactor plasticity is complicated by the ***irradiation-induced hardening***, that is the increase of cladding yield strength due to the accumulation of point defects. The ***PCMI*** might be influenced also by the presence of pellet defects such as chipped fragments or by fuel ***eccentricity***. This term is often used to indicate the imperfect alignment between the pellet and the cladding tube. Some degree of random eccentricity will always exist in the initial phases of irradiation, due to imperfect loading process and in-reactor vibrations. However, the average eccentricity decreases with time and virtually disappears when the gap starts to close. Another important contact scenario that has received attention in the past years is the so-called ***Stress Corrosion Cracking (SCC)***, part of the phenomenon called ***Pellet Cladding Interaction*** or ***PCI***, that consists in the cracking of the inner wall of the Zircaloy tube in the presence of high tensile stresses and in a corrosive environment. The latter is thought to be caused by some of the fission products such as Iodine that might be released in the vicinity of the point of contact or in the vicinity of a cladding micro-crack.

Corrosion processes and hydride formation: Although Zircaloy is a very corrosion resistant alloy, the aggressive water environment of a nuclear reactor will inevitably convert part of the metallic

Zr into a thin surface oxide layer through the following exothermic reaction also referred to as **water-side corrosion**:



The outer oxide layer is brittle so that it can be easily chipped away by the coolant (**spalling**), reducing the thickness of the remaining metallic cladding. Due to its lower thermal conductivity, the oxide also acts as an additional thermal resistance to the heat flow from the pellet to the coolant. The process of corrosion is strictly related to the **accumulation of hydrides**, in which a fraction of the hydrogen produced by the oxidation migrates into the metallic cladding. When the solubility limit is reached, the hydrogen precipitates into ZrH_2 , causing the cladding to become more brittle. Another oxidation reaction takes place on the inner side of the cladding. This phenomenon has been less investigated than the water-side corrosion, but it seems to be due either to the presence of free oxygen in the rod or to the diffusion of oxygen atoms from the pellet to the cladding in presence of a tight gap [51].

2.3 Fuel modeling approaches

In addressing the complex phenomenology outlined in Section 2.2, fuel performance codes must employ several simplifying assumptions if they are to achieve a sufficiently accurate solution within a reasonable amount of time. Naturally, what constitutes sufficient and reasonable is not fixed a priori and depends on the limitations of the code, on the objectives and requirements of the simulation, and on the time and computational resources available. For this reason, codes with largely different characteristics can coexist in the field of fuel performance modeling.

The most important set of assumptions is related to the geometry of the rod. Most of the codes used today follow the so-called **1.5-D approach**: it is assumed that the fuel rod keeps a cylindrical configuration throughout irradiation, with the pellet always concentric to the cladding, and that the neutronics and thermal hydraulics conditions remain axisymmetric. Because the axial gradients are small in comparison to the variations along the radial direction, it follows that the rod can be approximated as a stack of independent **1-D slices**. The heat transfer and other transport processes are solved only along the radial direction. The coupling between the slices is iteratively obtained through the energy transfer to the coolant, and through the gap pressure and gap gas composition which are affected by the fission gases released by any of the slices in the rod. The radial, azimuthal (Hoop) and axial stresses are obtained from the mechanical **equilibrium conditions** applied to a cylindrical framework, with the addition of the **modified plane strain** assumption: the axial deformation across a slice is considered radially uniform and it is derived from the force balance between the gas pressure, the expansion of the pellets, the force applied by the plenum spring and the pellet-to-cladding friction forces in case of contact.

A **2-D analysis** can be performed both for the ***r-z or radial-axial plane*** and for the ***r- θ or radial-azimuthal plane***. The former approach still assumes a cylindrical rod with axisymmetric conditions. However, the axial gradients are not neglected, the assumption of plane strain is dropped,

and the governing equations are solved both along the radial and axial directions. The r - θ analysis focuses on thin rod slices in plane strain, without the assumption of axisymmetric conditions. This modeling choice is not suited to represent the behavior of full-length rods, but it can be useful to study local effects such as PCMI in the vicinity of a pellet crack [52]. Finally, a fully **3-D approach** does not impose any a priori assumption on the geometry of the rod or on its irradiation conditions.

In 3-D and 2-D r - z simulations the level of details of the computational model can vary over a wide range. For example, the fuel can be reproduced either as a continuous **smeared column** or as series of **discrete pellets**, including dishes and chamfers if necessary. The latter approach allows one to capture end effects such as the pellet hourglass shape and the stress concentration around cladding ridges but introduces the complex numerical issue of the pellet-to-pellet contact.

Finally, regardless of the modeling approach, the computational model is discretized into a **mesh** or **grid**, composed of points, elements or control volumes depending on the chosen numerical scheme.

2.4 Main components of a fuel performance code

The main objective of a fuel performance code is to assess the state of the fuel rod under certain irradiation conditions which primarily involves the simultaneous consideration of the heat transfer and the equilibrium of forces in the rod. Indeed, the temperature distribution is of primary interest both because the code is often used to prove that fuel melting does not occur under a specific irradiation condition or scenario; and because many of the phenomena discussed in the previous section are strongly temperature-dependent. Predicting the stresses and deformations in the rod is equally important, as the integrity of the rod represents the first barrier against the release of the radioactive material produced during irradiation.

2.4.1 Thermal analysis

The temperature distribution in the rod is obtained from the solution of the **thermal conduction equation**, which usually translates in its **discretization on the computational mesh**, i.e. the original integral or differential problem is substituted with an approximated algebraic version. The heat diffusion equation is complemented by appropriate boundary conditions for the heat exchange with the coolant and for the gap heat transfer, and it considers the local power density produced by the fission reactions in the fuel. In typical base irradiation simulations, the relative power profile is calculated with a dedicated model, while the average value is imposed as it is derived from the linear heat rating provided as part of the input data. In more complex scenarios, for example a Reactivity Initiated Accident (RIA) transient, the heat source distribution might be provided from a coupled neutronics solver.

The complex evolution of the fuel thermal conductivity discussed in the previous Section is modeled with a temperature-dependent **experimental correlation** that typically considers additional variables such as the burnup or gadolinia content. This correlation is often obtained for fuel with

95% of its theoretical density and with perfect stoichiometry, and it is then adjusted with additional factors to correct for the actual porosity and oxygen-to-metal ratio. These correlations are semi-empirical in nature as most commonly they rely on the temperature dependency of the phonon contribution to heat conduction in the lattice as well as the interaction of phonons with the point defects. Experimental correlations are also used for the Zircaloy thermal conductivity and for the other thermo-mechanical properties such as heat capacity, density, emissivity, thermal expansion coefficient, Young's Modulus and Poisson's ratio.

The temperature jump across the gap is determined by the gap heat transfer characteristics. This is treated numerically with a dedicated **gap conductance model** that traditionally follows the **thin-gap** approximation: as the gap width is small compared to the fuel and cladding radii, the heat transfer across the gap is assumed to be 1-D. The local gap conductance is calculated as the sum of three additive terms, corresponding to: the conduction through the gas, highly dependent on the gap size, gas composition and temperature, and surface roughness; the radiative heat transfer, dependent on the surface emissivity and the fourth power of the temperature; and the conduction through the points of contact between fuel and cladding. The gap conductance model usually includes fitting parameters to partly account for the unavoidable uncertainties in gap size due to fuel cracking and fuel eccentricity.

A dedicated **gap model** is assigned with the task of keeping track of the gap gas composition and calculating its volume, temperature, and pressure. The evolution of the free volume available to the gap gas is derived from the deformations of the fuel and cladding, while the gas temperature is calculated via some form of average between the temperatures on the two sides of the gap. Many codes also include a model to calculate the temperature in the plenum, considering the heat exchange between the top of the fuel stack, the gas in the plenum, the plenum spring and the upper section of the cladding. For the calculation of the pressure, an **ideal gas law approach** is often followed, and the gas is assumed to equalize its pressure instantaneously throughout the rod free volume.

To address the heat exchange between the outer cladding wall and the coolant water, many fuel performance codes include a **coolant channel model** that provides the heat exchange coefficient for a variety of regimes (liquid cooling, nucleate boiling, film boiling etc.) and flow conditions (forced convection, natural convection etc.). If the conservation of mass, momentum, and energy is considered, the channel model can be used to predict the progressive increase in coolant temperature along the axial direction of the rod. To save computational resources, most of the channel models used today (even in multi-dimensional codes) assume a 1-D flow, treat the steam-water system as a homogeneous mixture and neglect multi-dimensional effects such as the perturbation in flow after the entry nozzles or the separation grids of the assembly. Alternatively, the fuel performance code can be coupled with dedicated thermal-hydraulics analysis codes. This is the strategy followed, among others, by the Paul Scherrer Institute (PSI) in [53], where thermal-hydraulics boundary conditions calculated with systems codes like TRACE [54] are passed to the fuel performance code Falcon [55]. Another example is given by the studies performed under CASL

[56], where the subchannel code COBRA-TF [57] is used for the thermal-hydraulics and BISON for the fuel behaviour. The coupling with a dedicated thermal-hydraulics or CFD code might be the best (and only) option for analysing the rod behaviour during complex thermal-hydraulics transient scenarios.

2.4.2 Stress analysis

The distribution of stress and strain in the fuel rod is obtained from the discretization and solution of the **momentum balance equations**. These are complemented by appropriate boundary conditions and models for the rheological behavior of the materials involved in the simulation such as plasticity or creep.

The boundary conditions for the mechanical analysis are set by: the outer coolant pressure on the outer cladding surface, generally part of the input data; and the inner gas pressure provided by the gas gap model. However, when the gap is closed, the contact stresses are calculated and are applied to the two surfaces facing the gap. The axial deformations in 1.5-D code are derived from an axial force balance performed for each 1-D slice, while in 2-D or 3-D code they can be directly obtained from the solution of the momentum balance equations with the use of appropriate boundary conditions.

Because the deformation of fuel and cladding changes the gap size and the fuel-to-cladding contact pressure, the structural analysis has a strong feedback effect on the gap conductance and on the thermal analysis of the rod. At the onset of contact, the gap conductance dramatically increases, causing the pellet to contract again due to the improved heat transfer which might lead to **numerical oscillations**. This tight coupling poses a challenge to the convergence of the solution scheme, in particular for scenarios characterized by rapid power ramps or large amount of Xe poisoning in the gap.

Fuel pellet cracks cannot be modeled explicitly in 1.5-D and 2-D simulations due to the assumption of axisymmetric conditions. Nevertheless, many codes try to approximate their effect on the fuel mechanics performance. A common approach, often called **isotropic cracking model** [58], is that of artificially decreasing the Young's modulus and Poisson's ratio as a function of the number of cracks, in turn calculated as a function of power. The **smearred cracking** approach, developed in more recent years, modifies the mechanical properties at each computational point: if one of the principal stresses surpass a maximum critical threshold then the material is considered cracked and cannot sustain any more stress in that principal direction. With the advent of 3-D codes there has been some attempt [59] at explicitly modeling cracks in the simulation. However, the crack pattern is necessarily arbitrary, and it is imposed at the beginning of the simulation. The modeling of time-dependent cracks has been done for example in some fracture simulation using the Extended FEM [60] but its use for routine calculations seems still out of reach even for the most modern fuel performance codes.

2.4.3 Main phenomena affecting the gap size

The thermo-mechanics structure outlined in the previous subsections is complemented by additional models to treat the complex phenomenology discussed in Sec. 2.2. Many efforts have been made over the years to correctly capture the effect of a large set of heterogeneous phenomena that directly impact the deformation of the rod and the gap size. This set includes relocation, densification, swelling and growth. The main approach has been avoiding the modeling of meso-scale processes and using ***semi-empirical correlations*** from out of pile or in-pile measurements. These correlations provide an additional component of the strain as a function of burnup and power. In particular:

- The relocation models currently used provide an additional tangential strain component as a function of burnup and linear heat rate. For example, the FRAPCON model shown in Figure 2.8 predicts, for constant linear heat rate, a relocation strain that linearly increases with burnup up to a saturation value reached at ~ 5 MWd/kgU. Usually, the relocation is not recovered when the rod power is reduced. However, some codes allow for partial relocation recovery when the pellet initially comes into contact with the cladding, a condition often called soft-contact. Only after the recovery is complete (usually up to 50% of the total relocation strain), additional pellet expansion causes the onset of contact stresses.
- Detailed densification models exist but the necessary model coefficients are often not known or difficult to obtain. Therefore, simplified densification models provide the densification strain as a function of the burnup and of the out-of-pile resintering density change, typically known as part of the rod data and coming from furnace tests performed by the fuel manufacturer.
- The growth mechanism depends on the Zircaloy crystalline structure achieved at the end of manufacturing. Thus, depending on the fabrication process and on the specific composition of the alloy, different correlations might be used. Nevertheless, many codes use simple burnup dependent correlations providing the axial elongation.

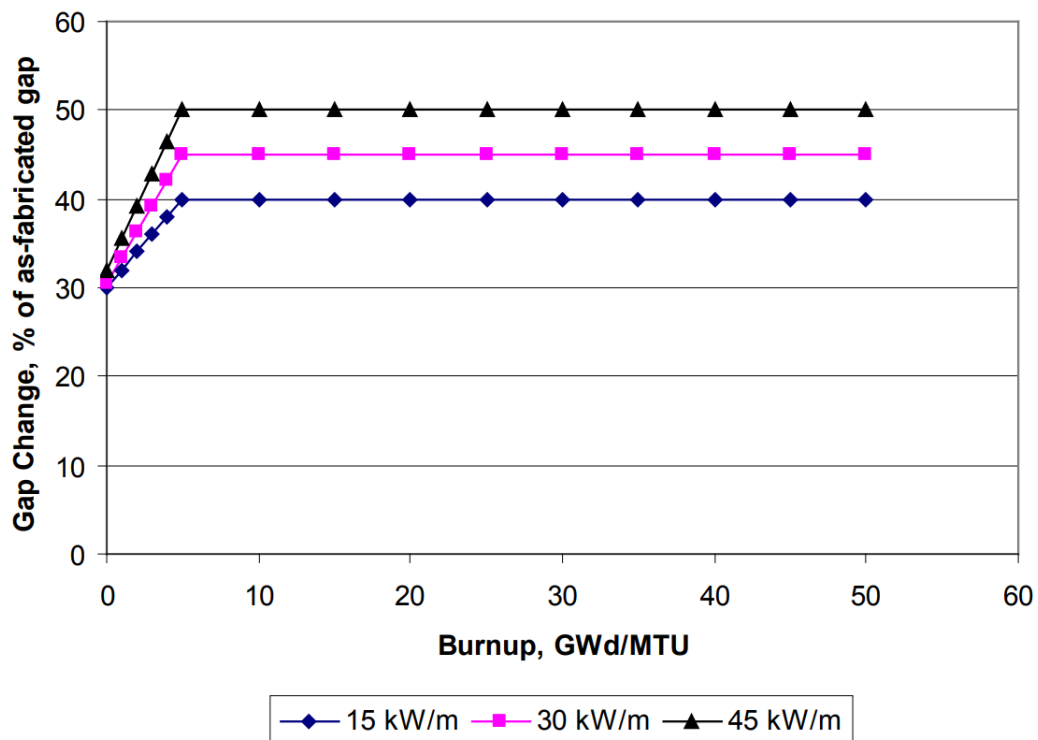


Figure 2.8 – Example of relocation model. From FRAPCON 3.4 [61]. The gap closure is given as a function of linear heat rate and burnup. A saturation value is reached after ~ 5 MWd/kgU

- The gaseous swelling strain should be strictly coupled to the fission gas behavior, but many codes employ temperature and burnup dependent correlations for both swelling contributions. However, since the development of mechanistic intergranular fission gas models, more and more codes today limit the use of empirical correlations to the solid swelling component and derive the gaseous swelling directly from the fission gas release module.

2.4.4 Fission gas release

Modeling FGR is essential for an accurate prediction of fuel behavior, even more so with the current tendency to increase the final discharge burnup. As it changes the gap gas composition poisoning the pure He with low conductive Xe and Kr atoms, the fission gas release model has a dramatic feedback effect on the thermal analysis of the rod. Also, as the gap is gradually filled with gaseous fission products, the gap pressure increases, although the effect of pressure on the gap conductance is small. Although empirical correlations are sometimes employed in fuel performance codes to calculate the FGR fraction as a function of burnup, their application is limited in range to the fuel rod designs and burnup levels used for their validation.

Therefore, many codes today are equipped with a dedicated **mechanistic FGR module**, typically subdivided into two components, an **intra-granular** and an **inter-granular module**. The intra-granular module considers the main mechanism leading to the release of fission gases, that is the

diffusion of single gas atoms in the fuel grains. Considerable efforts have been carried out since the seminal work of Booth [62], but the basic approach remains similar. At each computational unit, the model calculates the average fission gas atom concentration in the fuel grains, obtained from the solution of a simplified diffusion equation on a representative grain often assumed to be spherical. Different solution algorithms have been developed over the years such as the FORMAS or URGAS [63] to surpass the original limitations of the Booth model and extend the mechanistic treatment to time-varying irradiation conditions.

Many semi-empirical correlations for the temperature dependent **diffusion coefficient** have been obtained. In general, these correlations model both the purely thermally activated thermal diffusion that dominates at high temperatures and the irradiation enhanced diffusion, relevant at lower temperatures and due to the interaction between gas atoms and fission fragments. Some models also consider the **trapping** and **resolution** of gas atoms from intra-granular bubbles. These models often follow the work of Speight [64] that defined an effective diffusion coefficient derived assuming that the gas bubbles are immobile in the grain and that the trapping and resolution processes are in equilibrium. Also grain growth is typically modeled following the work of Ainscough [65] and some codes even include the contribution to FGR due to the phenomenon of grain boundary sweeping.

The original **inter-granular module** developed by Booth assumed the grain boundary to be a perfect sink (i.e. an immediate release once the gas atoms reach the grain surface). Nowadays, the main approach is to assume that the gas atoms arriving at the grain boundary (calculated by the intra-granular module) immediately precipitate into large lenticular inter-granular bubbles. Once a saturation concentration is reached, the additional gas arriving at the boundary is released, with the saturation value obtained from the ideal gas equation of state considering mechanical equilibrium between the gas pressure, the surface tension and the hydrostatic stress surrounding the bubble. More recently, many codes started adopting a different approach similar to the one of Pastore [66] where the inter-granular module also follows the time-dependent evolution of the inter-granular bubbles. These are allowed to grow in size due to the collection of fission gas atoms and vacancies but can also coalesce forming a large, interconnected network, leading to a smaller number of bubbles with a larger average bubble size. Finally, recent models also include the sudden FGR called **burst**, experimentally noticed during rapid transients, and believed to be caused by micro-cracks appearing at the grain boundaries that diminish their capability to retain fission gas bubbles.

2.4.5 Neutronics analysis

For an accurate prediction of the fuel temperature distribution, the fuel isotopic evolution and consequent formation of a radial power profile in the fuel pellets must be addressed. The ideal approach would be to couple the fuel performance code with neutron transport and depletion codes, that can provide an accurate neutron flux and a detailed fuel inventory. Due to the high

computational cost of such operation, most fuel performance codes prefer to include a **simplified neutronics module**. Typically:

- The module focuses the attention only on a selected number of isotopes relevant for power generation (the so-called higher actinides) and for the accumulation of gaseous fission products. The production and destruction channels (due to decay or neutron reactions) are often simplified with respect to full-inventory depletion codes.
- The neutron flux is not derived from the Boltzman neutron transport equation but from the solution of one dimensional one-group or few-group diffusion theory in cylindrical coordinates.
- One-group or few-groups cross sections are obtained from separate neutronics calculations and are typically hard-coded.
- The module might employ fitting functions to treat the spatial dependent resonance absorption in U^{238} and Pu^{240} .

Despite the simplifications, neutronics modules such as RADAR or TUBRNP have been extensively validated [67], [68]. However, their use remains limited to axisymmetric conditions and traditional LWR fuel configurations (representing nonetheless the main use of fuel performance codes). For example, the introduction of burnable absorbers such as Gd_2O_3 in BWRs causes a strong power gradients with significant self-shielding that cannot be accurately approximated with diffusion theory.

Finally, some codes such as FRAPCON allow the user to neglect the dedicated neutronics module and employ instead a predefined power profile shape derived from previous neutronics calculation that is known to provide sufficiently accurate results [69].

2.4.6 Chemical analysis

A dedicated **chemistry module** is included only in some of the most modern codes such as ALCYONE or BISON where it is used to follow the evolution of the fuel speciation, oxygen potential and stoichiometry. These advanced capabilities represent an interesting development frontier that can improve the understanding and modeling of complex phenomena such as SCC. Models for the waterside corrosion and its impact on the mechanical and thermal properties of the cladding are more common, although limited efforts have been done to include the accumulation and redistribution of hydrogen [70]. Other chemical phenomena such as the oxidation of the fuel by the coolant in accident conditions, the inner oxidation of the cladding and the chemical bonding between fuel and pellet are either neglected or treated with simplified models.

2.4.7 Base irradiation vs. transient analysis

A distinction is often made between **steady-state** or **base irradiation** and **transient** simulations. The former is interested in the long irradiation history of a full-length rod. The time scales are

those typical of long-term phenomena such as creep or the isotopic evolution of the fuel, thus the heat balance can be assumed to be always at steady state. A transient simulation is interested in shorter time scales where the rate of change of the temperature cannot be neglected, as it is typical for accident scenarios and power ramps. Due to the different temperature ranges and irradiation conditions considered, some of the correlations and models used to analyze the base irradiation may differ or not be present at all for the study of transient scenarios (and vice versa). For example, the creep model might be neglected during a rapid transient due to its large time scales, while the rate-independent plasticity model becomes relevant when the time scales are too short for the creep mechanism to relax the cladding stresses. It should be stressed that the distinction between base irradiation and transient codes might just be a heritage from the past when fuel performance codes were sometimes developed to run exclusively transient or steady-state simulations [71], while most modern codes are capable of performing both type of analysis.

2.5 Conclusions

This chapter has provided a concise review of the fundamental aspects of LWR fuel behaviour and modelling. The configuration of a typical oxide-in-cladding fuel rod used in a LWR has been described and the major phenomena affecting the fuel evolution during irradiation in normal operation have been outlined. The main assumptions and the general structure behind a typical fuel performance code have been presented, introducing the main components and models. This forms the basis for the methods to be developed in the next chapter.

Chapter 3

Finite volume framework for fuel performance

A primary objective of this PhD thesis is exploring the potential of the FVM for multi-dimensional fuel performance applications. The Finite Volume (FV) numerical scheme is very popular in the field of CFD but it is not often associated with CSM software, which typically employs the FEM. It has been shown [72] that the two methods share several features and can be used alternatively in both fields as demonstrated by the number of works carried out in the last decades to extend the FEM for CFD applications. More recently, there has been a growing interest toward the use of the FVM for CSM. Some comparisons have been made between the two numerical schemes [73]–[75] and, from a performance and accuracy point of view, there is no clear difference, as discussed by Cardiff in his comprehensive review [34], with both methods having their own strengths and weaknesses for CSM problems. Since the seminal work of Demirdzic [23] and that of Jasak and Weller [22], the cell-centered FVM has been successfully applied to a wide range of problems, while parallel research directions have investigated the use of other variants, such as the vertex-centered approach presented first by Freyer [76] or the meshless approach discussed by Atluri [77]. Despite these efforts carried out over the last thirty years, the FVM has not been considered by the fuel performance community in favor of the FEM or of the FDM.

Among the interesting features of the FVM is the simple formulation, based on control volume balances familiar to all engineers. This aspect is considered advantageous in a complex multi-physics framework, like that of fuel performance, which often requires the collaborative development of several experts. Building on the works of Jasak and Weller, Tuković and Cardiff, significant effort was dedicated to the development of a novel FV fuel performance code named OFFBEAT or OpenFOAM Fuel Behavior Analysis Tool. More specifically, the code is built using the cell-centered FVM in its application within the OpenFOAM C++ library. As the possible development strategy for such a code is neither unique nor obvious, the one adopted for OFFBEAT is described in this chapter and in the next two chapters.

This chapter describes the numerical framework that forms the foundation of the thesis. The governing equations, modelling assumptions and constitutive relations are introduced in Section 3.1, while the discretization procedure is outlined in Section 3.2, with particular attention towards the treatment of the surface integral terms and the implementation of the basic boundary conditions. The main multi-dimensional modeling options available within OFFBEAT are described in Section 3.3 and the relevant conclusions for this chapter are drawn in Section 3.4.

The numerical developments dedicated to the gap heat transfer and contact methodologies are described in detail in Chapter 4, while Chapter 5 focuses on the general structure of the code, with its main components, models, and solution scheme.

3.1 Governing equations and constitutive relations

OFFBEAT operates in a numerical framework for solid mechanics partly derived from the works of Jasak and Weller [22], [29], Tuković [33], [78] and Cardiff [30], [79]–[81]. This is combined with a framework for solid thermal-analysis and with numerical developments concerning the treatment of the gap heat transfer and contact (discussed in detail in the next chapter).

The main governing laws considered in OFFBEAT are the conservation of linear momentum and the conservation of energy, that determine the distribution of deformation and temperature in the nuclear fuel rod. As done by most CSM codes, OFFBEAT adopts a Lagrangian approach, thus the convection terms due to the flow of mass across the surfaces are not considered. In this framework, the conservation of energy for a solid body with arbitrary shape and volume V , bounded by a surface S with outward normal \mathbf{n} , can be expressed in the form of the heat diffusion equation:

$$\overbrace{\int_V \frac{\partial \rho c_p T}{\partial t} dV}^{\text{Rate of change}} = \overbrace{\oint_S \mathbf{n} \cdot \mathbf{q}'' dS}^{\text{Rate of heat flowing in}} + \overbrace{\int_V q''' dV}^{\text{Rate of generation}} \quad (1)$$

where ρ is the density, c_p is the specific heat capacity, T is the temperature, q''' is the volumetric power density and \mathbf{q}'' is the net heat flux entering through the surface S . The latter is a vectorial quantity, and it is defined as:

$$\mathbf{q}'' = (\kappa \nabla T) \quad (2)$$

where κ is the thermal conductivity. The heat diffusion equation above states that the rate of change of thermal energy stored in the volume V is equal to net rate of energy entering the body through the surface S plus the rate of energy generated.

For the same body of volume V and surface S , the strong form of the linear momentum conservation equation in a Lagrangian approach is given by:

$$\overbrace{\int_V \frac{\partial}{\partial t} \rho \mathbf{v} dV}^{\text{Rate of change or Inertia}} = \overbrace{\int_V \frac{\partial^2 \rho \mathbf{u}}{\partial t^2} dV}^{\text{Surface forces}} = \overbrace{\oint_S \mathbf{n} \cdot \boldsymbol{\sigma} dS}^{\text{Surface forces}} + \overbrace{\int_V \rho \mathbf{b} dV}^{\text{Body forces}} \quad (3)$$

where $\boldsymbol{\sigma}$ is the stress tensor, \mathbf{v} is the velocity vector, \mathbf{u} is the displacement vector and \mathbf{b} corresponds to the body force per unit mass. The equation above states that the sum of all the forces applied to the body is equal to the rate of change of its total linear momentum or its inertia.

OFFBEAT operates in a total Lagrangian, small-strain framework. This entails that the governing equations are always referred to the original configuration of the body and that the mesh is not updated with the displacement field. Also, the momentum equations are expressed in total strain form with the total small-strain tensor given as:

$$\boldsymbol{\varepsilon} = \frac{1}{2} [\nabla \mathbf{u} + (\nabla \mathbf{u})^T] \quad (4)$$

The Cauchy stress tensor is given by Hooke's theory of elasticity:

$$\boldsymbol{\sigma} = 2\mu \boldsymbol{\varepsilon}_{el} + \lambda \text{tr}(\boldsymbol{\varepsilon}_{el}) \quad (5)$$

where $\boldsymbol{\varepsilon}_{el}$ is the elastic component of the strain tensor, while the Lamé's coefficients μ and λ are functions of the Young's modulus E and Poisson's ratio ν , and are given as:

$$\mu = \frac{E}{2(1 + \nu)} \quad (6)$$

$$\lambda = \frac{\nu E}{(1 - 2\nu)(1 + \nu)} \quad (7)$$

An alternative incremental version of the momentum equations might be included in OFFBEAT in the future for the analysis of large strain scenarios within an updated Lagrangian framework.

As a fuel performance code, OFFBEAT considers several phenomena such as relocation or growth that are modeled with additional component of the strain tensor. At the same time, OFFBEAT includes thermal expansion and models for the rheological behavior of the materials involved in the simulation, such as plasticity or creep. The various resulting components of the total strain tensor are assumed to be additive, as in:

$$\boldsymbol{\varepsilon} = \boldsymbol{\varepsilon}_{el} + \boldsymbol{\varepsilon}_{add} \quad (8)$$

with the additional non-elastic terms condensed for simplicity into $\boldsymbol{\varepsilon}_{add}$.

The fact that OFFBEAT operates in a total strain framework should not be seen in contradiction to the inclusion of plasticity and creep described in Sec. 5.9. Indeed, the history- and path-dependent nature of the plastic phenomena imposes an incremental treatment of the evolution of the plastic strain [82]. However, once the increment is calculated it can be added to the total strain tensor given in Eq. (8) and the momentum equation can be solved in its original total strain form.

Following the definitions of total strain and stress tensors, it is useful to define the surface traction vector $\boldsymbol{\tau}$ as:

$$\boldsymbol{\tau} = \mathbf{n} \cdot \boldsymbol{\sigma} = \mu \mathbf{n} \cdot \nabla \mathbf{u} + \mu \mathbf{n} \cdot (\nabla \mathbf{u})^T + \lambda \text{tr}(\nabla \mathbf{u}) \mathbf{n} - \mathbf{n} \cdot [2\mu \boldsymbol{\epsilon}_{\text{add}} + \lambda \text{tr}(\boldsymbol{\epsilon}_{\text{add}})] \quad (9)$$

Finally, the definition of the mathematical problem described in this Section is completed by specifying appropriate initial and boundary conditions, usually of the type fixed-value (or Dirichlet), fixed-gradient (or Neuman) or symmetry.

3.2 Discretization procedure

The computational domain and the integral governing equations are discretized following standard cell-center finite volume techniques [22], [79], [83], which are recalled in the next pages. To clarify the terminology used in this section, the terms produced by the discretization of the governing equations are referred to as:

- Implicit, if they depend on the cell-center values at the current iteration.
- Explicit, if they either depend on the cell-center values at the previous iteration or do not depend at all on the cell-center values (in this case they are also called fixed-source terms).

3.2.1 Domain

In cell-centered FV codes, the domain is discretized into convex polyhedral Control Volumes (CVs) that do not overlap and fill the domain completely, and the mathematical problem represented by Eq. (1) and Eq. (3) is solved by applying the governing equations to each CV.

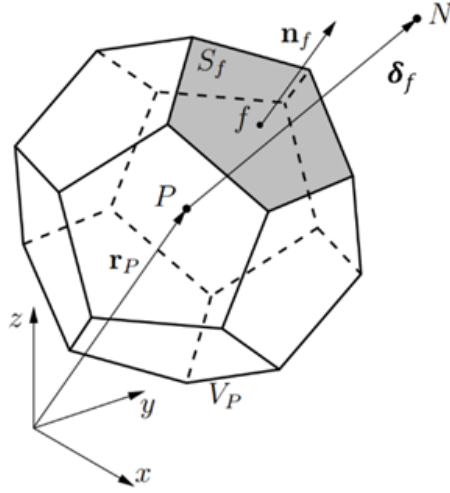


Figure 3.1 - Polyhedral cell or Control Volume (CV). From [33].

The well-known image in Figure 3.1 (borrowed from [33]) shows: the generic cell of volume V_P centered around the point P ; the face S_f centered around the point f with outward normal \mathbf{n}_f ; and the neighboring cell centroid N , separated from P by the distance vector δ_f . With respect to the face with outward normal \mathbf{n}_f , the cells centered in P and N are designated as the owner and the neighbor cell, respectively. The CV bounding surface S_P can be expressed as a combination of internal faces (f) and boundary faces (b):

$$S_P = \sum_f S_f + \sum_b S_b \quad (10)$$

Naturally, if the cell is internal to the domain the boundary faces subset is empty.

3.2.2 Temporal terms

The first time-derivative is calculated using a first order fully implicit Euler scheme. Thus, the rate of change of thermal energy for the cell centered in P is approximated as:

$$\int_V \frac{\partial \rho c_p T}{\partial t} dV \approx (\rho c_p)_P^i \frac{(T)_P^i - (T)_P^{i-1}}{\Delta t^i} V_P \quad (11)$$

where the index i indicates the current time step and Δt^i is the current time increment. The variation of density with time is not considered in the energy balance equation which is consistent with the Total Lagrangian approach (i.e. the volumes do not change, thus the density stays the same to conserve the mass). In the future, with the introduction of an alternative incremental mechanics

solver with updated mesh, neglecting the variation of density with time might become an issue. Indeed, for base irradiation conditions the time-dependent change in density due to densification, swelling or growth is negligible as it takes place over long time scales. For transients, the thermal diffusion equation might be corrected with an explicit term that takes into account the partial time derivative of the product ρc_p . However, its importance for the accuracy of the solution must be carefully evaluated.

The second time-derivative is equivalent to the rate of change of the rate of change of a field. Thus, applying the Euler scheme twice in a row, the inertia term for the cell P is discretized as:

$$\begin{aligned} \int_V \frac{\partial^2 \rho \mathbf{u}}{\partial t^2} dV &\approx \frac{\partial}{\partial t} \left[(\rho)_P^i \frac{(\mathbf{u})_P^i - (\mathbf{u})_P^{i-1}}{\Delta t^i} \right] V_P \\ &= \frac{V_P}{\Delta t^i} \left[(\rho)_P^i \left(\frac{(\mathbf{u})_P^i - (\mathbf{u})_P^{i-1}}{\Delta t^i} \right) - (\rho)_P^{i-1} \left(\frac{(\mathbf{u})_P^{i-1} - (\mathbf{u})_P^{i-2}}{\Delta t^{i-1}} \right) \right] \end{aligned} \quad (12)$$

3.2.3 Volume source terms

The volume source terms are discretized assuming that the value at the cell-centroid corresponds to the volume weighted average over the cell. Thus, the rate of thermal energy generated in the heat diffusion equation and the body force term in the momentum balance equations are approximated as:

$$\int_V \rho \mathbf{b} dV \approx \rho_P \mathbf{b}_P V_P \quad \text{and} \quad \int_V q''' dV \approx q_P''' V_P \quad (13)$$

These terms are treated as fixed-sources as they do not depend on the cell-center value of the main field (displacement or temperature).

3.2.4 Heat flux and forces over internal faces

The surface integrals in the heat diffusion and momentum balance equations are substituted with the sum of integrals over the cell faces, either internal to the domain (f) or on the boundaries (b). The surface integrals are then substituted with products over the cell faces calculated at the face center with the mid-point rule. Therefore, the rate of heat flowing through the surface S_P becomes:

$$\oint_{S_P} \mathbf{n} \cdot \mathbf{q}'' dS \approx \sum_f (\mathbf{n}_f \cdot \mathbf{q}_f'') S_f + \sum_b (\mathbf{n}_b \cdot \mathbf{q}_b'') S_b \quad (14)$$

while the sum of surface forces acting on the cell becomes:

$$\oint_{S_P} \mathbf{n} \cdot \boldsymbol{\sigma} dS = \oint_{S_P} \boldsymbol{\tau} dS \approx \sum_f \boldsymbol{\tau}_f S_f + \sum_b \boldsymbol{\tau}_b S_b \quad (15)$$

Leaving the treatment of the boundary terms to the next section, this section focuses on the contribution of the internal faces.

The rate of heat leaving the cell P through the internal faces is a Laplacian term, and it can be decomposed into an implicit orthogonal component¹ and an explicit non-orthogonal component:

$$\begin{aligned} \sum_f (\mathbf{n}_f \cdot \mathbf{q}_f'') S_f &= \sum_f \mathbf{n}_f \cdot (\kappa \nabla T)_f S_f \\ &= \sum_f \kappa_f S_f \left[\overbrace{\frac{|\Delta_f|}{|\boldsymbol{\delta}_f|} \frac{T_N - T_P}{|\boldsymbol{\delta}_f|}}^{\text{orthogonal contribution}} + \overbrace{\mathbf{k}_f \cdot (\nabla T)_f}^{\text{non-orthogonal correction}} \right] \end{aligned} \quad (16)$$

where, as shown in Figure 3.2, $\Delta_f = \frac{\boldsymbol{\delta}_f}{\mathbf{n}_f \cdot \boldsymbol{\delta}_f}$ is the orthogonal contribution vector, $\boldsymbol{\delta}_f$ is the distance vector between the cell-center P and the center N of the neighbor cell, and \mathbf{k}_f is the non-orthogonal correction vector given as:

$$\mathbf{k}_f = (\mathbf{n}_f - \Delta_f) \quad (17)$$

¹ This thesis retains the denomination of *orthogonal* for the implicit contribution of the gradient discretization. The naming might be confusing since the orthogonal contribution lies along the direction connecting the cell-center points of the two neighbouring CVs, not along the surface normal vector.

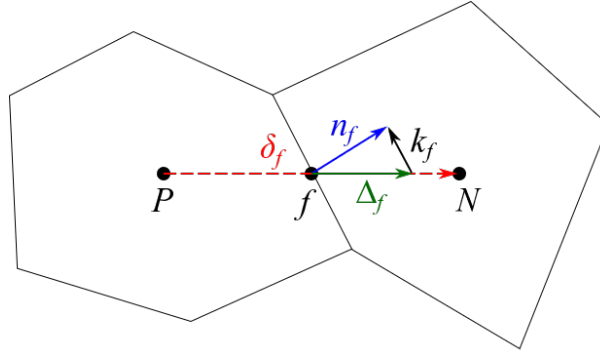


Figure 3.2 – Non-orthogonal correction vectors.

The surface traction $\boldsymbol{\tau}_f$ on the internal faces is split into a Laplacian component and an explicit source term. To improve the convergence of the discretization procedure, Eq. (9) is applied to the internal faces and is manipulated as follows:

$$\begin{aligned} \boldsymbol{\tau}_f = & \overbrace{(2\mu + \lambda)_f \mathbf{n}_f \cdot (\nabla \mathbf{u})_f}^{\text{Laplacian}} \\ & + \overbrace{\mu_f \mathbf{n}_f \cdot (\nabla \mathbf{u})_f^T + \lambda_f \text{tr}(\nabla \mathbf{u})_f \mathbf{n}_f - (\mu + \lambda)_f \mathbf{n}_f \cdot (\nabla \mathbf{u})_f - \mathbf{n}_f \cdot [2\mu_f \boldsymbol{\varepsilon}_{f,\text{add}} + \lambda_f \text{tr}(\boldsymbol{\varepsilon}_{f,\text{add}})]}^{\text{explicit}} \end{aligned} \quad (18)$$

Following the example of Cardiff [84] the equation above can be rewritten in the following equivalent and more readable form:

$$\boldsymbol{\tau}_f = \overbrace{(2\mu + \lambda)_f \mathbf{n}_f \cdot (\nabla \mathbf{u})_f}^{\text{Laplacian}} + \overbrace{\mathbf{n}_f \cdot \boldsymbol{\sigma}_f - (2\mu + \lambda)_f \mathbf{n}_f \cdot (\nabla \mathbf{u})_f}^{\text{explicit}} \quad (19)$$

Once the solution is converged, the implicit and explicit Laplacian terms above are identical and cancel out, and Eq. (19) is equivalent to Eq. (3). As done for the heat flux, the Laplacian is discretized into an implicit orthogonal and an explicit non-orthogonal component. Thus, the sum of the forces acting over the internal faces is approximated as:

$$\begin{aligned} \sum_f \boldsymbol{\tau}_f S_f = & \sum_f (2\mu + \lambda)_f S_f \left[\underbrace{\overbrace{\frac{|\Delta_f|}{|\delta_f|} \frac{\mathbf{u}_N - \mathbf{u}_P}{|\Delta_f|}}^{\text{implicit}} + \overbrace{\mathbf{k}_f \cdot (\nabla \mathbf{u})_f}^{\text{explicit}}}_{\text{explicit}} \right] \\ & + \sum_f S_f [\mathbf{n}_f \cdot \boldsymbol{\sigma}_f - (2\mu + \lambda)_f \mathbf{n}_f \cdot (\nabla \mathbf{u})_f] \end{aligned} \quad (20)$$

The explicit surface gradient of the displacement field, $(\nabla \mathbf{u})_f$, in the equation above is calculated using a least squares approach [85] to minimize skewness errors, i.e. the discretization error emerging when the line joining two neighboring cell-centers does not cross the shared face at the face center. The value of the stress at the face, $\boldsymbol{\sigma}_f$, is thereafter linearly interpolated using the cell-center value of the stress field in the neighboring CVs. The material properties are assumed to be continuous and smooth, therefore employing a linear interpolation to obtain the value $(2\mu + \lambda)_f$ and κ_f for the internal faces is a good approximation.

3.2.5 Heat flux and forces over boundary faces

The discretization of the heat flux \mathbf{q}_b'' and traction $\boldsymbol{\tau}_b$ on boundary faces depends on the specific boundary condition used.

Dirichlet type

A Dirichlet boundary condition fixes the face-center value of the field, which can either be constant or vary in time. When using a fixed-temperature boundary condition, the boundary value T_b is known and the rate of heat flowing through the boundary face is approximated as:

$$(\mathbf{n}_b \cdot \mathbf{q}_b'')S_b = (\mathbf{n}_b \cdot (\kappa \nabla T)_b)S_b \approx \kappa_b S_b \frac{T_b - T_P}{|\boldsymbol{\delta}_b|} \quad (21)$$

where $\boldsymbol{\delta}_b$ is the distance vector between cell-center and boundary face-center, while \mathbf{n}_b is the outward normal of the boundary face with area S_b .

When using a fixed-displacement boundary condition, the boundary value \mathbf{u}_b is known. As demonstrated by Cardiff [79], considering that the specified boundary condition is valid along the whole boundary face (as typically done in standard FV fluid dynamics simulations [86]) is not a good approximation for solid mechanics as it can lead to erroneous stresses. For this reason, a non-orthogonal correction is added to the Laplacian term and the force acting on the cell boundary face is approximated as:

$$\begin{aligned} \boldsymbol{\tau}_b S_b \approx & (2\mu + \lambda)_b S_b \left[|\Delta_b| \frac{\mathbf{u}_b - \mathbf{u}_P}{|\boldsymbol{\delta}_b|} + \mathbf{k}_b \cdot (\nabla \mathbf{u})_b \right] \\ & + S_b [\mathbf{n}_b \cdot \boldsymbol{\sigma}_b - (2\mu + \lambda)_b \mathbf{n}_b \cdot (\nabla \mathbf{u})_b] \end{aligned} \quad (22)$$

The Dirichlet type boundary condition results in one implicit term and one (for the temperature field) or several (for the displacement field) explicit terms.

Neuman type

A Neuman condition fixes the gradient of the field, either constant or time-varying, thus resulting in a single source term. When using a fixed-heat-flux boundary condition, the boundary normal

heat flux $\mathbf{n}_b \cdot \mathbf{q}_b''$ is known and the boundary value at the current iteration m is explicitly updated from Eq. (21) as:

$$T_b^m = T_P^{m-1} + \frac{(\mathbf{n}_b \cdot \mathbf{q}_b'')|\delta_b|}{\kappa_b} \quad (23)$$

When using a fixed-traction boundary condition, the boundary traction $\boldsymbol{\tau}_b$ is known and the definition of the traction is used to iteratively calculate the normal gradient. Applying Eq. (9) to the boundary face and rearranging the expression, the normal gradient at the current iteration m is obtained as:

$$(\mathbf{n}_b \cdot \nabla \mathbf{u}_b)^m = \frac{(\boldsymbol{\tau}_b - \mathbf{n}_b \cdot \boldsymbol{\sigma}_b^{m-1})}{(2\mu + \lambda)_b} + (\mathbf{n}_b \cdot \nabla \mathbf{u}_b)^{m-1} \quad (24)$$

In turn, the normal gradient is used to calculate the updated value of the boundary displacement:

$$\mathbf{u}_b^m = \mathbf{u}_P^{m-1} + |\delta_{Pb}|(\mathbf{n}_b \cdot \nabla \mathbf{u}_b^m) \quad (25)$$

3.2.6 Final form of the discretized equations

Once all the terms in the governing equations are discretized, they can be rearranged in the following algebraic forms:

$$a_{T,P}T_P + \sum_N a_{T,N}T_N = b_{T,P} \quad (26)$$

$$a_{u,P}\mathbf{u}_P + \sum_N a_{u,N}\mathbf{u}_N = \mathbf{b}_{u,P} \quad (27)$$

The coefficients and the source terms are obtained from the discretization of the various heat fluxes or tractions, hence the different subscripts T for the temperature and \mathbf{u} for the displacement. Fixed terms and explicit contributions deriving from the boundary conditions are also lumped in the source terms $b_{T,P}$ and $\mathbf{b}_{u,P}$.

The system of equations resulting from the complete discretization of the governing equations on each CV might be written in a more compact way as:

$$[A_T][T] = [b_T] \quad (28)$$

$$[A_u][u] = [b_u] \quad (29)$$

The coefficient matrices $[A_T]$ and $[A_u]$ collect the diagonal coefficients $a_{T,P}$ and $a_{u,P}$, and the off-diagonal coefficients $a_{T,N}$ and $a_{u,P}$, while $[b_T]$ and $[b_u]$ are the vectors collecting all the source terms $b_{T,P}$ and $b_{u,P}$. $[T]$ and $[u]$ are the solution vectors containing the values of the respective fields at the cell-center.

Because the displacement u is a vectorial field, the equation (27) is a system of three coupled equations, one for each Cartesian direction. Although efforts are being made in the OpenFOAM community toward the development of block-coupled solvers for solid mechanics applications in which the three components of displacement are solved as a single linear system [87], the most common solution approach and the one adopted in this work is the segregated solution scheme. The temperature field and the three components of the displacement field are solved separately and sequentially. The cross-coupling and the non-linear terms are added to the source vectors $[b_T]$ and $[b_u]$ and are accounted for with outer iterations.

Because of the presence of explicit terms in the system in Eq. (28) and Eq. (29), it is necessary to iterate the solution until a user pre-defined convergence criterion is met. In this work, the system is solved using the Geometric agglomerated Algebraic MultiGrid (GAMG) linear solver. The solution is iterated until the normalized L1-norm of the residual vector, or more simply the residuals r , falls below the threshold of 10^{-6} . As an example, the residual for the displacement field is:

$$r = \frac{1}{n} \sum | [b_u] - [A_u][u] | \quad (30)$$

The normalization factor n is calculated as:

$$n = \sum (|[A_u][u] - [A_u][\bar{u}]| + |[b_u] - [A_u][\bar{u}]|) \quad (31)$$

where $[\bar{u}]$ is the average solution vector for the displacement field.

3.3 Multi-dimensional analysis

As any solver built with the OpenFOAM library, OFFBEAT is an inherently 3-D code: the geometries are always 3-D and, by default, the code solves the equations in a 3-D Cartesian coordinate system. However, 2-D and even 1-D simulations can be performed using an appropriate geometry and by selecting appropriate boundary conditions.

When applied to faces that are normal to one of the three Cartesian axes, the empty boundary condition allows one to neglect the corresponding normal direction both in the discretization of the governing equations and in the solution of the system matrix. The simulation effectively becomes 2-D as for the block on the top-left corner of Figure 3.3, or even 1-D if the empty condition is applied simultaneously for two Cartesian directions as done for the slab on the top-right corner of Figure 3.3. The same boundary condition would be chosen for the top and bottom surfaces of a 2-D fuel rod disc, also called r - θ case and shown in the bottom portion of Figure 3.3.

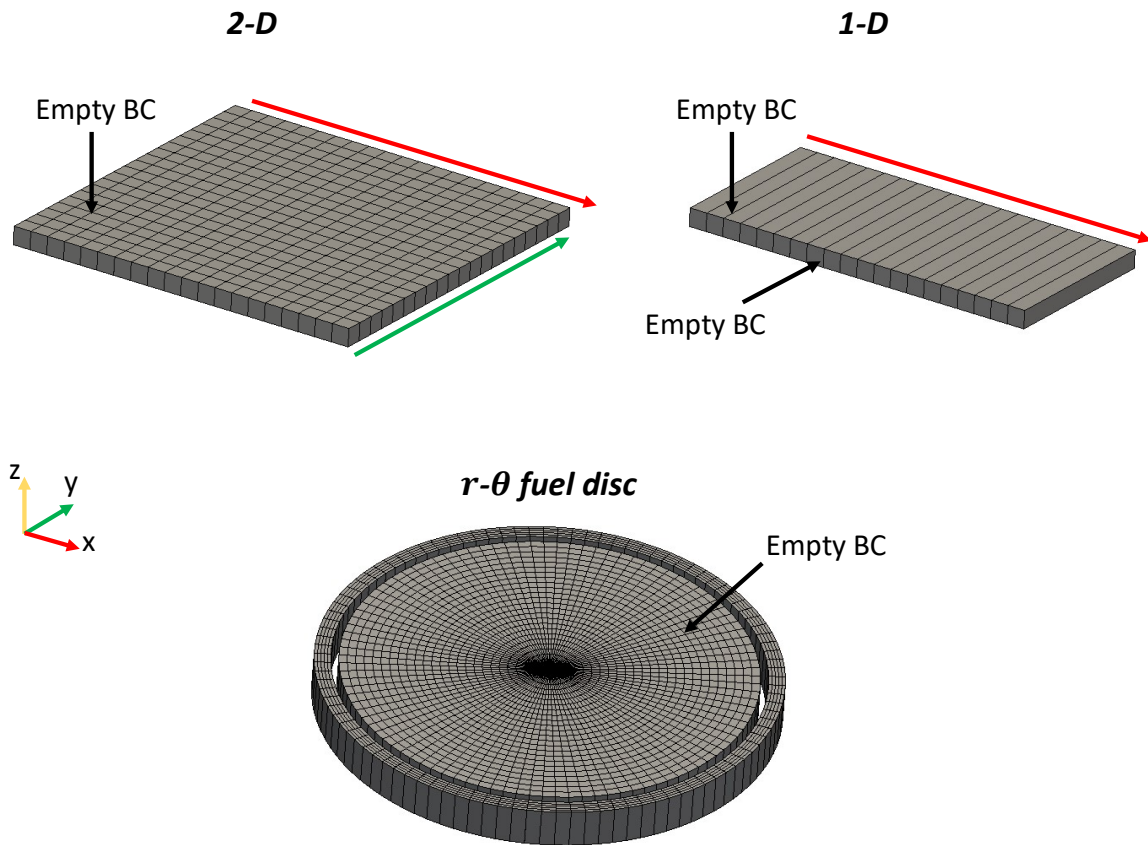


Figure 3.3 – 2-D block (top-left), 1-D slab (top-right) and r - θ case (bottom) with the use of empty boundary conditions.

Neglecting the conservation of the linear momentum along the axial direction is equivalent to imposing a fixed axial constraint, that is, the solution of the momentum balance equations results in zero axial deformation and zero axial strain ($u_z = 0$ and $\varepsilon_z = 0$). This unphysical constraint might cause high compressive axial stresses and might affect also the remaining components of the stress field through the Hooke's law, i.e. the constitutive relation between strains and stresses. For 2-D problems where the axial stress is known to be small, one can approximate the material to be in plane stress. If the corresponding option is activated, OFFBEAT corrects the axial strain right

after the solution of the momentum balance equations and the calculation of the strain tensor. The value of the strain is derived from the basic constitutive relation (simply the inverse of Hooke's law with $\sigma_z = 0$):

$$\varepsilon_z = -\frac{\nu}{E} \overbrace{(\sigma_x + \sigma_y)}^{\text{elastic strain}} + \overbrace{\varepsilon_{z,\text{add}}}^{\text{additional strain}} \quad (32)$$

Where all additional axial components of the strain fields (if present) are condensed in $\varepsilon_{z,\text{add}}$. The corrected ε_z is used to update the stress field which is then introduced in the discretization of the momentum balance equations at the next iteration.

An axisymmetric or r-z cases can be reproduced with a small angle wedge geometry, 1 cell thick in the azimuthal direction, and using the wedge boundary conditions on the radial planes. Figure 3.4 shows, as an example, how a 5-pellet 3-D fuel rodlet can be reduced to an axisymmetric model thanks to the use of the wedge boundary conditions. The Cartesian component which is closest to azimuthal direction (y in the example considered in the figure) is neglected in the solution of the system matrix, making the case effectively 2-D.

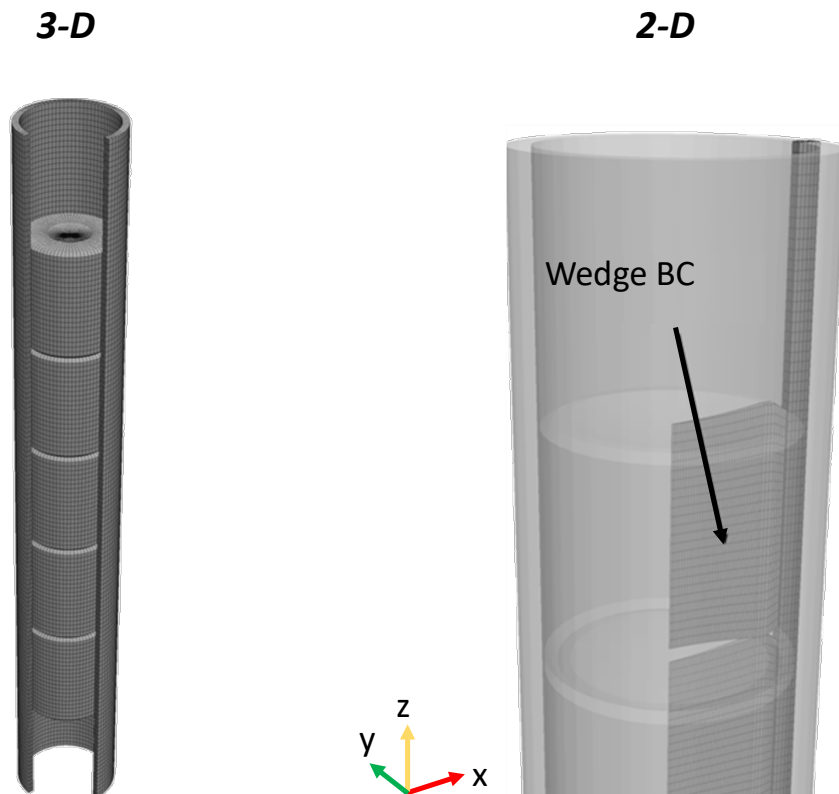


Figure 3.4 – Example of use of wedge boundary conditions: a 3-D 5 pellet rodlet (on the left) is reduced to a 2-D r-z case (on the right).

The wedge and empty boundary conditions can be combined to create a 1-D radial slice, as shown on the left of Figure 3.5. If several of these slices are stacked on top of each other, as done on the right of Figure 3.5, OFFBEAT can also perform a 1.5-D analysis like most traditional codes.

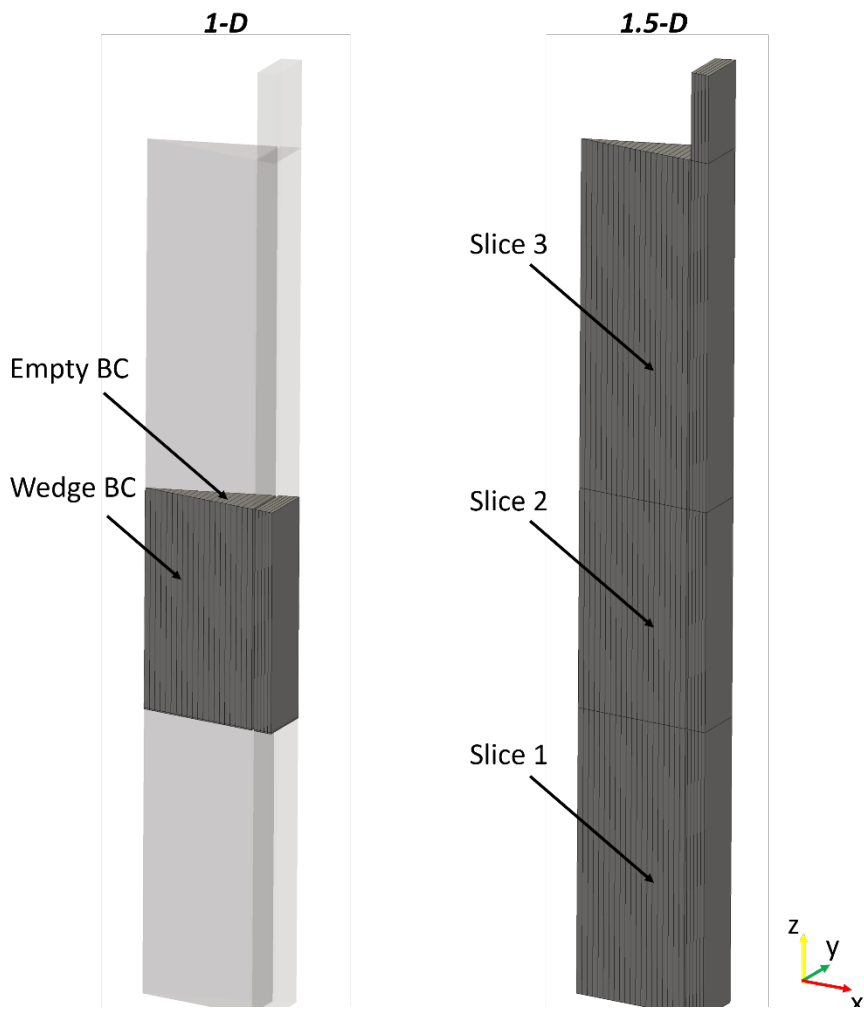


Figure 3.5 – The combination of wedge and empty boundary conditions produces a 1-D radial slice (left). If several slices are stacked on top of each other, separated by empty boundary conditions, OFFBEAT can perform 1.5-D simulations.

As done previously for the plane stress case, the axial strain must be corrected to account for the modified plane strain approximation typical of 1.5-D analysis (i.e. the slice axial deformation is assumed uniform along the radius). If the corresponding option is activated, OFFBEAT performs a balance between the expansion of the slice and the force of the plenum spring. The balance derives from the following constitutive relation of the axial strain:

$$\varepsilon_z = \frac{\sigma_z}{E} - \frac{\nu}{E} \overbrace{(\sigma_x + \sigma_y)}^{\text{elastic strain}} + \underbrace{\varepsilon_{z,\text{add}}}_{\text{additional strain}} \quad (33)$$

By extracting the axial stress σ_z from the previous equation and integrating it over the slice area, the total axial force on the slice is obtained as:

$$\int_A \sigma_z dA = \bar{\varepsilon}_z \int_A E dA + \int_A \nu(\sigma_x + \sigma_y) dA - \int_A E \varepsilon_{z,\text{add}} dA = F_s \quad (34)$$

where $\bar{\varepsilon}_z$ is the slice axial strain, constant by definition because of the modified plane strain assumption. The total force on the slice is equal to F_s that is the reaction of the plenum spring, in turn calculated integrating the axial displacement along the entire rod and multiplying it by a user defined spring modulus. From the previous equation, OFFBEAT derives the updated axial strain component $\bar{\varepsilon}_z$, constant along the slice radius. The new stress field is calculated with the Hooke's law and the code proceeds to the next iteration.

The modified plane strain option implemented in OFFBEAT is correct only for fresh fuel with open gap as the axial contact and friction forces between the fuel and cladding are currently missing from the force balance; these should be considered for future developments of the code.

3.4 Conclusions

While the FVM is used prominently in the field of CFD, the FEM is usually associated with CSM software. However, the two methods can be used alternatively in both fields and recently the application of the FVM for stress analysis has gained momentum. The potential of the FVM for multi-dimensional and multi-physics nuclear fuel modeling is explored in this PhD thesis with the development of a novel FV code named OFFBEAT and built using the OpenFOAM C++ library.

This chapter has presented the numerical structure at the foundation of the code. Building on the works of Jasak, Weller, Tuković and Cardiff, OFFBEAT is encapsulated in a total Lagrangian framework for small-strain solid mechanics with the equations always solved in their total form. This is coupled with a framework for thermal analysis and with numerical developments for the treatment of the gap as discussed in Chapter 4.

The system of governing equations considered includes the momentum conservation and the heat balance equations, discretized following standard cell-centered FV techniques. Additional laws might be included in the future, such as the conservation of species governing the oxygen diffusion in the fuel, or the hydrogen uptake and redistribution combined with hydride formation and reorientation. In particular, the explicit modelling of chemical species would facilitate dedicated studies of stress corrosion cracking (SCC). Material transport such as the one observed in fast reac-

tor fuels could be included by modeling the diffusion of porosities in the fuel and a few relevant nuclides as governed by thermal gradients. Phase change or melting is currently not considered but a homogenisation approach could be envisaged in a similar way as done for the FEM based code ALCYONE [88]. In all these cases, the extension of the discretization procedures described in this chapter to these additional laws is expected to be straightforward.

It must be stressed that, as a fuel performance code, OFFBEAT already considers other physics such as the diffusion of fission gases or the fuel isotopic evolution, but these phenomena are treated with dedicated simplified models, without the spatial discretization of the respective equations. The main models introduced in OFFBEAT are outlined in Chapter 5.

Chapter 4

Numerical developments

Any fuel performance code must address the numerical issues arising from the presence of the fuel-to-cladding gap with the combined occurrence of heat transfer and contact. Although some attempts have been made to develop fuel performance codes with gap elements [89], the most common approach is to have a discontinuous computational domain made of separate fuel and cladding regions. This approach is also followed in OFFBEAT.

In traditional codes with structured meshes each fuel slice is facing a single corresponding portion of cladding. The main numerical issue arising from the presence of the gap is the convergence of the solution scheme at the start of the feedback loop between gap conductance and thermal expansion on the one hand and contact stresses on the other.

In modern, multi-dimensional fuel performance codes, the use of unstructured meshes allows the modeling of more complex geometries and the use of automatic meshing algorithms. This requires an additional numerical infrastructure to correctly exchange information (e.g. heat fluxes and forces) between the two regions, fuel and cladding, with potentially different discretization.

This chapter presents the numerical developments necessary to extend the unstructured FV thermo-mechanics framework discussed in the previous chapter to the typical setup of a nuclear fuel rod, involving the heat exchange and mechanical interaction between two solids separated by a small gap. Thus, the decomposition of the computational domain and discretization of the governing equations in the presence of the gap are described in Section 4.1 together with the chosen mapping algorithm. Then, the gap heat transfer methodology is presented in Section 4.2, and the two contact methodologies implemented in OFFBEAT are outlined in Section 4.3. Finally, the relevant conclusions for this chapter are drawn in Section 4.4.

4.1 The gap and the AMI mapping algorithm

The discretization of the computational domain and governing equations presented in the previous chapter is adapted to properly treat the presence of the gap discontinuity. In Eq. (10), the CV bounding surface S_p of an isolated body was split into a combination of internal and boundary faces. Extracting the gap faces (g) from the subset of boundary faces (b), the definition of S_p is modified as:

$$S_P = \sum_f S_f + \sum_b S_b + \sum_g S_g \quad (35)$$

The surface integral terms in the governing equations Eq. (1) and Eq. (3) must be further split to include an additional gap component:

$$\oint_{S_P} \mathbf{n} \cdot \mathbf{q}'' dS = \sum_f \mathbf{n}_f \cdot \mathbf{q}_f'' S_f + \sum_b \mathbf{n}_b \cdot \mathbf{q}_b'' S_b + \sum_g \mathbf{n}_g \cdot \mathbf{q}_g'' S_g \quad (36)$$

$$\oint_{S_P} \mathbf{n} \cdot \boldsymbol{\sigma} dS = \oint_{S_P} \boldsymbol{\tau} dS = \sum_f \boldsymbol{\tau}_f S_f + \sum_b \boldsymbol{\tau}_b S_b + \sum_g \boldsymbol{\tau}_g S_g \quad (37)$$

Depending on how the normal component of the heat flux \mathbf{q}_g'' or the traction $\boldsymbol{\tau}_g$ are discretized, the coupling between the two surfaces might be explicit or implicit.

The former translates into a standard Dirichlet or Neuman type boundary condition, with the fixed value or the fixed gradient iteratively derived from the interaction with the opposing boundary, i.e. the explicit source terms derived from the discretization depend on the cell-center values on the two sides of the gap at the previous iteration.

With an implicit coupling, instead, the boundary term is discretized as done for the internal faces, with the coupled cell acting as the neighboring CV (naturally taking into account the difference in material properties across the interface). The implicit discretization at the boundary does not add to the source vectors $[\mathbf{b}_T]$ or $[\mathbf{b}_u]$ but results in diagonal and off-diagonal coefficients that can be introduced directly in the solution matrix, i.e. the discretization coefficients depend on the cell-center values on the two sides of the gap at the current iteration. It follows that the neighborhood of the cell centered in P might also include cells of the opposing solid centered in N_g which are either in direct contact with P or separated by the gap. The final form of the discretized equations is modified as:

$$a_{T,P} T_P + \sum_N a_{T,N} T_N + \sum_{N_g} a_{T,N_g} T_{N_g} = b_{T,P} \quad (38)$$

$$a_{u,P} \mathbf{u}_P + \sum_N a_{u,N} \mathbf{u}_N + \sum_{N_g} a_{u,N_g} \mathbf{u}_{N_g} = \mathbf{b}_{u,P} \quad (39)$$

To access the fields and geometrical data on the opposite side of the gap, the two surfaces must interact through a coupling interface. As imposing the use of conformal meshes would be too restrictive, OFFBEAT is designed using the Arbitrary Mesh Interpolation (AMI) [90] method as implemented in OpenFOAM [91], although the extension to the General Grid Interface (GGI) [92] mapping method as implemented in the Foam-extend fork of OpenFOAM [93] would be straightforward. While the AMI was designed for adjacent patches with dissimilar inner construction, in OFFBEAT it is readapted to connect two patches separated by a small and time-varying gap.

Figure 4.1 shows two non-conformal boundaries facing each other. The boundaries are typically designated as master (subscript m) and slave (subscript s) at the start of the simulation. In the example in the figure, the slave surface has twice the number of faces as the master, thus the owner cell centered in P_m has potentially two slave cells in his neighborhood. The AMI algorithm allows to reconstruct the single virtual neighbor cell, with its face-center f_{gs} , cell-center N_{gs} and related quantities. Naturally, the figure depicts the point of view of the master surface, but the AMI algorithm works in the same fashion when the traction or heat flux is discretized on the slave face. In this case, the slave cell centered in P_s is considered as the owner, while the coupled master cells centered in N_{gm} are the neighbors.

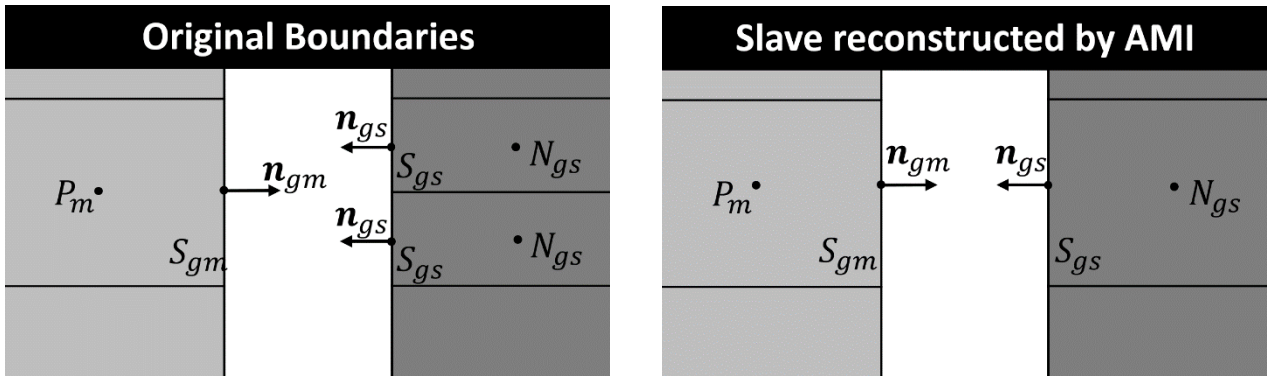


Figure 4.1 - Non-conformal master and slave surfaces facing each other across the gap (left). The AMI mapping algorithm reconstructs a single virtual opposing slave cell for each face on the master side (right), and vice versa.

The specific interpolation algorithm used in OFFBEAT is the face-area-weighting technique, which works as follows. At the beginning of the simulation, the user selects the master and slave surfaces. Then, for each master face, the AMI loops over the slave faces in its vicinity and calculates the

portion of overlapping area by projecting the master face along the direction \mathbf{n}_{gm}^* , taken as the average between the local master and slave normal vectors:

$$\mathbf{n}_{gm}^* = \frac{\mathbf{n}_{gm} - \mathbf{n}_{gs}}{|\mathbf{n}_{gm} - \mathbf{n}_{gs}|} \quad (40)$$

The addressing that is the list of neighboring faces that resulted in a non-zero overlap is stored by the AMI together with the values of the corresponding projected areas. Once normalized, the latter can be used as weights to map any quantity from one side of the gap to the other.

In the sections that follow, when dealing with non-conformal meshes, it is always implied that, when the traction is discretized on the master (or slave) boundary, the cell in N_{gs} (or N_{gm}) is the interpolated neighboring cell as determined by the AMI method.

4.2 Gap heat transfer methodology

The gap heat transfer methodology developed for OFFBEAT assumes that the heat is exchanged only between faces that are coupled via the AMI mapping algorithm described in the previous section. For axisymmetric or 3-D concentric simulations, this results in a multi-dimensional generalization of the thin-gap approximation of traditional fuel performance codes, in line with most of the gap conductance models available in the literature.

4.2.1 Issues with the thin gap approximation

The thin gap approximation becomes less and less accurate the more the gap size increases and the more the two surfaces are irregular, as is the case for unconventional fuel configurations such as pellets with severe eccentricity or missing fragments, but also for the more conventional chamfered pellet design. However, as the conduction through the gas is small due to the larger gap size, the main error lies in the radiative component, which generally provides only a minor contribution to the total gap heat transfer. For this reason, extending the thin-gap approximation to more complex geometries is expected to cause only second-order errors for most irradiation conditions, at least when not dealing with severe accidents and high fuel temperatures. A more accurate assessment of the gap heat transfer would require the explicit multidimensional modeling of conduction and the use of view-factor methods for the radiative heat exchange. Similar studies will be part of future development efforts of OFFBEAT and could lead to more realistic gap conductance models for multi-dimensional codes.

4.2.2 Discretization of the gap heat fluxes

In the thin-gap approximation the heat transfer is essentially 1-D, and it can be interpreted using the concept of thermal resistances. The heat exchange between the master cell centered in P_m and the slave cell centered in N_{gs} is then equivalent to a circuit where a temperature potential

difference ($T_{N_{gs}} - T_{P_m}$) causes a current of heat flux q''_{ms} to flow across the thermal resistances shown in Figure 4.2 and defined as:

$$\begin{aligned} R_m &= \frac{|\delta_{gm}|}{\kappa_{gm}} \\ R_h &= \frac{1}{h} \\ R_s &= \frac{|\delta_{gs}|}{\kappa_{gs}} \end{aligned} \quad (41)$$

Where κ_{gm} and κ_{gs} are the master and slave thermal conductivities, and h is the local gap heat transfer coefficient.

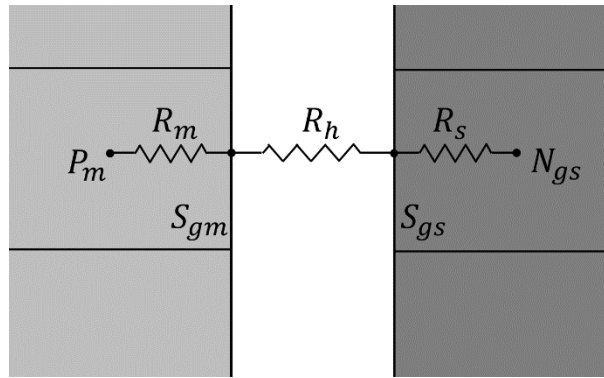


Figure 4.2 – Circuit of thermal resistances between master cell-center and slave cell-center.

The gap conductance model implemented in OFFBEAT is derived from FRAPCON and is described more in detail in the next chapter, but in theory any correlation for the gap conductance could be used. As the resistances in the circuit are in series, the heat flux q''_{ms} can be written alternatively as:

$$\begin{aligned} \ddot{q}_{ms} &= \frac{T_{gm} - T_{P_m}}{R_m} \\ \ddot{q}_{ms} &= \frac{T_{gs} - T_{gm}}{R_h} \\ \ddot{q}_{ms} &= \frac{T_{N_{gs}} - T_{gs}}{R_s} \end{aligned} \quad (42)$$

Rearranging and summing the three equations above, the heat flux can be rewritten as:

$$q''_{ms} = \frac{T_{N_{gs}} - T_{P_m}}{R_t} \quad (43)$$

where the total resistance R_t is simply the sum of the three resistances:

$$R_t = R_m + R_h + R_s \quad (44)$$

Using Eq. (43), the rate of heat flowing through the master face with area S_{gm} can be approximated as:

$$\oint_{S_{gm}} \mathbf{n}_{gm} \cdot \ddot{\mathbf{q}}_{gm} dS_{gm} \approx \ddot{q}_{ms} S_{gm} = S_{gm} \frac{T_{N_{gs}} - T_{P_m}}{R_t} \quad (45)$$

Combining the first Eq. (42) and Eq. (43) the temperature on the master boundary can be obtained with a simple linear interpolation:

$$T_{gm} = \frac{R_m}{R_t} T_{N_{gs}} + \frac{R_s}{R_t} T_{P_m} \quad (46)$$

The discretization presented in this section followed the point of view of the master face. When the heat diffusion equation is discretized for the slave cell, its cell-center point is designated as P_s and the neighbor master cell is centered in N_{gm} . After the exchange of position between the subscripts m and s , the rate of heat loss through the surface S_{gs} and the boundary temperature T_{gs} are given by equation equivalent to Eq. (45) and Eq. (46), respectively.

Finally, to conserve the total heat exchanged across the gap, the surface integral term in Eq. (45) is multiplied by a correction factor, which takes into account the difference in areas between fuel and cladding. This factor is obtained as:

$$C_m = \frac{\sum_j S_{gm \rightarrow sj}}{S_{gm}} \quad (47)$$

$$C_s = \frac{\sum_i S_{gm_i \rightarrow s}}{S_{gs}} \quad (48)$$

where $S_{gm_i \rightarrow s_j}$ is used to indicate the fraction of the master face m_i projected by the AMI on the slave face s_j . The index j runs over all the slave faces coupled to the master face m in Eq. (47), while the index i runs over all the master faces coupled to the slave face s in Eq. (48).

4.3 Contact methodology

The contact between two bodies plays a crucial role in several engineering applications [94], from metal forming to the deformation of structures' foundations, vehicle crash simulations, biomechanics and countless more. The numerical solution to contact problems can be challenging, as the mathematical treatment of contact mechanics introduces a severely discontinuous boundary non-linearity, even for the case of simple linear elasticity [95]. Numerous researchers have investigated this topic using the FEM and several methods have been developed to enforce the contact constraints in the FE formulation with the most common being the Lagrange multiplier method, the augmented Lagrange multiplier methods, and the penalty method.

The extensive literature review performed prior to this thesis reveals that limited work has been done in the FV community toward the development of robust algorithms for contact mechanics and that most of this work has been done using the collocated or cell-centered FVM. A first FV contact stress solver was developed by Jasak and Weller [29] in 2000. They complemented their basic linear elastic solver [22] with an additional boundary condition, capable of detecting the overlapping portion of the two facing surfaces and transmitting the normal component of the contact traction.

Cardiff et al [30] pointed out that the solver developed by Jasak and Weller was effective in two-dimensions (2-D), but it produced unrealistic stress peaks close to the contact region in three-dimensions (3-D). Moving from this limitation, Cardiff et al. developed an alternative frictionless contact boundary condition based on the penalty-method, which was later extended to include a Coulomb friction component [96] and it was implemented in a FV toolbox for solid mechanics and fluid-solid interaction named solids4Foam [81], valid both for small strain and finite strain simulations. However, the penalty method boundary condition developed by Cardiff is explicit, that is: the boundary contact stress is a source term, and it is calculated based on the displacements from the previous iteration. For cases that are ill-conditioned (such as the case of a free body pushed by a load against a fixed foundation), convergence can be reached only if the solution of the linear system resulting from the discretization of the governing equations is heavily under-relaxed. This combined with the level of mesh refinement typically necessary to obtain an accurate solution for contact problems, can make the simulation extremely slow.

An alternative implicit contact methodology was developed in the framework of this PhD thesis. The methodology moves from the consideration that two bodies in contact share strong similarities with bi-material solids. Indeed, when the two opposing surfaces are in contact, they share not just the same traction but also the same normal displacement, while the gradient of the displacement normally remains discontinuous across the contact interface due to possibly different ther-

mo-mechanical properties. The main differences with bi-material cases are that the contact interface cannot sustain positive traction and that the tangential component of the contact traction might be transmitted only partially, depending on the friction characteristics of the two surfaces.

Therefore, OFFBEAT is equipped with two contact algorithms. The first, described in Section 4.3.1, is based on the penalty-method and it is derived from the work of Cardiff. The second is the novel implicit methodology and it is presented in the following six sub-sections, gradually increasing the complexity of the contact problem considered to properly introduce all its features: First, Section 4.3.2 derives the contact traction for the simple case of fully closed gap for two identical boundaries with orthogonal meshes; then, Section 4.3.3 introduces the frictional component while Section 4.3.4 adds the correction term for non-orthogonal boundaries, which are also necessary in the case of non-conformal boundaries; with the introduction of a blending function that interpolates between contact stresses and gap pressure, the contact methodology is extended to scenarios with fully or partially open gap as discussed in Section 4.3.5, while the characteristics of the specific blending function adopted in this thesis are described in Section 4.3.6; finally, Section 4.3.7 shows how to extend the implicit methodology to the more general case of boundaries with different geometry and orientation.

4.3.1 Explicit contact based on the penalty method

Once a slave face-center is detected to penetrate a master face, the penalty method calculates the local interfacial pressure p_i as:

$$p_i = -\left(\gamma \frac{S_m}{V_m} K_m\right) g_m \quad (49)$$

where S_m and V_m are the master cell surface area and volume, K_m is the master bulk modulus, and $\gamma > 0$ is the so-called penalty factor which is introduced to prevent numerical instability at the expense of a larger penetration. The local gap width g_m on the master side (negative in case of penetration) is calculated as:

$$g_m = [(\mathbf{f}_{gm} + \mathbf{u}_{gm}) - (\mathbf{f}_{gs} + \mathbf{u}_{gs})] \cdot \mathbf{n}_{gm} \quad (50)$$

where \mathbf{f}_{gm} and \mathbf{f}_{gs} are the position vectors associated with the master and slave face-center points. Neglecting friction, the local contact traction on the master face is equal to:

$$\boldsymbol{\tau}_{gm} = \begin{cases} -p_i \mathbf{n}_{gm} & \text{if } g < 0 \\ -p_g \mathbf{n}_{gm} & \text{if } g \geq 0 \end{cases} \quad (51)$$

where the known gap pressure p_g is applied in case the gap is open. The pressure p_g can be either fixed or a function of the temperature and volume available to the filling gas. Thanks to the AMI algorithm, the traction is mapped to the slave side so that the total force acting on the two surfaces is conserved. The traction is added directly to the source term as done for the fixed-traction boundary type, while the corresponding normal gradient is obtained once again from Eq. (24).

The contact pressure is calculated as a function of the ratio between the penetration distance equivalent to the gap size $|g|$ and the cell thickness (equivalent to the ratio $\frac{s}{V}$). A penalty factor smaller than 1 effectively reduces the boundary stiffness of the cell allowing for higher degree of penetration, towards improving numerical stability. If the penalty factor is too low (usually below 0.1) the higher penetration can affect excessively the accuracy of the solution. Thus, penalty factors closer to 1 are preferable to obtain more accurate results. The price to pay for a converged solution is the use of under-relaxation factors which, in turn, have the effect of slowing down the convergence rate. One can under-relax the matrix system for the displacement equation, the displacement field (all standard features available in OpenFOAM) or one can under-relax the contact pressure itself. The latter in particular helps to slowly reduce the contact forces on those boundary faces that are leaving contact stabilizing the solution of the system of coupled thermo-mechanical equations. As a rule, the user should strive for a compromise between accuracy and stability taking into account also time restraint, computing resources available and the type of application.

4.3.2 Implicit contact with closed gap and conformal, orthogonal meshes

The implicit contact methodology can be first derived considering the two cells V_{P_m} and $V_{N_{gs}}$ shown in Figure 4.3, which are part of two boundaries in contact discretized with orthogonal and conformal meshes. The two outward normal vectors lie in the same direction, i.e. $\mathbf{n}_{gm} = -\mathbf{n}_{gs}$, and are parallel to δ_{gm} and δ_{gs} , defined as the cell-center to face-center distance vectors on the master and slave side, respectively.

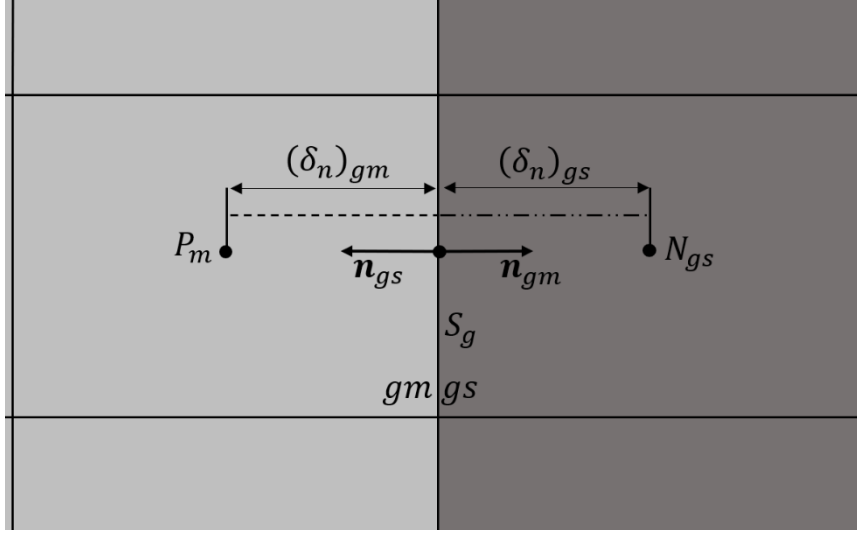


Figure 4.3 – Example of contact between master cell in P_m and slave cell in N_{gs} . The meshes are orthogonal and conformal.

Following the derivation described by Tukovic [78] for internal interfaces (see also Appendix A in [84] for the complementary derivation), the contact traction vector $\boldsymbol{\tau}_g$ can be decomposed into normal and tangent components:

$$(\boldsymbol{\tau}_n)_g = (2\mu + \lambda)_g \mathbf{n}_g \cdot (\nabla \mathbf{u}_n)_g + \lambda_g \text{tr}(\nabla_t \mathbf{u}_t)_g \mathbf{n}_g \quad (52)$$

$$(\boldsymbol{\tau}_t)_g = \mu_g \mathbf{n}_g \cdot (\nabla \mathbf{u}_t)_g + \mu_g (\nabla_t \mathbf{u}_n)_g \quad (53)$$

where the tangent gradient operator $\nabla_t = (\mathbf{I} - \mathbf{n}\mathbf{n})\nabla$ is introduced, and the subscripts n and t refer to the normal and tangent components of traction and displacement.

The normal component of the traction on the two opposite sides of the contact interface can be discretized as follows:

$$(\boldsymbol{\tau}_n)_{gm} = \frac{(\mathbf{u}_n)_{gm} - (\mathbf{u}_n)_{P_m}}{R_{nm}} + \mathbf{Q}_{nm} \quad (54)$$

$$(\boldsymbol{\tau}_n)_{gs} = \frac{(\mathbf{u}_n)_{gs} - (\mathbf{u}_n)_{P_s}}{R_{ns}} + \mathbf{Q}_{ns} \quad (55)$$

Borrowing terminology from circuit analysis, the equations above have introduced the normal resistances:

$$R_{nm} = \frac{(\delta_n)_{gm}}{(2\mu + \lambda)_{gm}} \quad (56)$$

$$R_{ns} = \frac{(\delta_n)_{gs}}{(2\mu + \lambda)_{gs}} \quad (57)$$

where the normal cell-center to face-center distances are defined as $(\delta_n)_{gm} = \mathbf{n}_{gm} \cdot \boldsymbol{\delta}_{gm}$ and $(\delta_n)_{gs} = \mathbf{n}_{gs} \cdot \boldsymbol{\delta}_{gs}$. For orthogonal boundaries they coincide with the norms $|\boldsymbol{\delta}_{gm}|$ and $|\boldsymbol{\delta}_{gs}|$. Also, in Eq. (54) and Eq. (55) the following substitutions have been introduced:

$$\begin{aligned} \mathbf{Q}_{nm} &= \lambda_{gm} \text{tr}(\nabla_t \mathbf{u}_t)_{gm} \mathbf{n}_{gm} \\ &= (\mathbf{n}_{gm} \mathbf{n}_{gm}) \cdot (\mathbf{n}_{gm} \cdot \boldsymbol{\sigma}_{gm}) - (2\mu + \lambda)_{gm} \mathbf{n}_{gm} \cdot (\nabla \mathbf{u}_n)_{gm} \end{aligned} \quad (58)$$

$$\begin{aligned} \mathbf{Q}_{ns} &= \lambda_{gs} \text{tr}(\nabla_t \mathbf{u}_t)_{gs} \mathbf{n}_{gs} \\ &= (\mathbf{n}_{gs} \mathbf{n}_{gs}) \cdot (\mathbf{n}_{gs} \cdot \boldsymbol{\sigma}_{gs}) - (2\mu + \lambda)_{gs} \mathbf{n}_{gs} \cdot (\nabla \mathbf{u}_n)_{gs} \end{aligned} \quad (59)$$

These substitutions are not just for clarity. Indeed, by simply adjusting the definition of strain and stress tensors, the expressions for the traction in Eq. (54) and Eq. (55) are not limited to linear-elastic materials but can be used also in the presence of additional strain components, already included in the formulation of the stress tensors $\boldsymbol{\sigma}_{gm}$ and $\boldsymbol{\sigma}_{gs}$.

When master and slave faces are in contact, it follows from the definition of the gap width in Eq. (50) with $g = 0$ that:

$$(\mathbf{u}_n)_{gm} + [(\mathbf{f}_n)_{gm} - (\mathbf{f}_n)_{gs}] = (\mathbf{u}_n)_{gs} \quad (60)$$

i.e. the normal component of the displacement field is continuous at the contact interface only if corrected for the initial face-center position. Making use of the continuity of the traction across the contact interface and considering that the outward normal vectors lie in opposite direction, the traction in Eq. (54) is equal to the opposite of the traction in Eq. (55), i.e. $(\boldsymbol{\tau}_n)_{gm} = -(\boldsymbol{\tau}_n)_{gs}$. Extracting and substituting $(\mathbf{u}_n)_{gs}$ from Eq. (60), the following expression for the normal component of the displacement at the boundary is derived:

$$(\mathbf{u}_n)_{gm} = w_n(\mathbf{u}_n)_{P_m} + (1 - w_n)(\mathbf{u}_n)_{P_s} - \frac{R_{nm}R_{ns}}{R_{nm} + R_{ns}}(\mathbf{Q}_{ns} + \mathbf{Q}_{nm}) - (1 - w_n)[(\mathbf{f}_n)_{cm} - (\mathbf{f}_n)_{cs}] \quad (61)$$

where w_n is the normal interpolation weight:

$$w_n = \frac{R_{ns}}{R_{nm} + R_{ns}} \quad (62)$$

The boundary displacement in Eq. (61) is a weighted linear interpolation between the cell-center values in the two opposing cells, plus an additional explicit term. Finally, substituting Eq. (61) in Eq. (54), the following expression is derived for the normal component of the contact traction on the master face:

$$(\boldsymbol{\tau}_n)_{gm} = \overline{(2\mu + \lambda)}_g \frac{(\mathbf{u}_n)_{P_s} - (\mathbf{u}_n)_{P_m}}{\delta_{ms}} - w_n \mathbf{Q}_{ns} + (1 - w_n) \mathbf{Q}_{nm} - \overline{(2\mu + \lambda)}_g \frac{(\mathbf{f}_n)_{cm} - (\mathbf{f}_n)_{cs}}{\delta_{ms}} \quad (63)$$

where $\delta_{ms} = (\delta_n)_{gm} + (\delta_n)_{gs}$, and $\overline{(2\mu + \lambda)}_g$ is calculated with harmonic interpolation. The normal traction on the slave face is simply the opposite of Eq. (63).

4.3.3 Frictional component

Depending on the surface characteristics of the two materials, only a fraction of the tangent or frictional force is transmitted across the contact surface, usually up to a certain fraction of the normal component. The friction coefficient $\alpha \in [0, \infty)$ is introduced so that:

$$(\boldsymbol{\tau}_t)_{gm} = \min(|(\boldsymbol{\tau}_t)_{gm,\infty}|, \alpha |(\boldsymbol{\tau}_n)_{gm}|) \frac{(\boldsymbol{\tau}_t)_{gm,\infty}}{|(\boldsymbol{\tau}_t)_{gm,\infty}|} \quad (64)$$

The vector $(\boldsymbol{\tau}_t)_{gm,\infty}$ is the tangent traction on the master face in case of infinite friction coefficient or bonding, i.e. when the two boundaries in contact cannot slide relatively to each other. Applying the same procedure presented in the previous section, the following relation is derived for the tangent traction on the master face in case of bonding:

$$(\boldsymbol{\tau}_t)_{gm,\infty} = \overline{\mu}_g \frac{(\mathbf{u}_t)_{P_s} - (\mathbf{u}_t)_{P_m}}{\delta_{ms}} - w_t \mathbf{Q}_{ts} + (1 - w_t) \mathbf{Q}_{tm} \quad (65)$$

where $\overline{(\mu)}_g$ is obtained with harmonic interpolation. As done for the normal component of the stress the following substitutions are introduced:

$$\mathbf{Q}_{tm} = \mu_{gm} \nabla_t \mathbf{u}_{nm} = (\mathbf{I} - \mathbf{n}_{gm} \mathbf{n}_{gm}) \cdot (\mathbf{n}_{gm} \cdot \boldsymbol{\sigma}_{gm}) - \mu_{gm} \mathbf{n}_{gm} \cdot \nabla \mathbf{u}_{tm} \quad (66)$$

$$\mathbf{Q}_{ts} = \mu_{gs} \nabla_t \mathbf{u}_{ns} = (\mathbf{I} - \mathbf{n}_{gs} \mathbf{n}_{gs}) \cdot (\mathbf{n}_{gs} \cdot \boldsymbol{\sigma}_{gs}) - \mu_{gs} \mathbf{n}_{gs} \cdot \nabla \mathbf{u}_{ts} \quad (67)$$

and the tangent resistances R_{tm} and R_{ts} , and tangent interpolation weight w_t are defined as:

$$R_{tm} = \frac{(\delta_n)_{gm}}{\mu_{gm}} \quad (68)$$

$$R_{ts} = \frac{(\delta_n)_{gs}}{\mu_{gs}} \quad (69)$$

$$w_t = \frac{R_{ts}}{R_{tm} + R_{ts}} \quad (70)$$

The slave traction is simply the opposite of Eq. (64). Given that the tangential traction is found explicitly as a function of the normal component, it is added directly to the source term as done for the fixed-traction boundary type. The corresponding tangent gradient is used to calculate the tangential component of the boundary displacement $(\mathbf{u}_t)_{gm}$ and $(\mathbf{u}_t)_{gs}$. For this reason, the implicit contact methodology proposed in this work is more precisely semi-implicit.

4.3.4 Correction for non-orthogonal boundaries and non-conformal meshes

In the previous sections, the cell-center to face-center vector $\boldsymbol{\delta}_g$ was assumed parallel to the outward normal vector and the meshes on both side of the contact interface were identical. Similar to [79], an explicit non-orthogonal correction term is added to accurately discretize the contact traction on non-orthogonal meshes.

As shown in Figure 4.4, the following correction vectors can be defined:

$$\mathbf{k}_m^{\text{corr}} = \boldsymbol{\delta}_{gm} - (\delta_n)_{gm} \mathbf{n}_{gm} \quad (71)$$

$$\mathbf{k}_s^{\text{corr}} = \boldsymbol{\delta}_{gs} - (\delta_n)_{gs} \mathbf{n}_{gs} \quad (72)$$

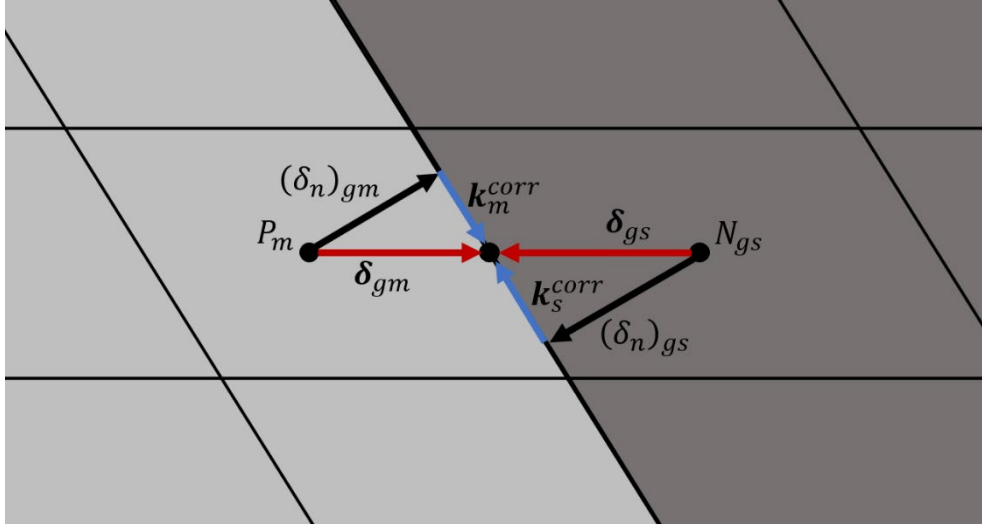


Figure 4.4 – Non-orthogonal correction vectors for master cell in P_m and slave cell in N_{gs} . The meshes are supposed to be conformal.

By extracting the outward normal vector from the equations above and by substituting in Eq (52), the normal traction on the master and slave side (previously defined in Eq. (54) and Eq. (55)) is rewritten as:

$$(\boldsymbol{\tau}_n)_{gm} = \underbrace{\frac{(\mathbf{u}_n)_{gm} - (\mathbf{u}_n)_{P_m}}{R_{nm}}}_{\text{orthogonal contribution}} - \underbrace{\frac{\mathbf{k}_m^{\text{corr}} \cdot (\nabla \mathbf{u}_n)_{gm}}{R_{nm}}}_{\text{non-orthogonal correction}} + \mathbf{Q}_{nm} \quad (73)$$

$$(\boldsymbol{\tau}_n)_{gs} = \underbrace{\frac{(\mathbf{u}_n)_{gs} - (\mathbf{u}_n)_{P_s}}{R_{ns}}}_{\text{orthogonal contribution}} - \underbrace{\frac{\mathbf{k}_s^{\text{corr}} \cdot (\nabla \mathbf{u}_n)_{gs}}{R_{ns}}}_{\text{non-orthogonal correction}} + \mathbf{Q}_{ns} \quad (74)$$

Following the same derivation presented in Sec. 4.3.2, the following normal non-orthogonal correction traction is obtained. Once again, the traction on the slave side is simply the opposite:

$$(\boldsymbol{\tau}_n)_{gm}^{corr} = \overline{(2\mu + \lambda)}_g \frac{\mathbf{k}_s^{corr} \cdot (\nabla \mathbf{u}_n)_{gs} - \mathbf{k}_m^{corr} \cdot (\nabla \mathbf{u}_n)_{gm}}{\delta_{ms}} \quad (75)$$

Applying the same procedure to the tangent component of the traction, the tangent non-orthogonal correction traction for the infinite friction case is:

$$(\boldsymbol{\tau}_t)_{gm,\infty}^{corr} = \overline{\mu}_g \frac{\mathbf{k}_s^{corr} \cdot (\nabla \mathbf{u}_t)_{gs} - \mathbf{k}_m^{corr} \cdot (\nabla \mathbf{u}_t)_{gm}}{\delta_{ms}} \quad (76)$$

A non-orthogonal correction term is always necessary in the presence of non-conformal meshes, even when the original boundaries are orthogonal. Indeed, the AMI can reconstruct the single opposing cell, but the reconstructed neighbor cell-center and its related fields do not necessarily lie in front of the owner face-center. In the example on the left of Figure 4.5 the master cell V_{P_m} is in contact only with the slave cell $V_{N_{gs}}$ in the original geometry. The face-area-weighting technique detects a single interpolation weight equal to one even if the slave cell extends beyond the area in contact with V_{P_m} . When the traction is discretized on the master face, the AMI reconstructs the neighbor slave cell as on the right of Figure 4.5 but the weighted average results in the values of the original slave cell V_{P_s} (this is valid for any quantity that needs to be reconstructed such as displacement or stress at the boundary or at the cell-center, face-center and cell-center location etc.). Thus, to calculate the neighbor traction at the owner face-center (at \mathbf{f}_{gm} in the example in Figure 4.5) it is necessary to add a non-orthogonal correction term as the one in Eq. (73) and Eq. (74). For this purpose, it is sufficient to redefine the neighbor $\boldsymbol{\delta}_g$ vector ($\boldsymbol{\delta}_{gs}$ in the example in Figure 4.5) as the distance vector between the owner face-center and the reconstructed neighbor cell-center. Naturally, this new definition includes the previous one for conformal boundaries as a special case.

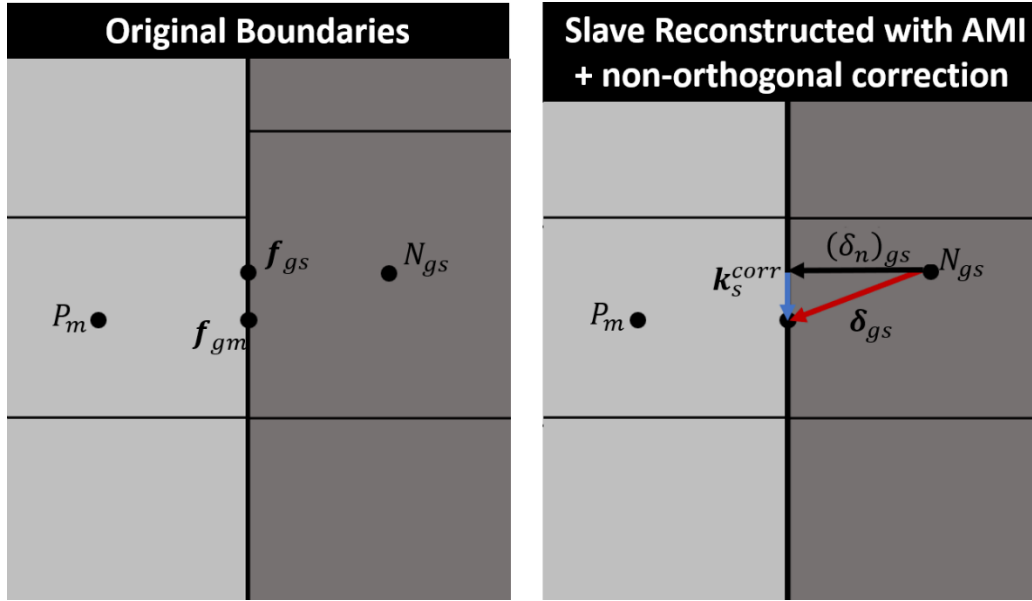


Figure 4.5 – Non-orthogonal correction for non-conformal boundaries. The AMI method introduces non-orthogonality even in the presence of orthogonal original boundaries.

4.3.5 Transition between open and closed gap

The traction τ_g must reduce to the pressure of the fluid in the gap region (i.e. $-p_g \mathbf{n}_g$) when the surfaces are not in contact, while the relations derived in the previous sections are valid only if the gap is closed. The sudden change in surface traction, i.e. the transition from closed to open-gap and vice versa, can be treated numerically with the introduction of a blending function interpolating between the gap pressure and the contact stresses.

Different choices of blending function are possible and more details about the one proposed in this thesis are given in the next section. More generally, the blending coefficient $\beta(g)$ is a function of the gap width g and must have the following characteristics:

$$\begin{cases} \beta(g) \in [0,1] \\ \lim_{g \rightarrow \infty} \beta(g) = 0 \end{cases}$$

It is also desirable that $\beta(g)$ is sufficiently small for $g > 0$, at least starting from some fraction of the initial gap width. This helps to avoid or limit spurious attractive forces that would be introduced if the two surfaces were considered partly attached, although they are still separated by an open gap. The meaning of “sufficiently small” cannot be defined a-priori and it depends on various factors, such as case setup, boundary conditions and mesh resolution.

To properly account for the presence of an open gap, it is necessary to modify the definition of the neighbor δ_g vector. As shown in Figure 4.6, the owner face-center is projected across the gap along the outward normal direction, to find the point f'_g on the neighbor face (f'_{gs} in the example

in Figure 4.6). The neighbor δ_g vector (δ_{gs} in the example in Figure 4.6) is then calculated as the distance between f'_g and the reconstructed neighbor cell-center.

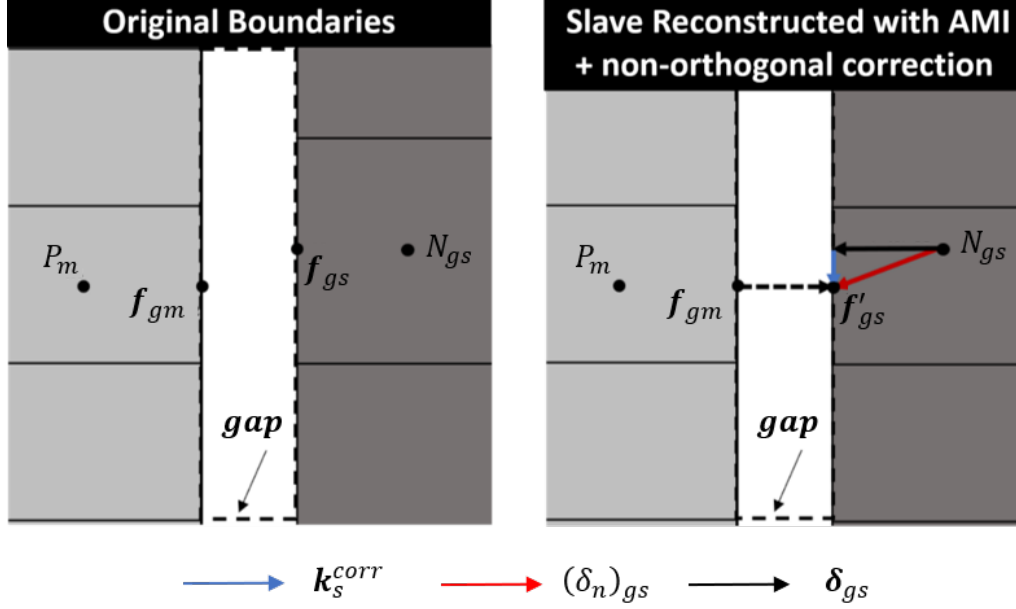


Figure 4.6 – Non-orthogonal correction with open-gap. The owner face-center must be projected on the neighbor face to calculate the neighbor traction.

With this minor modification to the definition of δ_g and with the addition of the blending function, the contact methodology can be finally extended to open gap scenarios. After adding (implicitly) and subtracting (explicitly) the tangential component of the normal gradient, the total contact traction on the master face can be rewritten as:

$$\begin{aligned}
 \tau_{gm} = & \overbrace{\beta(2\mu + \lambda)_g \frac{(\mathbf{u})_{N_{gs}} - (\mathbf{u})_{P_m}}{\delta_{ms}}}^{\text{implicit}} - \overbrace{\beta(2\mu + \lambda)_g \frac{(\mathbf{u}_t)_{N_{gs}} - (\mathbf{u}_t)_P}{\delta_{ms}}}^{\text{explicit}} \\
 & + \beta \left[\overbrace{-w_n \mathbf{Q}_{ns} + (1 - w_n) \mathbf{Q}_{nm}}^{\text{explicit}} - \overbrace{(2\mu + \lambda)_g \frac{(\mathbf{f}_n)_{gm} - (\mathbf{f}'_n)_{gs}}{\delta_{ms}} + (\tau_t)_{gm}}^{\text{explicit}} \right] \\
 & + \beta \left[\overbrace{(2\mu + \lambda)_g \frac{\mathbf{k}_s^{\text{corr}} \cdot (\nabla \mathbf{u}_n)_{gs} - \mathbf{k}_m^{\text{corr}} \cdot (\nabla \mathbf{u}_n)_{gm}}{\delta_{ms}}}^{\text{explicit}} \right] \\
 & + \overbrace{(1 - \beta)(-p_g \mathbf{n}_{gm})}^{\text{explicit}}
 \end{aligned} \tag{77}$$

It is important to note that, as for the penalty factor in the penalty method, the introduction of the blending coefficient in the implicit contact methodology can be interpreted as a softening of the contact interface. This inevitably changes the physics of the simulation with larger penetration and wider contact area to preserve the global force balance, but it is necessary for convergence in many situations. Different from the penalty method, the blending coefficient is not constant and, in most cases, one can select an appropriate blending function to avoid a discontinuous jump from the gap pressure (usually very weak) to the contact stresses (usually very high). Additionally, because the contact stresses are taken care of in a semi-implicit manner, the performances (stability and convergence properties) of the implicit contact methodology are expected to be superior to those of the penalty method.

4.3.6 The sigmoid blending function

A curve that respects the characteristics described in the previous section and at the same time allows for a smooth and gradual change in blending coefficient is the sigmoid function. The specific function proposed in this thesis is given as:

$$\beta(g) = \frac{1}{1 + \exp\left(\ln(10^6 - 1) \frac{(g + o)}{h}\right)} \quad (78)$$

The sigmoid above is completely defined by the two parameters shown in Figure 4.7: the offset o , that is the position of the inflection point along the g axis, and its width. This is defined as the half-width h of a symmetric interval around inflection point so that $\beta(h - o) = 10^{-6}$, although any value $\in (0, 0.5)$ could have been chosen. The user can provide the width and the offset as an absolute value (in meters) or in relative terms as a fraction of the cell-center to face-center distance (designated in this case as o_{rel} and h_{rel}).

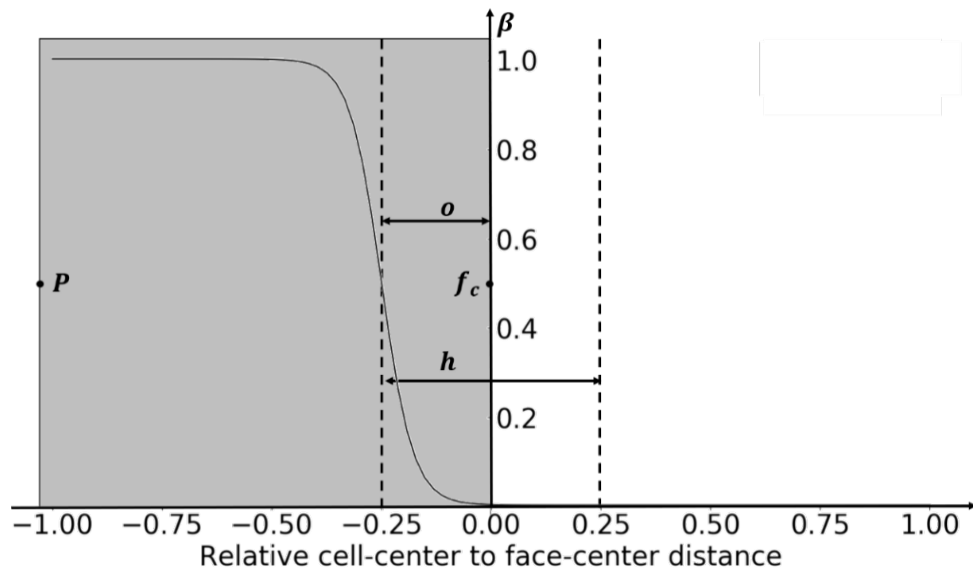


Figure 4.7 – Sigmoid blending function. The offset o and the half-width h are shown.

Figure 4.8 shows the effect of changing the offset and the width of the blending curve. For the same width, a larger offset causes a higher degree of penetration but reduces the spurious attractive forces when the gap is still open. In certain cases, a larger offset might also obstruct convergence, as the smaller is the blending coefficient the smaller is the implicit contribution of the traction in Eq. (77). Alternatively, for the same offset, a larger half-width allows a smoother change in blending coefficient but increases the risk of incurring in spurious attractive forces when the two bodies are not in contact.

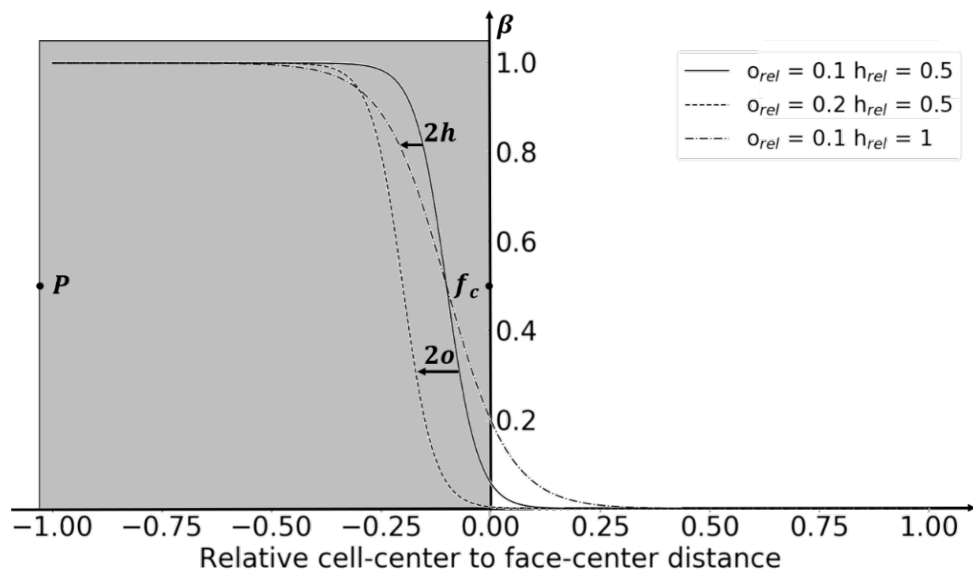


Figure 4.8 – Effect of changing offset and half-width on the blending function curve.

To avoid any spurious positive traction the sigmoid can be truncated, i.e. once the user activates the corresponding option the blending function is forced to be equal to 0 for $g \geq 0$. The main drawback is the discontinuity at the interface which might worsen the convergence of some simulations. This issue might be partially solved with a more significant relaxation of the displacement field or with smaller time-steps if the problem is time-dependent.

4.3.7 Implicit contact for boundaries with different geometry and orientation

All the relations derived in the previous sections assume that the two outward normal vectors \mathbf{n}_{gm} and \mathbf{n}_{gs} lie in the same direction. However, with few simple modifications, the implicit contact methodology can be extended to the more general case of boundaries with different orientation.

First, the common normal vectors \mathbf{n}_{gm}^* and \mathbf{n}_{gs}^* are introduced as²:

$$\mathbf{n}_{gm}^* = \frac{\mathbf{n}_{gm} - \mathbf{n}_{gs}}{|\mathbf{n}_{gm} - \mathbf{n}_{gs}|} = -\mathbf{n}_{gs}^* \quad (79)$$

Then, as done in Sec 4.3.5, the owner face-center is projected across the gap on the neighbor face, only this time the point is projected along the direction determined by \mathbf{n}_{gm}^* (or \mathbf{n}_{gs}^*). The corresponding point is used to calculate the neighbor δ_g as explained in Sec 4.3.4 and as shown in Figure 4.9.

² These vectors coincide with the search direction used by the face area weighting technique to calculate the weighting factors for the AMI mapping.

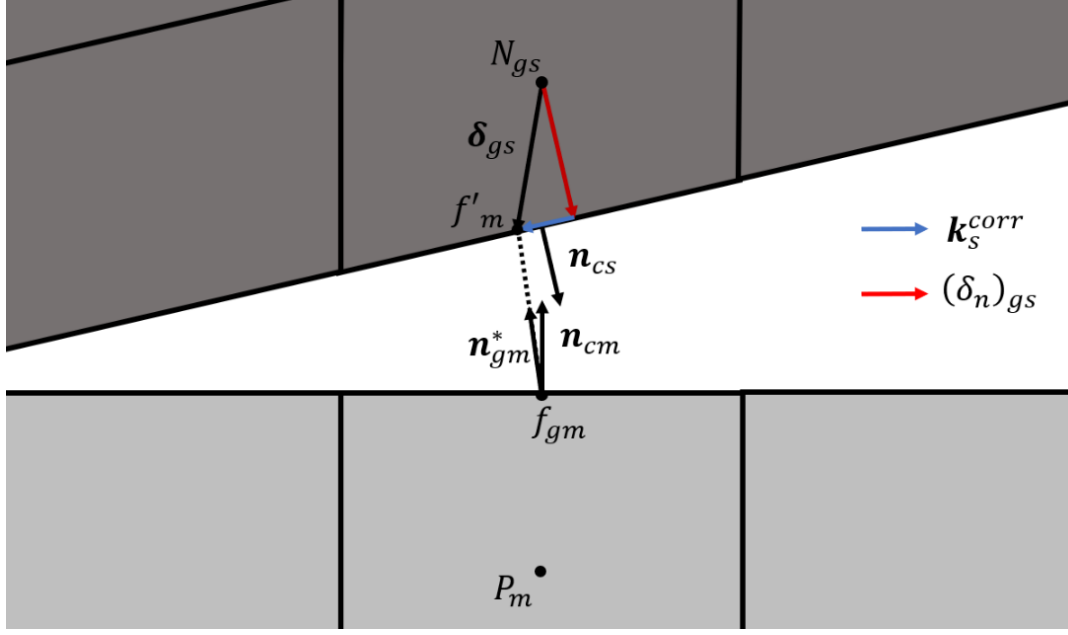


Figure 4.9 – Boundaries with different orientation. The owner face-center (the master face-center in this example) is projected along the common normal \mathbf{n}_{gm}^* .

The final form of the contact traction is obtained following the same derivation presented in the previous sections. First the contact traction is decomposed into a normal component along \mathbf{n}_{gm}^* (or \mathbf{n}_{gs}^*) and tangent component. It follows that the explicit terms in the definition of the traction must be changed into:

$$\begin{aligned} \mathbf{Q}_{nm}^* &= \lambda_{gm} \text{tr}(\nabla_{\mathbf{t}}^* \mathbf{u}_{\mathbf{t}}^*)_{gm} \mathbf{n}_{gm}^* \\ &= (\mathbf{n}_{gm}^* \mathbf{n}_{gm}^*) \cdot (\mathbf{n}_{gm} \cdot \boldsymbol{\sigma}_{gm}) - (2\mu + \lambda)_{gm} \mathbf{n}_{gm}^* \cdot (\nabla \mathbf{u}_n)_{gm} \end{aligned} \quad (80)$$

$$\begin{aligned} \mathbf{Q}_{ns}^* &= \lambda_{gs} \text{tr}(\nabla_{\mathbf{t}}^* \mathbf{u}_{\mathbf{t}}^*)_{gs} \mathbf{n}_{gs}^* \\ &= (\mathbf{n}_{gs}^* \mathbf{n}_{gs}^*) \cdot (\mathbf{n}_{gs} \cdot \boldsymbol{\sigma}_{gs}) - (2\mu + \lambda)_{gs} \mathbf{n}_{gs}^* \cdot (\nabla \mathbf{u}_n)_{gs} \end{aligned} \quad (81)$$

And:

$$\begin{aligned} \mathbf{Q}_{tm}^* &= \mu_{gm} \nabla_{\mathbf{t}}^* \mathbf{u}_{nm}^* \\ &= (\mathbf{I} - \mathbf{n}_{gm}^* \mathbf{n}_{gm}^*) \cdot (\mathbf{n}_{gm} \cdot \boldsymbol{\sigma}_{gm}) - \mu_{gm} \mathbf{n}_{cm}^* \cdot \nabla \mathbf{u}_{tm}^* \end{aligned} \quad (82)$$

$$\begin{aligned}\mathbf{Q}_{ts^*} &= \mu_{gs} \nabla_{t^*} \mathbf{u}_{ns^*} \\ &= (\mathbf{I} - \mathbf{n}_{gs}^* \mathbf{n}_{gs}^*) \cdot (\mathbf{n}_{gs} \cdot \boldsymbol{\sigma}_{gs}) - \mu_{gs} \mathbf{n}_{gs}^* \cdot \nabla \mathbf{u}_{ts^*}\end{aligned}\quad (83)$$

With these simple modifications, the relation for the total contact traction on the master side is finally obtained as:

$$\begin{aligned}\boldsymbol{\tau}_{gm} &= \overbrace{\beta(2\mu + \lambda)_g \frac{(\mathbf{u})_{N_{gs}} - (\mathbf{u})_{P_m}}{\delta_{ms}}}^{\text{implicit}} - \overbrace{\beta(2\mu + \lambda)_g \frac{(\mathbf{u}_{t^*})_{N_{gs}} - (\mathbf{u}_{t^*})_{P_m}}{\delta_{ms}}}^{\text{explicit}} \\ &+ \beta \left[\overbrace{-w_n \mathbf{Q}_{ns^*} + (1 - w_n) \mathbf{Q}_{nm^*} - (2\mu + \lambda)_g \frac{(\mathbf{f}_{n^*})_{gm} - (\mathbf{f}'_{n^*})_{gs}}{\delta_{ms}} + (\boldsymbol{\tau}_{t^*})_{gm}}^{\text{explicit}} \right] \\ &+ \beta \left[\overbrace{(2\mu + \lambda)_g \frac{\mathbf{k}_s^{\text{corr}} \cdot (\nabla \mathbf{u}_{n^*})_{gs} - \mathbf{k}_m^{\text{corr}} \cdot (\nabla \mathbf{u}_{n^*})_{gm}}{\delta_{ms}}}^{\text{explicit}} \right] \\ &+ \overbrace{(1 - \beta)(-p_g \mathbf{n}_{gm})}^{\text{explicit}}\end{aligned}\quad (84)$$

4.4 Conclusions

This chapter has described the efforts carried out to address, within the FV fuel modeling methodology developed in this thesis, the presence of the fuel-to-cladding gap and the combined occurrence of heat transfer and contact.

In OFFBEAT, the fuel rod is modeled as a discontinuous computational domain made of separate fuel and cladding regions. The discretization of the governing equations discussed in Chapter 3 has been extended to take into account the potential presence of CV faces on the gap.

The gap heat transfer has been modeled using the concept of thermal resistances resulting in a multi-dimensional generalization of the thin-gap approximation in line with gap conductance models available in the literature and used in traditional fuel performance codes. Standard OpenFOAM routines based on the use of AMI mapping algorithm have been readapted to allow the use of non-conformal meshes between fuel and cladding.

As the numerical solution to contact problems is challenging, significant efforts have been carried out to develop robust contact methodologies. More precisely, OFFBEAT has been equipped with two contact algorithms. The first one has been derived from the work of Cardiff and is based on the penalty method, also common for FEM codes. The second one is a novel methodology that has been derived in the context of this PhD thesis. Moving from similarities with multi-material bodies, this alternative contact algorithm allows one to discretize the boundary contact stresses (semi-

)implicitly. The methodology has been equipped with non-orthogonal correctors enabling the extension to non-conformal and non-orthogonal meshes, and with a blending function interpolating between fluid gap pressure and contact stresses.

At the moment, the frictional component of the contact force has been considered only for the implicit contact methodology, but the addition of a Coulomb frictional force to the penalty method boundary condition as done in [96] should be straightforward. Further work is needed to include the evolution of the friction between fuel pellets and cladding during irradiation to simulate the potential effect of bonding. This could be modeled, for example, with a time-dependent frictional coefficient that depends on the cladding inner corrosion layer thickness. Naturally, this interesting developments will be possible only once models for cladding oxidations are implemented in OFFBEAT.

The extensive testing, verification, and validation efforts for the gap methodologies are summarized in Chapter 7.

Chapter 5

The multi-dimensional fuel behavior code OFFBEAT³

The present chapter concludes the first portion of this PhD thesis focused on the development of the code OFFBEAT for multi-dimensional fuel performance applications. While the previous two chapters of this thesis presented the FV framework, with the governing equations, the discretization procedure, and the numerical developments for the treatment of the gap, this chapter describes the code's structure and its most relevant features.

The chapter is structured as follows. Section 5.1 briefly discusses the choice of the OpenFOAM library as the core software framework, while Section 5.2 outlines the structure of the code and how the different classes interact within the solution strategy. Then, the sections from 5.3 to 5.9 provide more details about the main classes that compose the code. Finally, Section 5.10 outlines the main opportunity for straightforward multi-physics coupling considered as part of the development of OFFBEAT. The relevant conclusions for this chapter are drawn in Section 5.11.

5.1 Software framework

Although known prominently as a software for state-of-the-art CFD simulations, the OpenFOAM library is first and foremost a C++ toolbox for the solution of PDEs and for the analysis of multi-physics problems, as demonstrated by the wide range of applications from chemistry and naval engineering to fluid structure interaction [97] and the modeling of avalanches [98]. In nuclear reactor analysis OpenFOAM has already been used for neutronics [38], [39], thermal-hydraulics [40], [41] and for the development of the multi-physics reactor simulation platform Gen-Foam [42].

OFFBEAT takes advantage of the extensive list of OpenFOAM features to accelerate the development and simplify its maintenance. The list includes: routines for mesh generation and manipulation, with the additional possibility to readily import geometries and meshes from separate tools such as Salome [99]; professional data processing and visualization with the ParaView open-source software [100]; finite volume discretization routines, with an intuitive formulation based on control volume balances; state of the art linear algebra solvers and massive parallelization.

³ The content presented in this chapter is partially available in [50], [151], [172].

Additionally, the governing equations are discretized on 3-D unstructured meshes with arbitrary geometry; this gives more flexibility compared to most traditional fuel performance codes, which use structured meshes or predefined geometries. 2-D and 1-D geometries can be modeled with the selection of appropriate boundary conditions as discussed already in Section 3.3. In theory, any type of fuel geometry can be reproduced provided that the necessary physical models are implemented (e.g. material transport in metallic fuels), opening OFFBEAT to the possibility of modeling unconventional fuel configurations, such as experimental rods, TRISO or plate-type fuel or new fuel designs.

5.2 Code structure and solution strategy

Observing standard object-oriented programming practices, OFFBEAT encapsulates separate functionalities in independent C++ classes. This modular approach simplifies the maintenance of the code and reduces the time needed for the introduction of new features or updated versions of existing classes.

The main components of OFFBEAT are a thermal and a mechanical sub-solver that calculate, respectively, the temperature distribution and the deformation of the fuel rod. The two sub-solvers discretize the respective governing equations on the same unstructured grid of arbitrary geometry. The computational model typically includes fuel and cladding regions, also referred to as cell-zones, a generic OpenFOAM term referring to groups of cells that do not overlap. In OFFBEAT, cell-zones are used to define separate material regions, e.g. UO_2 fuel and Zircaloy cladding. OFFBEAT can also perform simulations for models consisting only of fuel or cladding, as it could be of interest, for example, for the analysis of ballooning tests [101].

This basic structure is complemented by supplementary classes including:

- A gap/plenum model to track the gap gas pressure and composition.
- Fission gas release models.
- A class dedicated to the isotopic evolution of the oxide fuel and its burnup, and the formation of a radial power profile.
- A class handling the temperature- and burnup-dependent evolution of the material properties.
- A class dedicated to the nuclear specific phenomena affecting the gap size such as relocation or densification.
- A rheology class for the constitutive mechanical behavior of the materials involved in the simulation.

- Heat source and fast flux models, that allow the user to provide a history of spatial-dependent values, for example selecting an axially flat profile, a linear profile, or a different value for each axial section of the rod.

Figure 5.1 summarizes the modular structure of OFFBEAT. The figure shows the main dependencies with arrows as well as the hierarchy of the code, with the classes subdivided in primary solvers, closure models and supplementary models. Also, the most relevant near future developments are highlighted in red. The following sections provide additional details about the main components of the code.

5.2.1 Solution strategy

Like most OpenFOAM solvers, OFFBEAT employs a segregated solution or operator-splitting (and dimensional-splitting) scheme. The main idea behind this approach [87] is to take a complex problem (such as the coupled neutro-thermo-mechanical behavior of a fuel rod) and decompose it in simpler pieces, easier to solve. Thus, in OFFBEAT, each physics and each component are solved separately and sequentially, treating the dependence on other variables with explicit terms. The final solution is made implicit using fixed-point iteration. The segregated method is alternative to the use of a fully-coupled solution scheme, as done in the MOOSE framework [18], on which the INL codes BISON and MARMOT are based. The two approaches, if properly converged, provide the same result, and both have advantages and disadvantages. Mainly, a segregated solver simplifies the construction of the matrix system and is more memory efficient, but it requires more iterations to reach convergence if the various physics are strongly coupled, although each iteration of a segregated solver is generally faster than that of a coupled solver. Efforts are being carried out in other laboratories [84] to introduce in OpenFOAM block-coupled solvers for the solution of the momentum balance equations and in the future they might be used also in OFFBEAT. Alternatively, predictor-corrector algorithms or nonlinear acceleration techniques such as Aitken's delta squared, Wynn's epsilon, minimal polynomial extrapolation, reduced rank extrapolation among others could be introduced in order to accelerate the convergence rate. One should be aware, however, that the largest source of instability on the coupled system of equations and the largest detriment to the performance of the solution scheme is the thermo-mechanical behavior of the gap, which is highly nonlinear, stiff and discontinuous at the point where the gap closes; even the most advanced nonlinear coupled solvers of today are likely to suffer from stability issues.

The segregated solution scheme adopted in OFFBEAT is summarized in Figure 5.2. Three main loops are immediately identified: the time-iteration loop for advancing in time, the outer fixed-point iteration loop for solving the coupled physics and closure models and inner-iteration loops for each primary subsolver. A typical outer-iteration proceeds as follows.

- The volumetric power density is updated according to the spatial and time-dependent model chosen by the user. Usually, this operation is performed only once per time-step.

- The neutronics or radial heat power model calculates the fuel burnup and updates the isotopic composition. If TUBRNP is used, a radial power profile is superimposed to the average burnup of the slice.
- The fission gas release model reads the temperature distribution obtained at the end of the previous iteration, derives the fission rate from the heat source, and calculates the fission gas distribution in the fuel grains and grain boundaries, as well as the fraction of gas released to the rod free volume.
- The gap model updates the gap properties, including the gap free volume, the gas pressure and gas composition.
- The thermo-mechanical properties of fuel and cladding are updated, and the thermal sub-solver obtains the new temperature distribution by solving the heat diffusion equation. These two tasks form the thermal inner-iteration loop.

The mechanical sub-solver obtains the new displacement field by solving the momentum balance equations and updates the strain tensor. Taking into account phenomenological models such as relocation, swelling or densification, and the specific constitutive behavior of each material (e.g. purely elastic, viscoelastic, etc.), the rheology class calculates the elastic component of the strain tensor in each cell-zone and updates the stress tensor through Hooke's law. These tasks form the mechanical inner-iteration loop.

The two inner-iteration loops continue until the **inner-loop convergence criterion** is met, that is until the residuals of the respective main field, either temperature or displacement, fall below a user-defined threshold or the number of inner iterations (index j in the Figure) is above a predefined maximum value. From all the tests performed up to this moment, OFFBEAT shows better convergence properties if the maximum number of inner iterations is set to 1 (i.e. the inner-loop is actually performed only once).

Similarly, once the outer-iteration is completed, the code checks the **outer-loop convergence criterion**, that is whether both the temperature and the displacement residuals are below a user-defined threshold (typically set to $1e-6$) or the number of outer-iterations (index i in the Figure) has reached a pre-defined maximum value (typically set to 1000). If the convergence criterion is passed, then the code moves the next time step.

The solution of the differential equations is performed with standard linear solvers available in OpenFOAM, which are selectable by the user at runtime. Mostly used for OFFBEAT are the Generalised Geometric-Algebraic Multi-Grid solver, or GAMG, and the Preconditioned (Bi-)Conjugate Gradient solver, or PCG/PBiCG, with diagonal incomplete Cholesky preconditioning. The total simulation time is split into time step of fixed or varying size and a first-order implicit Euler scheme is used for time integration.

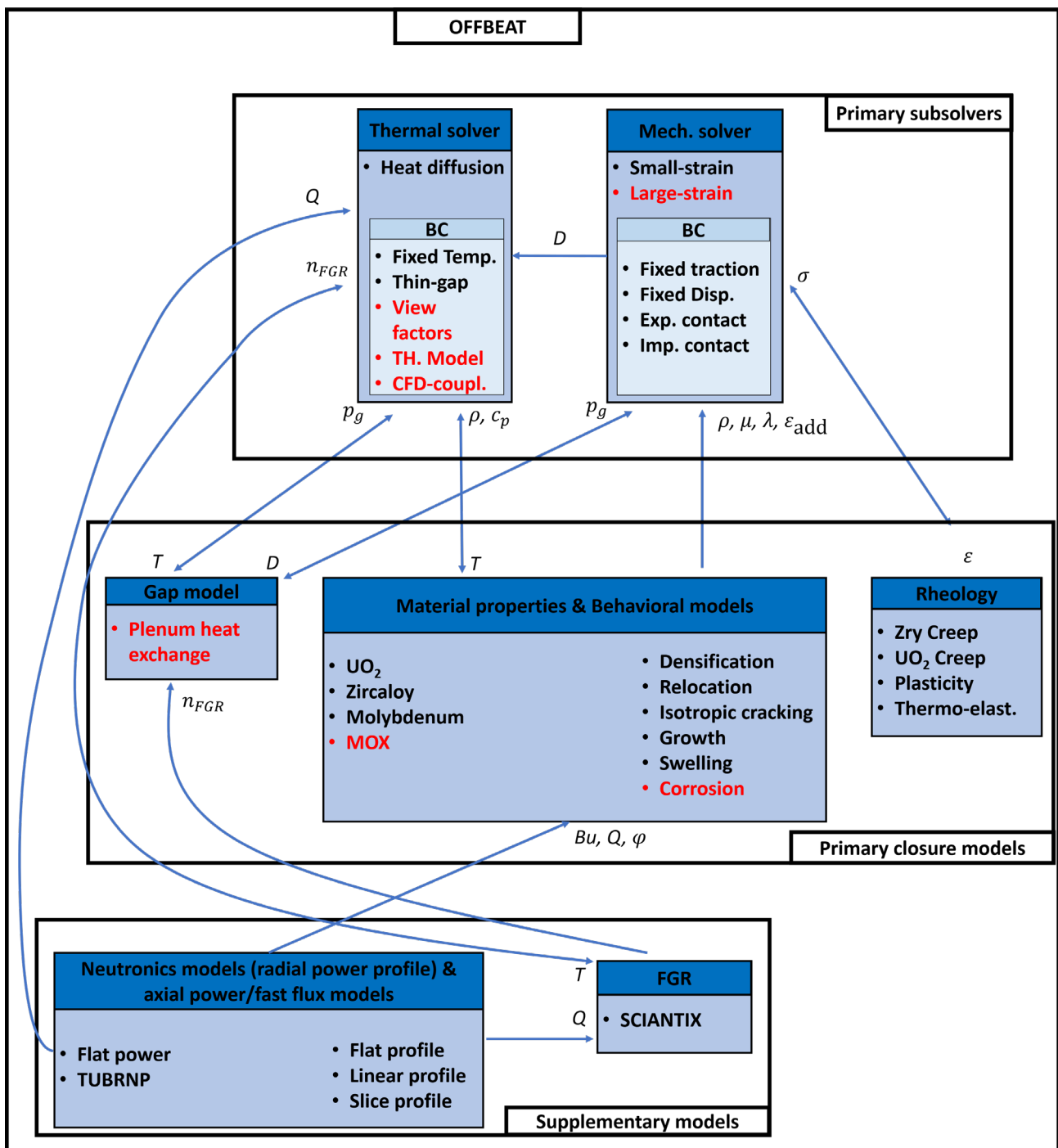


Figure 5.1 – Simplified class structure of OFFBEAT. The main dependencies are shown with arrows.

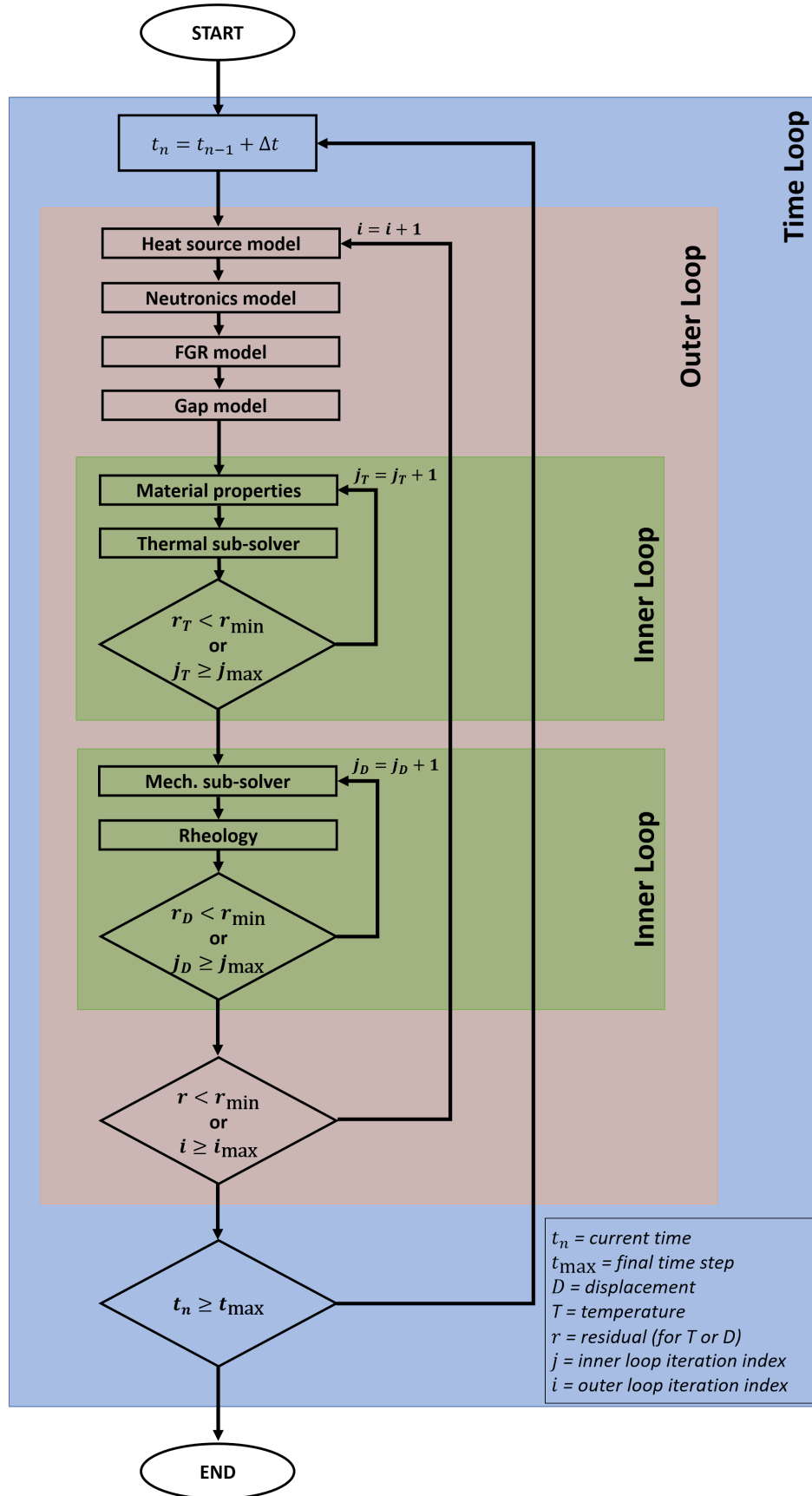


Figure 5.2 – Segregated solution scheme adopted for OFFBEAT.

5.2.2 Relaxation factors

Two under-relaxation strategies in OpenFOAM can be used to stabilize the solution for strongly coupled and non-linear problems. The first strategy, also called *explicit relaxation* [102], consists in under-relaxing a field. For a generic field φ (for example the contact pressure, the gap conductance, the temperature or the displacement), the value at the current iteration i is obtained by blending a fraction of the field φ_i^* deriving from the latest solution of the system matrix with the field φ_{i-1} obtained at the end of the previous iteration:

$$\varphi_i = \alpha \varphi_i^* + (1 - \alpha) \varphi_{i-1} \quad (85)$$

where α is the relaxation factor. Typical values of the relaxation factor are comprised between 0.8 and 0.999, although lower values might be used. For example, a very low relaxation factor for the contact pressure when using the penalty method boundary condition allows one to use substantially higher penalty factor, even equal or larger than 1. Indeed, the low penalty factor helps to stabilize the solution, in particular because of its smoothing effects on the removal of contact stresses for those boundary faces that are leaving the interpenetration zone.

It must be kept in mind, however, that the lower the relaxation factor, the longer it will take for the linear solver to reach the converged final solution and it might be even necessary to increase the number of maximum outer iteration to be sure that the convergence criterion does not stop the time step loop too early, when the residuals are not small enough.

The second relaxation strategy, also called *implicit relaxation* [102], consists in relaxing the system of equations before it is solved by the linear solvers. This more complex strategy aims at renormalizing the diagonal coefficient and the source vector to make the system more diagonally dominant, without modifying the equations mathematically. It is therefore used for the displacement field for cases with large explicit contributions, such as simulations involving bodies that are not fixed to the ground. The value of the relaxation factor is usually between 0.9 and 0.999, but even the smallest deviation from 1 has a significant impact on the performance of the simulation, making it significantly slower.

An additional technique that is often useful to stabilize the solution is the use of the adaptive time-stepping routines that have been implemented in OFFBEAT. The next time step size can be chosen in order to satisfy a series of different criteria such as maximum allowed power variation, maximum creep increment, maximum burnup increment etc. The parameters for the adaptive time-stepping can be selected by the user.

5.3 Thermal sub-solver

The thermal sub-solver obtains the temperature field T from the solution of the heat diffusion equation, already showed in Eq. (1) from Chapter 3. The rate of change of thermal energy, that is the term:

$$\overbrace{\int_V \frac{\partial \rho c_p T}{\partial t} dV}^{\text{Rate of change}} \quad (86)$$

can be explicitly omitted by the user in case of steady-state calculations, although its contribution for large time steps is automatically small.

The thermal sub-solver directly interacts with two separate classes. The first one is a dedicated model handling the heat source density q''' . This can be defined as a function of space and time, can be mapped from a previous calculation or it can be imported from a separate code (from neutronics calculations for example). A few preset axial profiles are available, and others can be developed in the future, to simplify the modeling of the rod history for base irradiation simulations where often the heat source is provided in the form of a time-dependent histogram, and the axial power profile is approximated with a few long axial sections. The second class interacting with the thermal sub-solver models the evolution of the temperature and burnup-dependent material properties and provides the updated value of density, heat capacity and conductivity.

The standard boundary conditions available in OpenFOAM can be used to fix the temperature field or its gradient, but additional ones have been developed for specific to fuel performance applications. The main possible choices are discussed below.

Fixed-temperature: This boundary conditions imposes a constant or time-varying temperature on one of the outer surfaces.

Zero-gradient: This boundary conditions imposes a zero-gradient or zero-heat-flux constraint, and it is typically used for the central hole walls.

Gap heat transfer model: Derived from the previous boundary condition, this model adds a time-varying gap conductance that depends on temperature, gap size, contact stresses and other parameters. The specific model implemented in OFFBEAT is derived from the coding of FRAPCON 4.0 and the traditional assumption of a thin gap relatively to the surrounding surfaces. The local gap conductance h_{gap} is calculated as the superposition of three components, each modeling a different physical mean of heat transfer:

$$h_{\text{gap}} = h_{\text{gas}} + h_{\text{rad}} + h_c \quad (87)$$

where h_{gas} is the term dedicated to the conduction through the gas, h_{rad} to the radiative heat exchange and h_c to the additional solid-to-solid conduction at the points of contact between pellet and cladding. The conduction through the gap gas is the principal mean of heat transfer in open gap conditions.

The value of h_{gas} is strongly dependent on the gap width and the gap gas temperature, and it is given by:

$$h_{\text{gas}} = \frac{\kappa_{\text{gas}}}{g + \exp(-A_1 p_i) (R_f + R_c) + A_2 (j_f + j_c) - A_3} \quad (88)$$

where g is the local gap size, κ_{gas} is the temperature dependent conductivity of the filling gas, R is the surface roughness, j is the temperature jumping distance and p_i is the interface contact pressure. The constant A_1 - A_3 are model parameters and the subscripts f and c refer to fuel and cladding, respectively. Because the two facing boundaries, also called master and slave, can have different size and total number of faces, in general the face centers do not lie in front of each other. As discussed in the previous chapter, OFFBEAT employs the AMI mapping algorithm to reconstruct, for each face center \mathbf{f}_{gm} on the master side of the gap, the neighbor face center \mathbf{f}_{gs} on the slave side (and vice versa) with all its related vectorial or scalar quantities. The local gap width is then calculated with Eq. (50).

The radiative heat conductance takes the form:

$$h_{\text{rad}} = \sigma \frac{(T_f^2 + T_c^2)(T_f - T_c)}{\frac{1}{\epsilon_f} + \frac{1}{\epsilon_c} - 1} \quad (89)$$

where σ is the Boltzman constant and ϵ is the surface emissivity. The radiative heat transfer, proportional to the fourth power of the temperature, becomes predominant only at high temperatures in conditions typical of accident scenarios.

The third and final term, that is the contact conductance, is strongly dependent on the contact pressure and takes the general form:

$$h_c = A_1 \frac{K_c p_i^{A_2}}{R_c} \quad (90)$$

where A_1 is a fitting parameter, K_c is the geometric mean conductivity of the two materials in contact, R_c is related to the roughness of the two surfaces, and the exponent A_2 is another fitting parameter that depends on the value of p_i . As the interface pressure increases, the solid conduct-

ance increases significantly prevailing over the other two components. The feedback on the temperature field is negative: with a higher conductance the fuel pellets tend to cool down and contract, alleviating the mechanical interaction between fuel and cladding. Although the FRAPCON contact conductance model was developed to stabilize the transition between open and closed-gap [103], convergence issues might still appear for scenarios involving high linear heat rating, fast power ramps and significant fractions of fission gas release. The use of relaxation factors generally helps to eliminate the oscillating behavior at the expense of the performance of the simulations.

Heat exchange with the coolant OFFBEAT includes a dedicated boundary condition for determining the outer cladding temperature (in case this is not provided with the experimental data) from the convective heat exchange with the coolant. The selection of the heat exchange is not automated yet and its value must be provided by the user together with the time-dependent coolant temperature. As a future perspective, improved boundary conditions on the outer surface of the rod could be obtained either by developing a simplified thermohydraulic model based on the energy balance within the coolant or by coupling OFFBEAT with GeN-Foam or one of the standard OpenFOAM CFD solvers. Whatever route is chosen, the ability to capture both pre- and post-critical heat flux (CHF) regimes will be necessary.

5.4 Mechanical sub-solver

The mechanical sub-solver obtains the displacement vector field \mathbf{u} from the solution of the 3 coupled momentum balance equations, already showed in Eq. (3) from Chapter 3. The inertia forces, that is the term:

$$\overbrace{\int_V \frac{\partial^2 \rho \mathbf{u}}{\partial t^2} dV}^{\text{Rate of change or Inertia}} \quad (91)$$

are usually neglected as they become relevant only for very rapid transient simulations, mostly outside the realm of interest of fuel performance modeling (even for accident conditions). Also, OFFBEAT does not consider body forces such as those due to gravity but their implementation would be straightforward.

From the displacement field, the mechanical sub-solver updates the total strain tensor $\boldsymbol{\varepsilon}$ following the definitions given in Eq. (4). OFFBEAT currently operates in a small-strain framework which is sufficiently accurate for most irradiation conditions, even for many transient scenarios. The introduction of an alternative finite strain mechanical sub-solver (in the form of a sister class) is planned for the near future and will be important to investigate scenarios where the rod undergoes considerable deformation, such as during ballooning.

The mechanical sub-solver provides the total strain tensor to a dedicated class handling the constitutive behavior of fuel and cladding. Once all the remaining components of the strain have been

updated (including the contributions from thermal expansion, relocation, densification, swelling and growth), the elastic component ϵ_{el} can be extracted and the stress tensor σ is calculated through Hooke's law.

The standard boundary conditions available in OpenFOAM can be used to fix the displacement field or its gradient, but additional ones have been developed specific to fuel performance applications. The main possible choices are discussed below.

Fixed-displacement: This boundary conditions imposes a constant or time-varying displacement on one of the outer surfaces. If the fixed value is set to 0 for all the three Cartesian directions, the boundary's movement is blocked in all degree of freedoms. This is often done for the bottom fuel or cladding surfaces. Although such a constraint is not realistic and might produce high unphysical stresses, these are relegated to a small region in proximity of the fixed boundary.

Fixed-traction: This boundary condition imposes a constant or time-varying traction, that is the force acting on the boundary. As explained in Chapter 3, the boundary value of the displacement field is obtained by iteratively correcting the normal gradient using the definition of the boundary traction.

Spring-traction: Derived from the fixed-traction type, this boundary condition reproduces the effect of the plenum spring on the fuel column. The traction acting at the top of the fuel stack is calculated as:

$$\tau_b = -K_s \frac{\mathbf{n}_b \cdot \mathbf{u}_b}{L_s} \mathbf{n}_b \quad (92)$$

where K_s and L_s are user-defined spring modulus and length, while \mathbf{u}_b is the area-weighted average displacement at the top of the fuel stack.

Symmetry plane: This boundary condition corresponds to the presence of a plane of symmetry in the body. Thus, the normal component of the displacement on this plane is fixed (the body cannot move away from the plane) while the other two components have a zero-gradient constraint. It can be used to reduce the size of the computational mesh allowing to model, for example, only half or a quarter of the entire geometry.

Fixed displacement – zero shear: This boundary is similar to the symmetry plane type. However, while the normal displacement is fixed as for the symmetry plane, the zero-gradient constraint is imposed to shear stresses (zero shear), that is to the tangential components of the stress field.

Contact: Two contact boundary conditions are included in OFFBEAT. The first one is explicit and is based on the penalty method approach, while the second one follows the implicit discretization scheme developed in Chapter 4.

5.5 Gap model

The evolution of the filling gas pressure, volume, temperature, and composition is tracked with a dedicated gap model.

At the start of the simulation, the composition of the gap gas is read from the input data while the number of moles is calculated from the gap initial conditions in terms of volume, temperature, and pressure. The first two variables are deduced from the model dimensions and boundary conditions, while the latter must be provided as input. During the simulation, the number of moles and the gap gas composition are updated according to the output of the fission gas release model.

The total free volume, that is the region of space delimited by the fuel outer surface and the cladding inner surface, is calculated by summing the inner products between the updated face center vectors $\mathbf{f}_g + \mathbf{u}_g$ (see Chapter 3 and Chapter 4 for their definition) and the outward normal \mathbf{n}_{gi} :

$$V_{\text{free}} = -\frac{1}{3} \left[\gamma_g \sum_i S_{gi} (\mathbf{f}_{gi} + \mathbf{u}_{gi}) \cdot \mathbf{n}_{gi} \right] \quad (93)$$

where the factor $1/3$ derives from the application of the Green-Gauss theorem to the calculation of the volume of an arbitrary polyhedral [104] and the index i runs over the faces on both sides of the gap. The correction factor γ_g has been introduced for cases where the surfaces bounding the gap do not form a complete enclosure. It equals 1.5 when the top and bottom bounding surfaces are not included in the model, as it is often done for axisymmetric simulations, otherwise it can be changed to 1. In most simulations, the volume V_{free} also includes the plenum volume V_{plenum} , as shown in Figure 5.3. This volume can be calculated using the same formula in Eq. (93) applied solely to the plenum section of the inner cladding surface.

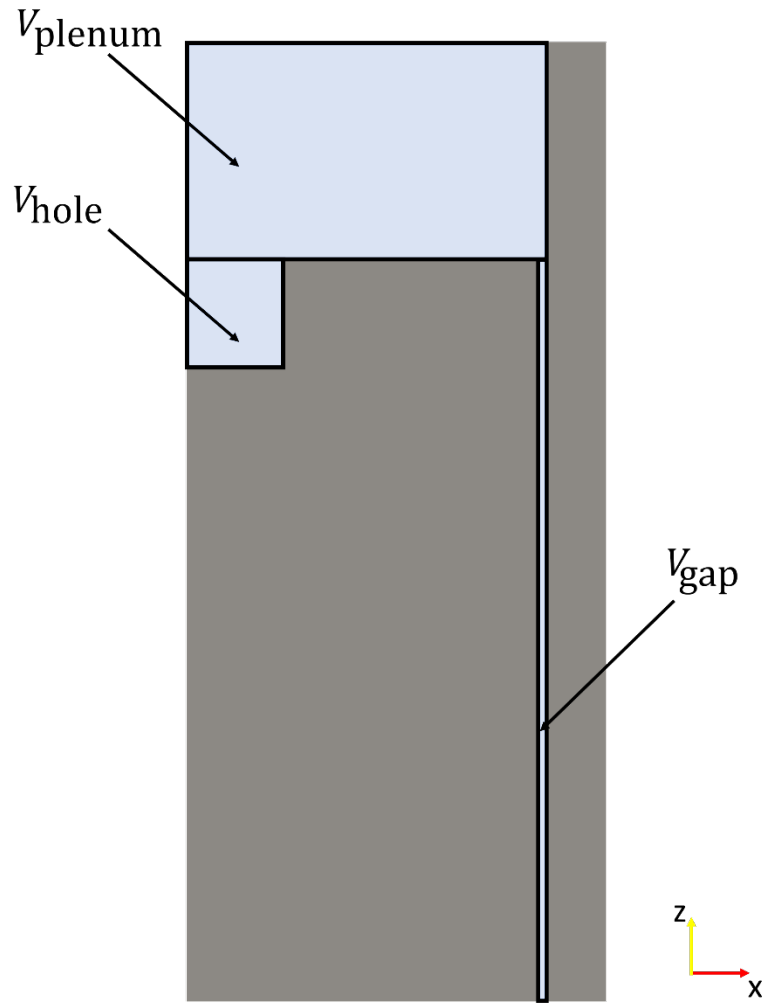


Figure 5.3 – Decomposition of the free volume into V_{gap} and V_{plenum} . The central hole volume V_{hole} present in some fuel designs is also included in the Figure.

Then, the fuel-to-cladding gap volume V_{gap} is simply given by:

$$V_{\text{gap}} = V_{\text{free}} - V_{\text{plenum}} \quad (94)$$

The gap gas pressure is assumed to be instantly equalized in the entire rod free volume, while the temperature can vary depending on the gas location (central hole, plenum, gap or cracks). Following an ideal gas law, the gas pressure is updated with:

$$p = \frac{nR}{\left[\frac{V}{T}\right]_{\text{gap}} + \left[\frac{V}{T}\right]_{\text{hole}} + \frac{V_{\text{plenum}}}{T_{\text{plenum}}} + \left[\frac{V}{T}\right]_{\text{cracks}}} \quad (95)$$

where R is the universal gas constant and n is the number of moles. More precisely:

- The term relative to the fuel-to-cladding gap is calculated as follows:

$$\left[\frac{V}{T}\right]_{\text{gap}} = 0.5 \sum_i \frac{S_{g_i} \cdot \max(g_i, 0)}{T_{g_i}} \quad (96)$$

where the index g runs over the cell faces on both sides of the fuel-to-cladding gap, g is the local gap width and the 0.5 factor avoids accounting the same local volume twice in the summation.

- The term relative to the central hole is approximated as:

$$\left[\frac{V}{T}\right]_{\text{hole}} \approx \frac{V_{\text{hole}}}{T_{\text{hole}}} \quad (97)$$

where V_{hole} is the hole volume and T_{hole} is the surface area weighted average temperature of the hole walls.

- The term relative to the gas in the fuel cracks is calculated as follows:

$$\left[\frac{V}{T}\right]_{\text{cracks}} = \sum_i \frac{2\varepsilon_{\text{rel}}V_i}{T_i} \quad (98)$$

where $2\varepsilon_{\text{rel}}V_i$ is assumed as the volume occupied by a crack in the i -th fuel cell (the factor 2 accounts for the 2D nature of the relocation strain).

- In the absence of a dedicated model for the complex heat exchange in the rod plenum, the average temperature of the plenum gas T_{plenum} is calculated simply as the surface-weighted average between the temperature on the plenum section of the inner cladding surface and the temperature at the top of the fuel stack.

5.6 Neutronics and burnup model

OFFBEAT is equipped with a simplified neutronics model to track the concentration of few selected isotopes relevant for the power generation in the fuel, including U^{235} , U^{238} , Np^{237} , Pu^{238} , Pu^{239} , Pu^{240} , Pu^{241} , Pu^{242} , Am^{241} , Am^{243} , Cm^{242} , Cm^{243} and Cm^{244} . The implementation is derived from the TUBRNP module of TRANSURANUS and a complete description of the original algorithm can be found in the seminal publication from Lassman [17].

TUBRNP was developed for a 1.5-D code, where the fuel column is modeled as a series of 1-D slices. In OFFBEAT, the original model is extended to a multi-dimensional, unstructured framework thanks to the use of a mapper class. The mapper creates ordered virtual slices that are superim-

posed to the 1-D, 2-D, or 3-D rod geometry. The addressing, i.e. the list of cells corresponding to each virtual slice, is calculated and stored at the start of the simulation, and can be readily accessed at any time to perform slice-based and slice-average operations.

For each fuel cell, the neutronics model solves a system of balance equations limited to the few isotopes listed above, and taking into account consumption by absorption or decay, and production due to capture or decay processes. The system of equations is made of simplified versions of the standard form of the Bateman equations:

$$\begin{aligned} \frac{dN_i(r, t)}{dt} = & -\sigma_{a,i}N_i(r, t)\Phi(r, t) - \lambda_iN_i(r, t) + \sum_j \left(\sigma_{c,ji}N_j(r, t)\Phi(r, t) \right) \\ & + \sum_k \left(\lambda_{ki}N_k(r, t) \right) \end{aligned} \quad (99)$$

where t is the time, r is the cell radius, N_i is the atomic density of the i -th isotope, $\sigma_{f,i}$ and $\sigma_{a,i}$ are the one-group averaged fission and absorption cross sections, $\sigma_{c,ji}$ is the capture cross section of the j -th isotope for the production of the i -th isotope, Φ is the one-group flux and λ_{ki} is the decay constant of the k -th isotope yielding the isotope i . Empirical factors are introduced in Eq. (99) for the resonance absorptions of U^{238} and Pu^{240} .

The power and time increment are known as part of the data set, thus the product $\Phi(r, t)dt$ is transformed into a local burnup increment with an appropriate conversion factor. Once the fissile isotope concentrations are updated, the normalized local power density or form factor $f(r)$ is calculated as:

$$f(r) = \frac{\sum_k \sigma_{f,k}N_{f,k}(r) \cdot \Phi(r)}{\bar{q}} \quad (100)$$

where the summation index k runs over the fissile isotopes, the flux $\Phi(r)$ is derived from one-group diffusion theory, and \bar{q} is the slice volume-weighted average power density, obtained thanks to the mapper addressing. The radial power profile is superimposed to the average volumetric power density provided as input and the local burnup is then calculated by simply integrating the power in time. As the nuclide concentration at the end of the time step depends on the local burnup, the steps just described are iterated until convergence. Nevertheless, the neutronics model is typically called only once at the beginning of the time step, given that the average heat source is fixed and the temperature feedback on the cross section is neglected.

The inclusion of TURBNP in OFFBEAT provides a reliable, validated method to calculate the isotopic distribution in the fuel and the radial power profile. However, its results are valid only for standard LWR fuel in axisymmetric conditions. In absence of a better option, the simplified neutronics

module might still be used in 3-D simulations with asymmetric conditions (e.g. for an asymmetric heat exchange or in presence of an MPS) or for less standard fuel configurations, but its accuracy must be carefully considered.

A higher-fidelity coupling strategy between the Monte Carlo code Serpent and OFFBEAT has been developed as discussed in Chapter 8. The coupling represents an interesting option to increase the accuracy of the calculations that lie outside the range of applicability of TURBNP, such as those that include new fuel types, strong absorbers, or asymmetries.

5.7 Fission gas release model

The fission gas behavior is considered in OFFBEAT either with a simplified model derived from the modified Forsberg-Massih model described in the FRAPCON 4.0 manual or with SCIANTIX [105], a 0-D open-source code developed at the Politecnico di Milano. The models implemented in SCIANTIX cover both the intra-granular and inter-granular inert gas behavior. The diffusion of the gas atoms in the fuel grain is solved either with the classic FORMAS algorithm [106] or with a novel algorithm developed by Pizzocri [107], informed by meso-scale simulations. The evolution of the inter-granular bubbles is modeled following the mechanistic approach of Pastore, with the bubbles growing and coalescing. Once the surface concentration is above a saturation value (by default equal to 0.5), part of the gas at the boundary is released to the rod free volume. SCIANTIX also includes models for grain growth and for grain boundary micro-cracking with consequent burst release during rapid transients. Additionally, a model has been added for boundary sweeping, so that grain growth results in an additional source of gas atoms arriving at the grain boundaries from the grain volume.

SCIANTIX has been wrapped in a C++ class within OFFBEAT that moves data between the local scope of SCIANTIX (0-D) and the larger scope of the OFFBEAT fields. At each iteration and for each fuel cell, OFFBEAT feeds SCIANTIX with the local values of temperature, fission rate and hydrostatic stress. In return, SCIANTIX calculates the number density (atoms/m³) of helium, xenon and krypton atoms. The difference between the fission gas produced and the sum of fission gases in the grain and at the grain boundary is equivalent to the amount of fission gases that has been released. This quantity is summed over the whole mesh, then converted into moles and transferred to the gap gas model. The integral FGR (in %) for each time step of OFFBEAT is calculated as follows:

$$\text{FGR}(\%) = 100 \frac{\sum_i V_i n_{\text{released}}}{V_i n_{\text{produced}}} \quad (101)$$

where V_i is the volume of the cell (m³) and n indicates the gas atom density. The concentration and the size of the gas bubbles is used to calculate the intra-granular and inter-granular fission gas swelling.

The implementation of SCIANTIX in OFFBEAT was verified by ensuring that identical results are obtained when using SCIANTIX as a stand-alone code and as a fission gas release model in OFFBEAT.

5.8 Material and behavioral models

Two dedicated classes are designed to handle, respectively, the evolution of the thermomechanical properties during irradiation and the occurrence of nuclear specific phenomena such as swelling or relocation.

Currently in OFFBEAT, material properties correlations and behavioral models are available only for UO_2 , Zircaloy, molybdenum and Inconel-600, but the addition of new material classes and fuel types (MOX in particular) is planned for the near future. The following subsections give brief descriptions of the main models used in OFFBEAT for the UO_2 fuel and for the cladding.

5.8.1 UO_2

The **specific heat capacity** of solid UO_2 is modeled as a function of the temperature and of the oxygen to metal ratio O/M. The correlation used in OFFBEAT derives from MATPRO v11 [46] and is given by:

$$c_p = \frac{K_1 \theta^2 \exp\left(\frac{\theta}{T}\right)}{T^2 \left[\exp\left(\frac{\theta}{T}\right) - 1\right]^2} + K_2 T + \left(\frac{O/M}{2}\right) \frac{K_3 E_D}{RT^2} \exp\left(-\frac{E_D}{RT}\right) \quad (102)$$

where K_1 , K_2 , K_3 , E_D and θ are model parameters. MATPRO indicates a standard error of ~ 3 J/kg·K which doubles in the case of non-stoichiometric fuels. The same correlation, with different values for the constant parameters, could be used also for PuO_2 . The total heat capacity of a MOX could be obtained weighting the contribution of the two oxides according to their weight fraction.

The **thermal expansion** of solid UO_2 is modeled only as a function of the temperature. The correlation used in OFFBEAT is a third-degree polynomial deriving from MATPRO v11 and is given by:

$$\varepsilon_{th} = -K_0 + K_1 T + K_2 T^2 + K_3 T^3 \quad (103)$$

where K_0 , K_1 , K_2 , K_3 are model parameters. This correlation is valid up until the melting point, at the moment approximated in OFFBEAT as a constant value. The melting point is actually a function of the fuel speciation, plutonia content and burnup, and could be obtained with the future implementation of a dedicated chemistry module.

The **surface emissivity** of solid UO_2 is modeled as a function of the temperature between 1000 and 2050 K. The correlation used in OFFBEAT deriving from MATPRO v11 is given by:

$$\epsilon = K_0 - K_1 T \quad (104)$$

where K_0 and K_1 are model parameters and the reported uncertainty is $\sim 10\%$. Below and above the temperature application range 1000-2050 K, the emissivity is modeled as constant.

The **Young's modulus** of UO_2 is modeled as a function of the temperature and fuel density D expressed as a fraction of theoretical density. The correlation used in OFFBEAT derives from MATPRO v11 and is given by:

$$E = K_1 [1 - K_2 T] [1 - K_3 (1 - D)] \quad (105)$$

where K_1 , K_2 and K_3 are model parameters. This correlation is valid for stoichiometric fuel for which the standard error S_E can be estimated as:

$$S_E = 0.06 \cdot 10^{11} + E \frac{T - 1600}{6052.6} \quad (106)$$

The same correlation in Eq. (105) multiplied by a correction factor could be used also for PuO_2 or non-stoichiometric fuels. The fuel **Poisson's ratio** is assumed to be constant and it is equal:

$$\nu = 0.316 \quad (107)$$

The UO_2 **thermal conductivity** can be calculated with the MATPRO routine FTHCON which is based on an equation proposed by Ohira and Itagakia [108] or with the NFIR model [109]. The implementation in OFFBEAT is derived from the BISON code and in both cases the correlation provides the conductivity of 95% dense fuel as the sum of a phonon and an electron component. The latter is an exponential of the inverse temperature multiplied by a certain function of the temperature; the former is the inverse of the sum of several functions of temperature, local burnup Bu (accounting for accumulation of lattice defects and fission products) and gadolinia content Gd . As an example, the MATPRO correlation for the 95% dense fuel takes the form:

$$\begin{aligned} & K_{95} \\ &= \overbrace{\frac{1}{K_0 + K_1 T + K_2 Bu + K_3 Gd + [(K_4 \exp(K_5 Bu)) K_6 Bu^{0.28}]}}^{\text{phonon}} + \frac{1}{(1 + K_7 \exp(-K_8/T))} \\ &+ \overbrace{\frac{K_9}{T^2} \exp\left(-\frac{K_{10}}{T}\right)}^{\text{electron}} \end{aligned} \quad (108)$$

where K_0 - K_{10} are model parameters. The conductivity must be corrected for the actual porosity of the fuel. Always taking the MATPRO model as an example, the κ_{95} is first multiplied by the factor 1.0789 to obtain the value for the 100% dense fuel, and then it is multiplied by a correction factor, function of the density fraction D :

$$\kappa = \kappa_{95} \left[1.0789 \frac{D}{1 + 0.5(1 - D)} \right] \quad (109)$$

The standard relative error for the conductivity correlations is often assumed to be on the order of 5 to 10%.

The fuel **densification** is calculated following the FUDENS routine from MATPRO. The change in fuel density follows an exponential curve function of the burnup, which reaches saturation around 3-5 MWd/kg. The maximum in-pile density change ΔD is provided in the input data as a percent of the theoretical density and is derived from out-of-pile resintering tests. The maximum densification strain is obtained as:

$$\varepsilon_{\text{den}}^{\text{max}} = -3 \frac{\Delta D}{D * 100 + \Delta D} \quad (110)$$

where D is the fuel density as a fraction of the theoretical density. The in-pile densification is given by the following correlation where Bu is the local burnup and B is a fitting parameter determined so that $\varepsilon_{\text{den}} = 0$ at the start of irradiation:

$$\varepsilon_{\text{den}} = \varepsilon_{\text{den}}^{\text{max}} + \exp[-3(Bu + B)] + 2\exp[-35(Bu + B)] \quad (111)$$

The **solid fission products swelling** model used in OFFBEAT is based on the coding of FRAPCON 3.4, in turn derived from the FSWELL routine of MATPRO. The swelling strain is calculated as a function of burnup:

$$\varepsilon_{\text{swel}} = \frac{\rho}{3} K_1 (Bu - Bu_0) \quad (112)$$

where ρ is the density, K_1 is a model parameter and Bu_0 is the lower burnup threshold equal to 6 MWd/kgU. The correlation is slightly modified for burnup values above 80 MWd/kg. The FRAPCON manual reports a standard relative uncertainty of 0.08% on the volumetric strain per 10

MWd/kgU. The gaseous fission products swelling is calculated by the fission gas release model SCIANTIX.

The effect of cracking in the fuel pellets is considered in two ways. The complex and random outward movement of the pellet fragments can be treated with a simple **relocation** model derived from FRAPCON 4.0. This model consists of an empirical correlation that assigns a radial displacement to the fuel pellet based on burnup, power, and cold gap dimension. The aim is to represent the average behavior of the fuel rod; indeed, the correlation is deduced from integral fuel center-line temperature measurements and is valid only for axisymmetric simulations. In detailed 3-D asymmetric cases an alternative method would be to explicitly model a pre-defined crack pattern, introduced since the beginning of the simulation. The relocation displacement is not allowed to immediately cause stress on the cladding. This corresponds to the so-called soft contact condition. Only when a certain amount of relocation is recovered (e.g. 50% by default) by additional swelling or thermal expansion, the relocation strain is considered to be permanent and the so-called hard contact between the two surfaces occurs.

The formation of cracks in the fuel changes its mechanical properties and stress distribution, as the cracked surface cannot sustain tensile stresses. This phenomenon is treated with the **isotropic cracking** model derived from the work of Barani et al. [58]. The model aims to represent the anisotropic behavior of the cracked pellet within an isotropic framework. The Young's modulus E_{iso} and Poisson's ratio ν_{iso} of the isotropic cracked pellet are calculated as a function of the number of cracks n :

$$E_{iso}(n) = \left[\frac{2}{3} \left(\frac{2 - \nu}{2 + \nu} \right) \left(\frac{1}{1 - \nu} \right) \right]^n E \quad (113)$$

$$\nu_{iso}(n) = \frac{\nu}{2^n + (2^n - 1)\nu}$$

In turn, the number of cracks is obtained from fitting experimental data as a function of the linear heat rate:

$$n = 1 + (n_{\infty} - 1) \left[1 - \exp \left(- \frac{LHR - LHR_0}{\tau} \right) \right] \quad (114)$$

where LHR is the linear heat rate, LHR_0 is the linear heat rate at which the first crack appears while $n_{\infty} = 12$ and $\tau = 21$ kW/m are fitting parameters.

5.8.2 Zircaloy

The **thermal conductivity** of Zircaloy is calculated with the MATPRO routine CTHCON. The correlation is a third-degree temperature dependent polynomial:

$$\kappa = K_0 + K_1 T - K_2 T^2 + K_3 T^3 \quad (115)$$

where K_0 - K_3 are model parameters and the reported standard deviation is of ~ 1 W/m·K.

The **surface emissivity** of Zircaloy is given by the first-degree polynomial derived from the FEMISS routine of RELAP5:

$$\epsilon = K_0 + K_1 T \quad (116)$$

where K_0 and K_1 are model parameters and the reported relative standard deviation is of $\sim 6.8\%$.

The **density** of Zircaloy is calculated following the approach described in the IAEA-TECDOC-1496. The density of the α -phase below 1083 K and that of the β -phase above 1144 K are calculated with temperature dependent first-degree polynomial, $\rho_\alpha(T)$ and $\rho_\beta(T)$. For intermediate temperature value, the density is interpolated as:

$$\rho = \rho_\alpha + (\rho_\beta - \rho_\alpha) \frac{T - 1083}{1144 - 1083} \quad (117)$$

A similar approach is followed for the **specific heat capacity** of Zircaloy. The IAEA-TECDOC-1496 provides a first-degree temperature dependent polynomial $c_{p,\alpha}(T)$ for the α -phase below 1100K, and a second-degree polynomial $c_{p,\beta}(T)$ for the β -phase above 1320 K. The data for the $\alpha + \beta$ transition phase have been fitted with a Gaussian function f given as:

$$f(T) = K_1 \exp \left[\frac{(T - K_2)^2}{K_3} \right] \quad (118)$$

where K_1 - K_3 are model parameters. For temperatures in the range $1100 \text{ K} < T < 1214 \text{ K}$, the heat capacity is given by $c_{p,\alpha} + f(T)$, while for temperatures between $1214 \text{ K} < T < 1320 \text{ K}$ the heat capacity is given by $c_{p,\beta} + f(T)$.

The **thermal expansion** of Zircaloy is calculated with the MATPRO CTHEXP routine that provides first-degree a temperature dependent polynomial for the α -phase $\epsilon_\alpha(T)$ below 1073 K and one for the β -phase $\epsilon_\beta(T)$ above 1273 K. Additionally, MATPRO differentiates between the radial and azi-

muthal strain on the one hand, and the axial strain on the other. For intermediate temperature values, the thermal expansion is interpolated as:

$$\varepsilon_{\alpha}(T) = \varepsilon_{\alpha}(1073) + [\varepsilon_{\beta}(1273) - \varepsilon_{\alpha}(1073)] \left(\frac{T - 1073}{1273 - 1073} \right) \quad (119)$$

Unlike the previous material properties, the **Young's modulus** of Zircaloy does not dependent only on the temperature field. The MATPRO CELMOD routine used in OFFBEAT provides the following correlation for the α -phase:

$$E_{\alpha}(T, OM, C, \phi) = \frac{K_0 - K_1 T + g(OM) + f(C)}{h(\phi)} \quad (120)$$

where K_0 and K_1 are model parameters, and g , f , h are functions of the oxygen-to-metal ratio OM , cold work C and fast flux ϕ . For the β -phase the MATPRO routine provides a first-degree temperature dependent polynomial. For intermediate temperatures, the Young's modulus is obtained by interpolating the values at the alpha to alpha+beta, and alpha+beta to beta boundaries. A similar routine is used to calculate the **shear modulus** G . The **Poisson's ratio** is then derived as:

$$\nu = \frac{E}{2G} - 1 \quad (121)$$

Currently OFFBEAT lacks a differentiation between Zircaloy-2 and Zircaloy-4 as well as between Stress Relief Annealed (SRA), Recrystallization Annealed (RXA) and Partially Recrystallization Annealed (PRXA) cladding. It must be said that specific correlation coefficients for the various zircaloy types are expected to have only a second order effect.

The Zircaloy **irradiation growth** is treated with a model derived from ESCORE, which calculate the additional axial strain as a function of the neutron fluence:

$$\Delta\varepsilon_{irr} = K_1 (\Phi_i^n - \Phi_{i-1}^n) \quad (122)$$

where K_1 and n are model parameters, and i is the current time step. Because irradiation growth is an isochoric phenomenon, the model provides a negative strain increment for the radial and tangential directions (i.e. the cladding elongates but becomes thinner).

It should be pointed out that for the various Zircaloy properties taken from the IAEA TECDOC, ESCORE or MATPRO, different temperature limits are often applied for the α - β phase changes.

Such inconsistencies probably have a negligible effect on the code validation and verification, but they should be addressed in the future versions of OFFBEAT.

5.9 Rheology

The mechanics sub-solver interacts with a separate class dedicated to the constitutive rheological behavior of the materials involved in the simulation. At each iteration, the mechanics sub-solver provides the displacement field and the total strain tensor, and in turn the rheology class updates the missing components of the strain field (e.g. thermal, plastic etc.), calculates the elastic strain tensor and from this derives the stress field in each material cellzone employing the Hooke's law constitutive relation.

Currently, OFFBEAT allows for: a purely thermo-elastic behavior; a thermo-elasto-plastic behavior with the inclusion of a rate-independent plasticity model; and a thermo-visco-elastic behavior which adds time-dependent creep strains to the basic instantaneous plasticity model.

5.9.1 Instantaneous and rate-dependent plasticity: mathematical model

When subjected to a load, most materials show an initial elastic and often linear response, with the deformations completely recovered once the load is removed. If the stress grows beyond a specific limit called the yield stress, the material starts to accumulate permanent plastic deformations due to the slipping of atomic planes and once the load is removed, only the elastic portion of the deformation is recovered. This phenomenon is usually called rate-independent or instantaneous plasticity, although simply plasticity is often used. Figure 5.4 shows the typical modeling of plasticity for a one-dimensional body. At the onset of plastic deformations, the yield stress starts to increase as a function of the cumulated strain. This phenomenon follows a straight line with a slope equal to the material's plastic modulus and it is called linear strain hardening. Also, the elastic strains are recovered along a line with the same elastic modulus as the body during loading. Although not all materials can be accurately described with this simplified modeling, it is often considered a good approximation for many loading conditions.

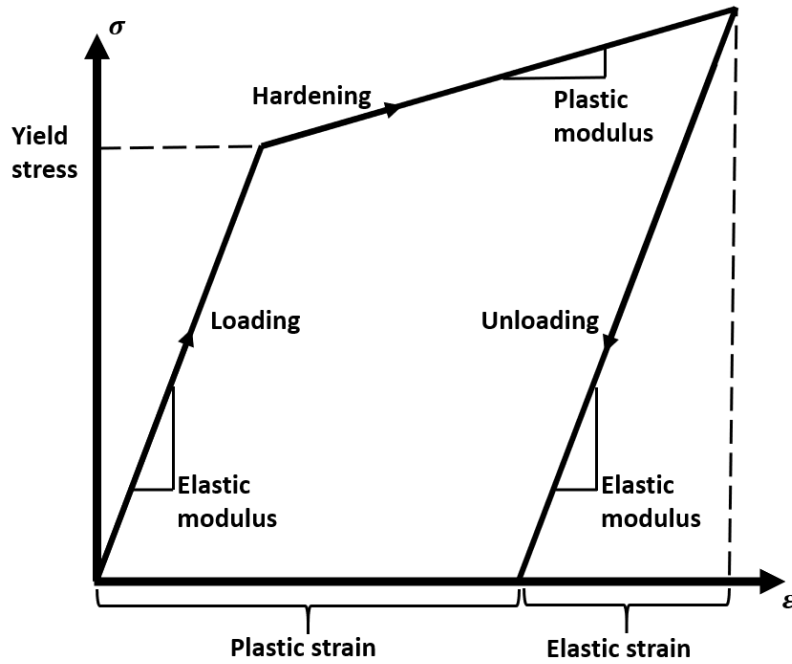


Figure 5.4 – Typical modeling of plastic loading and unloading cycle. When the load is removed only the elastic component of the strain is recovered.

Plastic deformations can appear also if the material is exposed to a load below the yield stress and high temperatures for a long period of time. This phenomenon is called creep or time-dependent plasticity and it is usually divided in three stages named primary, secondary, and tertiary creep, as discussed in Sec 2.2.

Because of the path-dependency and irreversibility of plastic phenomena, they must be treated in an incremental strain framework. The strain increment $\Delta\epsilon$ is assumed to be composed of additive terms:

$$\Delta\epsilon = \Delta\epsilon_{el} + \Delta\epsilon_{th} + \Delta\epsilon_{add} + \Delta\epsilon_p(\sigma) + \Delta\epsilon_c(\sigma) \quad (123)$$

where the thermo-elastic components are given by $\Delta\epsilon_{el}$ and $\Delta\epsilon_{th}$; the contribution of specific material-dependent phenomena such as densification or relocation are collected in the term $\Delta\epsilon_{add}$; and the instantaneous-plasticity and creep components are given by $\Delta\epsilon_p(\sigma)$ and $\Delta\epsilon_c(\sigma)$, both function of the current stress state.

The law $\Delta\epsilon_c(\sigma)$ determining the accumulation of creep strains is typically modeled with temperature and stress dependent experimental correlations, often subdivided in separate expressions for the primary, secondary, and tertiary creep rate. In the mathematical formulation of instantaneous plasticity, the criterion for starting plastic deformation is the yield function $f(\sigma, \epsilon_p)$, function of the stress and accumulated plastic strain. The yield function can be thought as a surface in stress

space that separates elastic and plastic behavior: stress states that make the yield function negative are allowed and correspond to purely elastic behavior; stress states that make the yield function positive are not allowed and thus yielding takes place only if $f(\boldsymbol{\sigma}, \boldsymbol{\varepsilon}_p) = 0$.

5.9.2 Instantaneous plasticity model: Von Mises plasticity

The instantaneous plasticity model implemented in OFFBEAT is based on the classic Von Mises theory of plasticity. The Von Mises definition of the yield function is:

$$f(\bar{\sigma}, \bar{\varepsilon}_p) := \bar{\sigma} - \sigma_Y(\bar{\varepsilon}_p) \quad (124)$$

where σ_Y is the yield stress and $\bar{\sigma}$ is the equivalent or von Mises stress representing the distortion energy in the material and given by:

$$\bar{\sigma} = \sqrt{\frac{3}{2} \boldsymbol{\sigma}^d : \boldsymbol{\sigma}^d} \quad (125)$$

where the deviatoric stress is indicated with $\boldsymbol{\sigma}^d$. The yield stress can be constant for plastic behavior that can be approximated as perfectly plastic or it can vary as a function of the equivalent plastic strain $\bar{\varepsilon}_p$ given by:

$$\bar{\varepsilon}_p = \sqrt{\frac{2}{3} \boldsymbol{\varepsilon}_p : \boldsymbol{\varepsilon}_p} \quad (126)$$

A rule is needed to move from the mono-dimensional plastic strain calculated in the Von Mises or equivalent space to the 3-D plastic strain increment. The model implemented in OFFBEAT applies the Prandtl-Reuss flow rule also called normality rule:

$$\Delta \boldsymbol{\varepsilon}_p = \Delta \lambda \cdot \nabla f \quad (127)$$

where $\Delta \lambda$ is the plastic multiplier and ∇f is the unity vector normal to the yield surface.

Finally, the model's closure is given by the traditional Kuhn-Tucker loading and unloading conditions, and the consistency condition:

$$\overbrace{f \leq 0, \quad \Delta\lambda \geq 0, \quad f\Delta\lambda = 0}^{\text{Kuhn-Tucker}}, \quad \overbrace{\Delta\lambda \frac{\partial f}{\partial t} = 0}^{\text{Consistency}} \quad (128)$$

implying that:

- stress states beyond the yield limit are inadmissible (the stress state remains always on or inside the yield surface);
- when the material yields the plastic strain flows in the same direction as the applied stress;
- if the plastic strain increases, the stress point must remain on the yield surface.

5.9.3 Instantaneous plasticity model: numerical implementation

The rate-independent plasticity model follows the description of elasto-plastic behavior given by J.C. Simo and T. J. R. Hughes [82] and it is derived from the implementation of the solids4Foam platform [81].

After the solution of the momentum balance equations, the displacement field is used to update the total strain tensor $\boldsymbol{\epsilon}^i$ where i is the current outer iteration. A trial stress is calculated as:

$$\boldsymbol{\sigma}_{\text{tr}}^i = 2\mu\boldsymbol{\epsilon}^i + \lambda\text{tr}(\boldsymbol{\epsilon}^i) - 2\mu\boldsymbol{\epsilon}_p^o \quad (129)$$

where the index o refers to the old-time value calculated at the end of previous time step. The equation above is equivalent to assuming that the new increment in strain tensor is entirely elastic. The yield function is then evaluated in terms of the trial state:

$$f^i = \overline{\sigma}_{\text{tr}}^i - \sigma_Y(\overline{\epsilon}_p^o) \quad (130)$$

If $f \leq 0$ the deformation is deemed as elastic and the plastic strain increment is zero. If $f > 0$ then the following flow rule is used:

$$\Delta\boldsymbol{\epsilon}_p^i = \Delta\lambda^i \frac{\partial f^i}{\partial \boldsymbol{\sigma}_{\text{tr}}} = \Delta\lambda^i \cdot \mathbf{n}^i \quad (131)$$

where \mathbf{n}^i is the current iteration vector normal to the yield surface calculated as:

$$\mathbf{n}^i = \frac{(\boldsymbol{\sigma}_{\text{tr}}^{i,d})}{\sqrt{\boldsymbol{\sigma}_{\text{tr}}^{i,d} : \boldsymbol{\sigma}_{\text{tr}}^{i,d}}} \quad (132)$$

The plastic multiplier is obtained as:

$$\Delta\lambda^i = \frac{f^i}{2\mu(1 + \frac{H}{3\mu})} \quad (133)$$

where H is the plastic modulus, allowing to model both perfect plasticity ($H = 0$) and linear strain hardening. The plastic strain and the stress are then updated:

$$\boldsymbol{\epsilon}_p^i = \boldsymbol{\epsilon}_p^o + \Delta\boldsymbol{\epsilon}_p^i \quad (134)$$

$$\boldsymbol{\sigma}^i = \boldsymbol{\sigma}_{tr}^{i,d} - 2\mu\Delta\boldsymbol{\epsilon}_p^i$$

The updated stress tensor field is used for the solution of the momentum balance equations in the following iteration $i+1$. The algorithm is repeated until convergence of the residuals.

5.9.4 Zircaloy creep: Limbäck model

The Limbäck and Anderson model is described in detail in the original publication from the authors [110] and in the work of Liu et al. [111]. Nevertheless, the main equations are reproduced here for clarity. The Limbäck model calculates the total equivalent creep strain of Zircaloy, $\epsilon_{c,eq}$, as the combination of two main components, i.e. the primary creep and the secondary creep, which in turn is composed of thermal and irradiation-induced creep.

The irradiation induced creep rate $\dot{\epsilon}_{irr}$ (hr^{-1}) is given as:

$$\dot{\epsilon}_{irr} = C_0 \phi^{C_1} \sigma_{VM}^{C_2} \quad (135)$$

where σ_{VM} is the effective or von Mises stress in MPa, ϕ is the fast neutron flux in $n/m^2\text{-sec}$, $C_0 = 3.557 \times 10^{-24} ((n/m^2\text{-sec})^{-C_1} (MPa)^{-C_2} / hr)$, $C_1 = 0.85$ and $C_2 = 1.0$.

The secondary thermal creep rate $\dot{\epsilon}_{th}$ (hr^{-1}) is given as:

$$\dot{\epsilon}_{th} = A \frac{E}{T} \left(\sinh \frac{a_i \bar{\sigma}}{E} \right)^n \exp \left(-\frac{Q}{RT} \right) \quad (136)$$

where T is the temperature (K), E is the Young's modulus (MPa) calculated as :

$$E = 1.148 \times 10^5 - 59.9T \quad (137)$$

a_i is an irradiation hardening parameter calculated as:

$$a_i = a[1 - A_1(1 - \exp(-A_2\Phi^{A_3}))] \quad (138)$$

and Φ is the fast neutron fluence (n/cm^2). The following values are used for the remaining parameters: $Q = 201$ (kJ/mol), $a = 650$, $n = 2.0$, $A = 1.08 \times 10^9$ (K/MPa-hr), $A_1 = 0.56$, $A_2 = 1.4 \times 10^{-27}$ (n/cm^2) $^{-A_3}$ and $A_3 = 1.3$.

The primary creep strain is derived from the Matsuo correlation for saturated primary creep [112]:

$$\varepsilon_{\text{prim}} = \varepsilon_{\text{prim}}^s [1 - \exp(-C\sqrt{\dot{\varepsilon}_s t})] \quad (139)$$

where t is the time in hr, $C = 52$ is a fitting parameter, $\dot{\varepsilon}_s$ is the secondary creep rate, $\dot{\varepsilon}_s = \dot{\varepsilon}_i + \dot{\varepsilon}_{\text{th}}$, and $\varepsilon_{\text{prim}}^s$ is the saturated primary creep strain given by:

$$\varepsilon_{\text{prim}}^s = B\dot{\varepsilon}_s^b [2 - \tanh(D\dot{\varepsilon}_s)]^d \quad (140)$$

where $B = 0.0216$ (hr^b), $b = 0.109$, $D = 35500$ (hr) and $d = -2.05$.

Finally, the total effective creep strain at time t is given as:

$$\bar{\varepsilon}_c = \varepsilon_{\text{prim}}^s [1 - \exp(-C\sqrt{\dot{\varepsilon}_s t})] + \dot{\varepsilon}_s t \quad (141)$$

5.9.5 UO₂ creep: MATPRO model

The creep model for UO₂ is derived from the FCREEP routine of MATPRO, following the implementation of BISON. The total creep strain rate is given by the sum of three terms:

$$\dot{\varepsilon}_c = \frac{A_1 + A_2\dot{F}}{(A_3 + D)G^2} \sigma \exp\left(\frac{-Q_1}{RT}\right) + \frac{A_4}{(A_5 + D)} \sigma^{4.5} \exp\left(\frac{-Q_2}{RT}\right) + A_6\dot{F}\sigma \exp\left(\frac{-Q_3}{RT}\right) \quad (142)$$

where \dot{F} is the fission rate density (fission/ m^3s), G is the grain size (μm), D is the fuel density in percent of the TD, R is the universal gas constant and the material constants are given by $A_1 = 0.3919$, $A_2 = 1.31 \cdot 10^{-19}$, $A_3 = -87.7$, $A_4 = 2.0391 \cdot 10^{-25}$, $A_5 = -90.5$ and $A_6 = 3.7226 \cdot 10^{-35}$.

The first term dominates at low stresses and low temperature conditions and represents the diffusional thermal creep. The second term dominates at high stress and high temperature conditions and reproduces the thermal dislocation creep characterized by a power-law. The third term takes into account the effect of irradiation also considered in the first term.

The activation energies Q_1 and Q_2 are given by :

$$\begin{aligned} Q_1 &= 74829 \cdot f(OM) + 301762 \\ Q_2 &= 83143 \cdot f(OM) + 469191 \end{aligned} \quad (143)$$

where $f(OM)$ is the following function of the fuel stoichiometry or oxygen-to-metal ratio OM :

$$f(OM) = \frac{1}{\exp\left(\frac{-20}{\log(OM-2)} - 8\right) + 1} \quad (144)$$

5.9.6 Time dependent creep: numerical implementation

The Limbäck and the MATPRO models obtain the creep strain components as a function of the stress state. The current stress state is proportional to the elastic strain tensor, $\boldsymbol{\varepsilon}_{el}$, which is just one component of the total strain tensor, $\boldsymbol{\varepsilon}$. As done for the instantaneous plasticity model, it is more suitable to decompose the instantaneous and time-dependent plastic strain terms into old time (o) and incremental components (Δ), obtaining:

$$\boldsymbol{\varepsilon}^i = \boldsymbol{\varepsilon}_{el} + \boldsymbol{\varepsilon}_c^o + \Delta\boldsymbol{\varepsilon}_c^i(\boldsymbol{\sigma}) + \boldsymbol{\varepsilon}_p^o + \Delta\boldsymbol{\varepsilon}_p^i(\boldsymbol{\sigma}) \quad (145)$$

Where i is the current outer iteration and the creep strain increment is a function of the stress state. This in turn is a function of the creep increment, therefore at iteration $i + 1$, the value of the stress is calculated using the strain increment obtained at the end of iteration i . In order to calculate the creep strain increment, an algorithm similar to the one proposed in the work of Liu et al. is followed.

At time step $t + \Delta t$, during the i -th iteration, the latest available displacement solution \mathbf{u}^i is used to calculate the total strain $\boldsymbol{\varepsilon}^i$ and the total strain increment $\Delta\boldsymbol{\varepsilon}^i$ using the definition of small strain tensor.

Assuming that the increment in strain is purely elastic, a trial stress tensor $\boldsymbol{\sigma}_{tr}^i$ and a trial effective stress $\bar{\sigma}_{tr}^i$ are calculated. The effective stress $\bar{\sigma}^i$ as a function of the trial stress and of the equivalent creep increment (from the previous iteration) is given by:

$$\bar{\sigma}^i = \bar{\sigma}_{tr}^i - 3\mu \bar{\Delta\epsilon}_c^{i-1} \quad (146)$$

The current effective strain increment is given by:

$$\bar{\Delta\epsilon}_c^i = f(\bar{\sigma}^i) \Delta t \quad (147)$$

where f is:

$$f(\bar{\sigma}^i) = \dot{\epsilon}_{irr}^i + \dot{\epsilon}_{th}^i + \frac{\epsilon_{prim}^{s,i} \left[1 - \exp \left(-C \sqrt{\dot{\epsilon}_s^i (\tau^i + \Delta t)} \right) \right] - \epsilon_p^o}{\Delta t} \quad (148)$$

and τ^i is:

$$\tau^i = C^{-2} (\dot{\epsilon}_{irr}^i + \dot{\epsilon}_{th}^i)^{-1} \left[\ln \left(1 - \frac{\epsilon_p^o}{\epsilon_{prim}^{s,i}} \right) \right]^2 \quad (149)$$

The various components of the creep strain rate are calculated using the formulas presented in the two previous sections. The multi-axial stress creep strain increment is obtained with the Prandtl-Reuss flow rule:

$$\Delta \epsilon_c^i = \frac{3\sigma^{d,i}}{\bar{\sigma}^i} \bar{\Delta\epsilon}_c^i \quad (150)$$

where $\sigma^{d,i}$ is the deviatoric component of the stress tensor.

The updated creep strain increment is introduced in Hooke's law to determine the stress tensor σ^{i+1} , eventually after the additional calculation of the instantaneous plastic strain. If the displacement residuals are still above the user defined threshold, σ^{i+1} , is introduced in the momentum balance equations to solve for u^{i+1} and the algorithm is repeated.

5.10 Multi-physics and coupling options

The interest towards multi-physics analysis is one of the main drive behind the development of OpenFOAM and partly motivates the choice of OpenFOAM as developing platform. Since it is designed as a set of C++ classes, OFFBEAT can be coupled directly to stand-alone OpenFOAM solvers dealing with additional physics. For example, one of the standard OpenFOAM CFD solvers could be

selected to calculate the temperature on the outer cladding wall instead of using a simplified model or boundary condition. The thermodynamic routines and chemistry solvers available in OpenFOAM could be adapted to describe the chemical behavior of the fuel, following the example of the ALCYONE and BISON codes [70], [113]. One could also envisage the coupling with the open-source code MAMBA [114] for simulating the thermo-chemical evolution of compositions along the outer metallic surface of the fuel rod, for example for the analysis of CRUD-induced localised corrosion problems.

Similarly, OFFBEAT could be embedded within a sub-channel thermal-hydraulics code or within the multi-physics nuclear reactor analysis platform named GeN-Foam, based on the porous medium approach, and developed at the LRS and PSI [115]. In this way, OFFBEAT could be used as a multi-dimensional fuel performance module, allowing a multi-scale and multi-physics analysis of the reactor core, with the coupling between the FA thermal-hydraulics and neutronics conditions and the thermo-mechanics behavior of the fuel rods.

Another opportunity for multi-physics simulation is through a coupling with the Monte Carlo neutron transport code Serpent. Typical fuel performance codes are equipped with a simplified neutronics module to follow the evolution of the neutron flux and fuel isotopic composition, but these solutions are limited to axisymmetric scenarios and standard LWR fuel. The coupling with Serpent represents an interesting option to expand the fuel performance capabilities toward new fuel types even in the presence of strong absorbers, unconventional fuel configuration and asymmetric irradiation conditions. Thanks to the Serpent multi-physics interface that was developed precisely to streamline the interaction with OpenFOAM solvers, a coupling strategy between Serpent and OFFBEAT has been developed with relatively limited effort. More details are given in Chapter 8.

Finally, the coupling between OFFBEAT and the European fuel performance code TRANSURANUS represents an interesting option for complementing traditional fuel behavior simulations. On the one hand, TRANSURANUS could benefit from OFFBEAT by informing the 1-D analysis with 2-D/3-D simulations. Also, TRANSURANUS could expand its area of application beyond the 1.5-D approximation using OFFBEAT as a plug-in multi-dimensional tool. On the other hand, OFFBEAT could take advantage of a well-validated and effective 1.5-D code to model the steady state behavior of the full-length rod, up to the start of a multi-dimensional transient. TRANSURANUS would provide a set of accurate boundary conditions for the more detailed 2-D or 3-D analysis, saving significant computational resources. The development of the coupling strategy between OFFBEAT and TRANSURANUS is discussed in detail always in Chapter 8.

Figure 5.5 summarizes the main coupling and interaction possibilities taken into consideration in the development plan of OFFBEAT.

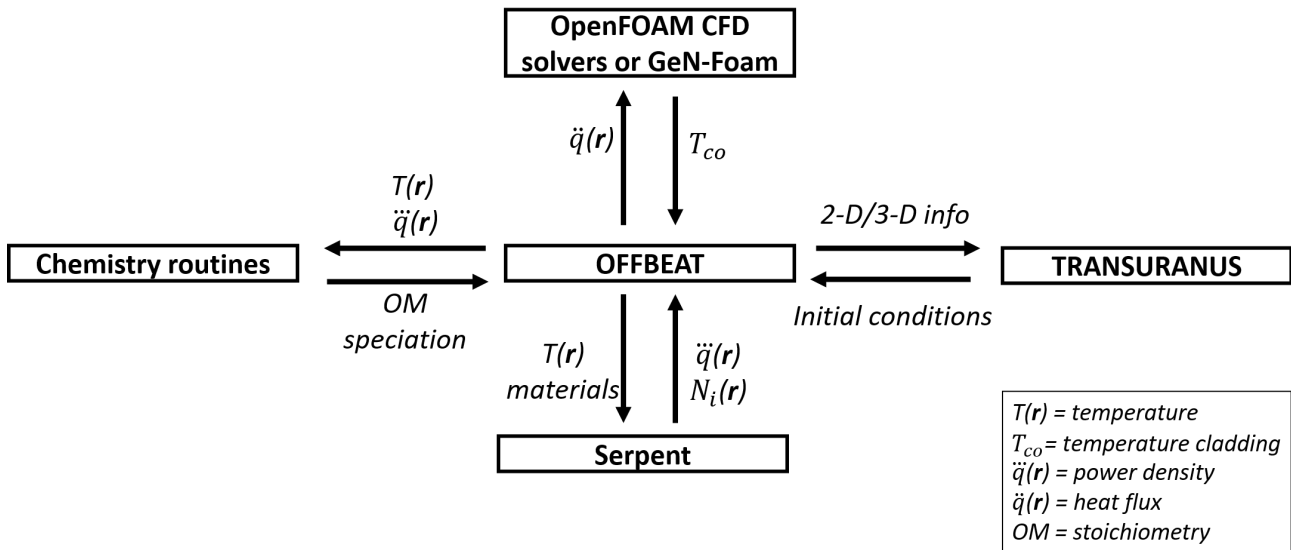


Figure 5.5 – Summary of main options for coupling and interaction considered in the development of OFFBEAT.

5.11 Conclusions

This chapter has presented the main features of OFFBEAT, concluding the first half of this PhD thesis dedicated to the development of a novel FV methodology for fuel performance applications.

OFFBEAT has been built with the OpenFOAM C++ library, making use of its extensive list of features for accelerating the development and simplifying the maintenance. The OpenFOAM library has been selected also for its inherent 3-D nature that allows one to model 1-D, 2-D or 3-D geometries with the simple selection of appropriate boundary conditions, and for its potential for multi-physics simulations.

OFFBEAT has been equipped with most of the behavioral models expected for a full-fledged fuel performance code such as custom boundary conditions for gap conductance and contact, semi-empirical models for relocation, densification and growth or correlations for capturing the temperature and burnup dependence of the material properties. Between the more relevant missing components there are a model for the cladding outer oxidation and a more accurate boundary condition or the coupling with a thermal-hydraulic solver for calculating the outer cladding temperature.

The 0-D code SCIENTIX developed at the Politecnico di Milano and representing a state-of-the-art tool for modeling the behavior of the fission gases in the fuel pellets, has been introduced in OFFBEAT as a dedicated fission gas release and gaseous swelling module. Its routines for capturing the isotopic evolution of the fuel are for the moment not included in OFFBEAT. A dedicated class derived from the TUBURNP module of TRANSURANUS has been created for modeling the evolution of the power profile in the fuel during axisymmetric simulations. Regarding the rheology of the nuclear materials, models for elasto-plasticity and for creep for both cladding and fuel have been introduced in the code.

The next chapter focuses on the efforts carried out in parallel with the development of the code to verify the various models discussed in this chapter and validate OFFBEAT against experimental data.

Chapter 6

Verification, validation, and demonstration cases⁴

The fuel performance code OFFBEAT was developed as part of this PhD thesis to explore the potential of the FVM for multi-dimensional fuel performance applications. The previous three chapters have presented, respectively, the numerical framework at the foundation of the code (Chapter 3), the gap heat transfer and contact methodologies (Chapter 1), and the code structure (Chapter 5). This chapter focuses on the validation and verification efforts carried out in parallel with the development of the code and with the introduction of new features.

Verification and validation are two essential tools to check whether a software is robust and reliable and whether it fulfills its intended purposes. Paraphrasing the IEEE 610-1990 standard [116], verification is the process of evaluating if a piece of software works as intended. That is, it addresses the question “was the code correctly developed?”. Verification is often considered as a prerequisite to or at least as a step that precedes validation and for computer assisted simulation software it typically consists in assessing the predictions of the code against known analytic solutions. In a complex and multi-physics framework like that of fuel performance, verification becomes particularly relevant because the compensation of errors can mask fundamental issues with the numerical scheme or with the implementation of a specific model [117]. The verification tests performed on OFFBEAT are presented in Section 6.1.

Always moving from the definition of the IEEE standard, validation is the process of evaluating that the code satisfies the requirements set at the beginning of the development process or of a development phase. That is, it addresses the question “was the right code developed considering the original purposes?” and for simulation software it consists in comparing the prediction of the code against experimental results. Validation is of primary importance for fuel performance codes as they are often used by the NPP operator or by the regulator for safety related decisions. For the code developer, it is often the only way to check whether the interplay between the multitude of models introduced (even if separately verified) captures the response of the real system with sufficient accuracy. The current validation base of OFFBEAT is presented in Section 6.2.

⁴ The content presented in this chapter is partially available in [50], [151], [173], [172].

An additional tool used in the development of OFFBEAT is the preparation of multi-dimensional case-studies to test the capability of the code to capture relevant multi-dimensional features such as the formation of the cladding ridge pattern. These case-studies involve the application of multiple sub-models and components of OFFBEAT (if not the entire code) and they focus on more realistic scenarios if compared to verification tests which are typically limited to a single model. At the same time, these test cases are significantly simplified with respect to real irradiation histories and are not a substitute for proper validation efforts. This allows one to focus the attention on eventual modeling issues or numerical aspects that might be difficult to assess in a complex validation campaign. Two examples of such multi-dimensional case studies are presented in Section 6.3.

Finally, some relevant conclusions for this chapter are drawn in Section 6.4.

6.1 Verification

To allow the comparison with an analytic solution, verification cases often focus on the implementation of a single model or on the numerical solution of the governing equations under simplified conditions. The verification of OFFBEAT is an ongoing process and new cases are added with the introduction of new features. The main tests realized in the framework of this thesis are presented in this section, with particular attention dedicated to the verification of the contact models.

6.1.1 Steady-state and transient temperature profile

The first verification case considers the temperature distribution of a uniform axisymmetric fuel rod in steady-state. By neglecting the axial gradients and assuming constant material properties, gap-width, gap conductance and convective heat exchange coefficient with the coolant, analytical solutions can be derived for the temperature distribution in the fuel and cladding [118].

The material properties and the case setup are given in Table 6.1. The case is reproduced with a 1-D wedge model (axisymmetric) and discretized with 30 radial cells in the fuel and 10 radial cells in the cladding. The simulation proceed until the relative residuals are below 10^{-6} . Figure 6.1 compares the radial temperature profile provided by OFFBEAT against the reference solution, showing that the code can correctly reproduce the analytic profile, with an overall error below 0.1%.

Table 6.1 – Dimensions and case properties for the steady-state verification case

Fuel	Radius, mm	4.22
	Heat source, W/m ³	$4 \cdot 10^8$
	Th. Conductivity, W/mK	3
	Young modulus, GPa	200
	Poisson's ratio	0.316
	Th. expansion coefficient, K ⁻¹	$9.89 \cdot 10^{-6}$
Gap	Width, mm	0.07
	Conductance, W/m ²	5000
Cladding	Width, mm	0.8
	Convect. heat-exchange coefficient, W/m ²	50000
	Water Temperature, K	550
	Th. Conductivity, W/mK	21.5
	Young modulus, GPa	99.3
	Poisson's ratio	0.37
	Th. expansion coefficient, K ⁻¹	$6 \cdot 10^{-6}$

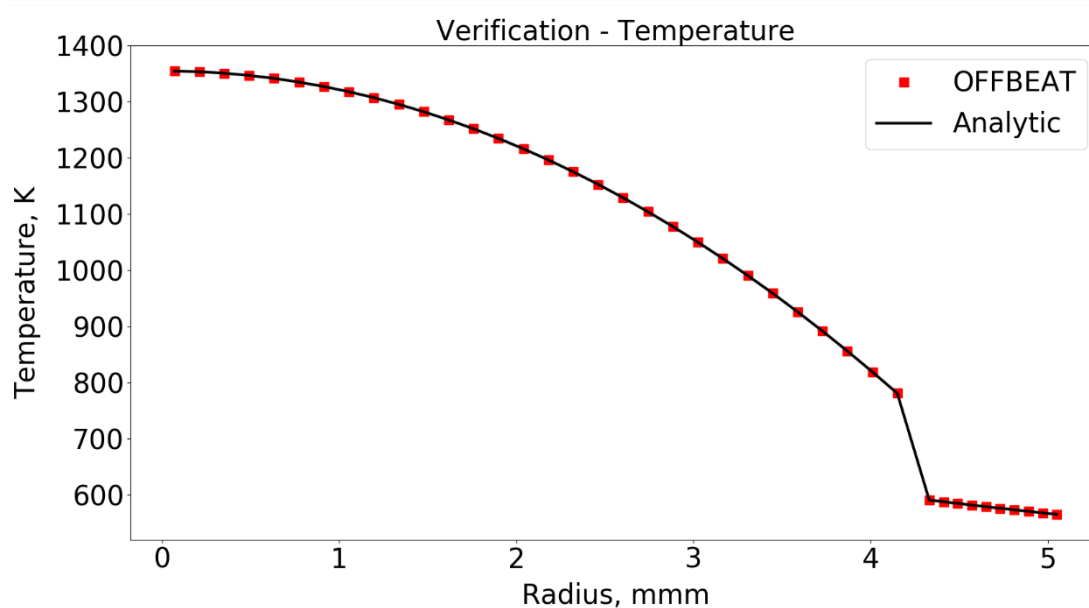


Figure 6.1 – Analytic and numerical temperature profile for the steady-state case.

An analytical solution exists also for an axisymmetric, infinitely long hot cylinder during a transient [119]. Thus, the second verification test considers four transient scenarios for the same thin fuel wedge of the steady-state case (the cladding is not considered this time). The transients are divided in two groups, that is, two power ramps and two shut down transients. Two boundary conditions are used for the outer pellet surface, either of the Dirichlet type (the temperature is fixed) or of the Neuman type (the heat flux is fixed), for a total of 4 simulations. Figure 6.2 compares the radial temperature profile calculated by OFFBEAT against the analytic solutions (only the results for the Dirichlet transient are displayed). The code correctly predicts the evolution of the radial temperature profile during the transient with an overall error below 0.1%.

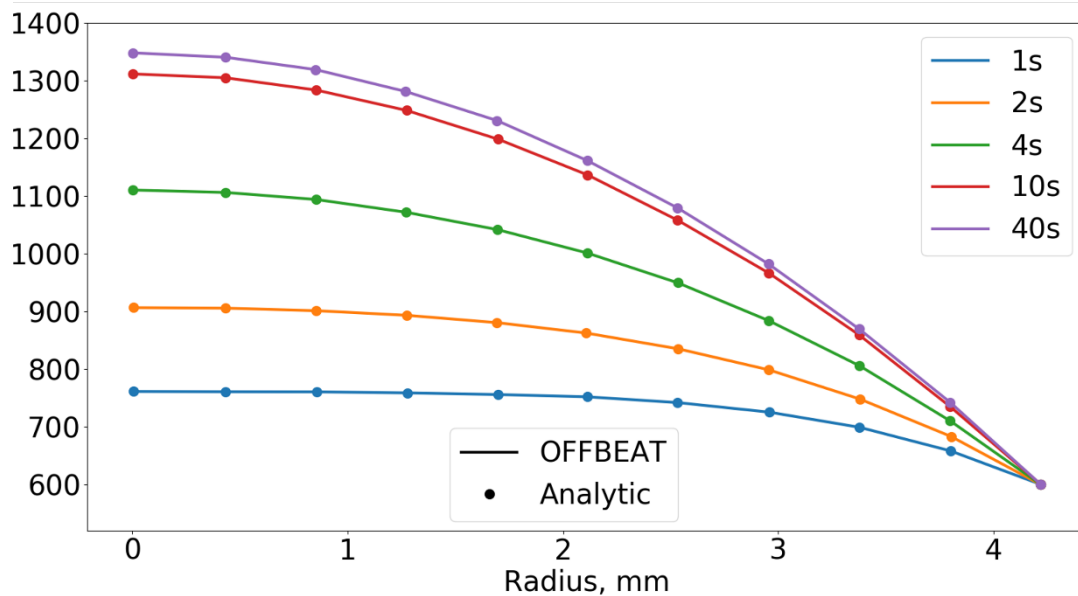


Figure 6.2 – Analytic and numerical temperature profile for the transient power ramp case with Dirichlet boundary condition (fixed temperature on the outside of the fuel pellet).

6.1.2 Steady-state stress profile

The third verification case considers the stress distribution in a uniform, axisymmetric fuel rod in steady-state. The same 1-D wedge model from the previous section is used, with the same material properties and simulation settings. Assuming plain strain condition, 1-D radial profiles for the radial and hoop stresses can be derived [118]. As shown in Figure 6.3, OFFBEAT can correctly reproduce the steady state stress profiles with an overall error of 0.1%. It should be noted that the analytic profiles might suggest that the solution is continuous as if there was no gap, but this is just a plotting error deriving from fitting a single continuous line between the analytic data-points. As the gap pressure is the same on both sides, the radial stress seems continuous. Also, the tensile

hoop stresses in the pellet are unrealistically high and would certainly cause pellet cracking. These high stresses however are obtained only because the isotropic cracking model was deactivated for verification purposes.

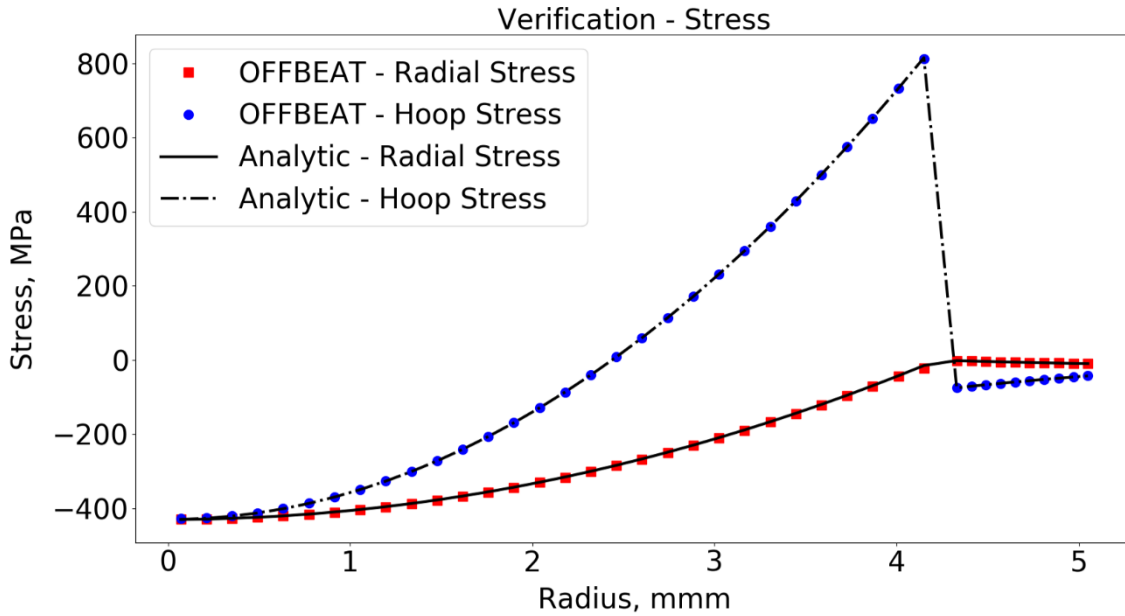


Figure 6.3 – Analytic and numerical stress profiles (radial and hoop) for the steady-state case.

6.1.3 Contact benchmarks: verification of implicit contact methodology

For two bodies in contact with infinite friction coefficient and without the formation of an open gap, the implicit contact procedure developed in Section 4.3.2 should be equivalent to the treatment for multi-material interfaces developed by Tuković.

To verify the use of the implicit contact methodology for similar scenarios, two cases are considered both consisting of a bi-material cylinder in plane stress with the dimensions shown in Figure 6.4. In Case I, the inner cylinder is pressurized with a constant pressure p_i , while the outer surface is modeled as stress-free; in Case II, the inner surface is fixed and a constant tangential load τ is applied to the outer cylinder.

Both test cases were analyzed in the original publication from Tuković [78]. The main difference is that in this thesis the bi-material cylinder is reproduced with two separate concentric cylinders. The two materials, indicated with different color in the Figure 6.4, have a Poisson's ratio of $\nu_1 = 0.35$ and $\nu_2 = 0.3$, while the Young's Modulus ratio E_2/E_1 ranges from 0.2 to 10. The computational model has a total of 50 cells in the radial direction. The cells in the azimuthal direction are 480 for the inner cylinder and 920 for the outer cylinder. The azimuthal difference is introduced to test the implicit contact methodology on non-conformal meshes.

As there is no gap opening, it is not necessary to truncate the sigmoid blending function (see Section 4.3.6) and the relative offset o_{rel} can be set to zero without incurring in the issue of spurious attractive forces. Also, the relative half-width h_{rel} can be set to the small value of 0.1 without affecting the convergence properties of the simulations. With this choice of blending parameters, the final interpenetration (relative to the radial size of the cells on the contact interface) is about 10^{-4} for Case I, which is considered negligible.

All simulations are in steady state and are performed on the same Intel Xeon CPU E5-1660 v4 using one of the eight 3.2 GHz cores. Relaxation factors are not necessary to reach convergence, and the simulation time varies from ~ 10 s to ~ 35 s depending on the boundary conditions (Case I or Case II) and on the E_2/E_1 ratio.

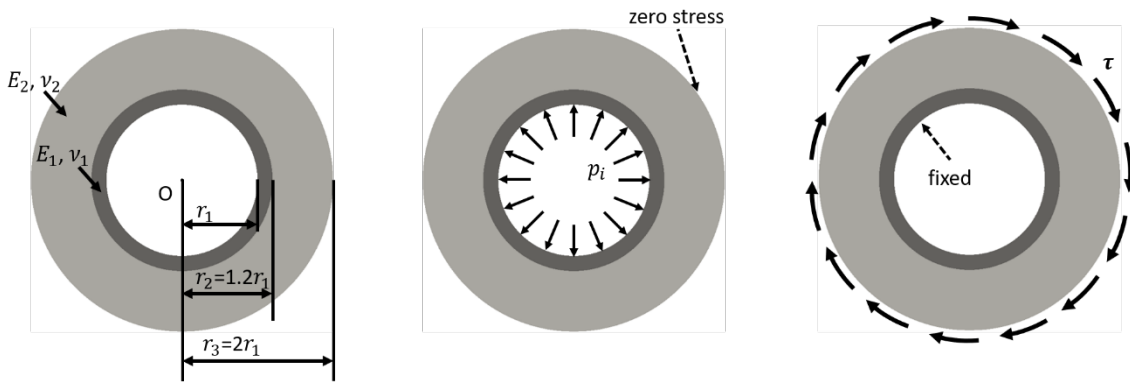


Figure 6.4 – Bi-material cylinder, dimensions (left), load for case with uniform internal pressure (center) and load for case with outer tangential traction (right).

Case I was already analyzed by A.V. Phan et. al in [120], where the authors have derived the analytical solutions for the radial and hoop stresses:

$$\sigma_r(r) = \begin{cases} \frac{r_1^2 p_i - r_2^2 p_{12} + (p_{12} - p_i) \left(\frac{r_1 r_2}{r}\right)^2}{r_2^2 - r_1^2} & , r_1 \leq r \leq r_2 \\ \frac{r_2^2 p_{12} - p_{12} \left(\frac{r_2 r_3}{r}\right)^2}{r_3^2 - r_2^2} & , r_2 < r \leq r_3 \end{cases} \quad (151)$$

$$\sigma_\theta(r) = \begin{cases} \frac{r_1^2 p_i - r_2^2 p_{12} - (p_{12} - p_i) \left(\frac{r_1 r_2}{r}\right)^2}{r_2^2 - r_1^2} & , r_1 \leq r \leq r_2 \\ \frac{r_2^2 p_{12} + p_{12} \left(\frac{r_2 r_3}{r}\right)^2}{r_3^2 - r_2^2} & , r_2 < r \leq r_3 \end{cases} \quad (152)$$

where p_{12} is the contact pressure at the interface:

$$p_{12}(r) = \frac{\frac{2r_1^2 p_i}{E_1(r_2^2 - r_1^2)}}{\frac{1}{E_2} \left(\frac{r_3^2 + r_2^2}{r_3^2 - r_2^2} + \nu_2 \right) + \frac{1}{E_1} \left(\frac{r_2^2 + r_1^2}{r_2^2 - r_1^2} - \nu_1 \right)} \quad (153)$$

Similarly, Case II was already analyzed by Nie and Batra in [121], where they derived the analytic solution for the shear stress:

$$\sigma_{r\theta}(r) = \tau \frac{r_3^2}{r^2} \quad (154)$$

The solution for the tangential displacement, instead, was derived by Tukovic:

$$\sigma_{\theta}(r) = \begin{cases} \frac{r_3^2 \tau}{2\mu_1} \left(\frac{r}{r_1^2} - \frac{1}{r} \right) & , r_1 \leq r \leq r_2 \\ \frac{r_3^2 \tau}{2} \left[\left(\frac{1}{\mu_1 r_1^2} - \frac{1}{\mu_1 r_2^2} + \frac{1}{\mu_2 r_2^2} \right) r - \frac{1}{\mu_2 r} \right] & , r_2 < r \leq r_3 \end{cases} \quad (155)$$

The results of the simulations are presented in the following graphs and agree well with those reported by Tuković in his original publication. The radial and hoop stress profiles for Case I are shown in Figure 6.5 and Figure 6.6 and show excellent agreement with the analytical solutions, with an overall error lower than 1%. Similarly, the shear stress obtained for Case II compares well to the analytical profile as shown in Figure 6.7. Always for Case II, the tangential displacement profile in Figure 6.8 presents a higher deviation from the analytical solution, about 3%. This is the result of the introduction of the blending function, given that a blending coefficient lower than one causes the displacement to readjust to conserve the global force balance. Indeed, repeating the simulations with a blending coefficient higher than 0.99 (as it can be done for example by using a negative offset) lowers the overall error down to 0.1%.

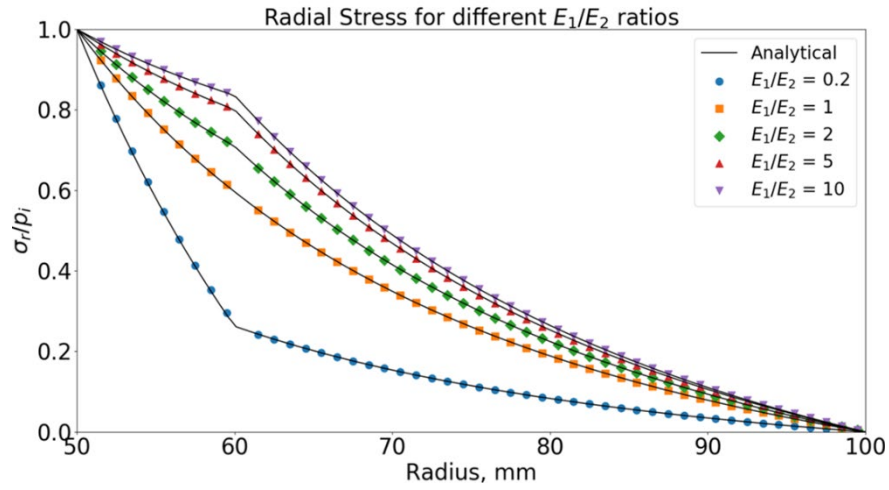


Figure 6.5 - Radial stress in bi-material cylinder with inner pressure p_i for various E_1/E_2 ratios.

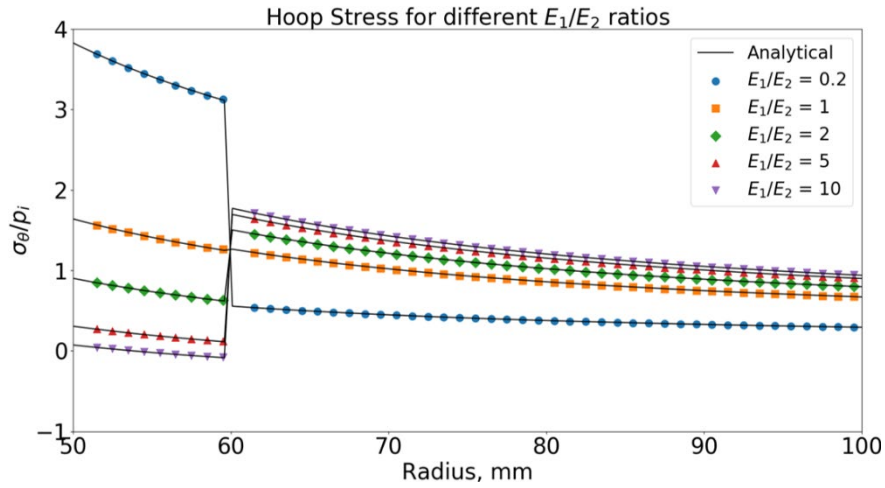


Figure 6.6 - Hoop stress in bi-material cylinder with inner pressure p_i for various E_1/E_2 ratios.

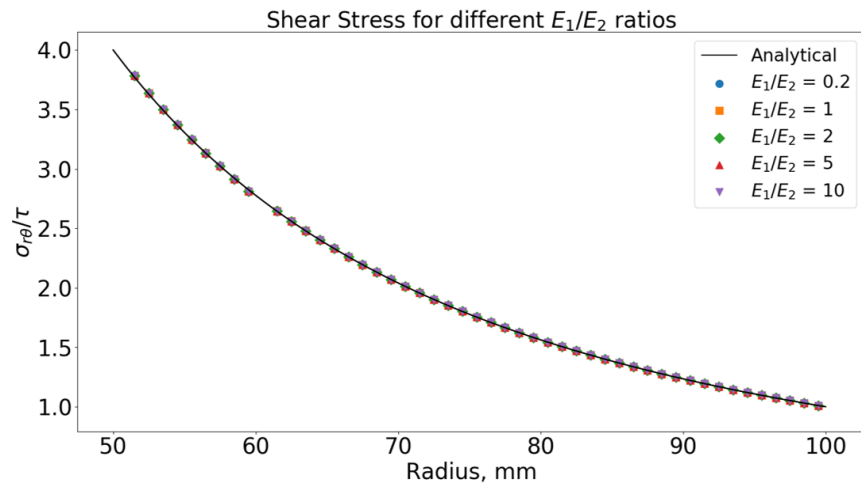


Figure 6.7 - Shear stress in bi-material cylinder with tangential load τ for various E_1/E_2 ratios.

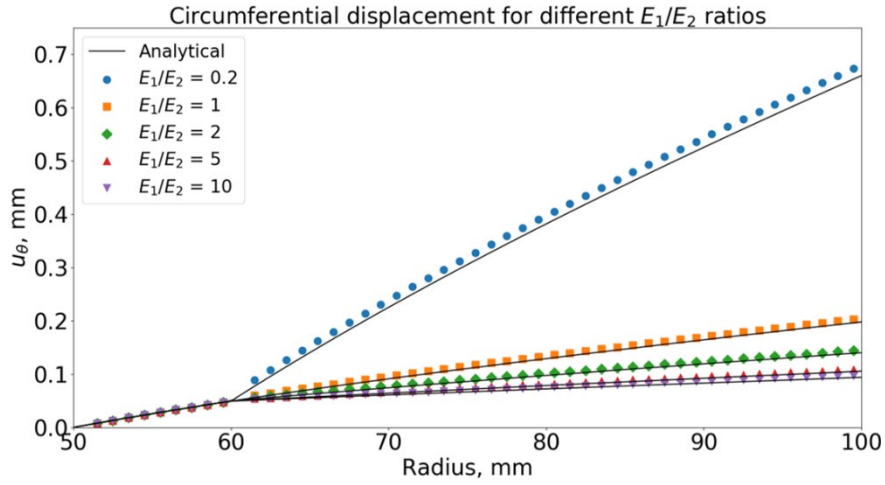


Figure 6.8 - Circumferential displacement in bi-material cylinder with tangential load τ for various E_1/E_2 ratios.

6.1.4 Contact benchmarks: 2-D punch test

The third contact verification case is a 2-D linear-elastic punch test from the NAFEMS benchmark series [122]. The case consists of a cylindrical steel punch pressed with a constant force of 35 kN (a point load applied on the top of the cylinder) on an aluminum foundation. This setup is shown with its main dimensions in Figure 6.9 where the two bodies are displayed with different colors. The Young's moduli are $E_{\text{foundation}} = 70 \text{ GPa}$ and $E_{\text{punch}} = 210 \text{ GPa}$, while both materials have the same Poisson's ratio of $\nu = 0.3$. The contact is assumed to be frictionless, therefore the friction coefficient α is set to zero.

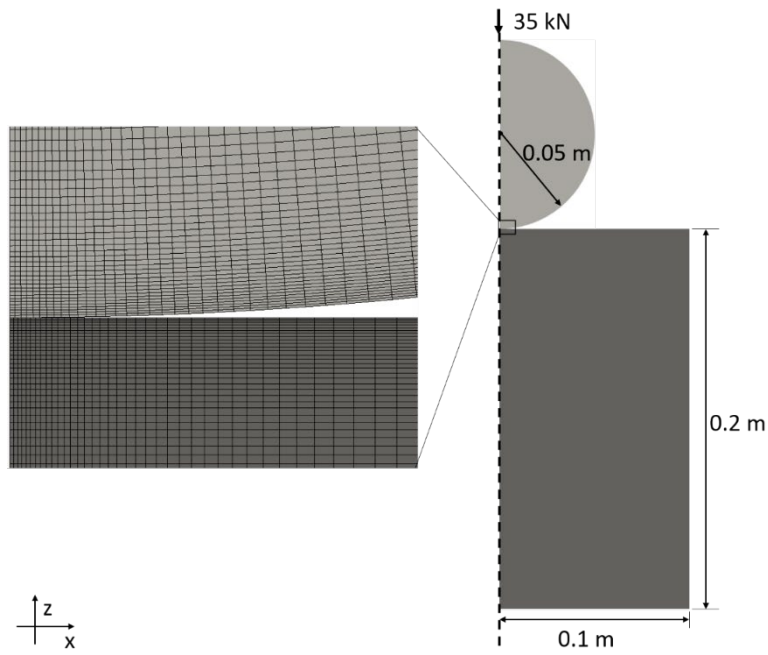


Figure 6.9 – Two-dimensional frictionless punch test: model (right) and mesh detail of the contact region (left).

The problem is symmetric and only half of the geometry is reproduced in the computational model, using symmetry boundary conditions. The case is solved with 3 different mesh refinement levels, from Level 1 to Level 3, with a total of 1'770, 6'700 and 28'000 cells, respectively. All computational models are progressively refined in the region closer to the contact area as shown in the detail of Figure 6.9 for the finest mesh. The relative offset and half-width are set to 0 and 0.1, respectively, leading to an average relative interpenetration (with respect to the cell size) of $\sim 5 \cdot 10^{-3}$ for the finest mesh, and the sigmoid function is not truncated. The benchmark case is solved a last time on the finest mesh employing a different boundary condition based on the penalty method, so that the performance and accuracy of the two contact methodologies can be compared.

All simulations are performed in steady state on the same Intel Xeon CPU E5-1660 v4, using one of the eight 3.2 GHz cores. A relaxation factor of 0.999 for the equation solution is required to reach convergence when employing the penalty-based boundary condition, while a relaxation factor of 0.8 for the displacement field is used to stabilize the solution for the implicit contact simulation.

The analytical solution for the contact pressure along the rounded edge of the punch is obtained in [122] using the Hertzian contact formulae:

$$p = p_{\max} \sqrt{1 - \xi^2} \quad (156)$$

where $p_{\max} = 3.58 \text{ GPa}$ is the maximum pressure, $\xi = x/l$ is the normalized coordinate along the rounded edge and $l = 6.21 \text{ mm}$ is the contact arc length along the punch outer surface.

In Figure 6.10 the calculated contact pressure is compared against the analytic solution. As expected, the predicted maximum pressure and contact arc length approach their analytic values p_{max} and l as the mesh refinement increases, moving from the 3.64 GPa and ~ 8.1 mm for Level 0, to the 3.61 GPa and ~ 7.5 mm for Level 1 and finally to the 3.59 GPa and ~ 6.7 mm for Level 2.

Although obtained on the finest mesh refinement levels, the contact pressure calculated with the penalty method boundary condition deviates more significantly from the analytical solution, with a maximum pressure of 3.16 GPa, a contact arc length of ~ 8 mm and higher peak stresses at the edge of the contact arc. This suggests that, when comparing the implicit contact methodology with the penalty method, a less refined grid is required to obtain results with the same (or better) accuracy, at least for the almost point-like contact case considered in this section. A better solution could be obtained with the penalty method by increasing the mesh refinement or choosing a penalty factor closer to one.

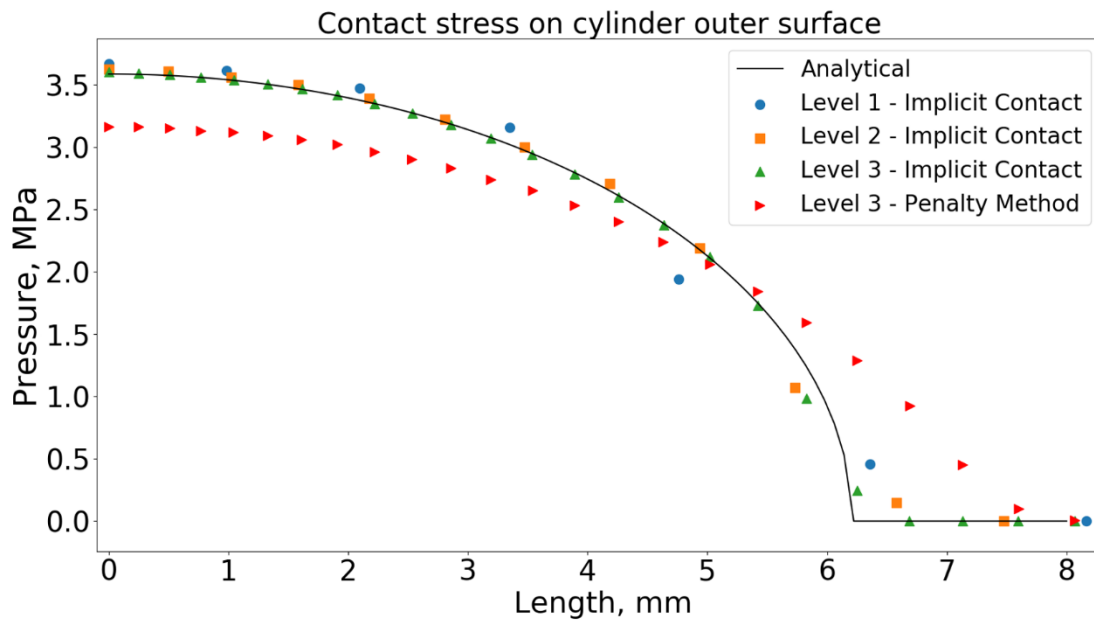


Figure 6.10 – Two-dimensional punch test: contact stresses on the cylinder outer surface.

The difference in performance is even more striking. While the simulation with the penalty-based boundary condition lasted for ~ 4.5 hrs, the residual threshold is reached in only ~ 30 s when using the implicit contact methodology on the finest mesh refinement level, with a speedup of $\sim 800\times$. The superior convergence properties for the benchmark case under examination are apparent also from Figure 6.11, where the residuals of the x- and y-components of the displacement field are plotted against the number of iterations of the linear solver (the residuals are limited to the first 2000 iterations for the simulation with the penalty-based boundary condition). The oscillations seen within the first 100 iterations on the implicit contact residuals should be investigated more, although they are probably the result of adjacent face centers approaching contact.

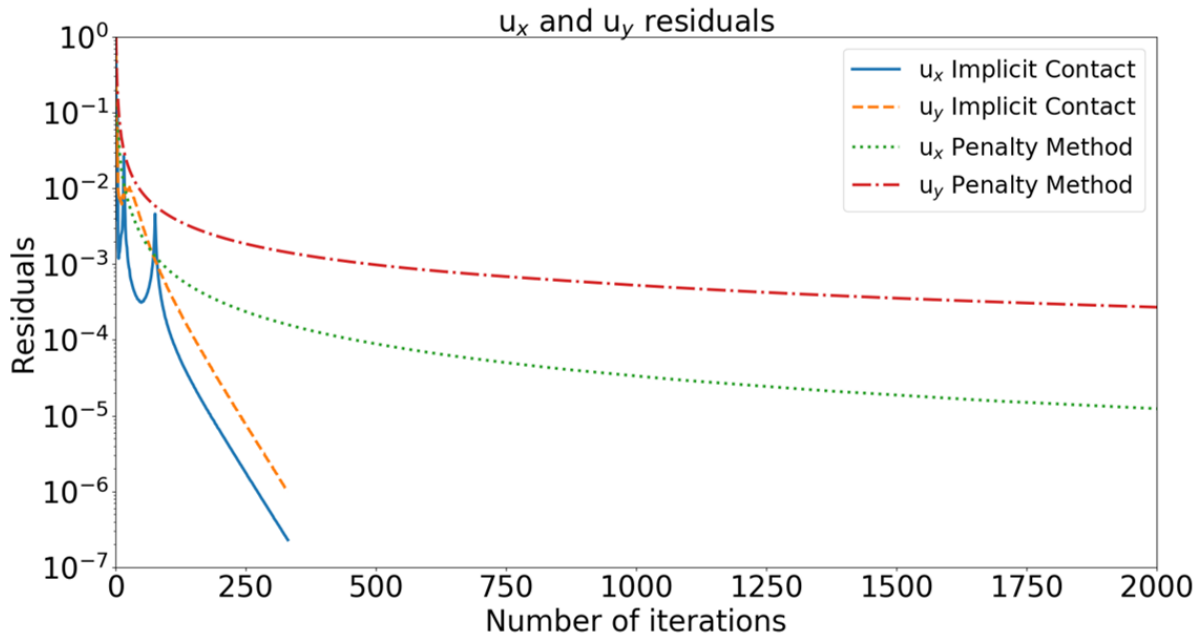


Figure 6.11 – Residuals against number of iterations for Case 3 on the finest mesh. Residuals are shown both for the implicit contact and penalty-method based boundary conditions.

6.1.5 Contact benchmarks: 3-D punch test with rounded edge

The last verification case is another linear-elastic punch test from the NAFEMS benchmark series. This time, the punch is a steel cylinder characterized by a rounded edge on its base and pressed with a constant pressure of 100 MPa against a cylindrical aluminum foundation. The setup and its main dimensions are shown in Figure 6.12, while the material properties for aluminum and steel are the same used in the previous benchmark (Case 3). This punch test has been studied in the past by several authors [123] [124], notably by Cardiff in [81] using a FV contact stress solver based on the penalty method.

As the case is axisymmetric, it is reproduced with a 2-D *wedge* geometry. The model is discretized with a mesh made of triangular prisms using 3 refinement levels, from Level 1 to Level 3, for a total number of cells of 1'389, 4'059, and 14'731, respectively. All computational models are created with the Salome platform [99] using the NETGEN algorithm, and are progressively refined in the region closer to the punch rounded edge, as shown in the detail in Figure 6.12 for the finest mesh. Regarding the settings for the sigmoid blending function, the relative offset is set to zero and the half-width is set to 0.1 for all the simulations, leading to an average relative interpenetration (with respect to the cell size) of $\sim 5 \cdot 10^{-4}$ on the finest mesh. The sigmoid function is truncated to limit the emergence of spurious positive traction forces along the rounded edge.

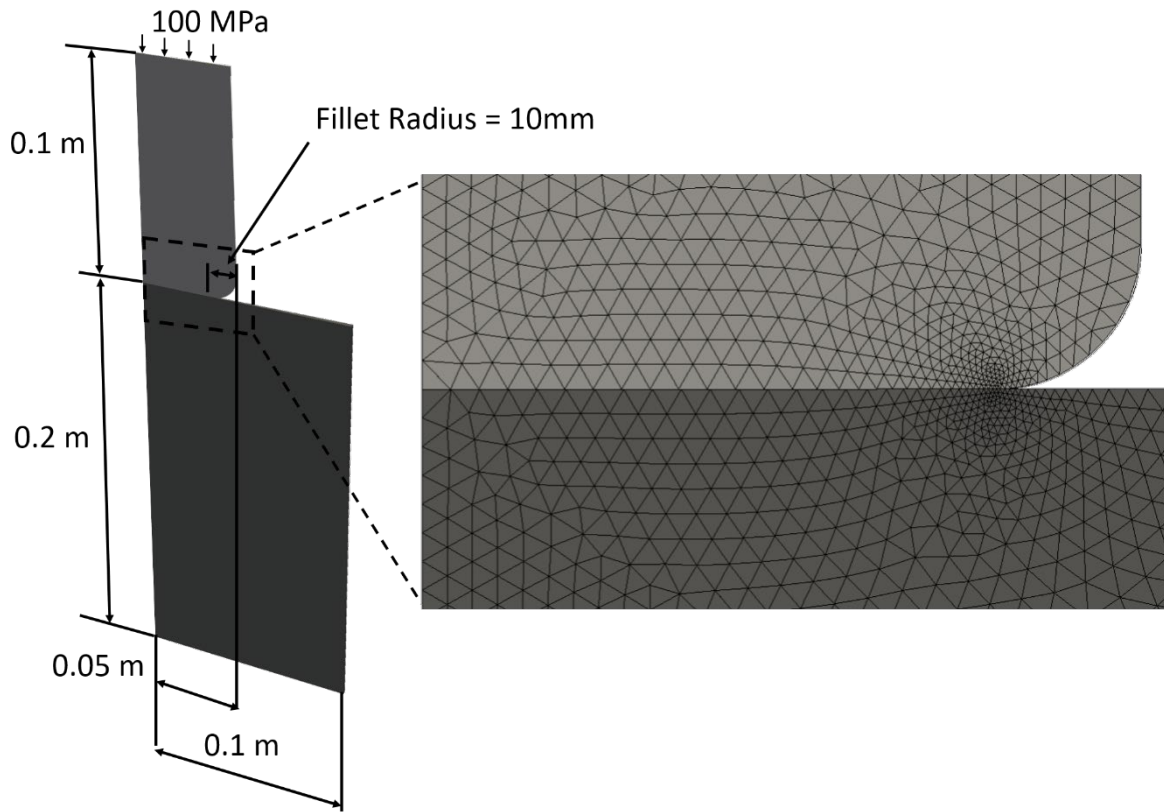


Figure 6.12 – Punch test with rounded edge, 2-D wedge model: main dimensions (left) and detail of the finest mesh (Level 3) near the contact area (right).

The benchmark is reproduced twice, first as a frictionless contact case and then considering a friction coefficient α equal to 0.1. The reference solution for both conditions is obtained with Code Aster [125] on the highest mesh refinement level or Level 3.⁵ Only for the frictionless case, we perform an additional simulation for each mesh refinement level employing a boundary condition based on the penalty method and using a standard penalty factor of 0.1.

The three following graphs show the axial displacement (Figure 6.13), the contact stress (Figure 6.14) and the axial displacement (Figure 6.15) calculated along the top horizontal edge of the foundation. These plots also include the reference solution from Code Aster and the solution obtained with the penalty method (although only for the finest mesh). To avoid overcrowded graphs, the results for the frictionless contact case (left part of the figures) and those for the frictional contact (right part of the figures) are displayed separately.

⁵ The reference documents [122] [123] [124] report a slightly different solution if compared to the Code Aster results presented in this thesis. This discrepancy is due to the much coarser mesh used in the mentioned publications. Before the preparation of this paper, by running Code Aster on the two finest mesh refinement levels (Level 2 and Level 3), it was verified that the mesh used to obtain the results presented in [122], [123] and [124] is relatively coarse and the solution therefore not fully converged.

The figures reveal that, at least for this benchmark, the accuracy of the implicit contact methodology proposed in this work compares well against the more traditional penalty method. The results are also in line with those obtained by Cardiff with his FV penalty method contact stress solver [81], although the convergence rate shown in this work might seem faster due to the use of local refinement at the edges of the contact region.

From the figures we can also deduce that the results of the implicit contact methodology approach the reference solution from Code Aster with increasing mesh refinement. Some minor differences seem to remain, however, as it emerges from a closer look at the radial displacement curves. Indeed, the implicit contact method (in agreement with the penalty method) predicts a sharper and more peaked profile where the rounded edge touches the foundation, both for the frictionless and frictional contact cases. It is difficult to identify the main reason for these differences, as the reference solution is not analytic. It is likely, however, that this is simply due to numerical differences that will become smaller as the mesh is further refined in both codes.

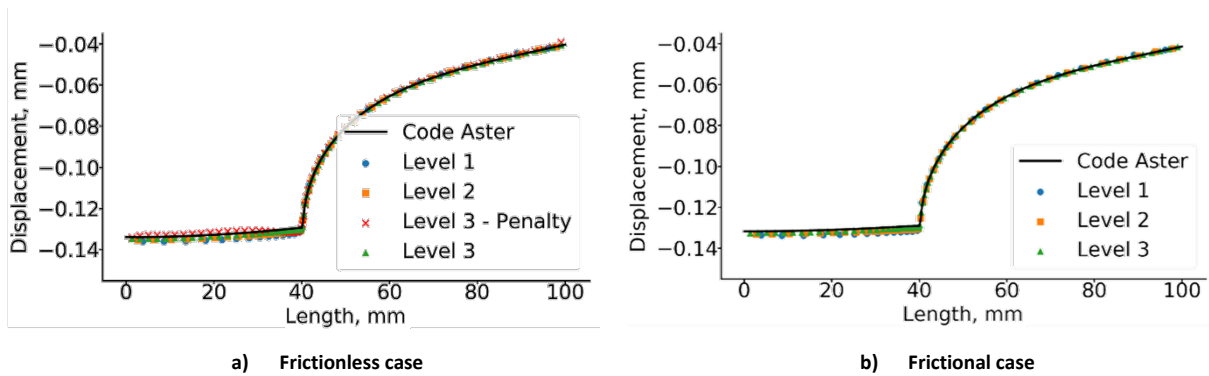


Figure 6.13 – Punch test with rounded edge, axial displacement on the foundation top edge. On the left, the results obtained for the frictionless contact case. On the right, the results obtained with a friction coefficient equal to 0.1.

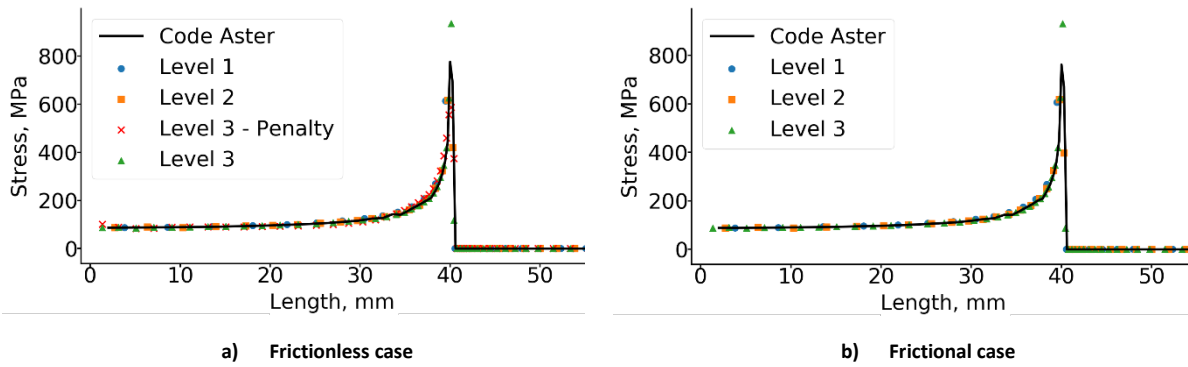


Figure 6.14 – Punch test with rounded edge, contact stress on the foundation top edge. On the left, the results obtained for the frictionless contact case. On the right, the results obtained with a friction coefficient equal to 0.1.

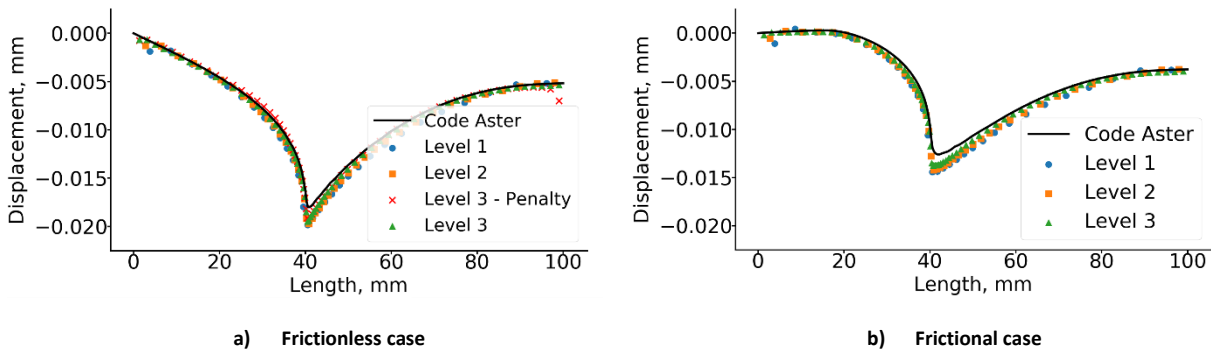


Figure 6.15 – Punch test with rounded edge, radial displacement on the foundation top edge. On the left, the results obtained for the frictionless contact case. On the right, the results obtained with a friction coefficient equal to 0.1.

Regarding the difference in performance between the penalty and implicit contact methods for the FV-based stress solver, the implicit methodology consistently proves to converge more quickly. Table 6.2 summarizes the running time required by the two methods on the three mesh refinement levels (the comparison can be done for the frictionless case only). The table also indicates the speedup provided by the implicit contact method, which varies between 4.7 for the coarsest mesh to 3.5 for the finest mesh. These values, although considerably smaller than those obtained for the previous punch test benchmark (Case 3), are still quite significant. Incidentally, the decrease in performance gain with increasing mesh refinement is expected, considering that the ratio of the number of boundary faces to the total number of cells ratio decreases. Each simulation was performed on an Intel Xeon CPU E5-1660 v4 with eight 3.2 GHz cores, using a single core. A relaxation factor of 0.999 for the equation solution was necessary to reach convergence when

employing the penalty-based boundary condition, while a relaxation factor of 0.9 for the displacement field was used to stabilize the solution with the implicit contact methodology.

Table 6.2 – Punch test with rounded edge: running times for the frictionless case on wedge geometry. The results are shown for each mesh refinement level (the number of cells and the number of faces is indicated) both for the implicit and penalty method.

Mesh refinement	Level 1	Level 2	Level 3
Number of cells	1389	4059	14'731
Number of faces on foundation top	31	43	70
Implicit contact running time	3 s	7 s	33 s
Penalty method running time	14 s	28 s	115 s
Speedup	4.7x	4x	3.5x

To test the applicability of the methodology for 3-D geometries, the frictionless punch test is performed once again using 3-D computational models. This time, the three refinement levels contain a total of 13'211, 33'645 and 131'142 cells, from Level 1 to Level 3 respectively. Both the implicit contact and penalty method boundary conditions are used, so that the computation time can be compared also for a 3-D simulation. To save computational resources, the model includes only a quarter of the geometry, making use of the symmetry of the setup. The mesh, shown in Figure 6.16 for the highest refinement level, is composed mainly of tetrahedral cells and it is generated with the NETGEN algorithm from the SALOME platform.



Figure 6.16 – Punch test with rounded edge: three-dimensional computational model for the finest mesh refinement level.

The results of the 3-D simulations compare well against the solutions obtained previously on the 2-D wedge geometry. As an example, Figure 6.17 shows the axial displacement along the horizontal top edge of the foundation calculated on the most refined 3-D mesh. For comparison, the figure includes the profiles obtained with Code Aster and with the implicit contact algorithm on the most refined 2-D wedge model.

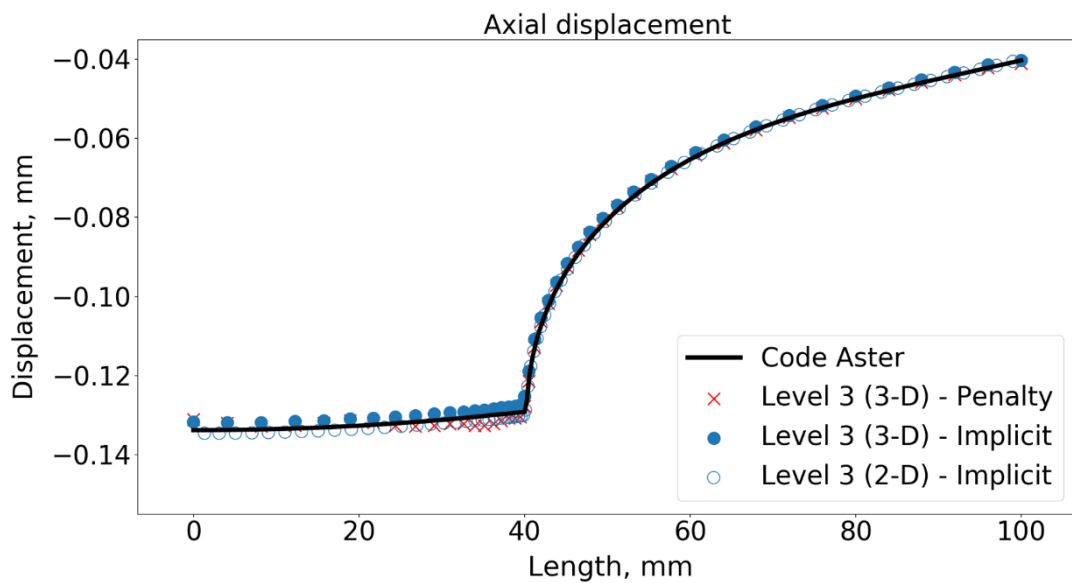


Figure 6.17 – Punch test with rounded edge: axial displacement on foundation top horizontal edge calculated with the most refined 3-D model. The reference solution calculated with Code Aster on a 2-D wedge model (and the respective implicit contact 2-D solution) are included in the graph.

Finally, as done for the 2-D wedge models, we report the running time required for the 3-D simulations in Table 6.3. The gain in performance guaranteed by the implicit contact method is larger than for the respective 2-D cases, although it is even more sensitive to mesh refinement. This confirms that the speedup given by the implicit methodology is case and mesh dependent.

Table 6.3 – Punch test with rounded edge: running times for the frictionless case on 3-D geometry. The results are shown for each mesh refinement level (the number of cells and the number of faces is indicated) both for the implicit and penalty method.

Mesh refinement	Level 1, 3-D	Level 2, 3-D	Level 3, 3-D
Number of cells	13'211	33'645	131'142
Number of faces on foundation top	862	1'976	4'854
Implicit contact running time	15 s	72 s	535 s
Penalty method running time	661 s	1328 s	5205 s
Speedup	44.1x	18.4x	9.7x

6.1.6 Plasticity benchmark

The implementation of a rate-independent plasticity model in OFFBEAT was discussed in Section 5.9. A simple verification case is provided by the NAFEMS 3D plasticity benchmark [126]. It consists of a uniform cube of 1 mm length, subjected to a 12-step displacement history: the block is expanded alternatively in the three Cartesian directions during the first 6 steps, and then is compressed back to the original shape in the following 6 steps, with the material undergoing elastoplastic deformations. Two cases are considered: perfect plasticity and linear hardening. The yield stress is 5 MPa, the Young's modulus is 250 GPa, while the plastic hardening modulus is 50 GPa.

The geometry (which in the NAFEMS benchmark is modeled with a single QUAD-4 element) is replicated in OFFBEAT both as a single cell and with a 10x10x10 mesh and the two cases provide the same results (the weighted average stress is calculated in the case of the denser mesh). The three normal components of the stress tensor obtained with OFFBEAT are plotted for the perfect plasticity case in Figure 6.18, with the reference values extracted using WebPlotDigitizer [127]. Addition-

ally, the benchmark documents provide the numerical value of the stress components only for the 6th step. These values are reported in Table 6.4 where they can be compared against the (identical) results provided by OFFBEAT. Similar results are obtained for the linear-hardening case.

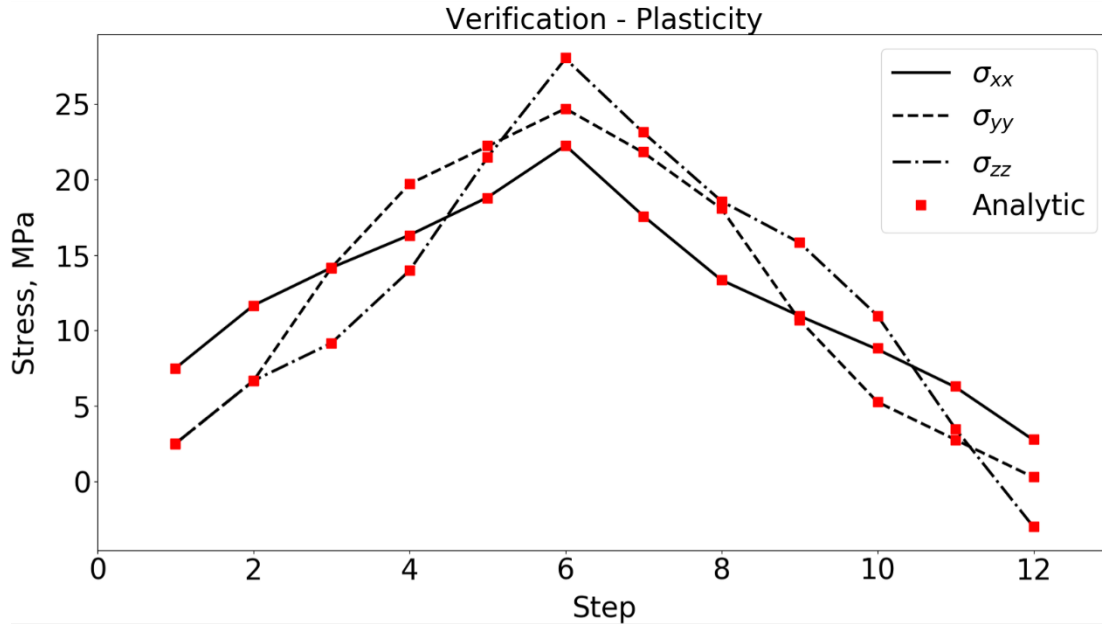


Figure 6.18 – Radial, tangential, and axial stresses for the plasticity benchmark case. Both the reference values and the results obtained with OFFBEAT are shown.

Table 6.4 – Plasticity verification case: stress components at the end of step 6.

Stress components	Reference Benchmark	OFFBEAT
σ_{xx}	22.27	22.27
σ_{yy}	24.70	24.71
σ_{zz}	28.03	28.02

6.1.7 Creep benchmark

The implementation of the Limbäck creep model in OFFBEAT discussed in Section 5.9 can be verified against the numerical benchmark proposed in the work of Liu et al. [111]. The case consists of a cladding segment irradiated for $1 \cdot 10^5$ seconds under uniform temperature and constant neutron flux. The pressure is higher on the outer side and the case is in plain stress, i.e. the axial stress is zero, and due to the operation time span considered the neutron fluence is assumed to be zero. The case setup is shown in Table 6.5.

Table 6.5 – Creep benchmark setup.

Parameter	Value
Inner Radius, mm	5.0
Outer radius, mm	5.5
Inner pressure, MPa	1.0
Outer pressure, MPa	15.5
Temperature, K	650
Neutron flux, $\frac{n}{\text{cm}^2 \cdot \text{s}}$	10^{14}

The cladding segment is reproduced as a single wedge cell, made of 8 nodes or vertices. A constant time step of $1 \cdot 10^4$ seconds was used, for a total of ten time steps. The main results obtained with OFFBEAT are summarized in Table 6.6 where they are compared to the corresponding analytical solution. As it can be seen, the code is able to accurately replicate the analytical values with relative errors lower than 0.1%.

Table 6.6 – Creep verification case: results compared against analytical solution [111].

Parameter	Analytical Solution	OFFBEAT
Irradiation creep rate, s^{-1}	$3.08 \cdot 10^{-10}$	$3.08 \cdot 10^{-10}$
Thermal creep rate, s^{-1}	$77.82 \cdot 10^{-10}$	$77.86 \cdot 10^{-10}$
Primary creep	$3.527 \cdot 10^{-3}$	$3.529 \cdot 10^{-3}$
Creep strain, effective	$4.336 \cdot 10^{-3}$	$4.339 \cdot 10^{-3}$
Creep strain, radial	$1.987 \cdot 10^{-3}$	$1.990 \cdot 10^{-3}$
Creep strain, azimuthal	$4.331 \cdot 10^{-3}$	$4.334 \cdot 10^{-3}$
Creep strain, axial	$2.344 \cdot 10^{-3}$	$2.344 \cdot 10^{-3}$

6.2 Validation

Comprehensive validation campaigns have been carried out in the past for several fuel performance codes, e.g. for FRAPCON [128], for TRANSURANUS [129] or for BISON [130]. Usually, the focus is on the so-called integral measurements. These are experimental results that are intrinsically 1-D if not 0-D such as the fuel centreline temperature (FCT), the gap pressure and the rod free volume, the cladding elongation, and the fission gas release (FGR) fraction.

The validation of OFFBEAT is an ongoing process. The main efforts carried out as part of this thesis are presented in this section and are focused exclusively on the FCT and FGR fraction for several rods from the IFPE database. Two additional experiments, namely the HBRP and the IFA-701, have been reproduced with OFFBEAT but they are discussed more in details in Chapter 7 followed by a 3-D analysis of the impact of eccentricity on fuel disc irradiation tests.

A validation step that focuses on classical 1-D quantities such as the FCT is necessary even for a high-fidelity tool as it allows to test the accuracy of the code without the complications added by poorly known phenomena and allows for a comparison with other codes. Also, the validation of the fuel temperature is essential for any fuel performance code as it affects all other models and material properties, and it is essential for assessing the safety of the rod.

An important future validation step will be the comparison against experimental data that show intrinsically multi-dimensional features. A multi-dimensional validation of OFFBEAT is ongoing and aims at comparing the cladding ridge pattern emerging at the end power transients for some IFPE rods against the experimental cladding profilometry. These ongoing efforts are part of the international collaboration with the JRC-Ka and the development of a coupling strategy with the TRANSURANUS code, as discussed in more details in Chapter 8.

6.2.1 IFA-562.1

The analysis of the IFA-562.1 provides the opportunity to validate OFFBEAT for rods in the low burnup range. These are not significantly affected by burnup effects such as fuel swelling or by fission gas release. Instead, accurate temperature predictions require models for fuel densification and relocation, and correlation for the temperature dependence of the fuel thermal conductivity. Also, the gap behavior model needs to correctly track the change of the gap width and its effect on the heat transfer.

The IFA-562.1 consisted of 12 instrumented rods and was irradiated in the HBWR from 1987 to 1989 up to a burnup of ~ 10 MWd/kgU. The rods were equally divided between a lower and an upper cluster of 6 rods fabricated by two different manufacturers. Each cluster contained a pair of rods filled with helium, while the remaining 4 were filled with xenon. All rods were instrumented with two thermocouples (TCs) at the top and bottom of the fuel stack to measure fuel centerline temperature and with extensometer to measure cladding elongation. As the experiment was designed primarily to study the effect of pellet surface roughness on LWR fuel rod performance, the rods contained either smooth or rough pellets. To better isolate the effect of surface roughness,

the rods were fabricated with a small initial gap to favor gap closure and were irradiated at low power to limit fission gas release. The base irradiation was followed by a short ramp to investigate the fuel grain growth during power transients.

All the 12 rods from the IFA-562.1 are reproduced with OFFBEAT. The predicted temperatures are compared against the respective measured values in Figure 6.19 and Figure 6.20 for the lower and upper cluster, respectively. For clarity of exposition, the results are reported only for the lower thermocouples. The dotted and dashed lines correspond to a commonly accepted $\pm 10\%$ relative error.

Besides a few outliers, the bulk of the data points fall between these two $\pm 10\%$ error lines. A partial overpredicting bias can be noted for the xenon filled rods of the lower cluster. This might be due to a systematic error in the axial power distribution that could affect differently the results in the two clusters (placed one on top of each other in the experimental reactor). Besides the difference in results between lower and upper cluster, it seems that the FCTs for the He-filled rods compare much better with the results than those of the Xe-filled rods, but the origin of the systematic overprediction is difficult to ascertain and could be studied more in detail. However, the predictions should be considered satisfactory given the modeling uncertainties. Important parameters such as the fast flux or the fuel densification had to be approximated because they were missing from the main documents of the experimental campaign. Also, as noted in [131], when analyzing rods from this or other experimental campaigns there is often an inherent scatter in the data as one can find rods with similar irradiation conditions and characteristics but different measured temperatures.

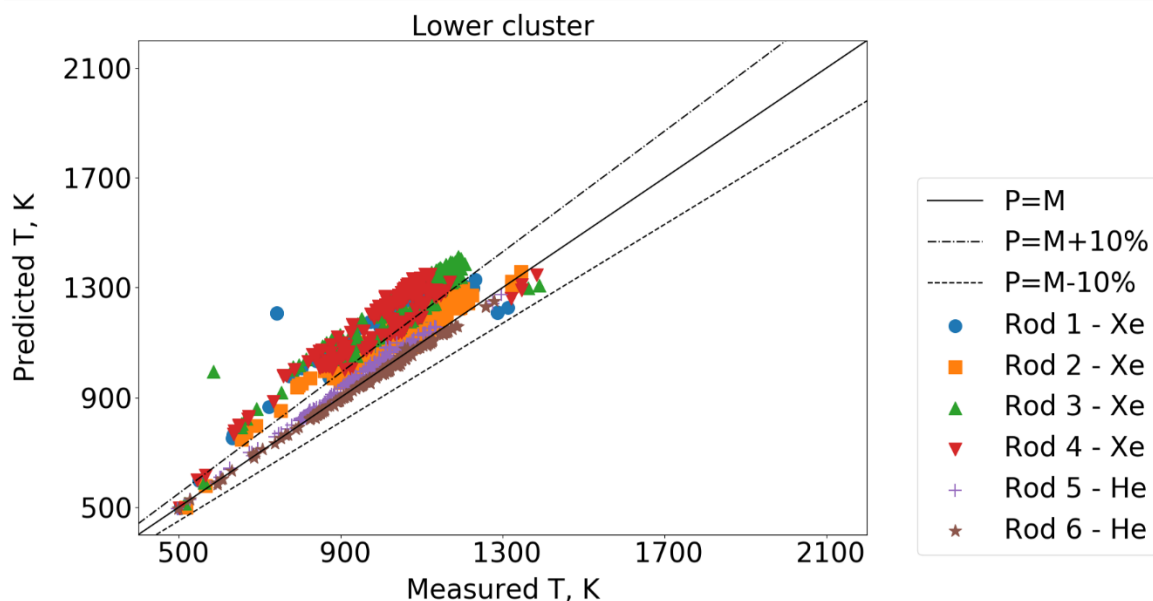


Figure 6.19 – Predicted temperature against measured temperature for the lower cluster rods of the IFA-562.1. The burnup varies from 0 to ~ 10 MWd/kgU. Only the values of the lower TCs are reported in the graph.

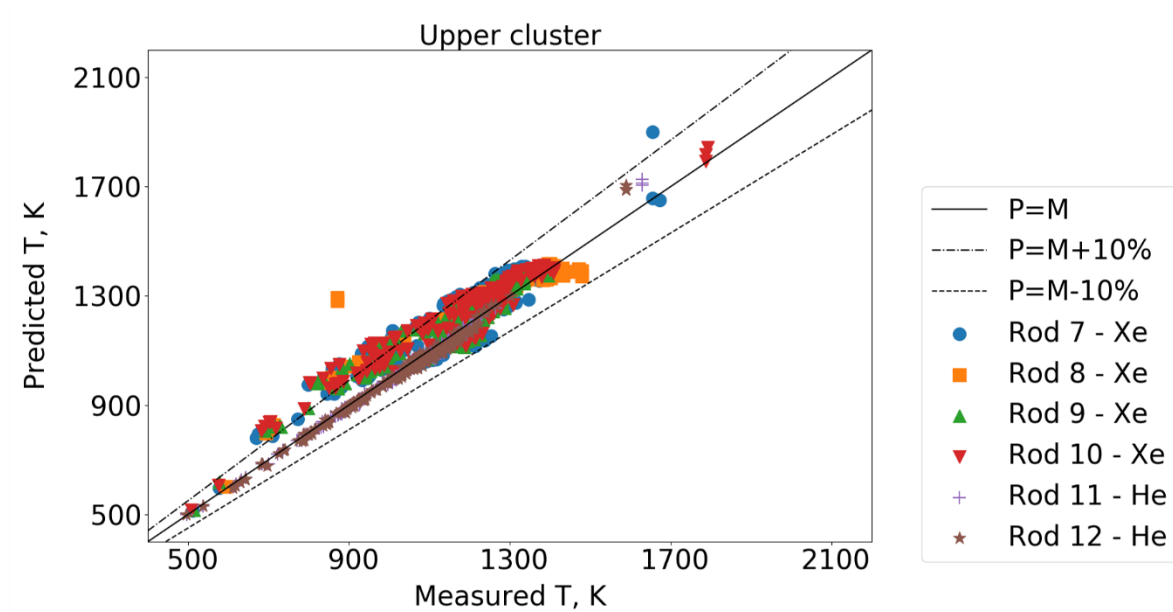


Figure 6.20 – Predicted temperature against measured temperature for the upper cluster rods of the IFA-562.1. The burnup varies from 0 to ~10 MWd/kgU. Only the values of the lower TCs are reported in the graph.

6.2.2 IFA-432

The analysis of the IFA-432 contributes to the validation of OFFBEAT for rods in the medium burnup range. The accurate prediction of the thermo-mechanical response depends mainly on the code's ability to capture higher burnup effects such as the fuel swelling, the fission gas release, the cladding creep-down and the fuel thermal conductivity degradation.

The IFA-432 consisted of 6 rods that were irradiated for several years in the HBWR in Norway. The experiment was designed to study the thermal and mechanical response of BWR fuel, up to a burnup of approximately 40 MWd/kgU. The rods were instrumented to monitor fuel centerline temperatures, cladding elongations, internal fuel rod pressures and local power. The fuel centerline temperature was measured with two TCs inserted through central holes in the bottom and top ends of the fuel stack.

Only the bottom TCs survived the irradiation, and no data related to Rod 4 is available due the failure of its instrumentation and its early discharge. Rod 1, Rod 2 and Rod 3 used a 95% dense fuel, stable to densification, i.e. the densification was limited to 0.3% of the theoretical density. While Rod 1 followed closely the geometrical design of commercial BWR rods, Rod 2 was characterized by a large gap to simulate instantaneous densification [132]. Rod 3, on the contrary, was designed primarily as a check for the rod powers and to reproduce the behavior of high burnup rods where the gap is closed. Thus, Rod 3 had a small initial gap that closed at soon as the rod went to power. Rod 5 and Rod 6 had the same dimensions of Rod 1 but used a 92% dense fuel:

Rod 5 contained a fuel stable to densification, while the fuel used in Rod 6 was expected to densify up to 3% of the theoretical density. As done in other studies [69], [133], Rod 2 and Rod 6 are excluded from this validation efforts as they do not represent typical fuel used in commercial LWR and the models used in fuel performance codes might not be suited for their analysis.

The calculated fuel centerline temperature for Rod 1, Rod 3 and Rod 5 are shown in Figure 6.21 where they are compared against the respective measured values. As done for the previous figures, two lines are added corresponding to a $\pm 10\%$ relative error. The comparison between the measured and predicted temperature appears to be satisfactory, considering in particular important sources of uncertainties such as the exact position of the thermo-couple and the fact that the description of the experiment only provides ranges for the value of the grain radius and that it was arbitrarily decided to employ the average value in this range. Another important source of uncertainty might derive from the grain size used in the simulations. Indeed, the campaigns document reported for each rod three very different values of grain size: one for the fuel periphery, one for the pellet mid-section and one for the central part of the fuel. In absence of more precise information, the average value was used. A more detailed analysis could be done in the future by considering an upper and lower limit for the grain size, thus enveloping the experimental data.

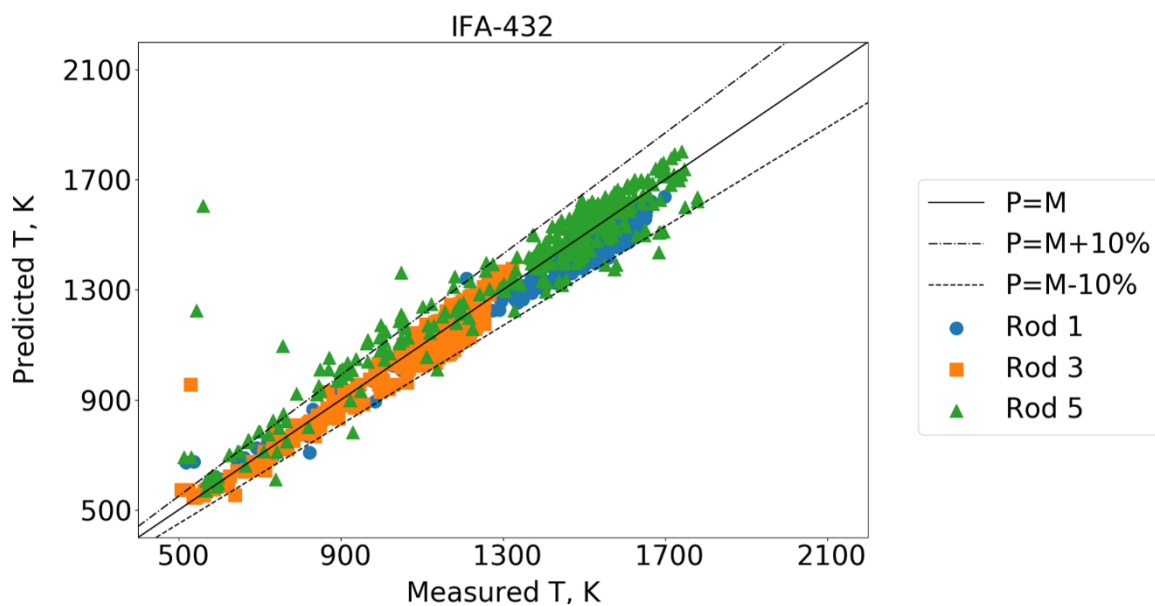


Figure 6.21 – Predicted temperature against measured temperature for Rod 1, Rod 3 and Rod 5 of the IFA-432. The burnup varies from 0 to ~ 40 MWd/kgU.

6.2.3 Super Ramp

The Studsvik Super-Ramp project lasted from 1980 to 1983 and aimed at investigating the failure propensity of LWR fuel rods subjected to power ramps. In particular, the PWR subprogram con-

sisted of 6 groups of rods with different designs, that were first base irradiated in the Obrigheim power reactor in Germany, at time-averaged power ratings of approximately 14 to 26 kW/m, and then ramp tested in the research reactor R2 at Studsvik in Sweden [18].

Out of the 28 rods that were part of the PWR subprogram, only 11 are considered in this chapter. These rods belonged to 3 separate groups, named PK1, PK2 and PK6. The first two groups were composed of standard fuel rods that sustained the power ramping without failures, despite large deformations and significant FGR. The rods of group PK6 featured large grain size, leading to a lower FGR if compared to groups PK1 and PK2. One rod, the PK1-6, failed and considerable fuel-to-clad bonding was revealed by the PIE. The 11 PWR rods were chosen following the example of previous works performed with the TRANSURANUS and BISON code [134]. In future campaigns, it would be interesting to extend the validation database to include the rods of the BWR subprogram from the Super-Ramp project.

The integral FGR calculated at the end of irradiation is compared to the measured values. The integral FGR corresponds to the ratio of the fission gas released in the fuel rod free volume to the generated gas. The results are shown in Table 6.7 and plotted in Figure 6.22 with the two dashed lines representing typical deviations of a factor of 2 from measured data [135]. The comparison can be considered satisfactory with OFFBEAT providing good prediction for most rods, notably considering the large deviations in predictions that are typically observed in the literature [134].

Table 6.7 – Comparison between calculated and measured integral FGR for PK and AN rods.

Fuel rod	Experiment	Average burnup (MWd/kgU)	FGR measured (%)	FGR calculated (%)
PK1-1	Super-Ramp	35.4	8.5	13.9
PK1-2	Super-Ramp	35.6	13.6	15.7
PK1-3	Super-Ramp	35.2	22.1	18.5
PK1-4	Super-Ramp	33.1	13.0	15.5
PK2-1	Super-Ramp	45.2	28.0	18.9
PK2-2	Super-Ramp	45.1	32.1	23.9
PK2-3	Super-Ramp	44.6	44.9	26.8
PK2-4	Super-Ramp	41.4	9.5	11.4
PK6-2	Super-Ramp	36.8	3.5	3.3
PK6-3	Super-Ramp	36.5	6.7	3.6
PK6-S	Super-Ramp	35.9	6.1	3.2
AN2	Risø-3		29.7	24.9
AN3	Risø-3		35.5	34.5

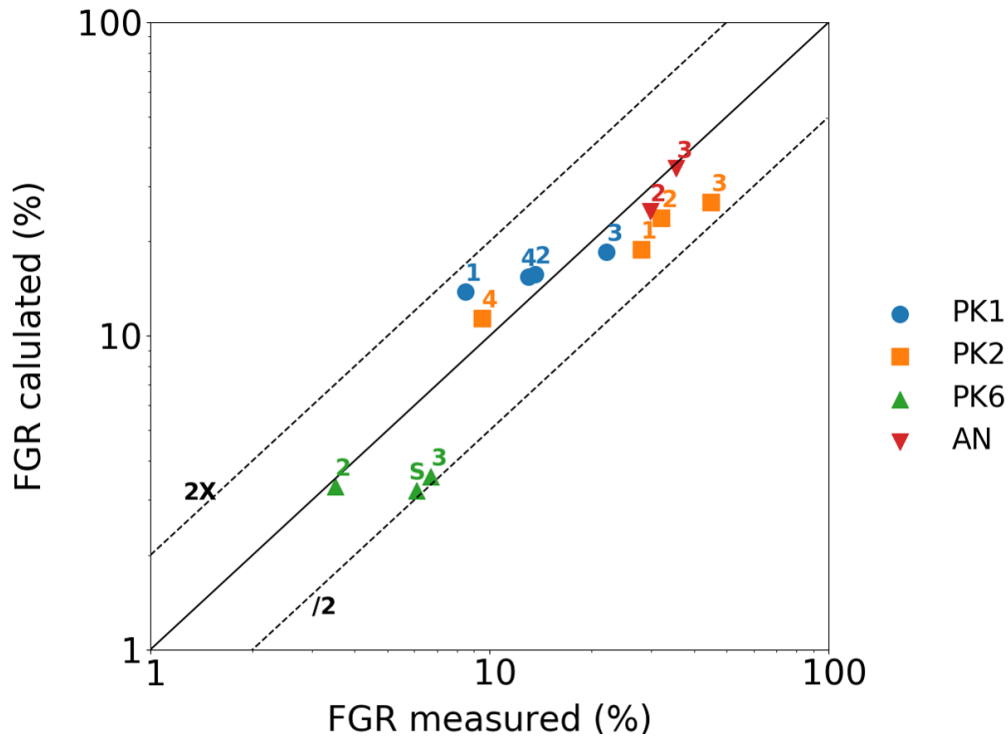


Figure 6.22 – Plot comparing calculated and measured FGR fraction for PK and AN rods.

6.2.4 Risøe AN3 and Risøe AN2

The Risø-3 is the last in a series of 3 bump test programs performed in the DR3 test reactor at Risø in Denmark. The experiment took place from 1986 to 1990 and investigated the fission gas release and microstructural changes of several rods, many of which were refabricated and re-instrumented. The two segments AN2 and AN3 considered in this Section were first base irradiated in the Biblis A PWR in Germany from 1982 to 1986, reaching a final burnup of approximately 40 MWd/kgU, before being bump tested during 72 hours in the test reactor DR3 at Risø in Denmark, under PWR conditions [19], [20].

After the base irradiation, the AN2 rod segment was neither punctured nor opened for refabrication. On the contrary, the AN3 rod segment was refabricated prior to the bump testing: in particular, the fuel segment was shortened, drilled at the top and refilled with helium at 14.7 bar. The segment was instrumented with a pressure transducer and a fuel centerline thermocouple, allowing to measure the temperature at a point situated 1.5 pellet lengths above the bottom of the thermocouple hole [21]. After the 72 hours ramp test, that reached a peak power around 40 kW/m and a final burnup around 41.8 MWd/kgU, the segments were punctured and the total FGR fraction was measured.

Figure 6.23 illustrates the difference between the measured and calculated FCTs during the bump test of rod AN3. The 2 profiles are in very good agreement, though some discrepancies can be observed after the power ramps, where the experimental temperature slightly decreases while the

OFFBEAT temperature remains flat. However, this type of discrepancy was observed also during the Coordinated Research Project on Fuel Modelling at Extended Burnup (FUMEX-II) sponsored by the IAEA [136]. A possible explanation might be found in the improper modeling of fuel creep that could cause the pellet to expand after each sudden power increase, decreasing the gap-width and the fuel temperature.

The comparison between the calculated final FGR ratios for segments AN2 and AN3 and the values obtained via rod puncturing are included in Table 6.7 and in Figure 6.22. Also, the time-evolution of the FGR ratio for AN3 is compared against the one experimentally deduced from the pressure transducer in Figure 6.24. The results are satisfactory as they are very close to their experimental counterpart. Thanks to the capabilities of the SCIANTIX model, OFFBEAT is able to well replicate the dynamics of the transient, even capturing the sudden increase in release at around 50hrs of ramp test.

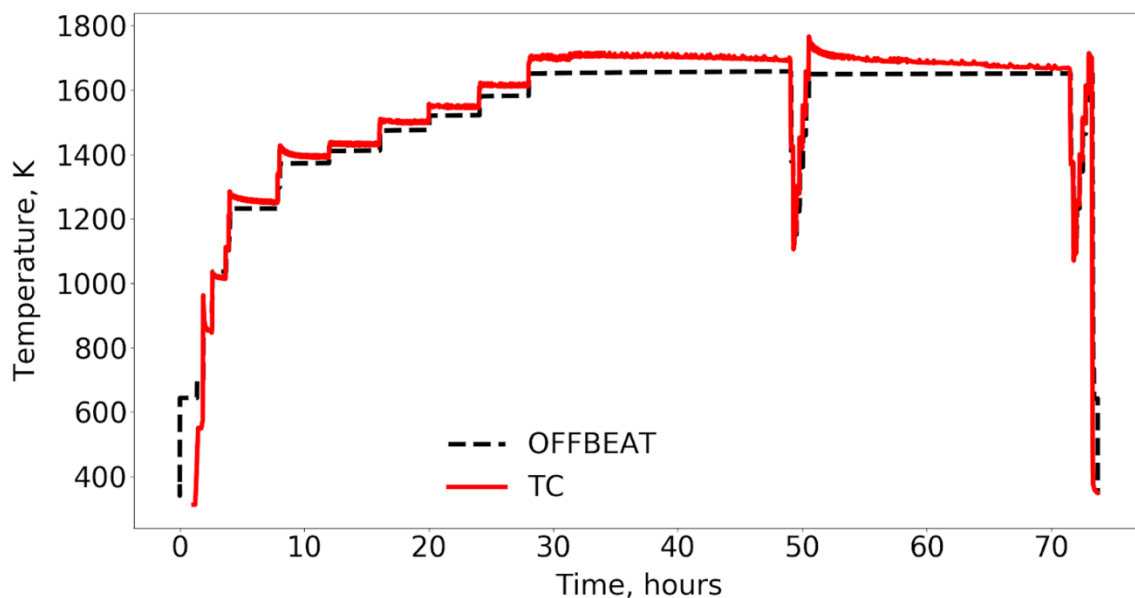


Figure 6.23 – Comparison between the FCT measured during the experiment and the FCT calculated by OFFBEAT for the Risoe3 AN3 segment.

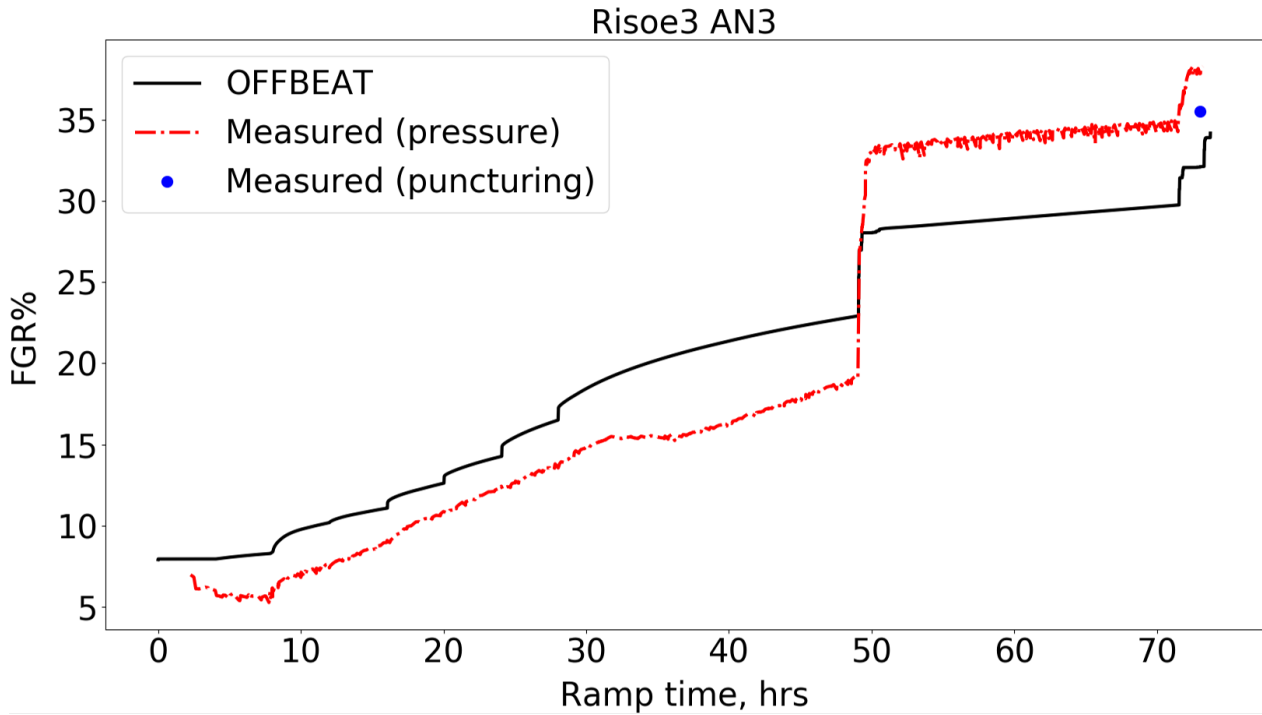


Figure 6.24 – Comparison between the FGR% measured during the experiment (from pressure transducer and from puncturing) and the one calculated with OFFBEAT for the Risoe3 AN3 segment.

6.3 Multi-dimensional demonstration cases

Multi-dimensional case-studies are a useful tool to test the capabilities of the code to capture relevant 2-D or 3-D features in a realistic scenario. It must be stressed that these demonstration cases are significantly simplified with respect to real irradiation histories and cannot be considered as a substitute for validation. They are useful to check the convergence properties and the capabilities of the code without the complication of a proper validation campaign. Two interesting examples of multi-dimensional test cases are presented in this section.

6.3.1 RIA scenario with MPS defect

The first test case mimics the thermo-mechanical during a RIA scenario. A total energy of ~500 kJ/kg is released in the fuel as a square power pulse of 40 ms. An alternative and more realistic approach would consider a Gaussian function in substitution of the square pulse. The transient is then followed for a total duration of 50s to allow the fuel to heat up, expand and finally cool down. The case consists of a short 3-D rodlet with the dimensions and specifics reported in Table 6.8 and containing a missing pellet surface defect. This represents an important testing ground for the code's ability in handling 3D asymmetries in a plastic framework.

Table 6.8 – Dimensions and specifics for the RIA scenario test case

Parameter	Value
Pellet height	10.3 mm
Cladding inner radius	4.4 mm
Cladding outer radius	5 mm
Gas	He at 1 atm
Energy released	~500 kJ/kg
Pulse duration	40ms
Fuel material	UO ₂
Pellet height	10.3 mm

For simplicity, the transient takes place at fresh conditions, with the rod at a uniform initial temperature of 573 K. This allows to neglect fuel swelling, densification and relocation, cladding creep as well as the effect of burnup and fission gas release on the material properties and gap conductance. However, the effect of tangential friction forces due to the presence of multiple pellet fragments that are known to appear already during the first rise to power would probably heavily influence the results of this analysis. A more accurate study could be performed in the future with a 3-D simulation of pellet fragments, as done by Michel et al. [137].

The rate-independent plasticity model is used solely for the cladding, with a yield stress of 500 MPa and with the assumption of perfectly plastic behavior. The outer cladding temperature is calculated using a constant heat exchange coefficient with the cooling water, assumed at a constant temperature of 573 K. Following the example of [138], the study of the cladding strain and stresses in the presence of a fuel defective surface could be extended in the future by considering a more complex and realistic irradiation history, including burnup effects such as cracking, relocation, swelling and fission gas release.

To reduce the computational cost of the simulation, the short rodlet is composed of only 5 pellets plus the surrounding cladding. The height of the cladding in the model is larger than that of the pellet column so that it can be ensured that, at any moment, the expanding fuel pellets face a portion of the cladding geometry. The standard OpenFOAM symmetry boundary conditions are used on the top and bottom patches to represent an infinitely long rod. Because the rod is fresh, fission gas release does not take place during the transient. This reduces the errors introduced by limiting the geometry to a small section of the rod. The gap conductance model derived from FRAPCON

and the penalty-based contact boundary condition are used to treat the gap heat transfer and the fuel-to-cladding contact, respectively.

The 3D OFFBEAT model is shown in Figure 6.25 with a detail of the mesh in the defective region. The missing surface is located on the central pellet and has a constant depth of 0.1 mm. The pellet chamfers and dishes are also reproduced, but the pellets are continuously connected through the flat portion or land between the dish and the chamfer. This allows to neglect the contact between pellets (simplifying the convergence of the solution) but certainly has some impact on the stress and strain distribution. However, an appropriate assessment of such impact is outside the scope of the test case presented in this section.

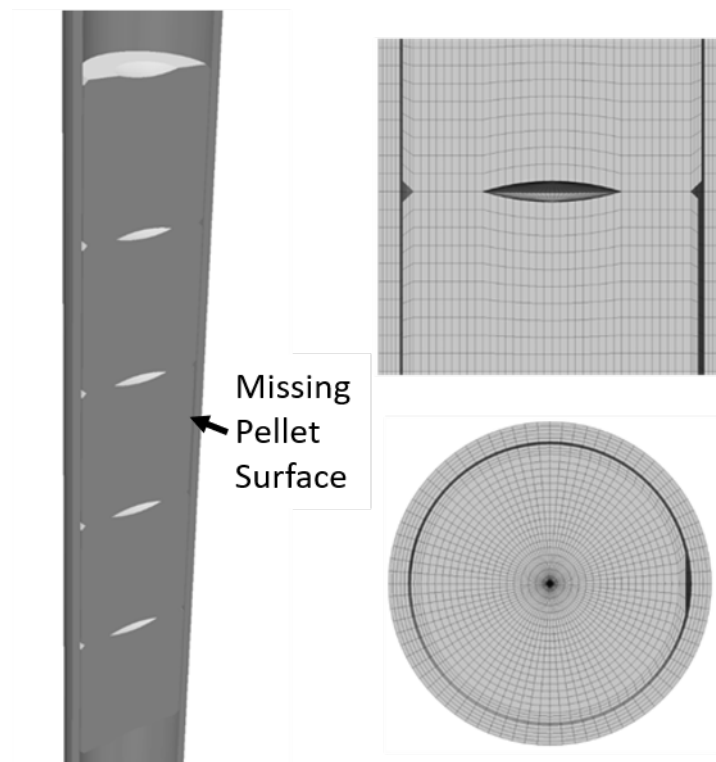


Figure 6.25 – RIA scenario test case: 3-D model of short rodlet with 5 pellets and a missing pellet surface defect. The two detailed views on the right show the defective region as well as the mesh.

The case was simulated on a desktop computer using an Intel® Xeon® CPU E5-1660 v4 with 8 3.2 GHz cores used in parallel. The transient consists of a total of 149 time steps, with a variable time step in order to capture the rapid expansion of the fuel during the energy release. A penalty factor of 0.1 is used for the contact model to ease the convergence and a relaxation factor of 0.99 for the solution of the displacement matrix is used in order to stabilize the solution. The total running time is of approximately 4 hours.

As expected [138], the presence of a defective pellet causes high stress concentration in the portion of the inner cladding directly facing the missing surface relatively early during the transient. As an example, Figure 6.26 shows the hoop stress and equivalent stress distribution at around $t = 35$ ms when the energy release in the fuel is still not complete.

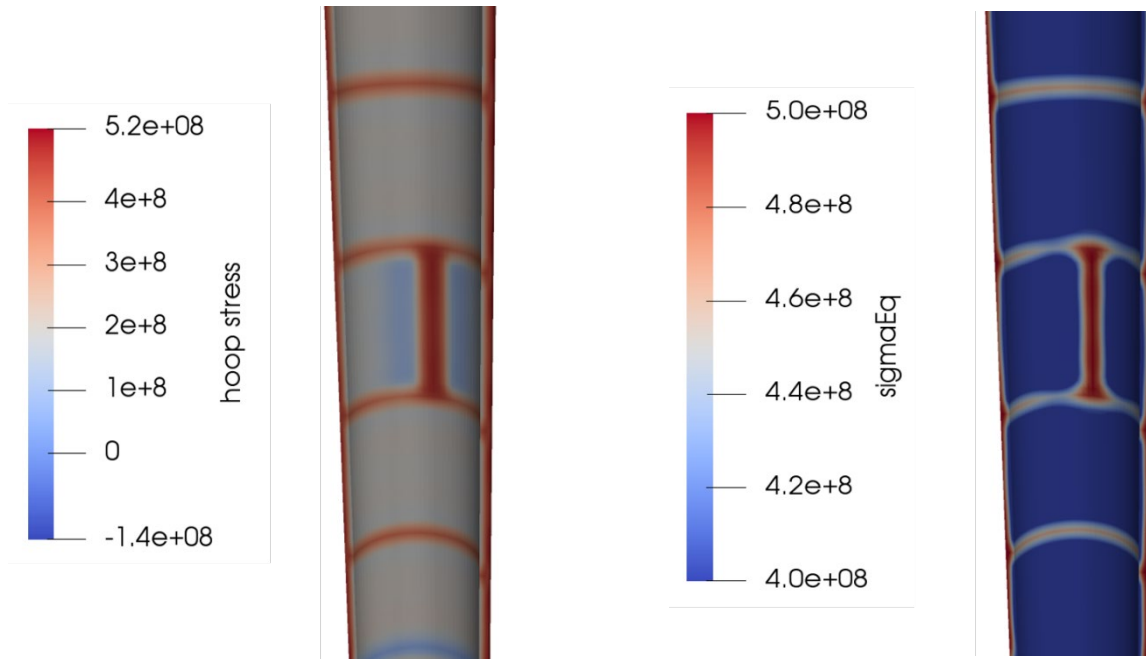


Figure 6.26 – Hoop stress (left) and equivalent or von Mises stress (right) distribution on the inner side of the cladding at $t = 35$ ms. The stress concentration on the area directly facing the defect can be observed.

Due to the high stresses, the cladding portion facing the missing pellet surface is the first one to experience plastic deformation and shows the maximum accumulated plastic strain at the end of the transient, as it can be shown in Figure 6.27. This figure also shows that the accumulated plastic strain is not recovered after the pellets contract and the stress decrease below the yield limit.

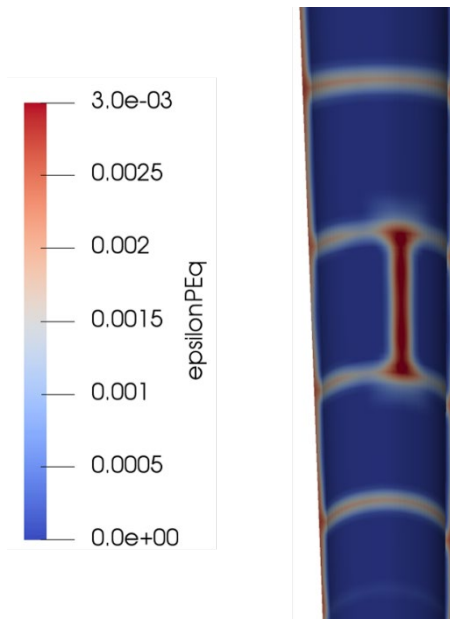


Figure 6.27 – Cumulative plastic strain at the end of the transient (i.e. $t = 50s$).

6.3.2 Constant irradiation with cladding ridges formation

The second test case was conceived as a more realistic scenario for the Zircaloy creep model, to show how OFFBEAT can capture important multi-dimensional features of fuel behavior. The case consists of a UO_2 rodlet made of 10 pellets with the dimensions and specifics shown in Table 6.9. The Zircaloy cladding extends a few millimeters above the top end of the fuel column, so that the expanding pellets are always facing a portion of the cladding. The rod starts from fresh conditions and it is filled with helium pressurized at 0.1 MPa at room temperature. Throughout irradiation, the coolant is kept at 15 MPa and 573 K. After a linear rise in power in the first 60 seconds, the rod is irradiated at 30 kW/m for 180 days (see Figure 6.28 for the power history), reaching a burnup of approximately 10 MWd/kg. At the end of irradiation, the shut-down transient lasts for 60 seconds, followed by an additional 100s to allow the rod to cool down and reach equilibrium with the coolant temperature.

Table 6.9 – Dimensions and specifics for the ridging test case

Parameter	Value
N. of UO ₂ pellets	10
Outer pellet radius	4 mm
Pellet height	13.8 mm
Dish radius/height	3/0.3 mm
Chamfer width/height	0.6/0.2 mm
Cladding inner radius	4.1 mm
Cladding outer radius	4.7 mm
Cladding Height	150 mm

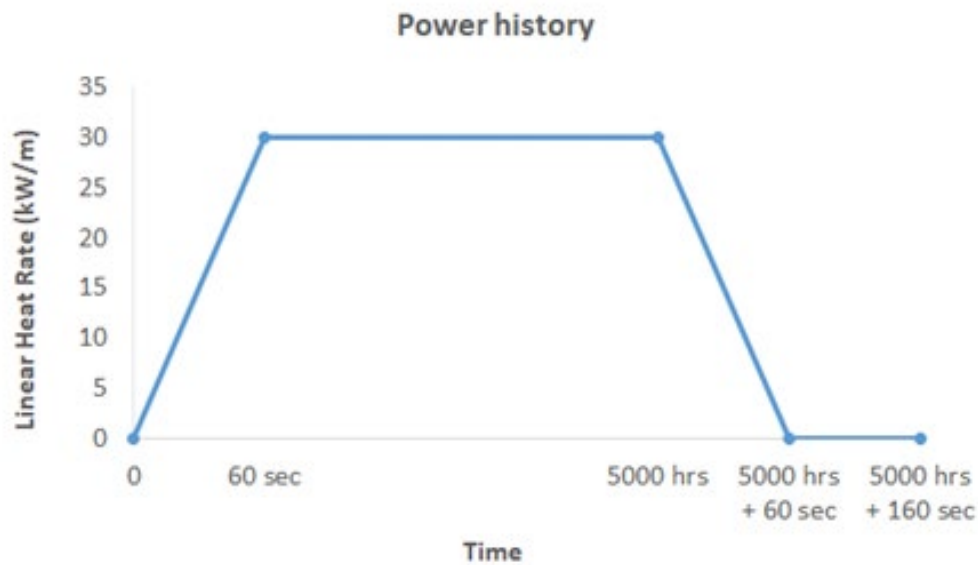


Figure 6.28 – Power history for the ridging test-case rodlet. The time axis is not to scale.

The rodlet is reproduced with the axisymmetric model shown in Figure 6.29. A mesh with 5x1200 cells is used for the cladding, while a 20x100 mesh is used for each pellet, for a total of 26000 cells. As shown in the detail on the right side of Figure 6.29, the pellet mesh is radially more refined in the land and chamfer region. This mesh is significantly denser along the axial direction than those typically used in traditional fuel performance codes. This level of refinement, however, is neces-

sary to accurately capture multi-dimensional local phenomena such as the formation of the cladding ridges.

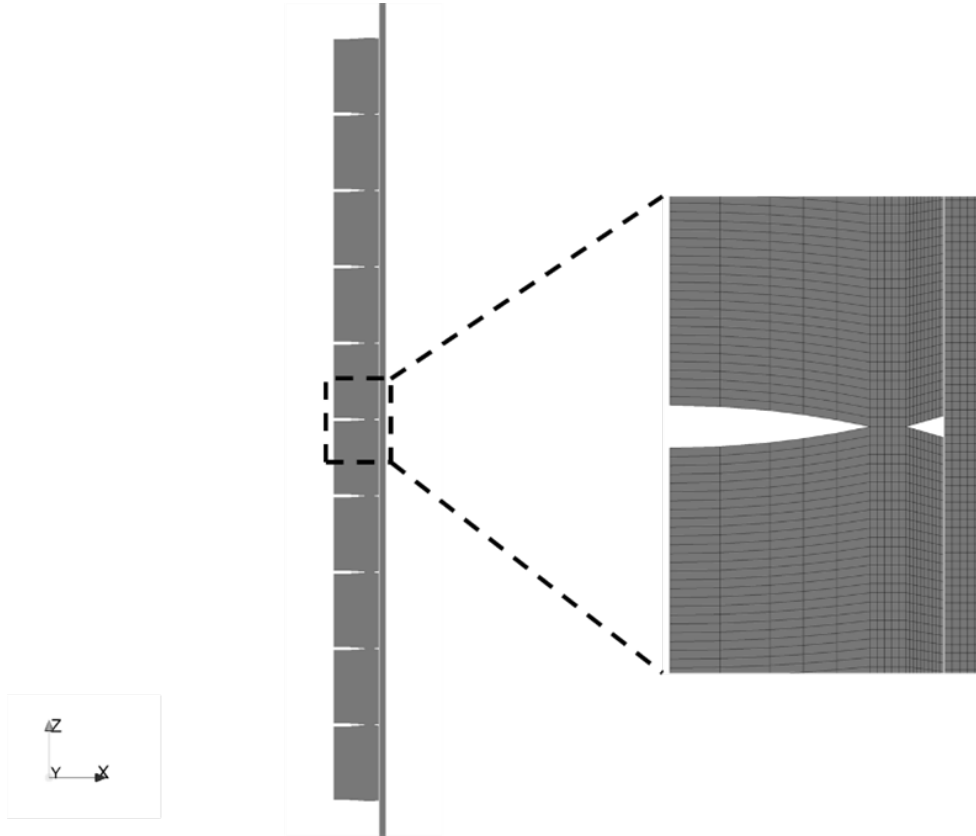


Figure 6.29 – Axisymmetric model used for ridging test-case rodlet simulations. The pellets are attached through the land region. A detail of the computational mesh is visible on the right.

As done for the previous test case, the pellet chamfers and dishes are included in the model, but the fuel forms a continuous column through the land (as it seems to be a common approach in similar works [138]). Certainly, this modeling choice influences the local stress distribution in the pellet in the vicinity of the land, but it greatly simplifies the numerical problem by avoiding the solution of the pellet-to-pellet contact mechanics while still capturing part of the hourglass-shape thermal expansion. The bottom surfaces of fuel and cladding are connected to the ground while a fixed pressure is imposed on the top surfaces. In particular, the filling gas pressure is imposed on the top fuel surface and the coolant pressure is imposed on the top cladding surface (adjusted for the annular geometry given that the top cap is not modeled). The gap conductance model and the penalty-method boundary condition are used to treat the gap heat transfer and the contact mechanics, respectively.

Two cases are considered, one where the cladding behaves as a thermo-elastic body and one where the models for Zircaloy creep and plasticity are activated. An adaptive time-step size is used

so that the change in power during the initial ramp and during the final power descent are well captured. The adaptive scheme allows either a maximum power increase of 25% or a maximum burnup increase of 0.1 MWd/kg. This corresponds to a time step of approximately $1.4E5$ seconds during the long phase at constant power. However, toward the end of the holding period the time step decreases gradually so that it is in the order of 10s during the final power descent.

At the beginning of irradiation, the rod response is purely thermo-elastic for both simulations and, because the initial gap is small, the pellets enter in contact with the cladding already during the power ramp. The graph on the left side of Figure 6.30 shows the outward displacement of the cladding outer and inner surfaces at 100s when the thermal diffusion in the rod has almost reached its steady-state (for fresh rod conditions). The graph shows the formation of cladding ridges with an amplitude of 4 microns, caused by the hourglass deformation of the pellets. This characteristic structure can be clearly seen also on the right of Figure 6.30 showing the von Mises stress distribution in a segment of the cladding. The geometry is warped using the displacement field magnified 50x times.

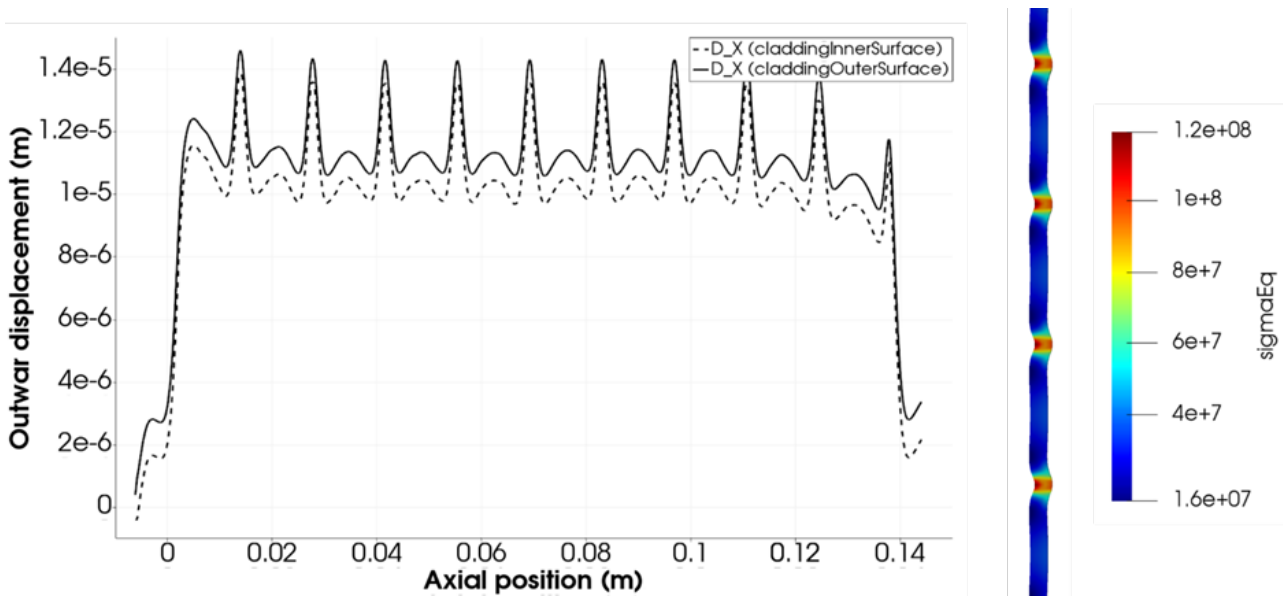


Figure 6.30 – Outward displacement of inner and outer cladding (left). Color plot of the von Mises or equivalent stress (Pa) for a segment section of the cladding (right). The geometry is warped using the displacement field multiplied 50 times.

Following this initial expansion, the rod starts to shrink due to the fuel densification, until this effect saturates between 1 and 2 MWd/kg. When the fuel reaches a burnup of approximately 5 MWd/kg, the fuel starts to swell, pushing the cladding outward. From this point on, the behavior of the cladding differs greatly between the two considered cases. The expansion of the fuel causes the stresses to increase significantly in the elastic cladding and, particularly at the location of the

ridges, the von Mises stress gradually approaches values close to the plastic yield point. When using the creep model, instead, the cladding accommodates the fuel expansion with permanent deformations and the stress relaxation due to creep keeps the von Mises stress at considerably smaller values. This different behavior can be seen on the graph Figure 6.31 where the cladding von Mises stress at the end of the 180 days is shown for both elastic and plastic cases. On the inner side of the elastic cladding, the equivalent stress in the ridges reach values larger than 250 MPa, while they remain below 70 MPa when the creep model is used.

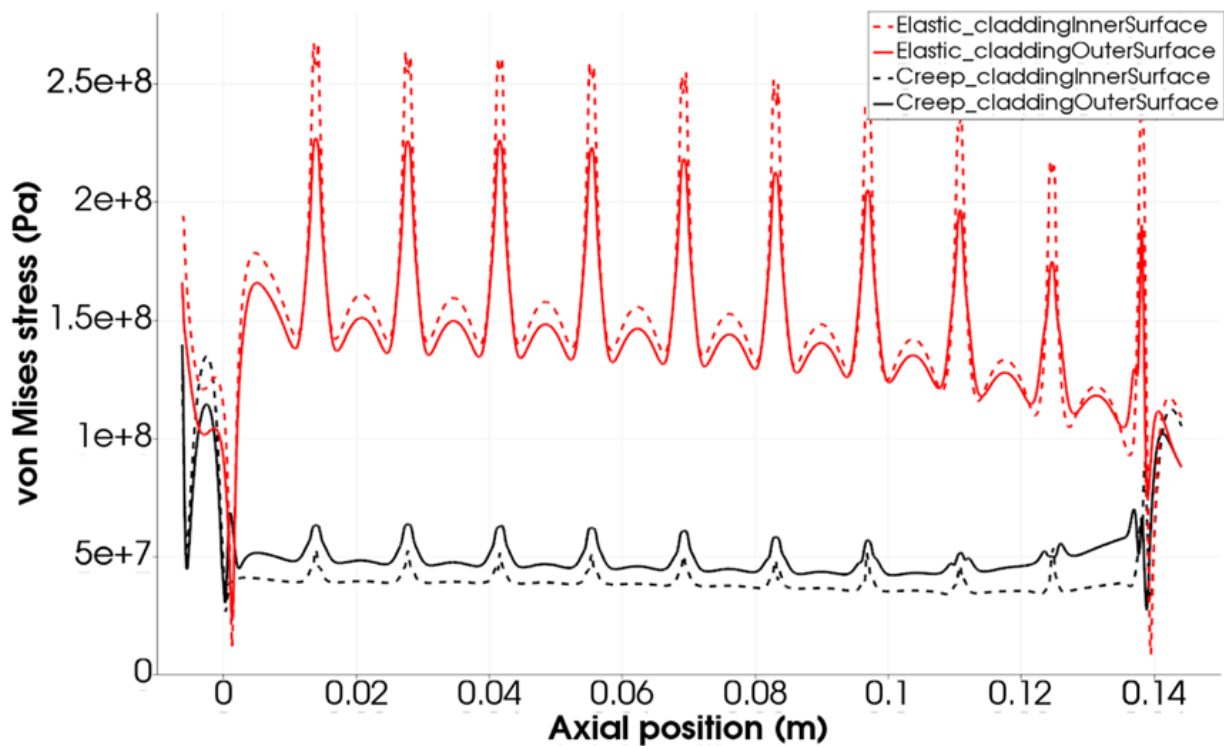


Figure 6.31 – Von Mises or equivalent stress on the inner and outer surface of the cladding at the end of the 180 days of constant power irradiation. The results for both elastic and non-elastic cladding are shown.

Finally, once the power generation stops and the rod cools down to the coolant temperature, the gap opens once again due to the contraction of the pellets. Figure 6.32 shows the displacement of the cladding inner and outer surfaces at the end of the simulation. The elastic cladding has no permanent deformation (only the uniform expansion for being at a high temperature), while deformations following the ridge structure are observed for the second rod.

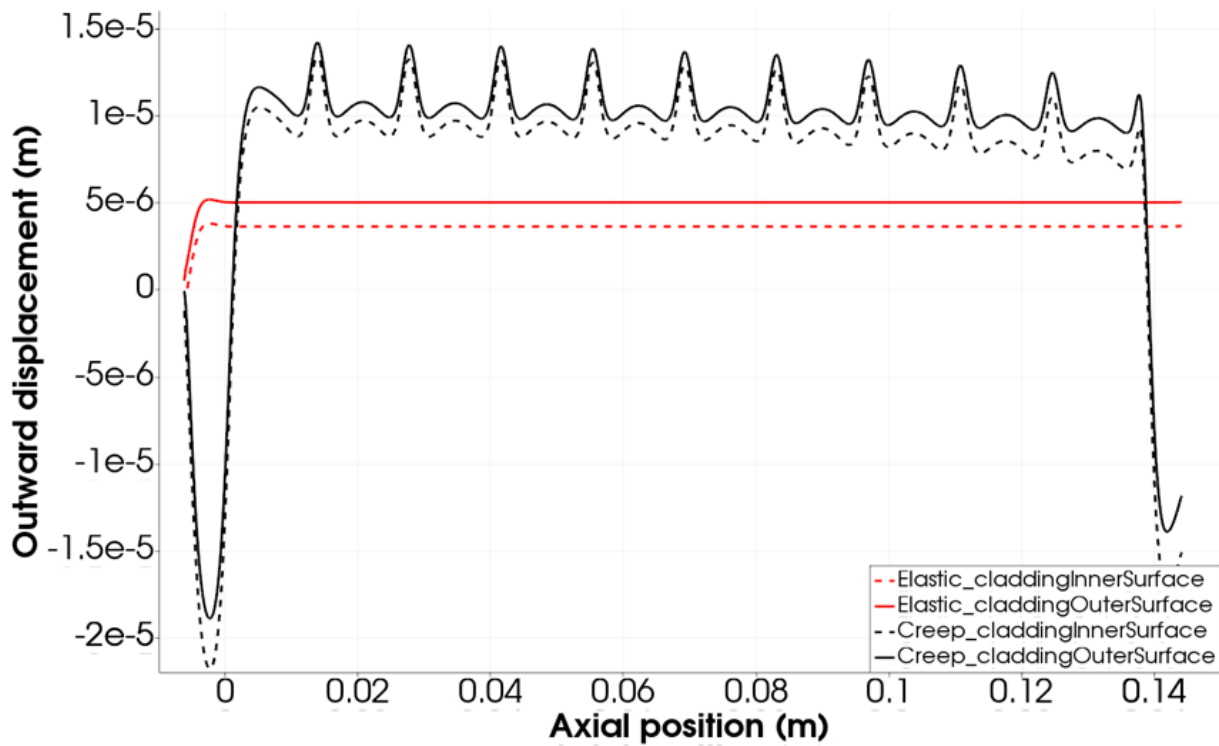


Figure 6.32 – Outward displacement of inner and outer cladding surfaces at the end of the simulation (with the rod in thermal equilibrium with the coolant). Permanent deformations due to creep following the ridges structure are visible for the second case.

The results presented in this section are obtained using a penalty factor equal to 1 for the contact boundary condition, resulting in only a minor penetration (approximately $1\text{E-}8\text{ m}$). While being more accurate, this makes the problem numerically more cumbersome and, in order to reach convergence, the linear system has to be under relaxed with a relaxation coefficient of 0.99, slowing down the simulation. A smaller penalty factor might be used to improve the code performance, but one must be aware that a lower penalty factor might have a significant impact on the results of the simulation. The case was completed in approximately 5 hours using one single core from a desktop unit equipped with an Intel® Xeon® CPU E5-1660 v4 processor with 8 GHz cores. Although not comparable with traditional fuel performance codes, this performance might be considered acceptable given the elevated detailed with which the contact and the ridging are captured, and the high number of time steps simulated. The implicit contact boundary condition was developed only after the preparation of this demonstration case. Once appropriate blending function parameters are found for the open-gap scenario, the application of the implicit method to this test case should speed up the convergence rate, in particular because of the almost total absence of power variation and gap re-opening during the simulated history.

6.4 Conclusions

This chapter has summarized the verification and validation efforts carried out in the framework of this thesis. Verification tests have been performed for the steady-state and transient temperature and stress profile under simplified conditions, for the Limbäck creep model and for the instantaneous plasticity model, but additional cases will continue to be realized with the introduction of new features. Notably, the established contact procedures have been extensively tested against several benchmarks with analytic or reference solutions, providing accurate results. Along the lines of the verification tests presented in the Section 6.1.3, one could consider the application of the novel implicit contact boundary condition to the reproduction of the recent results published with the BISON code for the evaluation of the performance of multi-metallic layered composite cladding for the light water reactor accident tolerant fuel [139].

A first validation base has been formed including several rods from the IFPE database. The cases presented in this chapter have shown that OFFBEAT is able to provide accurate results with what can be found in other similar validation works. However, the validation campaigns have focused solely on low to medium burnup rods (up to ~ 40 MWd/kgU) and on two fundamental integral results, namely the FCT and on the FGR fraction. Future efforts might extend the validation base to higher burnup levels and to different fuel materials such as MOX. This is particularly relevant in the Swiss context given that Swiss nuclear power plants regularly operate fuel into the 70 MWd/kg range.

Separate validation studies could be performed for the several models included in OFFBEAT, such as TUBRNP or SCIANTIX, comparing the results against references available in the open literature often based on separate-effect tests. The future validation campaigns should also consider extending the validation base to quantities besides the FCT and FGR, such as cladding elongation or strains. This shift in focus will be relevant for studying complex multi-dimensional scenarios involving fuel-to-clad contact and affecting the fuel rod integrity.

An important missing validation step requires the comparison against intrinsically multi-dimensional data. This task is made difficult by the scarcity of appropriate data, but the analysis of ridging formation in the framework of the collaboration with the JRC-Karlsruhe represents a promising first step.

The chapter has also presented two interesting demonstration cases. First a 3-D analysis of a short rodlet with 5 separately modeled pellets has been performed. The test case simulated the thermo-mechanics evolution during a fresh-rod RIA and included a missing pellet surface defect. Then, a 2-D r-z analysis of a short rodlet with 10 separately modeled pellets has been performed. The case has simulated a constant base irradiation, where the cladding creep has enough time to accommodate the strains and reduce the stresses. Despite being far from validation studies and representing more a qualitative analysis, the two demonstration cases have shown that OFFBEAT can reproduce relevant multi-dimensional features such as the formation of ridges and the concentration of plastic strain in the cladding region facing a defective pellet.

Chapter 7

Effect of eccentricity on fuel disc irradiation⁶

In-pile separate-effect tests are becoming increasingly more relevant in nuclear fuel research to obtain a better understanding of specific properties and phenomena. However, they are often characterized by features that cannot be accurately reproduced with traditional tools such as the 1.5-D TRANSURANUS code developed by the JRC. This chapter aims to illustrate how the advent of multi-dimensional codes such as OFFBEAT allows to improve further the interpretation and design of separate-effect tests which traditionally relied on a combination of conventional fuel performance codes and general-purpose finite element software. Suggesting new analysis or new experiments, this might lead to improvements in the models used in traditional codes.

The specific case-study chosen for this chapter focuses on the effect of fuel eccentricity on two fuel disc irradiation campaigns carried out in the OECD Halden Boiling Water Reactor (HBWR). The impact of misalignment is expected to be more relevant in rods with highly conductive fuels, large initial gaps and low conductivity filling gases, characteristics that can all be found in the two experimental campaigns chosen for the case-study. Using the multi-dimensional capabilities of OFFBEAT, 2-D axisymmetric and 3-D simulations are combined to investigate the effect of eccentricity on the fuel temperature distribution and outline the potential of such an analysis for upcoming experiments.

The chapter is structured as follows. While the first section provides a background on the effect of fuel eccentricity on traditional LWR, in terms of the main experimental and theoretical findings, Section 7.2 briefly describes the two HBWR experimental campaigns. In Section 7.3, the attention is focused on preliminary axisymmetric simulations, showing that the large differences between measured and predicted temperatures for some rods cannot be justified in the framework of a traditional fuel performance analysis, without considering 3-D effects. Section 7.4 presents a 3-D investigation on the effect that eccentricity might have on the temperature distribution in fuel disc irradiation tests. Finally, the last section summarizes the outcome of the multi-dimensional study and outlines the further possible developments and applications.

⁶ The content presented in this chapter is partially available in [174].

7.1 Effect of eccentricity during irradiation

Conventional fuel performance simulations assume the pellet stack to be concentric with the cladding, although a varying degree of eccentricity is inevitable in the initial rod configuration. The impact on typical LWR rods is small during most of the irradiation, as the gap closes at a relatively early stage due to thermal expansion, fuel fragment relocation and swelling, and cladding creep down. Additionally, the effect of eccentricity is generally embodied in the semi-empirical correlations and fitting parameters employed for the gap conductance modelling. However, under certain circumstances the uncertainties introduced by a misalignment of the fuel pellets may become much more important.

Already in 1974, it was pointed out that at the beginning of life, with the gap still open, the azimuthal asymmetry in gap conductance affects the heat transfer and can cause the heat flux to exceed its critical value, leading to film boiling and cladding failure [140]. In 1977, Williford and Hann [141] studied the impact of filling gasses and pellet eccentricity on the rods of the Instrumented Fuel Assembly IFA-431. They concluded that neglecting eccentricity leads to a significant underestimation of the average gap conductance, in particular for rods with high thermal gradient across the gap (due for example to large gap size or to filling gasses with low conductivity such as Xenon). In 1982, the importance of eccentricity was also analyzed experimentally during Reactivity Initiated Accident (RIA) condition tests [142], with temperature differences as high as 150 degrees measured along the cladding circumference. In parallel, the findings of McNary et al. [143] confirmed the work of Williford and Ann, adding that eccentricity is expected to play a relevant role not only for rods with large gaps and low gap conductance (i.e. with large thermal gradients across the gap) but also for high conductivity fuels such as carbide. More recently the effect of eccentricity on the fuel temperature distribution for UO_2 rods was studied by Desampaio et. al. [144] while BISON [145] was used to reproduce the temperature differences between concentric and eccentric rods in the IFA-431 [146][147].

Characteristics similar to those pointed out by Williford and Hann and by McNary can be found in some of the experimental setup of the in-pile separate effect studies carried out in the OECD Halden Boiling Water Reactor (HBWR). In particular, among the large database available at the Joint Research Center (JRC) in Karlsruhe, two fuel disc irradiation campaigns have been identified, where the combined presence of highly conductive materials, large gaps and low-conductivity filling gases hints at a significant impact of eccentricity. The next sections present a multi-dimensional study of the two campaigns, with OFFBEAT used to reproduce the fuel temperature distribution and compare it to the thermocouple readings by means of both 2-D axisymmetric and 3-D simulations.

7.2 Experimental campaigns

The experimental data used in this Chapter are obtained from two past fuel disc irradiation campaigns performed in the HBWR. To isolate the effect of temperature on fuel behavior, both campaigns were interested in fuel samples with radially uniform temperature profiles. Due to the large

temperature gradients that can be found in commercial fuel, the two campaigns adopted the irradiation of thin fuel discs sandwiched between molybdenum discs. With molybdenum having a thermal conductivity 40 times that of UO_2 , most of the heat generated in the fuel flows vertically toward the molybdenum discs and it dissipates radially through the molybdenum-cladding gap, causing only negligible radial gradients. This unusual setup requires a full (at least) 2-D analysis.

7.2.1 Test 1: the High Burnup Rim Project

The High Burnup Rim Project (HBRP) was initiated in 1991 and was completed at the end of 2000 [148]. This international project responded to the industrial need to study the High Burnup Structure (HBS), typically found in the rim of LWR fuel pellets. Combining the use of molybdenum discs with a highly enriched fuel allowed fuel samples with relatively flat temperature and burnup profiles to be obtained.

The HBRP consisted of 4 rods loaded within an Instrumented Fuel Assembly (IFA) and irradiated in the mid 1990's. Each rod was made of 4 separate stacks consisting of 10 fuel discs sandwiched between molybdenum discs. The bottom and top stacks were the only ones equipped with a thermocouple (TC) measuring the (external) temperature of the molybdenum disc. The cladding tube enclosing the discs was made of Zircaloy.

As shown in Figure 7.1, the experiment was designed to provide a burnup and temperature dependent matrix for the study of the HBS: the rods had different target temperatures, achieved by decreasing the radius of the molybdenum discs and switching the gas composition from pure helium to pure argon, while the stacks had different target burnups. To compensate for the axial power gradient and maintain the same rod temperature, different molybdenum disc thicknesses were used from the top to the bottom stack. More details about the geometrical configuration of each rod can be found in Table 7.1.

The top stack temperatures measured during operation were significantly lower than planned, due to an unexpected flux profile in the HBWR. In order to focus on the effect of the eccentricity in disc irradiations and for the sake of conciseness, the study performed in this Chapter is limited to the bottom stacks in each rod: S11, S21, S31 and S41 (see Figure 7.1).

The main documents of the experimental campaign do not provide any estimate about the average eccentricity of the stacks, but pictures taken during the Post Irradiation Examination (PIE) do reveal the presence of eccentricity (both between molybdenum and cladding, and between molybdenum discs and UO_2 discs). However, these pictures provide a single 2D slice of the rod, so their analysis remains inconclusive. Also, there seems to be no indication of the TC measurement uncertainty in the campaign documentation.

Table 7.1 - Dimension and design parameters of the HBRP rods [149].

		Rod1	Rod2	Rod3	Rod4
Filling gas		~100% He	~75% He + Ar	~45% He + Ar	~100% Ar
Fuel disc diameter (mm)		5	5	5	5
Fuel disc thickness (mm)		1	1	1	1
Mo disc diameter (mm)		8.26	8.16	8.01	7.76
Mo-Clad radial gap (mm)		0.05	0.1	0.175	0.3
Mo disc thickness (mm)	4 (Top)	1.2	1.2	1.2	1.2
	3	1.8	1.8	1.8	1.8
	2	2.4	2.4	2.4	2.4
	1 (Bottom)	3.0	3.0	3.0	3.0
Clad thickness (mm)		0.57	0.57	0.57	0.57
Clad material		Zircaloy	Zircaloy	Zircaloy	Zircaloy

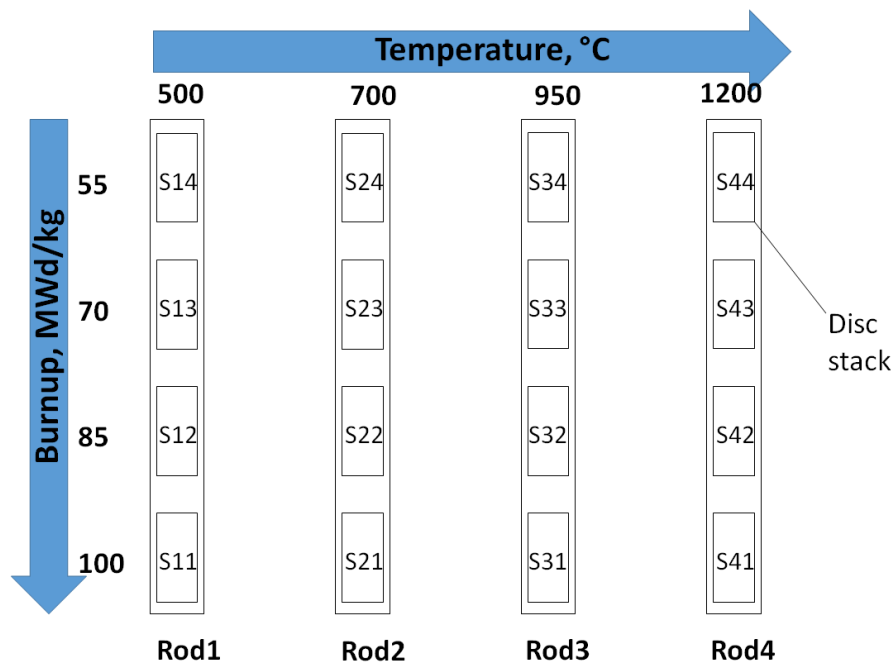


Figure 7.1 - General scheme of the HBRP experiment [149]. The Figure shows the target temperatures and burnups.

7.2.2 Test 2: the fuel creep test

This test [150] was originally designed to study the low temperature (below ~1000 °C) creep rate for different types of LWR fuel as a function of applied stress. In this temperature range, the fuel

creep behavior is dominated by an a-thermal fission-induced component, while fission-enhanced thermal creep is negligible.

The experiment consisted of 4 rods loaded in another IFA, between 2010 and 2012. Two types of fuel were used: standard UO_2 for the first pair of rods and Cr-doped UO_2 for the second. Most importantly, beside the fuel type and fuel disc diameter, the 4 rods had a similar geometrical configuration and were equipped with central thermocouples. More details can be found in Table 7.2.

Table 7.2 - Dimension and design parameters of the fuel creep test rods [150].

	Rod1	Rod2	Rod3	Rod4
Fuel type	Cr- UO_2	Cr- UO_2	UO_2	UO_2
Filling gas	He-Ar	He-Ar	He-Ar	He-Ar
Fuel disc diameter (mm)	8.48	8.48	8.19	8.19
Fuel disc thickness (mm)	1.7	1.7	1.7	1.7
Mo disc diameter (mm)	11.7	11.7	11.7	11.7
Mo-Clad radial gap (mm)	0.2	0.2	0.2	0.2
Mo disc thickness (mm)	5	5	5	5
Clad thickness (mm)	0.57	0.57	0.57	0.57
Clad material	Inconel600	Inconel600	Inconel600	Inconel600

Each rod was made of a single stack of 44 thin fuel discs sandwiched between thicker molybdenum discs. The discs were enclosed in a cladding tube made of Inconel600. The rods were equipped with fuel stack elongation detectors and with centerline TCs inserted in a center tube passing through the disc central holes. It is assumed that the center tube (absent in Test 1) limits the eccentricity of the disc column. A bellows-based system was designed to apply an axial stress during the creep tests while measuring the change in stack length. Although the same irradiation history is shared between the two rods of a pair, only one of each pair was attached to the bellows-based system. Thus, the unstressed reference rod represented the behavior of the fuel in the absence of creep deformations.

The second test was divided into 4 cycles: two irradiation periods at low applied stress, corresponding to cycles I and III; and two shorter creep testing periods at varying applied stress levels, corresponding to cycles II and IV. The analysis performed in this Chapter is limited to the first period up to ~110 days, when due to the low applied stress the change in fuel stack length was mostly due to thermal expansion and densification [150]. The rest of the irradiation will be analyzed in the future to improve the modeling of fuel creep behavior with the use of a multidimensional code and explore its potential implications for conventional fuel performance codes.

As for the HBRP, the campaign documentation does not provide any estimate about the average eccentricity of the rods nor it includes pictures derived from PIE. Also, indication of measurement uncertainty is lacking.

7.3 2-D analysis

The two experimental campaigns described above are first analyzed by means of 2-D axisymmetric simulations. The main objective is to assess if potential differences between predictions and measurements can be explained in the framework of traditional fuel performance analysis, without considering 3-D effects such as eccentricity. This would also pave the way for a reinterpretation of the disc irradiations, with a view to achieve more accurate boundaries for the HBS formation for instance.

7.3.1 Modeling approach and assumptions

In order to limit end-effects on the local temperature, while avoiding the full-length simulation of the entire stack, it is necessary to include at least a few fuel-molybdenum pairs surrounding the TC position. For this reason, the reduced stack shown in Figure 7.2 is considered for each rod, including 5 fuel discs, 4 molybdenum full-discs and 2 molybdenum half-discs at the two ends. Nevertheless, making use of the geometrical symmetry, the actual numerical model is limited to half of the reduced stack. The computational grid, also shown in Figure 7.2, was tested for convergence and a mesh refinement level of 20x5 divisions for the Mo discs, and 12x5 divisions for the UO₂ discs provided sufficiently accurate results (see also [151], Section 5.2).

The full irradiation history database acquired during the HBRP campaign was simplified to the ~30 data points per rod included in the final project report [148], including the experimental molybdenum temperature as well as the linear heat rate and burnup at the TC location. Likewise for the second test, the original irradiation history, containing more than 10000 data points recorded at 15 minutes intervals, was reduced to the more manageable size of ~400 using the FRA-TOOLBOX [152].

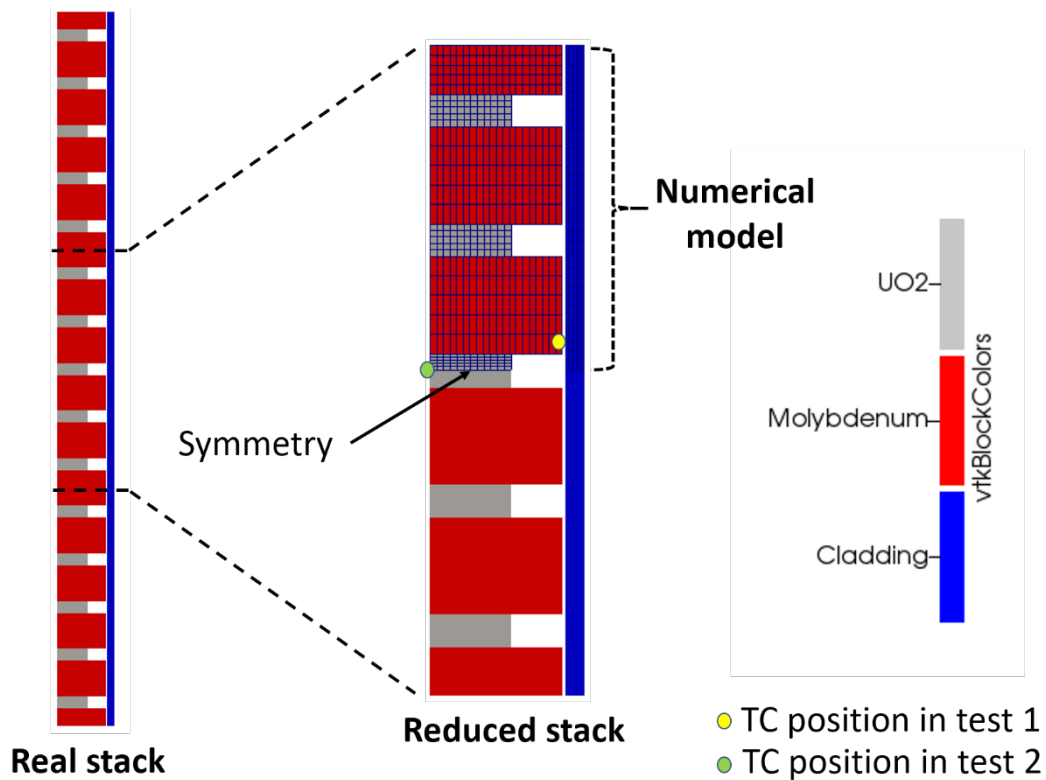


Figure 7.2 – Axisymmetric model for the separate-effect rods with discs. A reduced stack with 5 fuel discs is used to characterize the temperature distribution surrounding the TC position. Due to symmetry, the numerical model corresponds to the area overlaid with the mesh grid.

The numerical model in Figure 7.2 requires a careful consideration of the displacement at the boundaries. A symmetry type boundary condition is applied to the bottom surfaces because of the model half-symmetry. This fixes the axial displacement of the mechanical system considered (the normal displacement is zero in the symmetry plane), but it does not anchor its tangential movement. Thus, the top surface is fixed in all degrees of freedom to make the mechanical problem mathematically well-posed. Since this constraint inevitably causes non-physical high stresses, the Young's modulus in the top molybdenum half-disc is decreased to 10% of its theoretical value. Acting as a cushion or as a spring, the top disc thus accommodates the axial expansion of the fuel stack and confines the high stresses to a region sufficiently far from the location of the TC.

It must be underlined that decreasing the Young's modulus is only a numerical trick useful for reproducing a computational model like the one described in this section. Alternatively, one could model the entire reduced stack, fix the bottom surfaces, and use a traction type boundary condition at the top surfaces. The mesh grid would be twice as large, and the computational cost would be higher. In preparation for this work, it was verified that the difference in temperatures obtained with the entire-stack model is smaller than the experimental uncertainties, or the effect of eccentricity, which is the actual objective of this study.

Another important issue derives from the presence of multiple free bodies (i.e. without fixed points) in contact with each other. The application of the penalty method boundary condition would have terrible convergence properties. Experimental data are missing for the contact thermal resistance between fuel and molybdenum discs. However, the disc irradiation is setup to have a uniform temperature and burnup distribution in each disc. Based on this consideration, perfect contact can be assumed between subsequent discs. The HBS formation is also relatively uniform, and no deformation is expected that would invalidate the assumption of perfect contact between UO_2 and Mo, which seems justified also by a careful analysis of the PIE pictures. Thus, the UO_2 /molybdenum stack becomes effectively a single multi-material domain. When modeling such a domain in a FV framework numerical errors arise in the stress distribution close to the bi-material interface [78]. These numerical issues are solved using the novel implicit contact boundary condition with a very high (i.e. effectively infinite) friction coefficient. The penalty method is used instead for the surfaces facing the gap, although it reduces to applying the internal rod pressure in the absence of penetration.

Regarding the temperature field, symmetry boundary conditions can be used both at the top and bottom boundaries. This is equivalent to assuming that the reduced stack is part of an infinite rod made of fuel and molybdenum discs. Naturally, in this way full-length effects on the local temperature distribution are neglected but considering that the atmosphere of the rod is fixed and that there is no fission gas poisoning, this assumption will not affect the results. No additional thermal contact resistance is considered between fuel and molybdenum discs and the temperature field is assumed continuous between the two materials. Typical values of contact conductance are quite high and are not expected to have a significant impact on the disc temperature.

An important modeling choice concerns the gap heat transfer between molybdenum discs and Zircaloy cladding. In the absence of more appropriate alternatives, the classic gap conductance model implemented in OFFBEAT and derived from FRAPCON is chosen. The main issue is the presence of fitting parameters based on UO_2 rod data. The effect they have on the temperature jump across the gap cannot be known a priori. However, the main physical considerations on which the FRAPCON model is based are still valid, such as the decomposition of the heat conductance in the three components of conduction through the gas, radiative losses and contact heat exchange. Considering that the gap between the Mo discs and the cladding remains open and that the temperatures remain moderate the dominant contribution to heat transfer is due to conduction. Therefore, the FRAPCON model is assumed to be a good first approximation.

Regarding the molybdenum thermo-mechanical properties, correlations for conductivity, Young's modulus, Poisson's ratio, and thermal expansion are derived from the BISON manual [145] and introduced in OFFBEAT. The correlations found in the BISON manual and other references do not provide any uncertainty estimation. Also, no correlations were found in the public literature for the molybdenum emissivity. The few sources available agree in reporting values around 0.2 for the surface emissivity of molybdenum between 1500 °C and 2000 °C, hence this value is adopted in this work. The same sources report a much higher emissivity (from 0.8 to 0.9) for oxidized molyb-

denum but no information is found in the test reports about the oxidation state of the molybdenum discs. Due to inert gas filling in the rods under consideration, it is reasonable to assume that little to no oxidation took place during irradiation.

7.3.2 Results and discussion

The results of the axisymmetric simulations are summarized in Figure 7.3, where the temperatures calculated with OFFBEAT are plotted against the corresponding measurements. A temperature prediction matching the TC reading would lie on the diagonal “ $P = M$ ” (full line “Predicted = Measured”), while the two dashed lines correspond to a temperature difference of $\pm 100\text{K}$, a range that is generally considered to embody a large fraction of the uncertainty on fuel temperature predictions under normal operation conditions (see [153]). Due to the different TC position, the outer molybdenum temperature is plotted for the HBRP, whereas the fuel centerline temperature is provided for creep test.

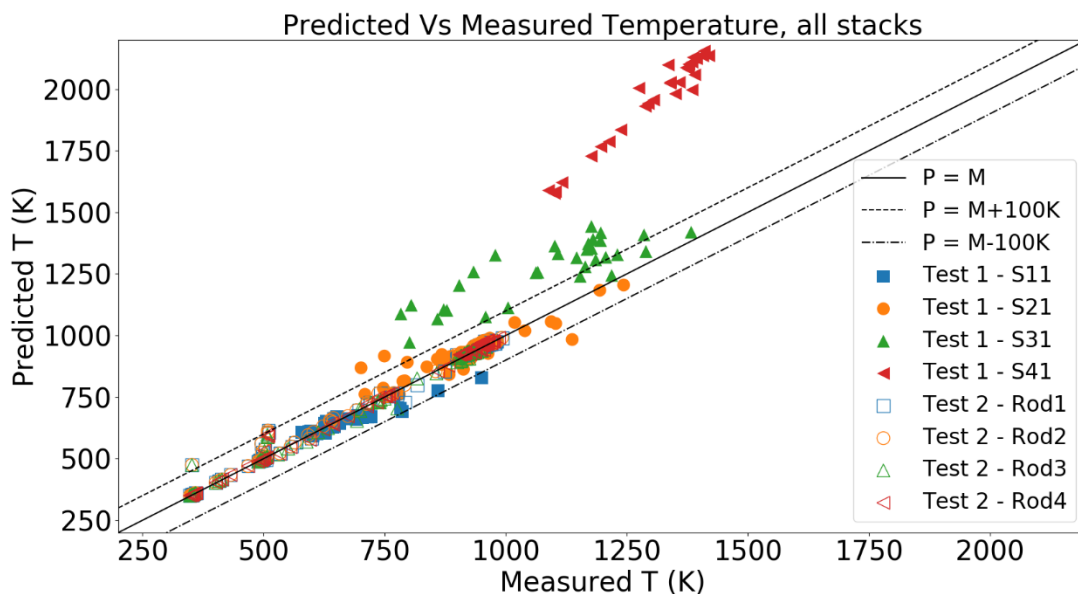


Figure 7.3 – Results of the axisymmetric simulations. Temperatures obtained with OFFBEAT are plotted against the corresponding TC measurements.

The temperatures calculated for the second series of rods lie very close to the “ $P = M$ ” line in Figure 7.3. The deviations are small and hint at a minor role, if any, of eccentricity. This is surprising if considering the characteristics of the rods, similar to those pointed out by McNary in his publication. The fact that the central tube is passing through the center holes of the entire rod is ex-

pected to limit the misalignment of the disc column. Eccentricity could only be relevant if the discs were broken, which has not been reported.

The deviations are considerably larger for the first series of test rods. While the predictions for the stacks S11 and S21 lie mostly within the band of $\pm 100\text{K}$, OFFBEAT overestimates the temperature for the stacks S31 and S41 by more than 300K and 700K, respectively. Also, a pattern can be identified in the first test series. Indeed, it appears that the deviations gradually increase from the low-temperature small-gap rods filled mostly with helium, to the high-temperature large-gap rods filled mostly with argon.

The deviations might be partially linked with neglected irradiation effects in the molybdenum discs, such as swelling. However, they are not mentioned in the campaign documents and no information can be found about similar phenomena in the relevant literature. Besides, the magnitude of the temperature deviations is too high to be justified with any reasonable expansion due to disc swelling. Additionally, the PIE pictures show that the molybdenum discs were intact at the end of irradiation, thus fragmentation can be excluded. Other relevant material properties have been taken into consideration in the sensitivity study in this chapter.

The deviations might also be caused by poorly modeled mechanical effects in the fuel discs (such as relocation or densification), by the assumption of perfect contact (because it could limit the tangential movement of the UO_2 discs), or by a change in fuel microstructure due to the formation of the HBS (which is not considered in OFFBEAT). However, given that most of the heat flows vertically toward the highly conductive molybdenum, it is unlikely that the temperature distribution would be affected by small variations in the fuel microstructure or in the fuel-clad gap (which remains extremely large compared to the molybdenum-clad gap). This was verified in preparation for this work by running test simulations where the various nuclear models of OFFBEAT are sequentially shut down and where the top and bottom disc surfaces are left free to expand. The temperature results changed only slightly, in the order of few tens of degrees. Considering the rather uniform temperature and burnup profiles in the discs, the formation of the HBS is also not expected to change the assumptions in the calculation model (e.g. for the contact conditions).

In the HBRP rods, the TC is located near the edge of the molybdenum disc. Therefore, in the framework of a 2-D fuel performance analysis neglecting 3-D effects (and based on the arguments brought forth in the previous paragraphs), large deviations from the measurements can mostly be attributed to the errors and uncertainties embedded in the heat transfer model chosen for the molybdenum-cladding gap.

Naturally, the thin-gap approximation of the FRAPCON model is not accurate for the small fraction of heat transferred across the fuel-cladding gap. This region is quite large (more than 1.5 mm) if compared to commercial rods, and the radiative heat exchange involves also non-negligible portions of the top and bottom surfaces of the surrounding molybdenum discs. A proper assessment would require an explicit modelling of the gap heat transfer in the absence of contact with the use of view factor models for the radiative heat exchange. However, considering the low temperatures

measured by the TCs (always lower than $\sim 1400\text{K}$), it is reasonable to assume that errors in the fuel-cladding heat exchange would have a negligible effect on the molybdenum temperature distribution.

7.3.3 Parametric study on the gap heat transfer model

To better understand the potential effect of various gap conductance model parameters on the observed discrepancies for test 1, a parametric study was carried out. The temperature jump across the molybdenum-cladding gap is directly proportional to the gap heat resistance and is affected mainly by:

- the filling gas conductivity k_{gas} , which contributes greatly to the conductive term of the heat resistance,
- the surface emissivity ε_{Mo} of the molybdenum discs, which limits the radiative heat exchange in the gap and
- the molybdenum thermal expansion α_{Mo} which changes the gap size.

Attention should be drawn to the effect that large uncertainties in these parameters would have on the temperature distribution. Focusing on the Ar-filled stack S41, the original axisymmetric simulation is repeated, each time increasing by 20% the value of one of the three parameters, k_{gas} , ε_{Mo} and α_{Mo} , while the other two parameters keep the nominal value. A fourth simulation is performed with an emissivity of 0.8 to include also the effect of possible molybdenum disc oxidation (see Sec. 7.3.1).

The results are summarized in Figure 7.4 where the calculated temperatures are plotted against the corresponding measurements. Increasing α_{Mo} or ε_{Mo} by 20% has a negligible effect, while the change in k_{gas} causes the temperature to decrease by $\sim 100\text{K}$. Finally, with an emissivity of 0.8, realistic only if the molybdenum discs were oxidized, the deviations remain larger than $\sim 300\text{K}$. This first parametric study suggests that even (improbable) large errors on the main parameters affecting the gap heat exchange do not justify the large deviations seen for the stacks S31 and S41.

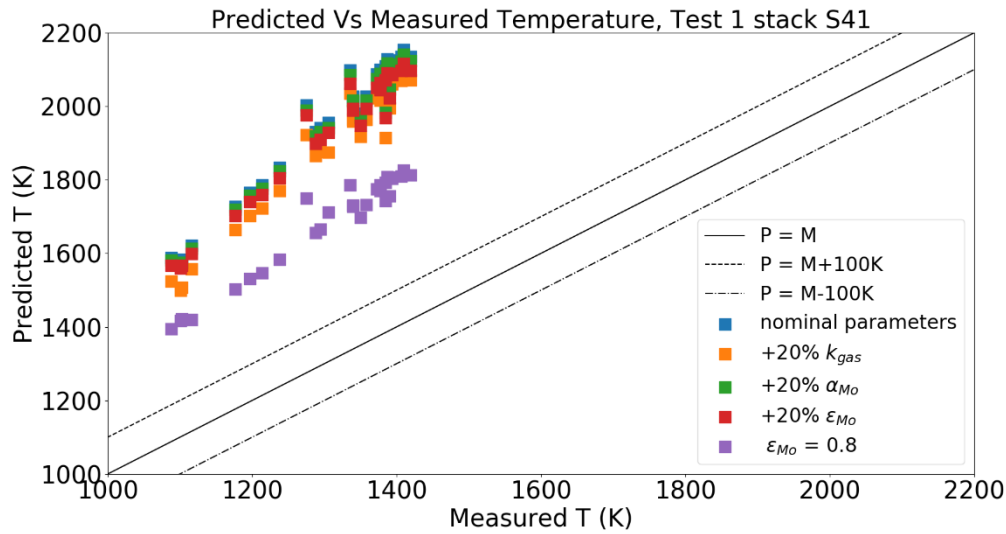


Figure 7.4 – Results of the parametric study on the gap heat transfer model. Temperatures obtained with OFFBEAT are plotted against the corresponding TC measurements.

7.4 3-D analysis of eccentricity

As shown in the previous section, it is difficult to explain the deviations seen for the HBRP stacks in the framework of a traditional axisymmetric analysis as applied in conventional fuel performance codes. For this reason, a set of 3-D simulations is performed with OFFBEAT to evaluate the impact of eccentricity on the two experimental assemblies considered in this Chapter. It is important to underline that this section refers only to the eccentricity between the inner stack (UO_2+Mo) and the cladding, although the PIE revealed also a considerable and variable amount of offset between consecutive discs. Due to the high conductivity of the molybdenum discs, it is reasonable to assume that their position relative to the fuel has a second order effect on the temperature distribution and it is not analyzed further.

7.4.1 Modeling approach and assumptions

For each stack, the irradiation history is combined with three different degrees of eccentricity, given as the amount of closed gap on the narrow side (in percent) and equal to 20%, 50% and 100%. Thus, an eccentricity of 100% is equivalent to the molybdenum disc touching the cladding at cold conditions. As shown on the left of Figure 7.5 with a cross section view of the 100% eccentric model used for the stack S41 from the first campaign, only the bottom fuel-molybdenum pair where the TC is located is modeled as eccentric. The computational grid is similar to the one used for the 2-D axisymmetric simulations, with 40 total divisions in the azimuthal direction. The same boundary conditions and assumptions discussed in Sec. 7.3.1 are used.

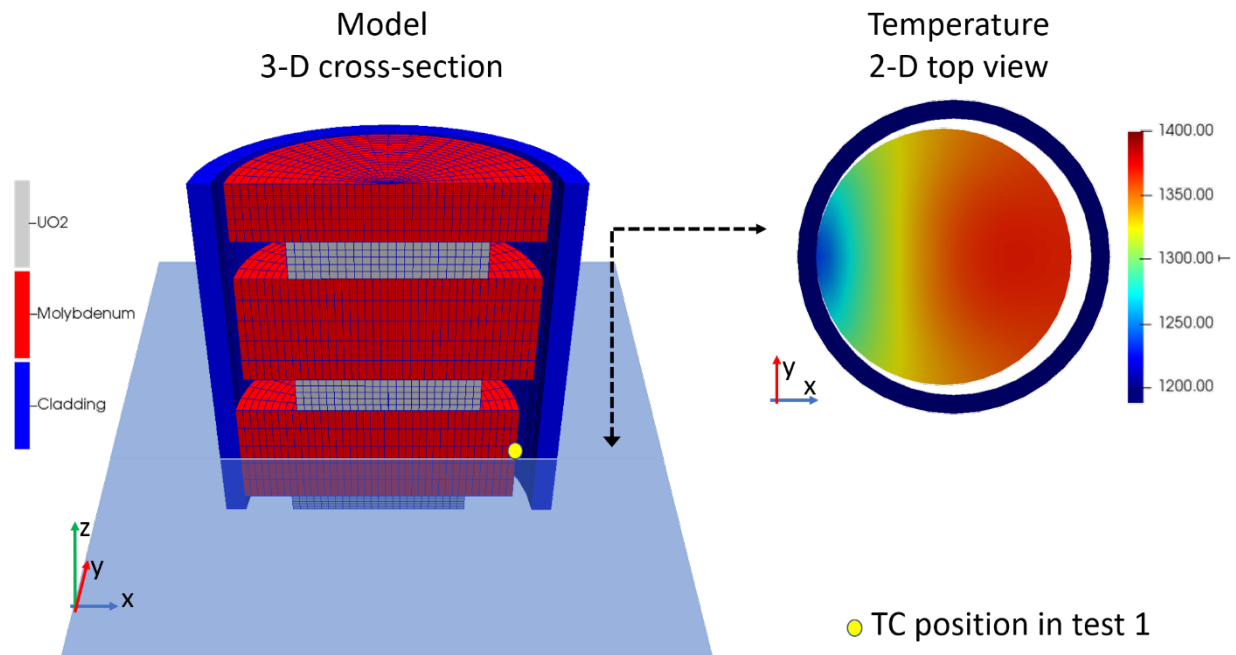


Figure 7.5 – Cross section of the 100% eccentricity model used for the stack S41 from the first campaign (left). Detail showing the 2-D temperature distribution on a horizontal slice at the center of the eccentric molybdenum disc (right).

7.4.2 Results

Figure 7.6 shows the results of the 3-D analysis for Rod1 of the second test. The fuel centerline temperature calculated with the three different degrees of eccentricity is plotted against the irradiation time. The results of the axisymmetric simulation and the TC measurements are added for comparison, showing a very good agreement. Similar graphs (not shown) are obtained for the remaining rods. As expected for a rod with a relatively large gap and partly filled with argon, OFF-BEAT predicts a significantly lower temperature with respect to the axisymmetric case once eccentricity is considered in the model. A difference of $\sim 200\text{K}$ compared to the concentric simulation is obtained when the molybdenum disc is already in contact with the cladding at the start of irradiation.

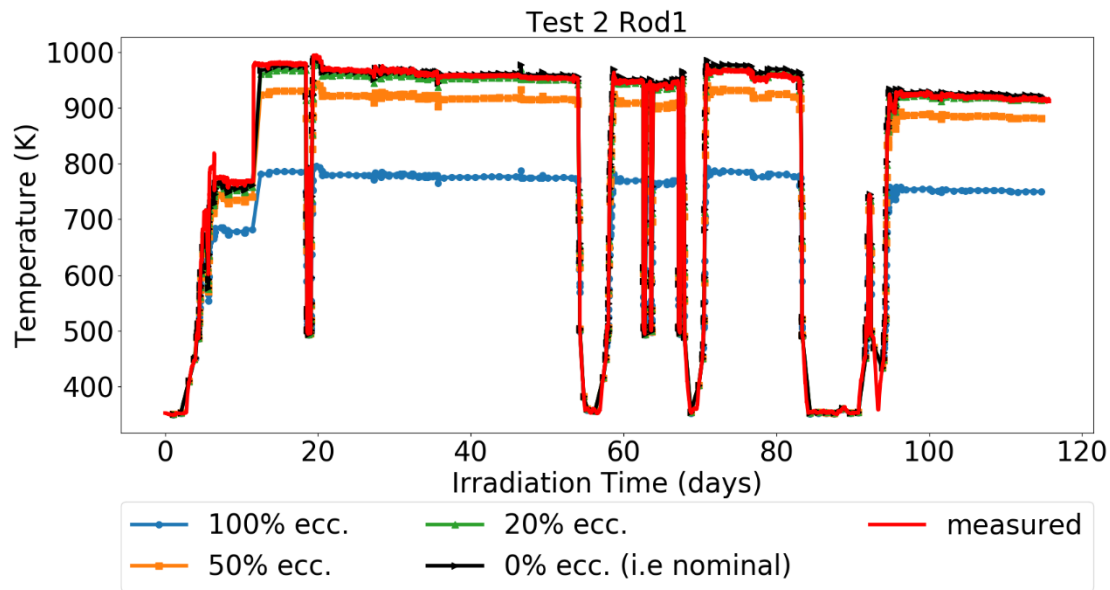


Figure 7.6 – Results of 3-D analysis for Rod1 of test 2 with varying degrees of eccentricity. Fuel centerline temperatures obtained with OFFBEAT are plotted against irradiation time. The measurements from center-line TC are included in the graph.

Figure 7.7 and Figure 7.8 show the results of the 3-D simulations performed for the stacks S11 and S41 in the first test, which represent the two opposite ends of the spectrum for this campaign in terms of temperature range. The distance between the calculation point and the TC location (which remains unknown) introduces a new degree of uncertainty in the results, given that, as shown in the top view on the right of Figure 5, the eccentricity causes a temperature gradient across the molybdenum disc. However, although the temperature difference between the two sides of the disc can reach ~150K in the most extreme case, the presence of such gradient cannot explain the 300K and 700K deviations seen for S31 and S41, and does not change the nature of the conclusions drawn in this and in the following section. For the sake of conciseness and clarity of exposition, only the temperatures on the wide side gap (corresponding to the yellow dot in Figure 7.5) are plotted in the following graphs.

Figure 7.7 reveals an initial temperature decrease measured during irradiation, which is caused by a change of the gas composition, as reported in the campaign main document (the change in gas composition is explicitly modeled with OFFBEAT). The temperatures displayed in Figure 7.7 and Figure 7.8 are taken from the molybdenum outer surface on the wide gap side, close to the area of maximum temperature as it can be seen in Figure 7.5. Because the results of the 3D simulations are always lower than those obtained with the nominal gap size, they suggest that any amount of eccentricity causes the temperature of the entire molybdenum disc to decrease. This is different from what is normally expected for traditional UO_2 pellets, where the wide gap side of the fuel surface becomes hotter than in the concentric case, and it is due to the much higher thermal conductivity of the molybdenum. The results also reveal that the effect of eccentricity is not linear:

the reduction in temperature is more pronounced as the molybdenum surface approaches the cladding.

The large difference between the 50% and the 100% eccentricity curves in Figure 7.6 and Figure 7.8 (but partially also in Figure 7.7) might seem excessive at a first glance. Because the conductance of the gap is dominated by its conductive component, one might expect that the temperature jump across the gap ΔT_{gap} would decrease in an approximately linear fashion with the gap size, and indeed this would be the case for two planar slabs approaching each other. However, when gradually increasing the eccentricity between two cylinders, the average gap conductance does not change linearly, as while the gap size decreases on one side, it increases on the other. This is evident from the curves for 50% eccentricity, which are far from showing a 50% decrease in ΔT_{gap} (the inner cladding temperature is always $\sim 580\text{K}$). It is only when a large part of the molybdenum outer surface is close to the cladding (i.e. at very high eccentricity values) that the average conductance increases significantly. The effect of eccentricity, although always present, is relatively much more important for rods with large gradient across the gap (as for the rods with large gaps and/or filled with Argon discussed in this Chapter) as already noticed by Williford and Hann in their analysis of the IFA-431.

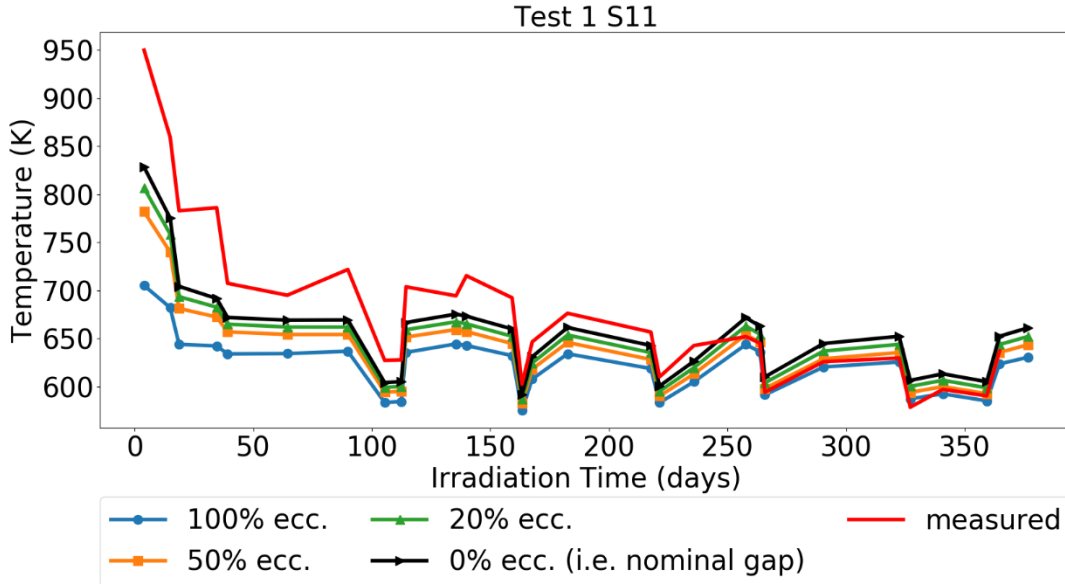


Figure 7.7 – Results of 3-D analysis for stack S11 from test 1 with varying degrees of eccentricity. Outer molybdenum temperatures obtained with OFFBEAT are plotted against irradiation time. The measurements from the TC are included in the graph.

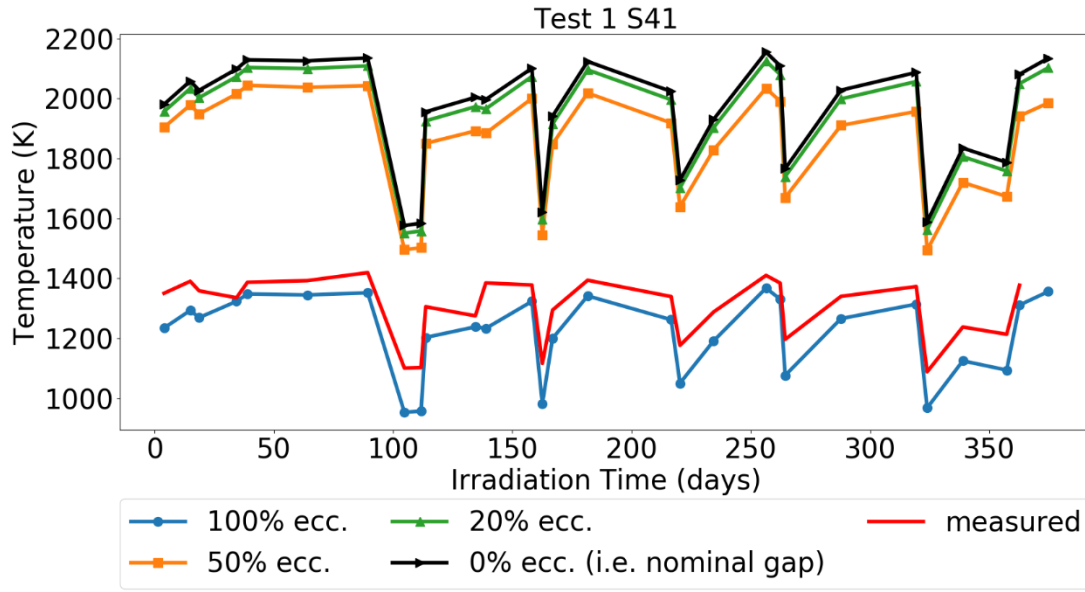


Figure 7.8 – Results of 3-D analysis for stack S41 from test 1 with varying degrees of eccentricity. Outer molybdenum temperatures obtained with OFFBEAT are plotted against irradiation time. The measurements from the TC are included in the graph.

As a summary, Figure 7.9 shows the results of the calculations obtained with the 100% eccentric assumption for all the stacks from the first test plotted against the corresponding TC measurements. The results obtained with the axisymmetric models are included for comparison. Once again, it is possible to notice that, although the qualitative behavior is the same in all the stacks, the relative importance of eccentricity increases from the small-gap He-filled S11 to the large-gap Ar-filled S41. When the gap is large, and the rod is filled with low-conductivity gas the axisymmetric gap conductance is very low. Thus, minor changes in eccentricity have a greater effect on the gap temperature jump, because the relative change in gap conductance is large. For helium-filled rods with smaller gaps, the axisymmetric conductance is very high, and the effect of eccentricity is less pronounced. This pattern is in line with the work of McNary et al [143] who analyzed the effect of eccentricity on the fuel-clad gap conductance in two dimensions. According to their findings, the azimuthal asymmetry in heat transfer is more relevant for low values of the Biot number, defined as:

$$B = \frac{(h \cdot r)}{\kappa} \quad (157)$$

where h represents the azimuthal average gap conductance, r corresponds to the disc radius and κ is the disc thermal conductivity. The presence of the highly conductive molybdenum makes the Biot number small if compared to traditional LWR rods. Moreover, given the disc dimensions and

gas compositions, the Biot number in the HBRP stacks is progressively decreasing, hence the effect of asymmetry is also expected to be gradually more pronounced from stack S11 to stack S41.

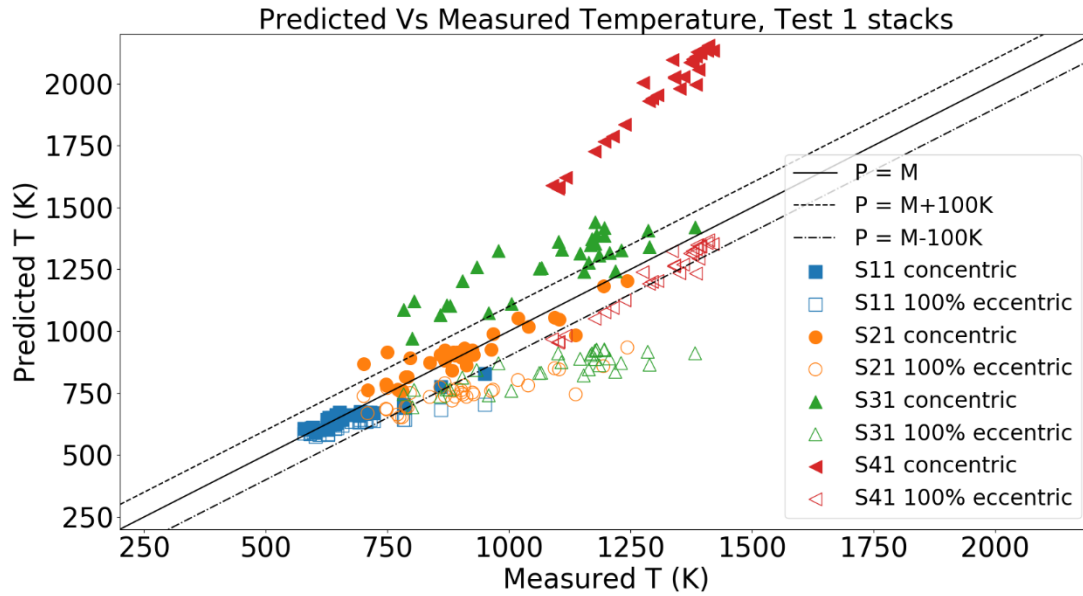


Figure 7.9 – Results of 3-D simulations with 0 and 100% eccentricity for the test 1 stacks. The calculated temperatures are plotted against the corresponding measurements.

For commercial rods, the Biot number is larger, since the filling gas is pressurized helium (except when poisoned with fission gas, but then usually the gap is small if not closed), and the conductivity of the UO_2 is about 40 times smaller in comparison with Mo. Thus, the effect of eccentricity is expected to be less relevant for LWR fuel rods. This is in line with earlier findings obtained with OFFBEAT [154], confirming that pellet eccentricity might affect the heat flux distribution but the overall effect on maximum and average fuel temperatures is relatively small for BWR fuel at low burnup during base irradiation.

To better visualize the impact of eccentricity and the conclusions drawn in this section, we calculate for each of the Test 1 stacks the quantity $\Delta T_{100\%}$:

$$\Delta T_{100\%} = \overline{T_{\text{Mo},100\%}} - \overline{T_{\text{Mo},0\%}} \quad (158)$$

defined as the time-average difference in molybdenum outer surface temperature between the 100% and 0% eccentricity curves. The metric $\Delta T_{100\%}$, shown in Table 7.3, is plotted against the respective Biot number in Figure 7.10. The Biot number used in the Figure is calculated with the time-averaged quantities, always shown in Table 7.3, obtained from the simulations with nominal gap size (i.e. 0% eccentricity). For comparison, we include in the Figure 7.10 the Biot number range for typical LWR rods, which according to McNary et. al. is between 8 and 20.

Table 7.3 –Time-averaged quantities for the calculation of the Biot number for Test 1.

Stack	Average h, W/(m ² K)	Average k, W/(mK)	r, m	B	$\Delta T_{100\%}$
S11	4.82E+03	123	0.00413	1.62E-02	~35
S21	1.65E+03	115	0.00408	5.87E-02	~140
S31	7.12E+02	103	0.00401	2.76E-02	~430
S41	3.33E+02	90	0.00388	1.44E-02	~750

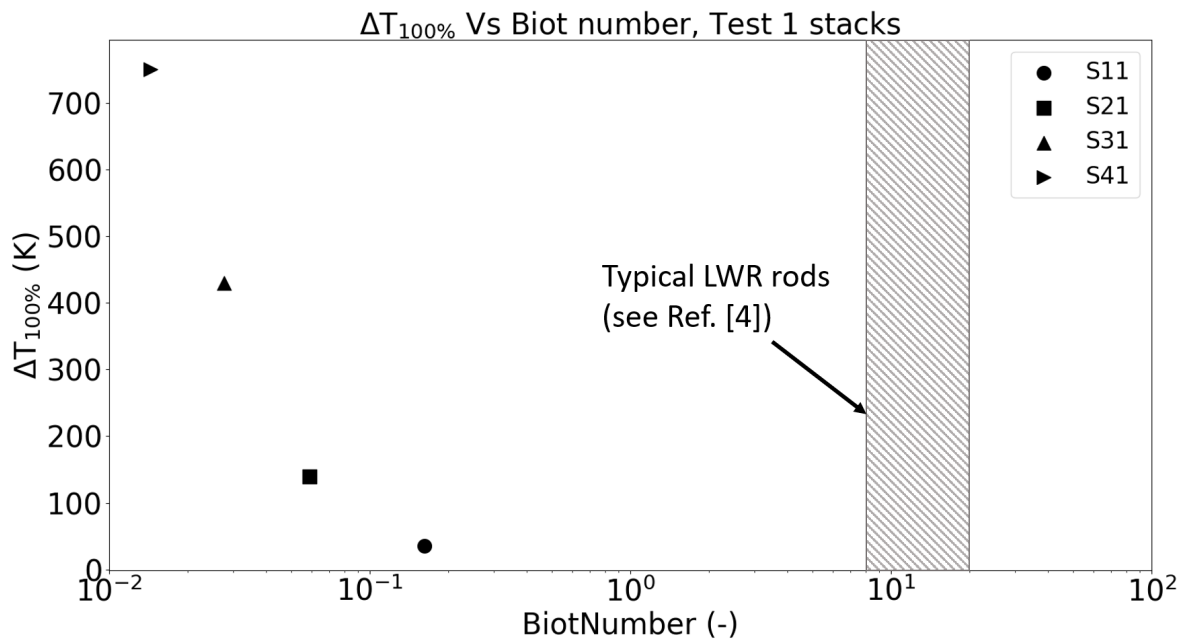


Figure 7.10 – Impact of eccentricity against Biot number for the stacks from Test 1. The impact of eccentricity is measured as $\Delta T_{100\%}$, i.e. the average temperature difference between the simulations with 100% and those with 0% eccentricity.

7.5 Conclusions

The work of Williford and Hann [141], and McNary et al. [143] pointed out that fuel eccentricity is expected to have a large impact on the temperature distribution of rods with high conductive fuel and large thermal gradients across the gap, due to large gaps or low conductive filling gases. This Chapter has investigated similar characteristics in the experimental setup of two fuel disc irradiation campaigns carried out in the HBWR, comparing the temperatures predicted by the multi-dimensional fuel performance code OFFBEAT against on-line measurements from thermocouples.

For the 4 rods of the first campaign, the results of 2-D axisymmetric simulations revealed a pattern, with the deviations gradually increasing from small-gap helium filled rods to large-gap argon filled rods. A sensitivity study on the main parameters affecting the gap heat transfer model con-

firmed that the large deviations seen for the two highest-temperature rods cannot be explained in the framework of a conventional fuel performance analysis without 3-D effects. For the 4 rods of the second experimental campaign, the temperature calculated with OFFBEAT were surprisingly close to the corresponding measurements, hinting at a minor role of eccentricity. This was attributed the presence of a central tube passing through the disc holes (absent in the first test) which limits the stack misalignment.

A set of 3-D simulations with increasing degree of eccentricity was performed, suggesting that eccentricity can indeed cause a large range of uncertainties in fuel disc temperature. In line with the findings of previous theoretical studies, the results of the 3-D simulations showed that the rods with larger gaps and low-conductivity filling gasses are more sensitive to the relative position between fuel column and cladding. Supported by the almost perfect predictions for the rods of the second campaign, the eccentricity was identified as the main factor contributing to the uncertainty in fuel disc temperature in the first test.

Nevertheless, no definitive conclusion can be drawn and a more quantitative estimation of the effects of eccentricity is premature at this stage. This would require knowledge about the exact positioning of all discs in each stack analyzed, as well as more temperature measurements. An extension of this work should also include assessing the effects of the fitting parameters of the FRAPCON gap conductance model. Being developed for conventional UO_2 -filled Zircaloy rods, the fitting parameters should be re-evaluated to take into consideration the presence of molybdenum. Also, a small-scale analysis of the heat transfer in the large gap between fuel discs and cladding might reveal the impact of the thin-gap approximation on the measured molybdenum temperature. Such an analysis would benefit from a set of out-of-pile experiments with corresponding rod slices heated by means of laser beams, as already applied in the POLARIS facility of the JRC Karlsruhe.

More importantly, the analysis performed in this chapter constitutes an example of how the advent of modern fuel performance tools with multi-dimensional capabilities can help the design and interpretation of separate-effect experiments. For instance, the design of a similar disc irradiation campaign in the High Flux Reactor in the Netherlands in the frame of the INSPYRE project for advanced fuel creep studies relied on the combined application of the TRANSURANUS code and a separate general-purpose tool for the 2D temperature calculations. A multi-dimensional fuel performance code is thus perfectly suited for the interpretation of such disc irradiations and for designing future experiments in new experimental reactors such as JHR. In view of the required computational costs, the coupling option between OFFBEAT and TRANSURANUS (discussed in the next Chapter) might be considered. The results of inexpensive 1.5D full-length simulations would help define more realistic initial and boundary conditions for computationally heavier multi-dimensional transients on a reduced geometry. This would allow the investigation of in-pile experiments with complicated irradiation histories addressing specific local phenomena such as PCMI, extending the analysis even for medium and high burnup.

Chapter 8

Multi-physics and coupling options⁷

This final chapter describes the first efforts carried out in the framework of this thesis to enable the interaction between OFFBEAT and other relevant codes used in the fuel modeling community. While multi-dimensional codes offer new application opportunities, allowing one to simulate complex phenomena such as ridging or an asymmetric heat exchange, their potential might be limited by the lack of behavioural models and input data that are appropriate for a multi-dimensional analysis. Also, despite the numerical advancements of recent decades and the increase of the available computational power, 2-D and 3-D simulations still have (and probably will always have) a significantly higher computational cost than legacy codes.

The limitation of traditional models derived from 1-D codes can be partly overcome by means of coupling with separate solvers dedicated to specific physics. MOOSE [18], CASL [56] and PLEIADES [137] are a few important examples of multi-physics and multi-scale framework used for fuel behavior analysis. Indeed, one of the most interesting aspect of the choice of OpenFOAM as development platform, is the possibility of a straightforward interaction between OFFBEAT and any other solvers developed with OpenFOAM, be it for chemistry, CFD, thermal-hydraulics or other physics.

Moving in this direction, a coupling methodology between OFFBEAT and the Monte Carlo neutron transport code Serpent has been developed in the context of this PhD thesis and is presented in Section 8.1. The methodology provides a high-fidelity solution for the neutron flux, isotopic composition and power distribution and allows one to extend the range of application of OFFBEAT to unusual configurations or new fuel types for which the response of traditional neutronics models is not accurate.

A way to assist the multi-dimensional simulation and alleviate the computational burden might derive from the realization that in many scenarios of interest the multi-dimensional aspect under analysis is either localized to a short section of the rod (e.g. a single defective pellet) or it starts to be relevant only after a certain portion of the base-irradiation history (e.g. a power transients at medium or high burnup). The coupling between a high-fidelity tool and a legacy code, with the latter providing the initial conditions for a multi-dimensional transient analysis, might be an interesting opportunity to take make the best use of both codes. The first steps toward the develop-

⁷ The content presented in Section 8.1 are partially available in [175].

ment of a coupling strategy between OFFBEAT and the European fuel performance code TRANSURNUS are discussed in Section 8.2. Finally, the relevant conclusions for this chapter are then drawn in Section 8.3.

8.1 Coupling with the Monte Carlo neutron transport code Serpent

At an early stage of irradiation, a radial power profile establishes in the fuel pellets with a characteristic peak in the pellet rim. Part of the thermal energy production is shifted closer to the cooling water, affecting the thermal response of the fuel rod. Additionally, a complex interplay exists between radial profile and fuel burnup. This follows the non-uniform production and consumption of fissile atoms and the changes in neutron flux level and spectrum.

In the context of a base irradiation fuel performance simulation, the radially averaged power produced in the fuel is usually known as part of the case data and it is provided to the code as a constant or time-varying input parameter. The radial profile, instead, is not known and it must be calculated for an accurate prediction of the fuel temperature. For this purpose, several neutronics models have been developed over the years and are now implemented in most of the traditional fuel performance codes. The RAPID model [155] used in COSMOS, the TUBRNP model [17] used in TRANSURANUS and FRAPCON or the PLUTON model [156] used in FEMAXI3 are few important examples, but a more comprehensive review can be found in the article by Van Uffelen et al. [4].

To calculate the fuel radial power profile, the neutronics models need to track the evolution of the fuel composition and determine the neutron flux. Because of the complexity of this task and due to computational requirements, the models found in fuel performance codes are considerably simpler than stand-alone neutronics codes, as they:

- Focus on a selected number of isotopes, relevant for power production and neutron transport.
- Use the diffusion theory approximation, with few energy groups, for the determination of the neutron flux.
- Employ effective cross sections or radial form factors to take into account resonance effects, burnup, enrichment level or the content of burnable absorbers.

These simplified neutronics models have been shown to provide accurate power profiles up to high burnups for traditional LWR fuel rods and have been validated in multiple occasions, using either depletion and neutronics codes or measured radial profiles for actinides concentration and burnup [67], [157], [158]. However, larger deviations are expected in the presence of strong absorbers such as Gadolinium or for unusual fuel configurations such as those found in many experimental reactors.

The coupling between a fuel performance code and a higher-fidelity neutronics code is an interesting option to increase the accuracy of the calculations, at the cost of higher computational re-

quirements, and it has been already considered for legacy codes such as TRANSURANUS [159]. The coupling is particularly relevant for multi-dimensional codes like OFFBEAT as a way to overcome the limitations imposed by traditional simplified models, allowing for a proper multi-physics analysis of asymmetric cases. This possibility is becoming particularly attractive in the present days thanks to the availability of HPC as well as powerful desktop machines. For this reason, a coupling methodology between the fuel performance code OFFBEAT and the Monte Carlo neutron transport code Serpent has been developed in the framework of this PhD thesis and it is presented in the next sections. The coupling strategy is described in Section 8.1.1. Then it is put to a test in Section 8.1.2 and Section 8.1.3 with two cases, a UO₂ rod and a Gd₂O₃-UO₂ rod. Finally, the relevant conclusions and outlook are discussed in Section 8.1.4.

8.1.1 Coupling strategy

The coupling between OpenFOAM-based solvers and Serpent is relatively straightforward thanks to the Serpent multi-physics interface [160], [161], which was successfully employed in the past for the coupling of neutronics and CFD [162], [163]. An interface file is used to import the OFFBEAT geometry, materials, and temperatures into the Serpent model. The power is calculated with Serpent and is written in a readable format for OpenFOAM. The evolution of the isotopic concentrations is handled within Serpent as well, using predictor/corrector-based burnup schemes. In each Serpent simulation, the corresponding OFFBEAT cell is found for each interaction point using a Cartesian search mesh overlaid over the OFFBEAT mesh. The density of the search mesh is gradually refined in the areas of the model with the highest number of cells, significantly reducing the memory consumption of the searching algorithm.

The Serpent multi-physics interface only allows for a simple explicit coupling between the two codes. To simulate the full rod history with an implicit coupling scheme, a Python wrapper code is developed to manage and synchronize the two codes. At the beginning of the coupled simulation, the two codes are initialized: the initial temperatures and the subdivision in material zones are set in OFFBEAT, while the initial material compositions are set in Serpent and the cross sections library is loaded. The coupling procedure between Serpent and OFFBEAT at a given time step is summarized in Figure 8.1 and it is described in the following paragraphs.

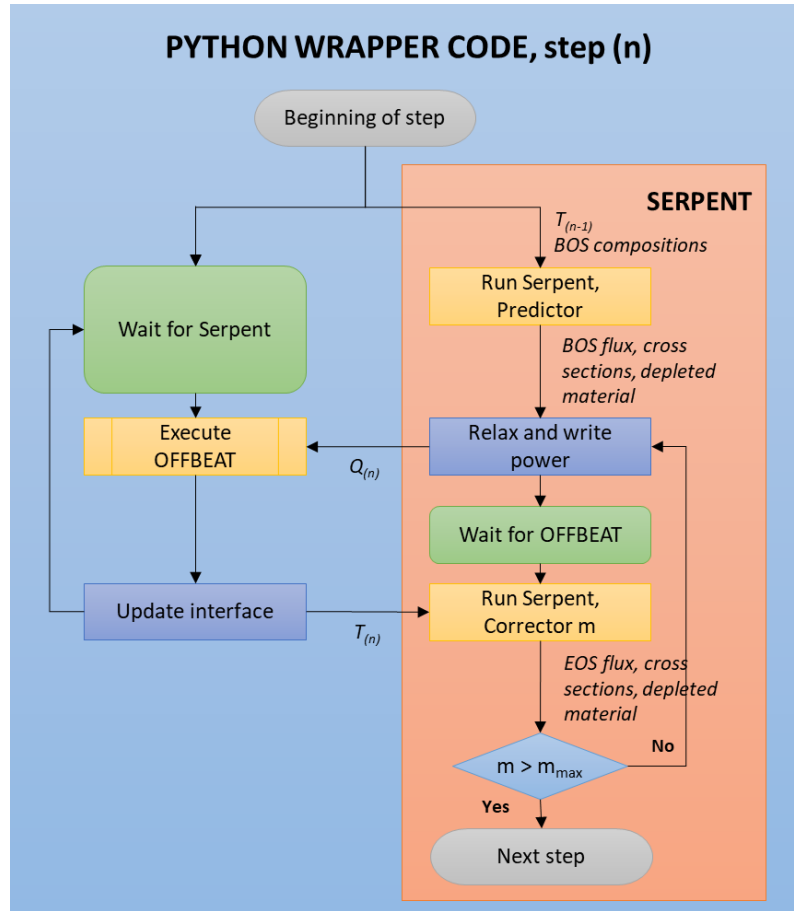


Figure 8.1 - Flowchart of the external coupling between OFFBEAT and Serpent

At the beginning of the time step t_n , Serpent calculates the flux at t_{n+1} using the cross sections obtained at the end of time step t_{n-1} . The corresponding volumetric power is passed to OFFBEAT, and the materials are depleted for the given burnup increment. This is the end of the predictor step and Serpent is paused.

With the updated power profile, OFFBEAT calculates the t_{n+1} temperature distribution which is mapped back to the Serpent model. OFFBEAT is paused and Serpent proceeds to the corrector step. The new set of cross sections is calculated based on the updated temperatures and depleted materials. The flux at t_{n+1} , as well as the end of step fuel composition, are calculated once again.

Finally, the predictor and corrector cross sections are averaged for a more accurate representation of the fuel depletion through the burnup step ($t_{n+1} - t_n$). This corresponds to a linear interpolation between the predictor and corrector step and the described method is called Constant Extrapolation/Linear Interpolation (CE/LI). Other methods are available in Serpent for calculating the updated cross sections, such as the Constant Extrapolation (CE), Linear extrapolation with linear interpolation (LE/LI) or Linear extrapolation with quadratic interpolation (LE/QI) methods.

The burnup step can be divided in a few sub-steps (without running additional transport or OFFBEAT simulations) to provide more accurate results. Also, the implicit coupling is obtained by repeating the corrector step m times (with the integer m chosen by the user) before the final average is performed.

8.1.2 PWR test case

The coupling methodology represented in the previous section is put to a test with two cases, representing a typical PWR rod and a Gd-doped BWR rod. For simplicity, only the temperature is solved for in OFFBEAT and constant material properties are used.

The first test case is a 3.5% enriched UO_2 rod burned up to 102 MWd/kgHM with the dimensions and composition shown in Table 8.1. The case is derived from a study comparing the results obtained with TURBNP and with the Monte Carlo code ALEPH [164].

Table 8.1 - PWR case characteristics

Fuel pellet	
Radius	4.65 mm
Material	UO_2 (3.5 wt.-% enriched)
Density	10.42 g/cm ³
Length	1 mm
Linear power	20 W/mm
Gas	
Gap width	190 μm
Component	He
Cladding	
Cladding thickness	0.535 mm
Material	Zircaloy-4
Density	6.55 g/cm ³
Water	
Temperature	600 K
Boron concentration	420 ppm
Pitch	1.496 mm

The rod is approximated as an axisymmetric cylinder in plain strain. Thus, in OFFBEAT, only a quarter of a thin vertical slice is replicated, with empty boundary conditions on the top and bottom patches. Figure 8.2 shows the corresponding Serpent model, where reflective boundary conditions are applied at the borders. The fuel region is divided into 20 radial zones, with a finer radial mesh towards the rim in order to correctly capture the power gradient.

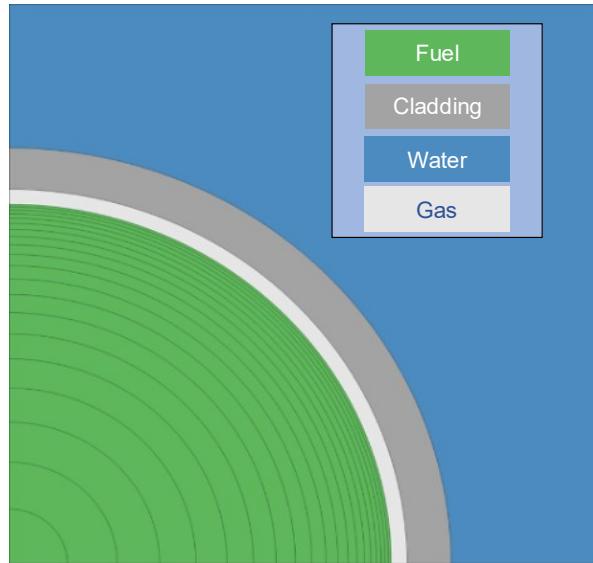


Figure 8.2 – PWR case Serpent model

The fission source is initialized with 50 inactive cycles, while 300 active cycles with 50,000 neutrons per cycle are chosen to reach good statistical accuracy. An integration step of 2 MWd/kgHM is used, but each burnup step is further split into 10 sub-steps. A predictor-corrector CE/LI scheme is employed, with 1 corrector step. The coupled simulation was performed on a desktop computer using 8 3.50 GHz cores. The running time is largely influenced by the Serpent simulations, each step taking approximately 60 min. The running time of OFFBEAT (in particular for this simplified case where only the temperature field is solved for) is negligible compared to that of Serpent. The same case is simulated also with the TUBRNP standalone model from the TRANSURANUS code.

Figure 8.3 shows the evolution of the total plutonium concentration along the burnup, obtained with the OFFBEAT/Serpent coupling and TUBRNP. Up to around 50 MWd/kgHM, the profile predicted by the coupled codes does not differ significantly from that obtained with TUBRNP. However, at higher burnups, the TUBRNP profile seems to reach a saturation value, underestimating the final plutonium content in the rod. As noted already in the comparison with the ALEPH code [164], this is probably due to the fact that only a selected group of isotopes is considered in the TRANSURANUS neutronics model. Therefore, there is only a limited number of paths that can lead to the production of plutonium while, in Serpent, virtually all possible paths are taken into account.

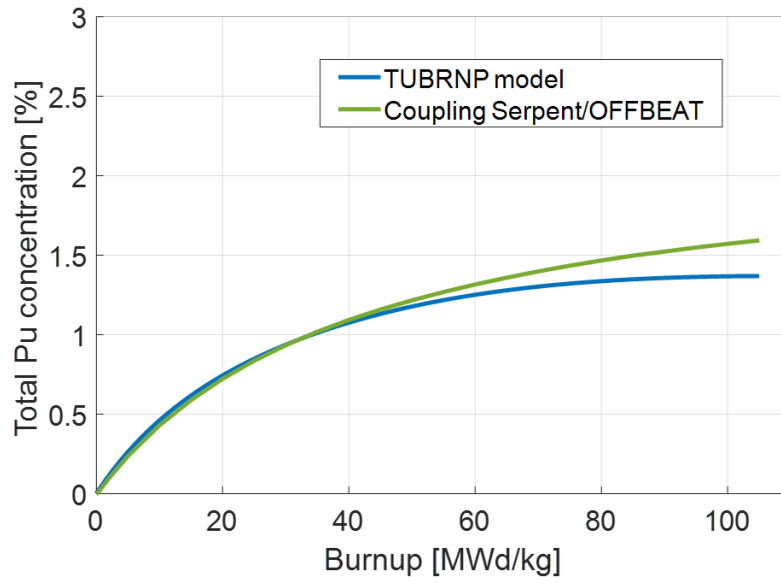


Figure 8.3 – Comparison between the plutonium concentration evolutions calculated by TUBRNP and the OFFBEAT-Serpent coupling.

However, as expected for a typical PWR rod, the coupling with Serpent does not improve significantly the prediction of the normalized radial concentration profiles for many of the isotopes of interest, even up to 102 MWd/kgHM. This can be observed for Pu^{239} in Figure 8.4 at 5 (left figure) and 100 MWd/kgHM (right figure).

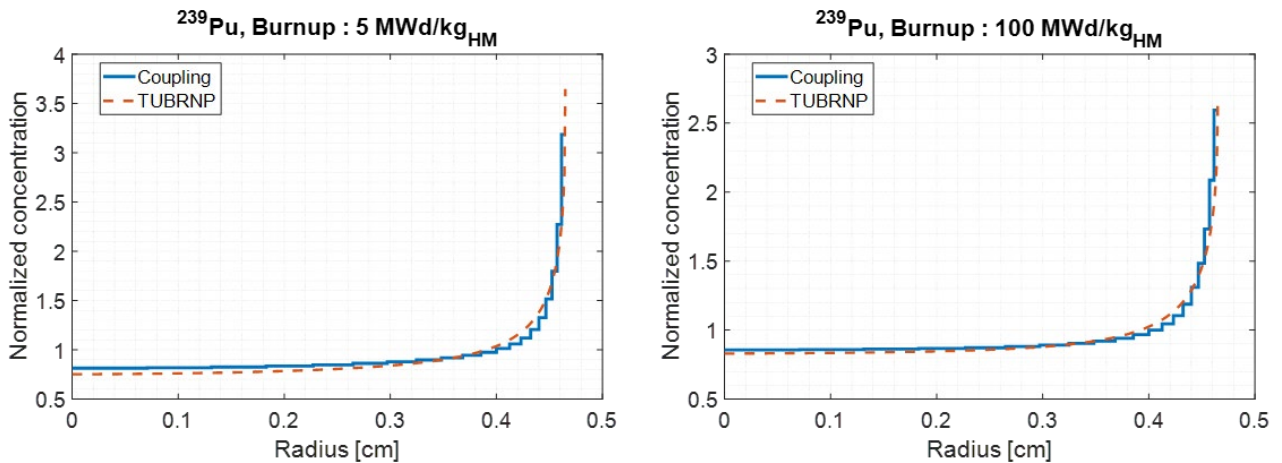


Figure 8.4 – Comparison between the Pu^{239} radial concentration obtained with OFFBEAT/Serpent and TUBRNP at 5 MWd/kgHM (left) and 100 MWd/kgHM (right).

Larger deviations between the predictions of the two tools are observed for the U^{235} radial profile, in particular at medium and high burnups. This can be seen in the left and right portion of Figure 8.5, respectively at 50 and 100 MWd/kg_{HM}. However, these differences do not translate in large deviations for the normalized radial power profile as can be seen for the same burnup levels in Figure 8.6. This is probably due to the fact that, as the fuel is burned and U^{235} is depleted, the Pu^{239} and Pu^{241} relative importance for power production increases, reducing the effect of the larger deviations found for U^{235} .

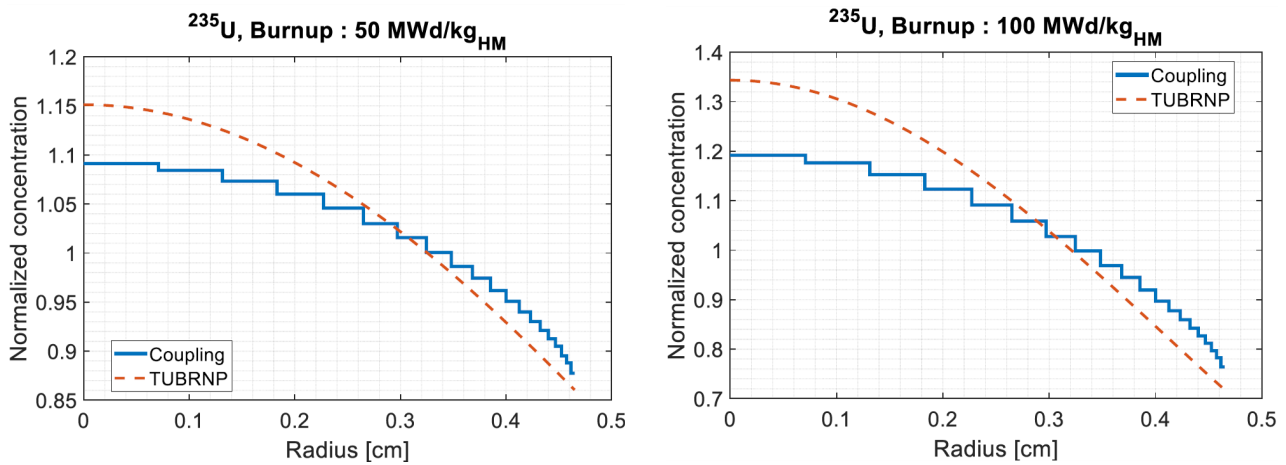


Figure 8.5 – Comparison between the U^{235} radial concentration obtained with OFFBEAT/Serpent and TUBRNP at 50 MWd/kg_{HM} (left) and at 100 MWd/kg_{HM} (right).

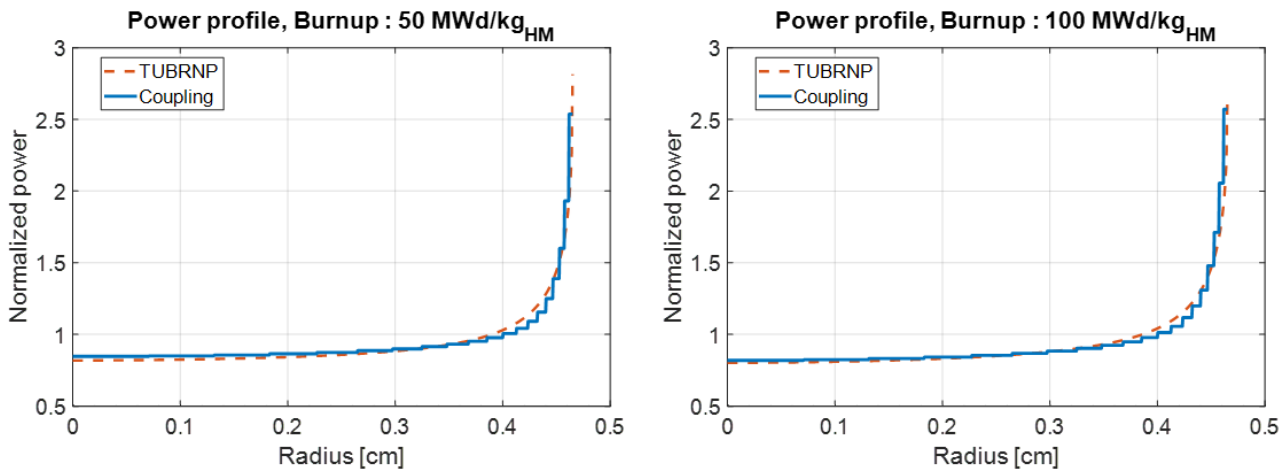


Figure 8.6 – Comparison between the normalized radial power profile obtained with OFFBEAT/Serpent and TUBRNP at 50 MWd/kg_{HM} (left) and at 100 MWd/kg_{HM} (right).

8.1.3 Gd-doped BWR test case

The second test case is a Gd-doped UO_2 rod, irradiated up to a burnup 110 MWd/kgHM. The case is taken from the study of BWR lattice with Gadolinium pins [165], and the dimensions and composition are shown in Table 8.2. The rod belongs to a 4x4 assembly, made by fourteen 3.5% enriched UO_2 rods and two Gd-doped rods (3% in weight), placed close to the center of the assembly.

A single Gd-doped rod is modeled in OFFBEAT, as a thin vertical slice with empty boundary conditions at the top and bottom patches. The corresponding Serpent model is shown in Figure 8.7. The coupled rod (the one in violet close to the center) is just one of the 16 rods of the assembly. Indeed, due to the non-uniformity of the rod compositions, this time the entire assembly must be modeled in Serpent to accurately reproduced the flux in the coupled rod. Periodic boundary conditions are applied at the border of the model. Symmetrical features of the assembly are used to reduce the number of materials to deplete in the burnup step. Thus, two fuel regions sharing the same color in Figure 8.7 indicates that the rods are burned as one material, using an average flux. In TUBRNP, the same test case is replicated modeling a single Gd-doped UO_2 rod.

The same desktop computer is used for this second test case. A higher number of material zones is needed, given that the remaining 15 rods of the assembly are also modeled. Therefore, due to RAM limitations, the radial subdivisions in the coupled fuel region are decreased from 20 to 10. In order to maintain a reasonable running time, the number of inactive cycles, active cycles and neutrons per cycles stay fixed to 50, 300 and 50'000 respectively. An integration step of 0.25 MWd/kgHM is used until a burnup of 10 MWd/kgHM so that the rapid depletion of the Gadolinium isotopes can be captured. Afterwards, the step changes to 2 MWd/kgHM. Once again, each burnup step is further split into 10 sub-steps and a predictor-corrector CE/LI scheme with 1 corrector is employed.

Table 8.2 - BWR case characteristics

Fuel pellet	
Radius	5 mm
Material	UO ₂ (3 wt-% enriched)
Density	10.0 g/cm ³
Power density	20 W/g
Gd-doped pins content	3 wt-%
Temperature	873.15 K
Cladding	
Cladding thickness	0.5 mm
Material	Zircaloy-2
Density	6.55 g/cm ³
Temperature	573.15 K
Water	
Temperature	559.15 K
Pitch	1.496 mm



Figure 8.7 – BWR case Serpent model.

Figure 8.8 shows the evolution of the total plutonium concentration during irradiation, comparing the results from OFFBEAT/Serpent and those from TUBRNP. In contrast with the plain UO₂ case, the use of the coupled codes provides significantly different results starting from an early burnup, with a maximum relative difference of about 20% at 40 MWd/kgHM.

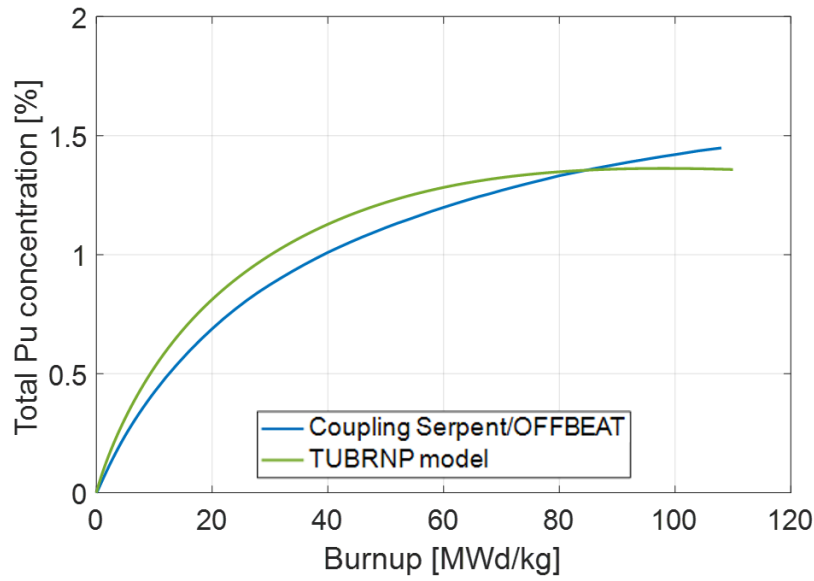


Figure 8.8 – Comparison between the plutonium concentration evolutions with TUBRNP and the coupling for the Gd-doped BWR

The presence of the strong absorbing Gd^{155} and Gd^{157} causes steep gradients in the flux that make the diffusion approximation less accurate. Indeed, a significant difference at low burnups is observed for the normalized radial concentration profiles. As an example, the left of Figure 8.9 shows the results for Pu^{239} at 5 MWd/kgHM.

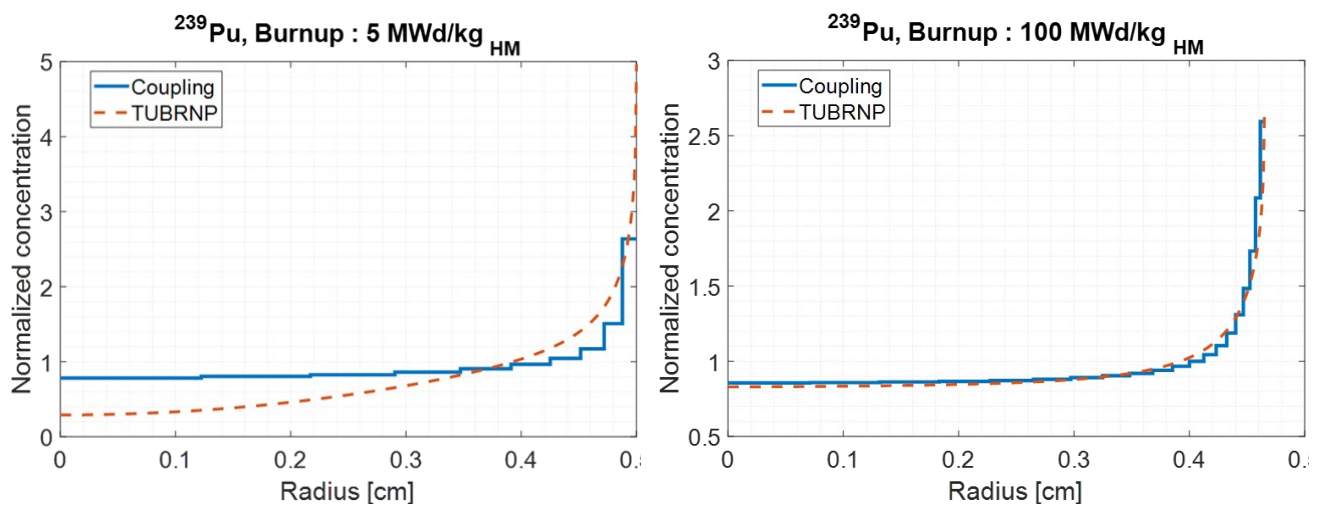


Figure 8.9 – Comparison between the Pu^{239} radial concentration obtained with OFFBEAT/Serpent and TUBRNP for the Gd-doped rod at 5 MWd/kgHM (left) and at 100 MWd/kgHM (right).

Gd^{155} and Gd^{157} are entirely depleted between 6 and 10 MWd/kgHM as shown on the left of Figure 8.10. From this point onward, the rod approaches the behavior of a traditional UO_2 rod and TUBRNP once again compares well with OFFBEAT/Serpent, as shown on the right of Figure 8.10. Similar conclusions can be drawn for the normalized radial concentration of Pu^{239} and normalized power profile at 100 MWd/kgHM shown respectively on the right of Figure 8.9 and in Figure 8.11.

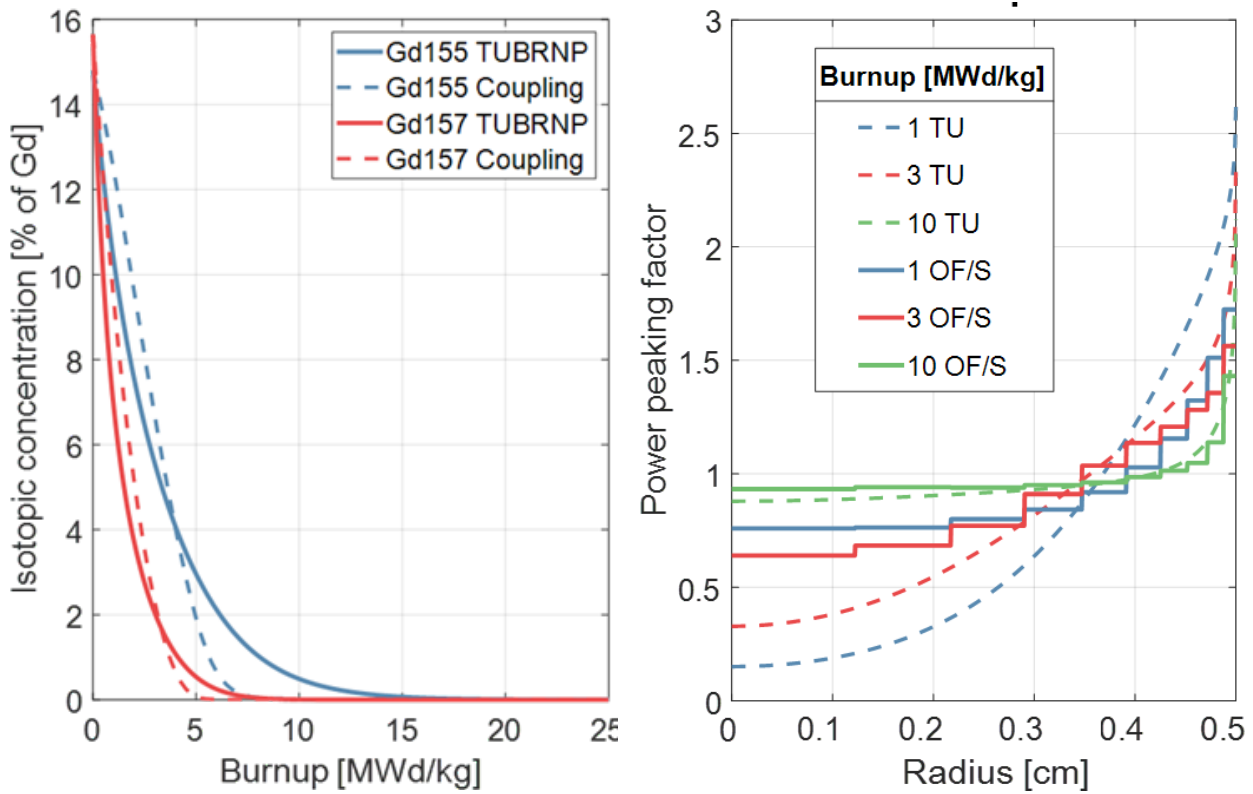


Figure 8.10 – BWR case, comparison between OFFBEAT/Serpent and TUBRNP: the evolution of the Gd^{155} and Gd^{157} total concentration is shown on the left; the power peaking factor or normalized radial power profiles at 1, 3 and 10 MWd/kgHM is shown on the right.

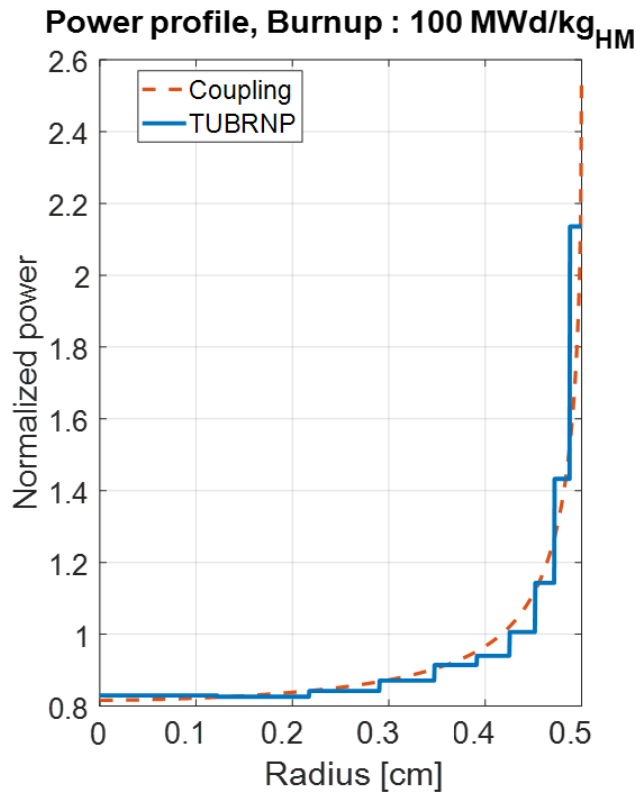


Figure 8.11 – Comparison between the normalized radial power profile obtained with OFFBEAT/Serpent and TUBRNP at 100 MWd/kgHM for the BWR test case.

8.1.4 Remarks and outlook

The coupling methodology between OFFBEAT and the Serpent2 code suffers from some limitations that should be addressed in the future. The methodology has been tested on simplified cases, with OFFBEAT calculating only 1-D temperature profiles and using constant material properties.

The next development steps should consider activating the full list of features of OFFBEAT and introducing the update of the Serpent geometry with the strains calculated by OFFBEAT. Because the running time is dominated by the Serpent calculations and the change of cross sections and power profile due to the variation in temperature is small, one could expect that neglecting the thermo-mechanical behavior of the rod should not affect excessively the coupling performance. Nevertheless, this hypothesis must be put to test with the analysis of more complex scenarios.

Also, the neutron flux calculated by Serpent has been azimuthally averaged to calculate the fuel depletion, even for the intrinsically 2-D case studied in Section 8.1.3. Although it will certainly make the coupled simulation even more demanding from a statistical point of view, some form of strategy for the azimuthal discretization must be introduced to accurately assess the effect of asymmetries in fuel power distribution deriving for example from an asymmetric heat exchange with the coolant due to non-uniform oxide and/or clad layers.

Another interesting application could be the analysis of the axial variation in the fuel rod power profile due to the insertion of a control rod in the assembly. This would require the extension of the coupling methodology to 2-D r-z or 3-D cases, although the axial discretization would contribute to increase the computational demand.

It must be stressed, however, that the coupling methodology has been tested only on single desktop machines. In the future, the use of high-performance clusters up to thousands of cores is advisable, making good use of the excellent scalability of Serpent.

8.2 Coupling with TRANSURANUS

During normal operation, the average behavior of a traditional LWR fuel rod is usually accurately captured by the 1.5-D approximation. However, the multi-dimensional nature of the rod might become relevant under certain irradiation conditions, for example during a transient such as a fast power ramp that takes place at a medium or high burnup. In other scenarios, the multi-dimensional phenomena under study such as the presence of a defective pellet remains localized to a limited section of the fuel pin, and it can be assumed not to influence the average behavior of the full-length rod. In all these cases, despite being necessary for fixing accurate initial and boundary conditions, simulating the entire base irradiation of the full-length rod consumes a considerable portion of the available computational resources.

The coupling between a legacy 1.5-D code and a modern multi-dimensional tool could offer an interesting opportunity to overcome this issue and make the best use of the peculiar characteristics of both approaches. An efficient and well-validated legacy code could be used to simulate the full-length rod base irradiation, transferring only the necessary data and fields as initial and boundary conditions for a detailed 2-D or 3-D simulation. As an example of this possible application, a coupling between the European code TRANSURANUS and OFFBEAT has been envisioned in the framework of this PhD thesis. The first steps toward the development of such coupling strategy are presented in the next sections. The coupling methodology, presented in Section 8.2.1, is put to test for simulating the final power ramp of the AN3 segment from the Risoe3 experiment. The case setup is described in Section 8.2.2 and after a quick verification against a separate stand-alone TRANSURANUS run discussed in Section 8.2.3, the results of the coupled simulations are presented and analyzed in Section 8.2.4. Finally, the relevant conclusions are drawn in Section 8.2.5.

8.2.1 Coupling strategy

The coupling methodology between TRANSURANUS and OFFBEAT makes use of the restart option available in TRANSURANUS. When activated, the code stops the simulation at a specified time-step and prints the rod information necessary for the restart into a binary file.

First, a series of Fortran routines extract the rod data (such as the rod geometry and the gap pressure) and fields (such as temperature, strains, or stresses) from the restart binary file, writing them into a text file as a series of readable arrays.

Then, this text file is accessed by a Python script that maps the information into the OFFBEAT geometry, taking care of applying appropriate unit conversion when needed (i.e. the units of some fields are different between the two codes). More precisely, the Python script performs an intermediate step creating a 3-D OFFBEAT version of the TRANSURANUS geometry, with a computational mesh consistent with the TRANSURANUS discretization. The 1-D fields are translated to this intermediate geometry with a 1-to-1 mapping as each TRANSURANUS grid point corresponds to a point in the mesh of OFFBEAT. Finally, using standard volume-average routines available in OpenFOAM, the fields are mapped to the actual OFFBEAT case, which might correspond to the entire rod or to just a short section, and can be modelled in 1-D, 2-D or 3-D with an arbitrary mesh. The intermediate step is not necessary per se, but it is useful to avoid possible errors due to custom mapping routines when having geometries with significantly different meshing.

If needed, the Python script can select for the mapping only a subset of the fields available in the TRANSURANUS restart file. This could be useful first of all because the two codes might have different models for treating the same phenomena, but also for performing sensitivity analysis on the initial conditions of the transient.

The two coupling tools (the Fortran routines on one hand and the Python script on the other) have been developed to be independent from each other. When the format of the intermediate text file containing the 1-D fields is set, a similar coupling methodology could be developed between TRANSURANUS and another multi-dimensional code or between OFFBEAT and a different 1.5-D code.

The coupling methodology just described is summarized in Figure 8.12. Consistency checks were performed to verify that the mapping routines work as intended.

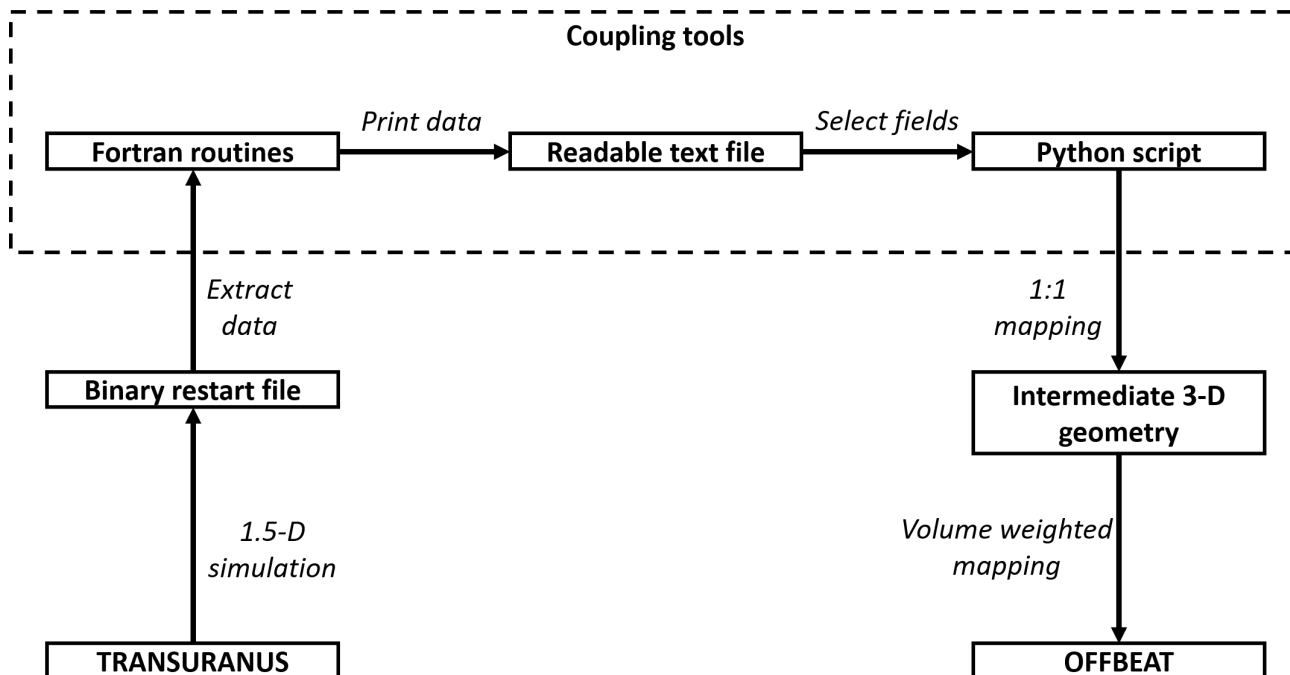


Figure 8.12 – Coupling scheme between TRANSURANUS and OFFBEAT.

8.2.2 Risoe3 AN3 segment simulation setup

The coupling methodology is tested on the AN3 segment from the Risoe3 experiment, already analyzed in Chapter 6 for validation purposes. The main objective of this study is predicting the final cladding outer diameter and the formation of the cladding ridges. It is here recalled that after a base irradiation up to a burnup of ~ 30 MWd/kgU, the AN3 segment was refabricated, re-filled with helium, and bump tested for 72 hours. The full power history with a closeup view of the bump test is shown in Figure 8.13, where the power is normalized with respect to the bump test peak value. Besides showing the fission gas release fraction obtained after puncturing the rod, the PIE provided the outer cladding profilometry prior and after the bump test. The data show a shrinkage of the outer rod diameter after base irradiation due to cladding creep-down, followed by a permanent expansion during the bump test with significant ridging.

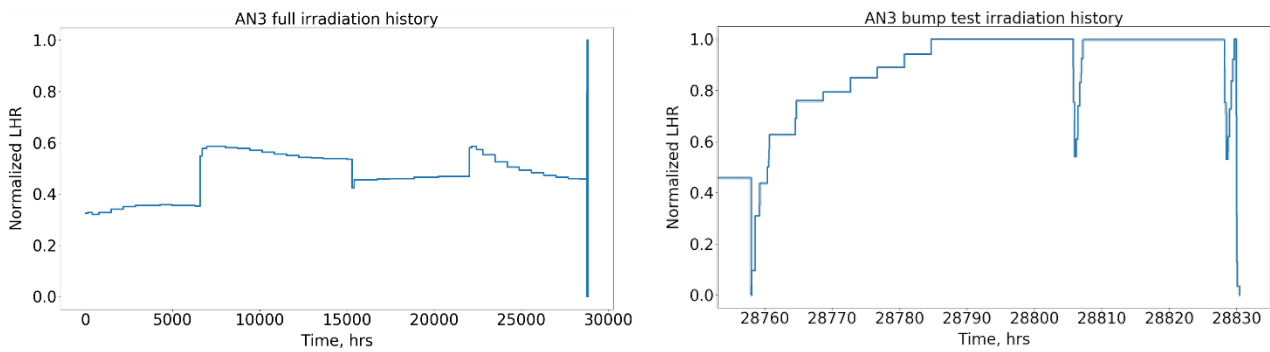


Figure 8.13 – Full (left) and bump test (right) irradiation history for the AN3 segment. The power is normalized to the bump test peak value.

The coupling approach consists in modeling the steady-state base irradiation with TRANSURANUS and the bump test with a transient OFFBEAT simulation. The long list of fields transferred from TRANSURANUS to OFFBEAT includes swelling, relocation, densification, plastic, and creep strains, as well as the fission gas concentration in the fuel grain and grain boundaries and all the remaining fields related to the fission gas release module. As done in other studies [166], the geometry of the refabricated segment is used for both base irradiation and bump test. Only the plenum is adjusted to reflect the difference in free volume available between mother rod and refabricated segment.

To verify the mapping methodology (and as an additional consistency check for OFFBEAT), three OFFBEAT models are separately coupled to TRANSURANUS: a 1.5-D model consistent with the TRANSURANUS model; a 2-D axisymmetric model with a smeared pellet column and a coarse mesh; and a 2-D axisymmetric model that includes 7 more refined discrete pellets in the central section of the rod. The 2-D models include the rod's bottom and top caps. The three geometries and related meshes are shown in Figure 8.14. After careful mesh convergence studies, the radial cell size (along the x-direction) in the three OFFBEAT meshes is chosen to be identical to the TRANSURANUS model, i.e. the fuel is radially divided in 35 cells progressively refined toward the outer surface while the cladding is divided in 8 cells. The number of axial cells (along the z-direction) is particularly relevant for the discrete pellet model in order to capture the hourglass and ridging phenomena. The mesh convergence study revealed that 80 axial divisions per pellet are optimal for this case, even though already 40 cells per pellet might provide sufficiently accurate results. Regarding the boundary conditions applied to the OFFBEAT models, the bottom surfaces of the rod are fixed, while the top and bottom surfaces of the discrete pellets in the third model are coupled with the implicit contact boundary condition. The penalty method is used for the surfaces facing the gap with a high penalty factor of 0.5 and with significant under-relaxation of the interfacial pressure. This leads to a stable solution with negligible interpenetration.

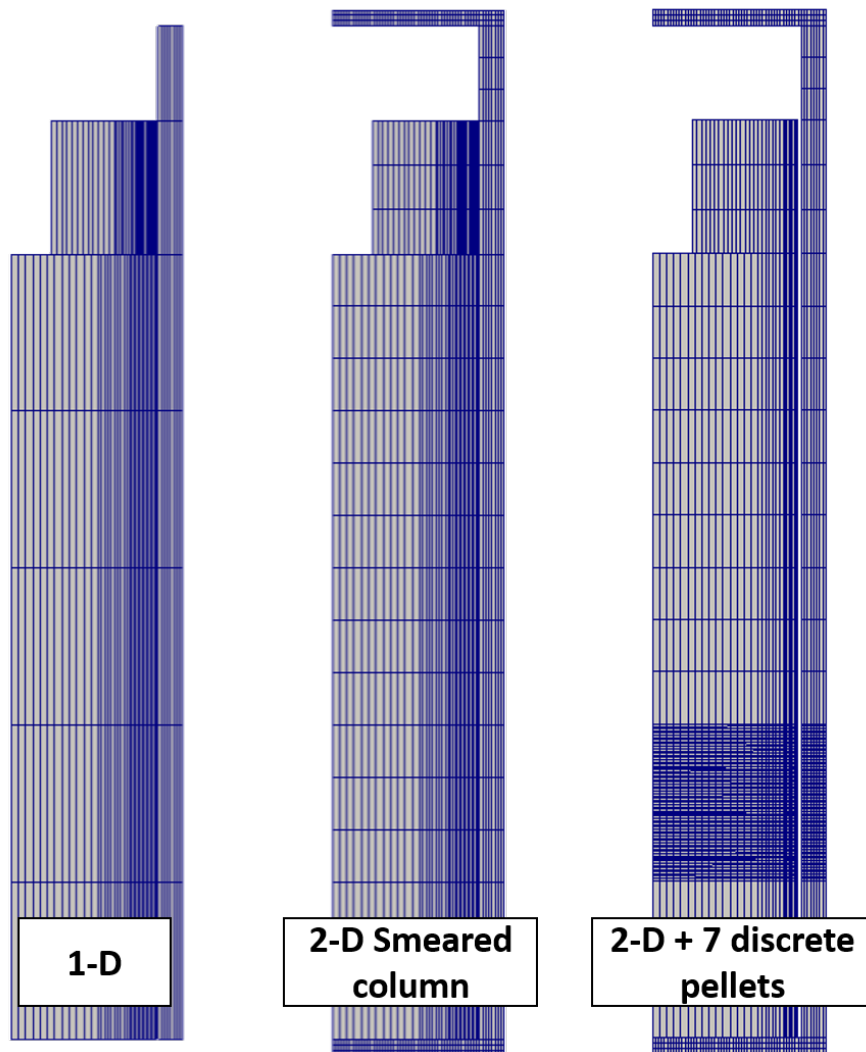


Figure 8.14 – Three OFFBEAT models coupled to TRANSURANSUS for the study of the AN3 segment.

A preliminary analysis performed with TRANSURANUS revealed a significant underprediction of the cladding shrinkage after base irradiation. Also, the larger gap at the beginning of the ramp might reduce the final permanent deformation after the bump test and could tramp the possibility to obtain any significant ridging from the multi-dimensional study. The underestimation seems to be independent on the chosen fission gas release module, as it is shown in Table 8.3 where the results obtained using alternatively SCIANTIX and the more classical URGAS as fission gas release model for the TRANSURANUS simulation are compared against the PIE.

Table 8.3 – Comparison against PIE data for two TRANSURANUS simulations of the AN3 segment. The first simulation employs the URGAS module while the second one employs the SCIENTIX module. The cladding deformations are severely underpredicted.

	TU+URGAS	TU+SCIENTIX	PIE
Base irradiation diameter change, μm (from initial cold state)	-66	-64	-108
Base irradiation FGR, %	0.2	1.3	0.2

To obtain cladding dimensions at the beginning of the bump test which are closer to the experimental value, the cladding creep model of TRANSURANUS is multiplied by a factor of 2x. Naturally, this modeling choice is not realistic, and it is arbitrary, and could have been achieved by other similarly arbitrary measures such as increasing the fast flux. Nevertheless, as shown in Table 8.4, the simple hack of modifying the cladding creep-down is effective in providing a more realistic prediction of the base irradiation creep-down. A more thorough analysis of the main reasons behind TRANSURANUS's underprediction will be conducted in the future.

Table 8.4 - Comparison against PIE data for a full-history TRANSURANUS simulations of the AN3 segment employing SCIENTIX as fission gas release module. The cladding creep model is multiplied by a factor of 2x to increase creep-down and obtain higher cladding deformations at the end of the base irradiation.

	TU+SCIENTIX	PIE
Base irradiation diameter change, μm (from initial cold state)	- 94	-108
Base irradiation FGR, %	0.5	0.2

8.2.3 Verification against a stand-alone TRANSURANUS simulation

As an additional verification test for the coupling methodology, a fourth simulation is performed using only TRANSURANUS for both base irradiation and bump test. It is not possible to know a-priori how close the OFFEBEAT and TRANSURANUS results should be, due to inherent differences between the codes, but one could expect them to provide at least the same order of magnitude for both cladding deformations and total fission gas release. Nevertheless, the comparison with the experimental measurements remains the ultimate validation goal for this case.

While preparing this thesis, the version of TRANSURANUS that includes SCIANTIX as fission gas release module was not equipped with a complete restart option. That is, the code can print the rod data into a restart binary file, but it is not able to properly restart the simulation. However, using this version of TRANSURANUS is necessary for the coupling with OFFBEAT as SCIANTIX is the only fission gas release module compatible with OFFBEAT between the ones available in TRANSURANUS, and its activation is necessary to set the proper initial conditions for the multi-dimensional transient (e.g. for setting the mols of fission gases in the grain at the beginning of the ramp, or the mols of fission gases in the grain boundaries etc.).

To allow for a proper comparison between the coupled simulations and the stand-alone TRANSURANUS run, it was decided to not change the gap pressure and composition at the end of the base irradiation. Thus, the restart option in TRANSURANUS is used only to print the binary restart file that is later accessed by the coupling Fortran routine. It must be stressed that this modification is performed only for the sake of the comparison between the coupling methodology and TRANSURANUS presented in this section. The results presented in the next section (Sec. 8.2.4) are obtained after correctly refilling the post refabrication fuel rod atmosphere with Helium.

Figure 8.15 shows the cladding deformation at the end of the bump test as calculated by OFFBEAT and TRANSURANUS. To focus on the code-to-code comparison, only the results of the 1.5-D and 2-D smeared column OFFBEAT models are included. The analysis of ridging and the validation against the experimental results are left to the next section. The graph shows a difference of just $\sim 5 \mu\text{m}$ ($2.5 \mu\text{m}$ in radius) between the coupled simulations and the TRANSURANUS run. This difference, already small, is probably caused by the 2x multiplier for the cladding creep model present only in the TRANSURANUS run (i.e. the multiplier cannot be eliminated after the base irradiation for the same reason why a proper restart cannot be performed). Therefore, at least according to this preliminary analysis, the coupling does not seem to introduce significant errors when transferring information from TRANSURANUS to the OFFBEAT models.

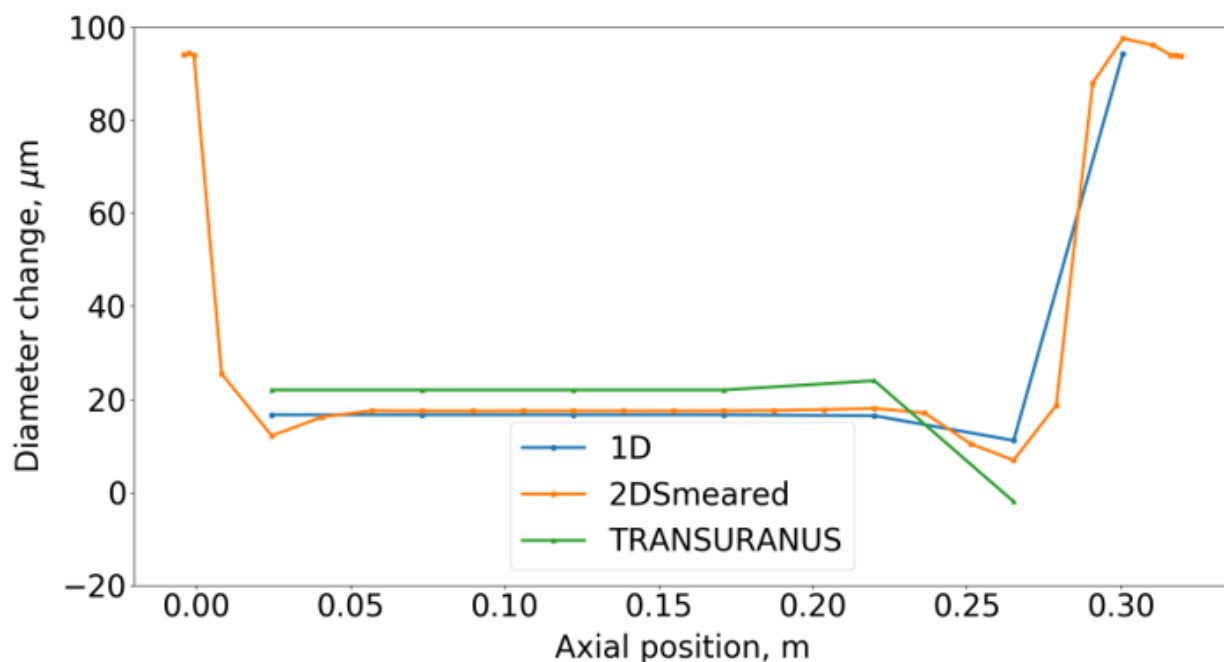


Figure 8.15 – Cladding permanent deformations at the end of the bump test. The rod atmosphere is not changed between base irradiation and bump test. The values are given as diametral variation with respect to the cold state at the start of the bump test as calculated by TRANSURANUS. The values obtained with the 1.5-D and 2-D smeared column OFFBEAT model are compared against the TRANSURANUS standalone run.

8.2.4 Results

The coupled OFFBEAT simulations are now performed after correctly refilling with Helium the rod atmosphere. The graph in Figure 8.16 shows the cladding deformation at the end of the bump test as calculated by OFFBEAT using the 1.5-D model, the 2-D smeared column model and the 2-D model with 7 discrete pellets. The cladding experimental profilometry is extracted from the campaign documents using WebPlotDigitizer [127] and is included in the graph

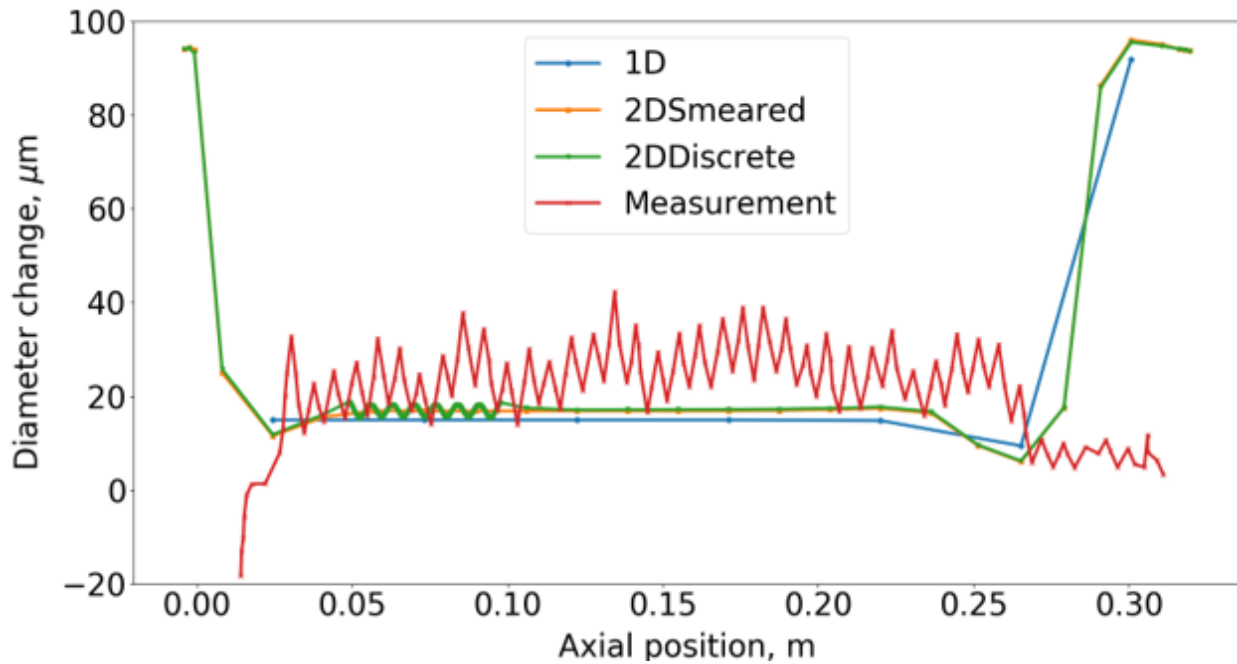


Figure 8.16 – Cladding permanent deformations at the end of the bump test. The values are given as diametral variation with respect to the cold state at the start of the bump test as calculated by TRANSURANUS. The values obtained with the three OFFBEAT models are compared with the experimental measurements.

As expected, the three OFFBEAT models provide consistent results, with the 2-D smeared model predicting an average outer cladding deformation that is contained between the ridges calculated with discrete pellets. The average cladding deformation is slightly underpredicted in all simulations ($\sim 7 \mu\text{m}$ in diameter), but this could be justified by the larger gap at the start of the bump test (see Table 8.4) if compared to the PIE values. More importantly, the ridge height in the discrete pellet model is significantly underpredicted with diametral ridges of only $\sim 2.5 \mu\text{m}$ against experimental values between ~ 10 and $\sim 15 \mu\text{m}$.

Since large penalty factors and fine meshes were used (leading to very small penetrations on the order of some fractions of μm), it is suspected that the ridge height underprediction might be caused by other factors. A potential cause is identified in the isotropic cracking model (see Section 5.8.1), which has been developed [58] to reduce the fuel Young's modulus and Poisson's ratio as a mean to soften the fuel pellet. This strategy is certainly effective to capture in a 1-D framework the stress state of the cracked pellets as well as the fission gas release (dependent on the hydrostatic stress) and the fuel creep (dependent on the equivalent stress). However, as the cracked fuel and the cladding come into contact, the compressive forces should gradually restore the fuel Young's modulus and Poisson's ratio close to their original values, otherwise the fuel is not able to force the cladding to adapt to its hourglass shape. While this effect is taken into consideration in other codes such as FEMAXI-7 [167], it is currently not included in the cracking model implemented in OFFBEAT or in TRANSURANUS. It appears that similar considerations were made also for the

BISON code [168] and it seems that an elastic fuel model is used when simulating the formation of cladding ridges.

A new set of simulations is devised to test this hypothesis: the isotropic cracking model is switched off, but a relocation recovery value of 0.5 is now used to avoid a too large average deformation of the cladding diameter as the relocation recovery acts as a retarding agent for the establishment of hard contact. It must be noted that the relocation recovery was not used (i.e. the recovery was put to 0) in the previous set of simulations. This choice was done to be consistent with the TRANS-URANUS code which is currently lacking the recovery model.

The results of the new simulations are shown in Figure 8.17, this time only for the 2-D model with 7 discrete pellets. The graph reveals that the average cladding deformation has not changed appreciably if compared to the previous set of simulations, suggesting that the recovery of relocation and the absence of fuel softening compensate each other. However, the stiffer fuel is now able to produce more significant permanent ridges with a height of $\sim 8.5 \mu\text{m}$ in diameter (more than triplicated with respect to the previous set of simulations). This value is still somewhat lower if compared to the experiments but the modified modeling approach pushes the results in the right direction towards the experimental measurements.

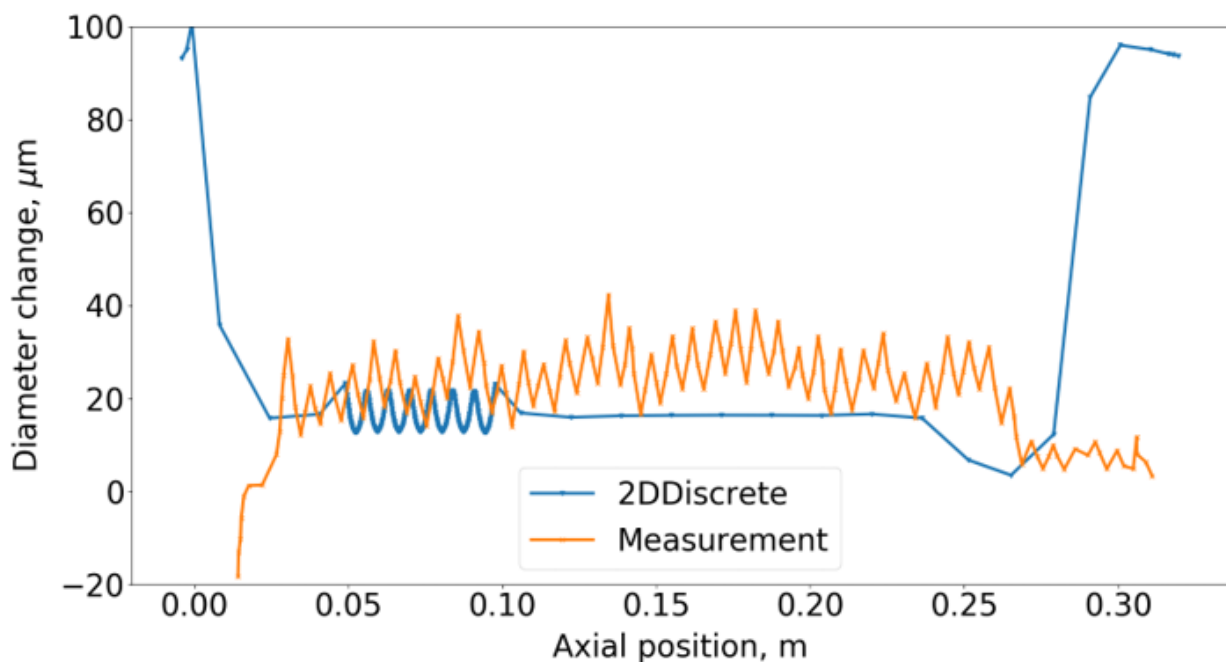


Figure 8.17 – Cladding permanent deformations at the end of the bump test. The values are given as diametral variation with respect to the cold state at the start of the base irradiation. The isotropic cracking model is now switched off. The experimental measurements are included.

8.2.5 Remarks and outlook

The coupling methodology between OFFBEAT and TRANSURANUS has been tested on the AN3 segment from the Risoe3 experiment with the objective of calculating the average cladding deformation and ridge height. The analysis of the results has shown that the coupled simulations compare well against a stand-alone TRANSURANUS run, suggesting that the mapping of information from 1.5-D to higher dimensions works as intended. In the future, a similar analysis could be expanded to other rods, such as the I15 segment or other segments always from the Risoe3 experiment.

An important extension of the methodology might be the creation of automated routines that couple OFFBEAT and TRANSURANUS continuously during irradiation. This would allow one to test asymmetric 3-D conditions at different burnup levels. In this manner, OFFBEAT would represent almost a multi-dimensional plug-in module for the TRANSURANUS code. Also, for long fuel rod segments like the AN3, it might be important to model the full stress history in OFFBEAT, only transferring the power, burnup, rod outer surface temperature, gap pressure and filling gas composition from TRANSURANUS, in order to ensure consistency in the solutions while still respecting the typical approach to modelling the fuel rods in the two codes.

Despite the consistency check for the mapping methodology have been satisfactory, the coupled simulations performed for the AN3 segment have shown a significant underprediction of the ridge height. The analysis of the results has suggested that the fuel isotropic cracking model used in classical 1.5-D approaches might overestimate the softening of the fuel leading to unrealistically low stresses in the fuel pellets. Indeed, an alternative set of simulations has shown that the ridge height improves significantly if the isotropic cracking model is switched off, this time coupled to a relocation recovery value set to 0.5 to limit the cladding average expansion. In the future, the isotropic cracking model should be modified with the introduction of the Young's modulus recovery due to the compressive contact forces. An alternative approach along the lines of what has been done with the ALCYONE code could investigate the effect of fuel cracking with 3-D simulation of pellet fragments, representing a more realistic approximation of the cracked pellet state if compared to a simplified isotropic cracking model. Also, a potential comparison could be suggested with results published by Kim et al [169] for the development of the FEM analysis tool NUFORM3D coupled to FRAPCON based on a case studied in the frame of the FUMEX-II coordinated project of the IAEA.

8.3 Conclusions

This chapter has presented two coupling tools that have been developed in the framework of this thesis to extend the capabilities of OFFBEAT and enable the interaction with other codes that are relevant for the fuel modeling community.

First, a coupling methodology between the multi-dimensional code OFFBEAT and the Monte Carlo code Serpent has been presented. The coupling is based on the Serpent multi-physics interface

and it uses a wrapper Python code to manage and synchronize the two codes. The methodology has been tested on two simplified cases and the results have been compared with those obtained with the TUBRNP a standalone neutronics model available in the TRANSURANUS code.

The analysis of the results has shown that, for a traditional UO_2 rod, the use of a higher fidelity neutronics code like Serpent does not lead to appreciable differences in the predicted radial power profiles, with respect to the use of a well-validated more efficient neutronics model like TUBRNP. The coupling predicts more accurate radial profiles in the presence of strong absorbers such as Gadolinium, probably due to the limitations of the diffusion and one-group approximations used in simplified neutronics models. However, once the Gadolinium is depleted (that is after the first 10 MWd/kgHM) the gain in accuracy gradually disappears and TUBRNP compares well once again with the OFFBEAT/Serpent solution. Overall, the very encouraging results shown in this chapter could be considered as a contribution to the verification of the TUBRNP module within the OFFBEAT code.

In conclusion, the increase in computational cost due to the coupling with a Monte Carlo code is compensated by a higher accuracy of the results, but its use seems justified mainly for new fuel types, experimental setup with spatial effects or in the presence of strong absorbers. The next development steps could test the use of the methodology for more realistic multi-dimensional scenarios, for example studying the 2-D or 3-D flux and power profile in the presence of a complex asymmetric heat exchange with the coolant due to the partial crud and/or oxide layers, or the axial power profile variation due to the insertion of a control rod in the assembly. In this regard, a benchmark or code-to-code comparison against the work carried out for TRANSURANUS [159] could be considered in order to point out the benefits of the 2-D simulation capabilities of OFFBEAT when analysis a fuel assembly.

The second work presented in this chapter is the coupling between OFFBEAT and the legacy code TRANSURANUS. The methodology has been based on the one hand on a series of FORTRAN routines that extract the rod data from the TRANSURANUS restart binary file and on the other hand on a Python script that maps the extracted data to the 2-D or 3-D OFFBEAT model.

The coupling has been tested on the AN3 segment from the Risoe3 experiment already analyzed in Chapter 6 for validation purposes. The objective of this preliminary study has been that of capturing the cladding ridges measured by the PIE. The coupling approach has consisted in simulating the base irradiation with TRANSURANUS, and then transferring the necessary information to OFFBEAT for setting the initial and boundary conditions for a 2-D transient simulation with discrete pellets.

The analysis of the results has shown that the average cladding deformations obtained by the coupling methodology compare well against a stand-alone TRANSURANUS run. The inevitable small deviations, expected due to intrinsic differences between the two codes, have been considered to be well within typical uncertainties of fuel performance analysis.

The comparison against experimental results has shown a significant underprediction of the ridge height. This has been shown to be potentially caused by an excessive softening of the fuel following to the application of the isotropic cracking model. This suggest either the reconsideration of the model with the introduction of the recovery of the fuel's stiffness or the exploration of other approaches such as the 3-D modeling of pellet fragments as done by the ALCYONE code.

Chapter 9

Conclusions

Fuel performance codes have been traditionally developed following the 1.5-D approach. In the last decades, the fuel modeling community has shown a growing interest towards higher-fidelity tools with multi-dimensional and multi-physics capabilities. The main development efforts have followed the long-established tradition in the field of computational solid mechanics that favors the use of the FEM. The aim of this thesis has been to investigate the potential of an unexplored and less conventional approach, namely that of the FVM, for the study of complex scenarios affecting the fuel integrity.

9.1 Main outcomes and takeaways

To reach the aim and objectives set at the start of this thesis, a FV multi-dimensional fuel performance code has been developed. The code is named OFFBEAT, and it has been designed to be readily-available, flexible, and open to multi-physics applications. OFFBEAT has been built with the C++ library OpenFOAM, already used in the laboratories involved in this thesis for the development of nuclear reactor modeling codes. Thanks to its extensive list of features, its C++ object-oriented structure and its open-source nature, which allows one to leverage from the previous works done by its active community, the choice of OpenFOAM has certainly contributed towards an accelerated development and a higher quality code

OFFBEAT has been developed according to a cell-centered FV framework for small-strain solid mechanics. A total Lagrangian approach has been applied, with the momentum balance equations always solved in their total form. The main stress/strains solver has been coupled to a framework for thermal analysis, and the system of coupled thermo-mechanics equations solved using a segregated scheme based on fixed-source iteration.

Appropriate methodologies have been developed to address the presence of the fuel-to-cladding gap with the combined occurrence of heat transfer through the gap and fuel-pellet thermo-mechanical contact. The OpenFOAM mapping routines based on the AMI algorithm have been readapted for coupling two surfaces separated by a small gap. The treatment of the gap heat transfer has been based on a thin-gap approximation and on the concept of thermal resistances, in line with the available gap conductance models used.

Significant efforts have been carried out for the implementation of robust contact methodologies. A first contact algorithm based on the penalty method has been derived from previous works of the FVM community, while a second contact methodology has been developed in the framework

of this thesis. This novel algorithm allows one to implicitly discretize the normal component of the contact stresses, leading to faster convergence and more accurate results for many contact scenarios. The two methodologies have been extensively verified with well-known benchmarks including numerically demanding punch tests between a flat base and rounded objects.

OFFBEAT has been equipped with most of the features expected from a fuel performance code. Experimental correlations have been added for the temperature and burnup dependence of the UO_2 and Zircaloy thermo-mechanical properties, together with semi-empirical models for treating complex meso-scale phenomena such as fuel swelling, relocation and densification or cladding growth. This basic structure has been complemented by the additional capability of handling the occurrence of plastic and creep strains and the evolution of the fuel isotopic composition. Notably, the 0-D SCIENTIX code developed at the Politecnico di Milano has been included in OFFBEAT as the main fission gas behavior and gaseous swelling module.

The code has been implemented according to a modern object-oriented programming paradigm, allowing for a full encapsulation of its different features in stand-alone classes that can be easily modified without affecting the rest of the code. This paves the way for a simplified code maintenance; streamlined extension in terms of new models and additional experimental correlations; and possibility of coupling with other OpenFOAM-based solvers and routines.

The development of the FV methodology and associate software has proceeded in parallel with verification and validation efforts. In addition to the already mentioned benchmarks for the contact models, verification tests have been performed for the steady state and transient thermal analysis as well as for the creep and plasticity models. A first validation base of OFFBEAT has been created including several rods from the IFPE database. The validation cases have focused on two fundamental integral results, namely: the fuel centerline temperature and the total fission gas release fraction. Additional test cases have been performed to confirm that the code is able to capture relevant multi-dimensional aspects such as cladding ridging within simplified but realistic irradiation conditions. The tests and validation performed in the context of this thesis have confirmed that the FVM is indeed a viable alternative to the FEM for fuel performance applications providing satisfactory results both in terms of accuracy and computational time.

To investigate the potential role of the FV fuel analysis methodology in the modern fuel performance landscape, the code has been used to analyze two fuel disc irradiation campaigns that took place in the past in the Halden Boiling Water Reactor. These campaigns were characterized by large gaps and highly conductive fuels, characteristics that hint at a potential significant role of eccentricity. The combination of 2-D and 3-D simulations performed with OFFBEAT has suggested that the experiments might have been affected by a higher impact of eccentricity than what was originally assumed and has suggested a potential re-analysis of the results. This study has shown how a multi-dimensional code is suited for the interpretation of such disc irradiations and has the potential to improve further the investigation of separate effect tests, which traditionally relied on

the combined application of legacy codes and a separate general-purpose tool for the 2D/3-D temperature calculations.

A coupling methodology between OFFBEAT and the Monte Carlo neutron transport code Serpent2 has been developed to expand the multi-physics capabilities of the code and to allow one to obtain a higher-fidelity solution for the neutron flux and for the fuel isotopic composition. The methodology has been tested on simplified cases representing typical rods used in PWRs and BWRs. The analysis of the results has shown that the coupling methodology provides more accurate results with respect to traditional simplified neutronics models at the cost of a significantly higher computational cost. Its use seems justified for the analysis of new fuel types, unconventional configurations and all those scenarios outside the range of application of traditional models. Also, it has been suggested that the coupling between OFFBEAT and Serpent2 might be used to derive effective cross section for new fuel types to be later used in legacy codes.

A second complementary tool developed in the framework of this thesis has been a coupling between the legacy code TRANSURANUS and OFFBEAT. This allows using a well-validated and fast 1.5-D code to simulate the base irradiation and set accurate initial conditions for a multi-dimensional transient performed with OFFBEAT. The coupling has been tested on the AN3 segment from the Risoe3 experiment with the objective of capturing the cladding ridges measured by the PIE. The coupling approach has provided results which are consistent with a separate stand-alone TRANSURANUS run. However, the comparison against the experimental measurements has revealed a considerable underprediction of the ridge heights. A separate set of simulations has shown that the isotropic cracking model could cause an excessive softening of the fuel pellets. Alternative modeling approaches and future extension of this work have been proposed.

9.2 Future Works

The multi-dimensional FV fuel analysis methodology developed in this thesis could be developed further along several research directions, investigating different possible applications. Also, a number of limitations and weaknesses remain within the procedures implemented in OFFBEAT and they should be addressed in future development efforts. The next subsections summarize the future works and recommendation resulting from this thesis.

9.2.1 Thermo-mechanics framework and code structure

The small strain approximation has been selected because it is well-suited for base irradiation and for most accident conditions. However, certain scenarios of interest such as cladding ballooning during LOCA would benefit from a finite-strain analysis. To this end, a user-selectable alternative version of the stress solver could be developed, following an updated Lagrangian and incremental approach. This might require that the classes handling the mechanical constitutive laws are re-adapted to reflect the new finite-strain framework. Also, to accurately model the large deformation of the cladding, it would be necessary to expand the current Limbäck creep model with a secondary thermal creep rate correlation suited for the high temperature regime characteristic of a LOCA.

Additional work is required for improving the calculation of the outer cladding temperature, currently either fixed or derived from the coolant water temperature using a constant, user-defined heat exchange coefficient. To capture both pre- and post-critical heat flux (CHF) regimes it will be necessary to obtain improved boundary conditions on the outer surface of the rod either by developing a simplified thermohydraulic model based on the energy balance within the coolant or by coupling OFFBEAT with GeN-Foam [115] or one of the standard OpenFOAM CFD solvers.

Compared to traditional 1.5-D codes and following the adoption of the more general discretization framework that is necessary for multi-dimensional analysis, OFFBEAT suffers more from instabilities and convergence issues. This is relevant in particular for scenarios involving multiple independent discrete pellets and detailed models with localized contact. Relaxation factors are a powerful tool to stabilize the solution in all these scenarios at the cost of longer running time. However, the choice of the appropriate relaxation value is often not immediately evident, and it is left to the experience of the user. For this reason, more advanced coupling schemes, adaptive relaxation, and other numerical workarounds could be investigated. At least, best-practice guidelines should be laid out for the selection of the relaxation factors should be a priority for the future development of OFFBEAT.

To improve the numerical performance of the solution scheme, a block-coupled solver might be adapted from the ones available in the FVM community. This however is expected to improve the convergence rate only when studying very long sections of the rod, as their main advantage seems to be related to the analysis of long beams [84]. Alternatively, predictor-corrector algorithms or nonlinear acceleration techniques such as Aitken's delta squared, Wynn's epsilon, minimal polynomial extrapolation, reduced rank extrapolation among others could be introduced in order to accelerate the convergence rate. One should be aware, however, that the largest source of instability on the coupled system of equations is the thermo-mechanical behavior of the gap, which is highly nonlinear, stiff, and discontinuous at the point where the gap closes; even the most advanced nonlinear coupled solvers of today are likely to suffer from stability issues.

As an additional future perspective, the bi-material interface treatment developed by Tuković might be implemented in OFFBEAT to model oxide/crud layers. Alternatively, this could be done adapting the implicit contact method developed in this thesis.

9.2.2 Gap heat transfer and contact methodologies

The thin-gap approximation becomes less accurate when modeling irregular or distant surfaces. Although it can be reasonably assumed that the error introduced is of second order, a detailed investigation should be carried out to quantify this effect. A possible strategy would combine the explicit modeling of the heat conduction within a discretized gap that adapts to the fuel and cladding surfaces with the use of view factors for modeling radiative heat transfer. Although all the necessary routines are readily available in the OpenFOAM library, numerical issues might arise if this method is extended to cases with contact due to the formation of infinitesimal gap mesh cells.

The contact procedures developed for OFFBEAT have been shown to provide accurate results for the simulations analyzed in this work. However, some issues remain regarding numerical performance. Under certain irradiation conditions, usually involving high power ramp rate and low conductive fuels like xenon, the presence of contact makes convergence difficult to achieve. This is often due to the highly non-linear thermo-mechanical coupling between contact and gap heat transfer. However, sometimes it is simply the displacement imposed on the fuel outer surface by phenomena like relocation or swelling that creates a non-uniform interfacial pressure distribution that causes the stress solver to oscillate or, worse, to diverge.

The current solutions are effective but are limited to the use of adaptive time-stepping to reduce the change in outer fuel dimension within a single time-step or the use of under-relaxation factors for the contact interface pressure. Once again, automatic selection of best-practice guidelines to help evaluate the most appropriate penalty factor or the right blending parameters for the implicit method should be a priority of future development efforts. As a future perspective, one might consider linearising the displacement as a function of temperature and vice versa towards introducing corrections terms that reduce the gap oscillation for nearly closed gaps. Other options might include some form of meta-modeling to solve the coupled system as a predictor in a predictor-corrector scheme.

The implicit contact methodology has been extensively tested for cases with partially closed gap and it has been used for treating the intra-pellet contact. However, additional testing is required to find optimal blending settings for the application to open-gap scenarios typical of a fuel pin.

9.2.3 Validation

The validation base of OFFBEAT is currently limited to UO_2 rods in the low to medium burnup range, up to ~ 40 MWd/kg. The extension to other fuel types such as MOX and higher burnup levels would increase further the confidence in the methodology developed in this thesis and is particularly relevant in the Swiss contact given that Swiss plants regularly operate fuel into the 70 MWd/kg range. To this purpose, it might be necessary to include models for the outer corrosion of the cladding and for the effect of the HBS on the fuel material properties and on the fission gas release, as these phenomena might affect the response of the rod over long irradiation periods. The introduction of new correlations for the thermo-mechanical properties of MOX fuels (if available in the literature) are expected to require only a limited effort.

The validation of OFFBEAT should be made more systematic by analyzing the evolution of deviations with burnup to highlight potential error trends and by performing code-to-code comparisons against the vast library of results of the open literature (such as those obtained in the coordinated research projects of the IAEA called FUMEX, FUMEX-II and FUMEX-III) and available in the IFPE database of the OECD-NEA.

The future validation efforts should also consider additional quantities besides the fuel centerline temperature and the fission gas release. Gap pressure and cladding elongation are two common examples examined in validation campaigns performed for other codes.

A fundamental missing validation step is the comparison with experimental results that are intrinsically multi-dimensional. This is certainly made difficult by the scarcity of appropriate data, but the simulation of cladding ridging as currently done as part of the collaboration with JRC-Karlsruhe could be a first relevant application. Ideally, combined efforts with experimental teams might lead to the design of new experiments and to the production of experimental data better suited for the validation of multi-dimensional codes. Ultimately, it would be useful to take part in the activities organized by the OECD-NEA expert group on multi-physics experimental data, benchmarks and validation [170].

9.2.4 Possible code extensions

Several future extensions could be considered for OFFBEAT. Besides the already mentioned cladding outer oxidation and HBS models, the code is currently missing models for hydrogen uptake and hydride modeling that would be beneficial in the modeling of cladding embrittlement and failure.

Currently, OFFBEAT models the effect of cracking employing relocation and isotropic cracking approaches derived from axisymmetric traditional codes. These might not be suited for the 3-D context, with the isotropic cracking model leading to unrealistically low stresses in the fuel. Future studies could consider the analysis of pre-determined 3-D cracking pattern or the analysis of pellet fragments along the lines of what is often done with the ALCYONE code.

OpenFOAM would be an ideal tool for modelling diffusion of fission products, chemistry and SCC. To this purpose OFFBEAT could be coupled to OpenFOAM chemistry routines or to dedicated chemistry tools like GEMS [171].

The development of OFFBEAT has focused on LWR rods as this type of reactor represents the vast majority of the current operating fleet around the world. It might be useful to the fuel performance community to expand the area of application of the code to plate-type fuel, TRISO pebble or fast reactor fuel rods. For some of this fuel types, complicated modeling issues might arise due to complex phenomena such as the opening of the central hole for fast reactor fuel pellets.

Other important perspectives might include the introduction of models for fuel restructuring and material transport, the addition of friction forces between fuel and cladding in the penalty method, the consideration of phase changes (melting), and the potential requirements for design basis accident analysis.

9.2.5 Separate effect studies

The analysis of the HBRP and of the IFA-701 has shown that multi-dimensional codes can contribute to improving the design and interpretation of separate effect tests. The simulation performed in Chapter 7 could be complemented with an explicit modeling of the gap heat transfer. Also, the PIE pictures available in the campaign documents might be used to deduce approximate values of eccentricity both between UO_2 and molybdenum discs and between fuel and cladding discs. This could lead to more accurate estimation of the impact of eccentricity which could then be used to better evaluate the possibility of a new correlation for the HBS threshold.

Also, the analysis of the IFA-701 could be extended further to include the remaining irradiation periods (second, third and fourth). Not only would this provide additional validation points for OFFBEAT, but it could lead to an evaluation of the fuel creep correlations used in fuel performance codes despite being limited to low temperature regimes dominated by irradiation creep rates.

Finally, similar studies could be performed focusing on other separate effect tests. In view of the required computational costs for detailed simulations, the coupling option between OFFBEAT and TRANSURANUS might be considered. This would allow the investigation of in-pile experiments with complicated irradiation histories addressing specific local phenomena such as PCMI, extending the analysis even for medium and high burnup. The analysis of eccentricity might also be extended to other, more traditional experimental rods filled with low conductive gases such as the xenon-filled rods of the IFA-562.1 studied in Chapter 6 where a larger scatter of data and a over-predicting bias could be seen with respect to their helium-filled counterparts.

9.2.6 Coupling with Serpent

The coupling methodology with the Serpent2 code has been tested only on simplified cases, with the neutron flux and fuel depletion azimuthally averaged in the fuel rod under analysis. The next development step might involve the simulation of more complex scenarios. A first case of interest might be analogous to the Gd-doped BWR rod studied in Section 8.1.3, this time with an azimuthal discretization of the fuel depletion and thus a 2-D power distribution. This will certainly make the coupled simulation even more demanding from a statistical point of view and the computational cost should be carefully re-evaluated. Another interesting test case might be the analysis of the axial variation of the power distribution in a fuel rod due to the insertion of a control rod in the assembly, which would require the extension of the coupling methodology to 2-D r-z or 3-D cases.

9.2.7 Coupling with TRANSURANUS

The coupling with TRANSURANUS has showed interesting results that promise to expand the possibilities offered to conventional analysis and simplify the definition of initial and boundary conditions for a multi-dimensional high burnup transient simulations. The next step is the analysis of a second rod from the Riso3 experiment, the segment II5 for which post bump test axial profilometry is available in the campaign files. The analysis of the results obtained for the AN3 segment has also shown that the soft contact methodology typically employed in 1.5-D code could be cause

unrealistically low stresses in the fuel and should be reconsidered in a 3-D framework for the analysis of phenomena such as ridging.

An important extension of the methodology might be the creation of automated routines that couple OFFBEAT and TRANSURANUS continuously during irradiation. This would allow one to test asymmetric or multi-dimensional conditions at different burnup levels.

9.3 Closing remarks

A novel multi-dimensional fuel analysis methodology and related software have been developed using the finite volume method. The contact procedures implemented have been extensively tested and verified against analytical benchmarks, providing accurate predictions. The code has been equipped with most features expected from a full-fledged fuel performance code. Its prediction of fuel centerline temperature and fission gas release have been validated against several rods of the IFPE database. The multi-dimensional possibilities offered by the newly developed code have been used to analyze the effect of eccentricity on fuel disc irradiation tests, showing how multi-dimensional codes can assist the design and interpretation of separate effect tests. A coupling with the Monte Carlo neutron transport code Serpent2 has been implemented to achieve a higher fidelity solution for the fuel power distribution under unconventional fuel rod configurations. The first step towards the development of a coupling strategy between a multi-dimensional and a legacy code have been presented. The coupling might expand the possibilities offered to traditional analysis as well as simplify the setting of appropriate initial conditions for high burnup multi-dimensional transients. Finally, the main future works and recommendations resulting from this thesis have been outlined.

References

- [1] J. R. Matthews, “Computer models for fuel element behaviour,” *Bull. Mater. Sci.*, vol. 8, no. 2, pp. 93–106, 1986, doi: 10.1007/BF02744175.
- [2] Friedrich and C. M, “CYGRO-1 stress analysis of the growth of concentric cylinders (LWBR Development Program).” Jul. 01, 1966.
- [3] GODESAR R, GUYETTE M, and HOPPE N, “COMETHE II-A COMPUTER CODE FOR PREDICTING THE MECHANICAL AND THERMAL BEHAVIOR OF A FUEL PIN,” *Nucl Appl Technol*, vol. 9, no. 2, pp. 205–217, 1970, doi: 10.13182/nt70-a28809.
- [4] P. Van Uffelen, J. Hales, W. Li, G. Rossiter, and R. Williamson, “A review of fuel performance modelling,” *Journal of Nuclear Materials*. 2019, doi: 10.1016/j.jnucmat.2018.12.037.
- [5] “Water cooled nuclear reactors (WCR) | IAEA.” <https://www.iaea.org/topics/water-cooled-reactors> (accessed Mar. 28, 2021).
- [6] K. Lassmann, “TRANSURANUS: a fuel rod analysis code ready for use,” *J. Nucl. Mater.*, 1992, doi: 10.1016/0022-3115(92)90487-6.
- [7] G. A. Berna, C. E. Beyer, K. L. Davis, and D. D. Lanning, “FRAPCON-3: A Computer Code for the Calculation of Steady-State, Thermal-Mechanical Behavior of Oxide Fuel Rods for High Burnup, Idaho National Engineering and Environmental Laboratory , NUREG/CR-6534,” *Off. Nucl. Regul. Res. NUREG/CR-7022*, vol. 2, no. c, 1997.
- [8] K. J. Geelhood, W. G. Luscher, C. E. Beyer, and J. M. Cuta, *FRAPTRAN 1.5: A Computer Code for the Transient Analysis of Oxide Fuel Rods*, vol. 1, no. Rev. 1. 2014.
- [9] Y. Udagawa, “Development and release of fuel performance code FEMAXI-8燃料挙動解析コードFEMAXI-8の開発と公開,” *J. At. Energy Soc. Japan*, vol. 62, no. 10, pp. 555–559, 2020, doi: 10.3327/jaesjb.62.10_555.
- [10] P. A. Jackson, J. A. Turnbull, and R. J. White, “Enigma fuel performance code,” *Nucl. Energy*, 1990.
- [11] J. Y. R. Rashid, S. K. Yagnik, and R. O. Montgomery, “Light water reactor fuel performance modeling and multi-dimensional simulation,” *JOM*. 2011, doi: 10.1007/s11837-011-0144-9.
- [12] P. Van Uffelen, R. J. M. Konings, C. Vitanza, and J. Tulenko, “Analysis of Reactor Fuel Rod Behavior,” in *Handbook of Nuclear Engineering*, Springer US, 2010, pp. 1519–1627.
- [13] “OECD NEA/NSC: WPRS EGRFP: PCMI Benchmark.” https://www.oecd-nea.org/science/wprs/egrfp/pcmi_benchmark/ (accessed Mar. 30, 2021).
- [14] G. Hansen, C. Newman, D. Gaston, and M. Methods, “BISON: An implicit solution framework

for fuel performance simulation,” *Methods*, 2009.

- [15] A. Soba and A. Denis, “DIONISIO 2.0: New version of the code for simulating a whole nuclear fuel rod under extended irradiation,” *Nucl. Eng. Des.*, 2015, doi: 10.1016/j.nucengdes.2015.06.008.
- [16] V. Marelle *et al.*, “New developments in ALCYONE 2.0 fuel performance code,” in *Top Fuel 2016: LWR Fuels with Enhanced Safety and Performance*, 2016.
- [17] K. Lassmann, C. O’Carroll, J. van de Laar, and C. T. Walker, “The radial distribution of plutonium in high burnup UO₂ fuels,” *J. Nucl. Mater.*, 1994, doi: 10.1016/0022-3115(94)90331-X.
- [18] D. Gaston, C. Newman, G. Hansen, and D. Lebrun-Grandié, “MOOSE: A parallel computational framework for coupled systems of nonlinear equations,” *Nucl. Eng. Des.*, vol. 239, no. 10, pp. 1768–1778, Oct. 2009, doi: 10.1016/J.NUCENGDES.2009.05.021.
- [19] C. Introïni, J. Sercombe, and B. Sundman, “Development of a robust, accurate and efficient coupling between PLEIADES/ALCYONE 2.1 fuel performance code and the OpenCalphad thermo-chemical solver,” *Nucl. Eng. Des.*, vol. 369, p. 110818, Dec. 2020, doi: 10.1016/j.nucengdes.2020.110818.
- [20] “Ansys Mechanical | Structural FEA Analysis Software.” <https://www.ansys.com/products/structures/ansys-mechanical> (accessed Apr. 07, 2021).
- [21] E. DICKINSON, H. EKSTRÖM, and E. FONTES, “COMSOL Multiphysics,” *Electrochem. commun.*, vol. 40, pp. 71–74, 2014.
- [22] H. Jasak and H. G. Weller, “Application of the finite volume method and unstructured meshes to linear elasticity,” *Int. J. Numer. Methods Eng.*, 2000, doi: 10.1002/(SICI)1097-0207(20000520)48:2<267::AID-NME884>3.0.CO;2-Q.
- [23] I. Demirdžić and D. Martinović, “Finite volume method for thermo-elasto-plastic stress analysis,” *Comput. Methods Appl. Mech. Eng.*, 1993, doi: 10.1016/0045-7825(93)90085-C.
- [24] I. Demiredzic, D. Martinovic, and A. Ivankovic, “Numerical simulation of thermal deformation in welded workpiece,” *Zavarivanje*, vol. 31, no. 5–6, 1988.
- [25] H. Osman, S. Ahmad, and K. A. Arshad, “A one- dimensional simulation of an electrofusion welding process,” in *2011 4th International Conference on Modeling, Simulation and Applied Optimization, ICMSAO 2011*, 2011, doi: 10.1109/ICMSAO.2011.5774989.
- [26] H. Bašić, I. Demirdžić, and S. Muzaferija, “Finite volume method for simulation of extrusion processes,” *Int. J. Numer. Methods Eng.*, vol. 62, no. 4, pp. 475–494, 2005, doi: 10.1002/nme.1168.
- [27] I. Demirdžić, E. Džaferović, and A. Ivanković, “Finite-volume approach to thermoviscoelasticity,” *Numer. Heat Transf. Part B Fundam.*, vol. 47, no. 3, pp. 213–237, 2005, doi: 10.1080/10407790590901675.
- [28] K. Zarrabi, and A. Basu, “An Axisymmetric Finite Volume Formulation For Creep Analysis,” *J.*

Mech. Behav. Mater., vol. 10, no. 5–6, pp. 325–340, 2011, doi: 10.1515/jmbm.1999.10.5-6.325.

- [29] H. Jasak and H. G. Weller, “Finite Volume Methodology for Contact Problems of Linear Elastic Solids,” in *Proceedings of 3rd International Conference of Croatian Society of Mechanics*, 2000.
- [30] P. Cardiff, A. Karač, and A. Ivanković, “Development of a finite volume contact solver based on the penalty method,” in *Computational Materials Science*, 2012, doi: 10.1016/j.commatsci.2012.03.011.
- [31] A. Ivankovic, I. Demirdzic, J. G. Williams, and P. S. Leever, “Application of the finite volume method to the analysis of dynamic fracture problems,” *Int. J. Fract.*, vol. 66, no. 4, pp. 357–371, 1994, doi: 10.1007/BF00018439.
- [32] A. Ivankovic, S. Muzaferija, and I. Demirdzic, “Finite volume method and multigrid acceleration in modelling of rapid crack propagation in full-scale pipe test,” *Comput. Mech.*, vol. 20, no. 1–2, pp. 46–52, 1997, doi: 10.1007/s004660050215.
- [33] Ž. Tuković, H. Jasak, A. Karač, P. Cardiff, and A. Ivanković, “Openfoam finite volume solver for fluid-solid interaction,” *Trans. Famena*, vol. 42, no. 3, pp. 1–31, 2018, doi: 10.21278/TOF.42301.
- [34] P. Cardiff and I. Demirdžić, “Thirty years of the finite volume method for solid mechanics,” *arXiv*. 2018.
- [35] I. Clifford, M. Pecchia, R. Mukin, C. Cozzo, H. Ferroukhi, and A. Gorzel, “Studies on the effects of local power peaking on heat transfer under dryout conditions in BWRs,” *Ann. Nucl. Energy*, vol. 130, pp. 440–451, Aug. 2019, doi: 10.1016/J.ANUCENE.2019.03.017.
- [36] “The OpenFOAM Foundation.” <https://openfoam.org/> (accessed Feb. 05, 2021).
- [37] H. G. Weller, G. Tabor, H. Jasak, and C. Fureby, “A tensorial approach to computational continuum mechanics using object-oriented techniques,” *Comput. Phys.*, 1998, doi: 10.1063/1.168744.
- [38] I. Clifford and H. Jasak, “The application of a multi-physics toolkit to spatial reactor dynamics,” in *American Nuclear Society - International Conference on Mathematics, Computational Methods and Reactor Physics 2009, M and C 2009*, 2009, vol. 3, pp. 1585–1596.
- [39] M. Aufiero *et al.*, “Calculating the effective delayed neutron fraction in the Molten Salt Fast Reactor: Analytical, deterministic and Monte Carlo approaches,” *Ann. Nucl. Energy*, vol. 65, pp. 78–90, Mar. 2014, doi: 10.1016/j.anucene.2013.10.015.
- [40] F. Roelofs, V. R. Gopala, L. Chandra, M. Viellieber, and A. Class, “Simulating fuel assemblies with low resolution CFD approaches,” *Nucl. Eng. Des.*, vol. 250, pp. 548–559, Sep. 2012, doi: 10.1016/j.nucengdes.2012.05.029.
- [41] F. Roelofs, V. R. Gopala, S. Jayaraju, A. Shams, and E. Komen, “Review of fuel assembly and pool thermal hydraulics for fast reactors,” *Nucl. Eng. Des.*, vol. 265, pp. 1205–1222, Dec.

2013, doi: 10.1016/j.nucengdes.2013.07.018.

- [42] C. Fiorina, I. Clifford, M. Aufiero, and K. Mikityuk, "GeN-Foam: A novel OpenFOAM® based multi-physics solver for 2D/3D transient analysis of nuclear reactors," *Nucl. Eng. Des.*, 2015, doi: 10.1016/j.nucengdes.2015.05.035.
- [43] J. Leppänen, M. Pusa, T. Viitanen, V. Valtavirta, and T. Kaltiaisenaho, "The Serpent Monte Carlo code: Status, development and applications in 2013," *Ann. Nucl. Energy*, vol. 82, pp. 142–150, Aug. 2015, doi: 10.1016/j.anucene.2014.08.024.
- [44] D. R. Olander, *Fundamental aspects of nuclear reactor fuel elements*. U.S. Department of Energy, 1976.
- [45] B. Barré, "Front End of the Fuel Cycle," in *Cacuci D.G. (eds) Handbook of Nuclear Engineering*, Springer, Boston, MA.
- [46] D. L. Hagerman and G. A. Reymann, "MATPRO-Version 11: a handbook of materials properties for use in the analysis of light water reactor fuel rod behavior," 1979. doi: 10.2172/6442256.
- [47] R. E. MacFarlane, "Neutron Slowing Down and Thermalization," in *Handbook of Nuclear Engineering*, Springer US, 2010, pp. 189–277.
- [48] D. Knott and A. Yamamoto, "Lattice Physics Computations," in *Handbook of Nuclear Engineering*, Springer US, 2010, pp. 913–1239.
- [49] J. R. Lamarsh and A. J. Baratta, "Introduction to Nuclear Engineering, 3rd ed.," *Prentice Hall*, p. 783, 2001, [Online]. Available: <http://www.sciencedirect.com/science/article/B6V3F-497B9NS-H/2/119fb9d6bf5237677d991e2083411241>.
- [50] A. Scolaro, C. Fiorina, I. Clifford, and A. Pautz, "Multi-Dimensional Creep Analysis Using the Novel OFFBEAT Fuel Performance Code," in *IAEA Technical Meeting on Progress on Pellet Cladding Interaction and Stress Corrosion Cracking*, 2019.
- [51] J. B. Minne, L. Desgranges, V. Optasanu, N. Largeton, L. Raceanu, and T. Montesin, "Specific aspects of internal corrosion of nuclear clad made of zircaloy," in *Defect and Diffusion Forum*, Jan. 2012, vol. 323–325, pp. 227–232, doi: 10.4028/www.scientific.net/DDF.323-325.227.
- [52] G. Khvostov, W. Lyon, and M. A. Zimmermann, "Application of the FALCON code to PCI induced cladding failure and the effects of missing pellet surface," *Ann. Nucl. Energy*, vol. 62, pp. 398–412, 2013, doi: 10.1016/j.anucene.2013.07.002.
- [53] C. Cozzo *et al.*, "Full core LOCA analysis for BWR/6 - methodology and first results," *Top Fuel 2016. LWR fuels with Enhanc. Saf. Perform.*, 2016, Accessed: Apr. 27, 2021. [Online]. Available: <https://www.dora.lib4ri.ch/psi/islandora/object/psi%3A23148/>.
- [54] U. S. N. Regulatory, "TRACE v5.840 Theory Manual, Division of Safety Analysis."
- [55] Y. Rashid, R. Dunham, and R. Montgomery, "Fuel Analysis and Licensing Code: FALCON MOD01 Volume 1: Theoretical and Numerical Bases," vol. 1, no. 3, p. 246, 2004.

-
- [56] P. J. Turinsky and D. B. Kothe, "Modeling and simulation challenges pursued by the Consortium for Advanced Simulation of Light Water Reactors (CASL)," *J. Comput. Phys.*, vol. 313, pp. 367–376, 2016, doi: 10.1016/j.jcp.2016.02.043.
- [57] R. K. Salko *et al.*, "Development of COBRA-TF for modeling full-core, reactor operating cycles," in *5th Topical Meeting on Advances in Nuclear Fuel Management, ANFM 2015: Advances in Nuclear Fuel Management V*, 2015, pp. 178–194.
- [58] T. Barani, D. Pizzocri, G. Pastore, L. Luzzi, and J. D. Hales, "Isotropic softening model for fuel cracking in BISON," *Nucl. Eng. Des.*, vol. 342, pp. 257–263, Feb. 2019, doi: 10.1016/J.NUCENGDES.2018.12.005.
- [59] J. Sercombe, I. Aubrun, and C. Nonon, "Power ramped cladding stresses and strains in 3D simulations with burnup-dependent pellet–clad friction," *Nucl. Eng. Des.*, vol. 242, pp. 164–181, Jan. 2012, doi: 10.1016/J.NUCENGDES.2011.08.069.
- [60] B. Spencer, H. Huang, J. Dolbow, and J. Hales, "Discrete Modeling of Early-Life Thermal Fracture in Ceramic Nuclear Fuel Proceedings of WRFPM 2014 Discrete Modeling of Early-Life Thermal Fracture in Ceramic Nuclear Fuel," Accessed: Jun. 08, 2018. [Online]. Available: <https://indigitallibrary.inl.gov/sites/sti/sti/6366077.pdf>.
- [61] K. J. Geelhood, W. G. Luscher, and C. E. Beyer, "FRAPCON-3.4: A Computer Code for the Calculation of Steady-State, Thermal-Mechanical Behavior of Oxide Fuel Rods for High Burnup," Mar. 2011. Accessed: Apr. 27, 2021. [Online]. Available: <http://www.nrc.gov/reading-rm.html>.
- [62] A. H. Booth, "A method of calculating fission gas diffusion from UO₂ fuel and its application to the X-2-f loop test," 1957.
- [63] P. T. Elton and K. Lassmann, "Calculational methods for diffusional gas release," *Nucl. Eng. Des.*, vol. 101, no. 3, pp. 259–265, May 1987, doi: 10.1016/0029-5493(87)90054-9.
- [64] M. V. Speight, "A Calculation on the Migration of Fission Gas in Material Exhibiting Precipitation and Re-solution of Gas Atoms Under Irradiation," *Nucl. Sci. Eng.*, vol. 37, no. 2, pp. 180–185, 1969, doi: 10.13182/nse69-a20676.
- [65] J. B. Ainscough, B. W. Oldfield, and J. O. Ware, "Isothermal grain growth kinetics in sintered UO₂ pellets," *J. Nucl. Mater.*, vol. 49, no. 2, pp. 117–128, 1973, doi: 10.1016/0022-3115(73)90001-9.
- [66] G. Pastore, L. Luzzi, V. Di Marcello, and P. Van Uffelen, "Physics-based modelling of fission gas swelling and release in UO₂ applied to integral fuel rod analysis," *Nucl. Eng. Des.*, vol. 256, pp. 75–86, Mar. 2013, doi: 10.1016/j.nucengdes.2012.12.002.
- [67] A. Schubert, P. Van Uffelen, J. van de Laar, C. T. Walker, and W. Haack, "Extension of the TRANSURANUS burn-up model," *J. Nucl. Mater.*, vol. 376, no. 1, pp. 1–10, 2008, doi: 10.1016/j.jnucmat.2008.01.006.
- [68] P. Botazzoli *et al.*, "Extension and validation of the TRANSURANUS burn-up model for helium production in high burn-up LWR fuels," in *Journal of Nuclear Materials*, 2011, vol. 419, no. 1–3, pp. 329–338, doi: 10.1016/j.jnucmat.2011.05.040.

-
- [69] A. M. Phillippe *et al.*, "Validation study of pin heat transfer for UO₂ Fuel based on the IFA-432 Experiments," *Nucl. Sci. Eng.*, vol. 177, no. 3, pp. 275–290, 2014, doi: 10.13182/NSE13-18.
- [70] E. Lacroix and A. Motta, "Validation of bison calculation of hydrogen distribution by comparison to experiment," in *The Minerals, Metals & Materials Society (eds)*, 2016, doi: 10.1007/978-3-319-48254-5_33.
- [71] H. S. Aybar and P. Ortego, "A review of nuclear fuel performance codes," *Prog. Nucl. Energy*, vol. 46, no. 2, pp. 127–141, Jan. 2005, doi: 10.1016/J.PNUCENE.2005.01.004.
- [72] S. R. Idelsohn and E. Oñate, "Finite volumes and finite elements: Two 'good friends,'" *Int. J. Numer. Methods Eng.*, vol. 37, no. 19, pp. 3323–3341, 1994, doi: 10.1002/nme.1620371908.
- [73] M. Vaz, P. A. Muñoz-Rojas, and G. Filippini, "On the accuracy of nodal stress computation in plane elasticity using finite volumes and finite elements," *Comput. Struct.*, vol. 87, no. 17–18, pp. 1044–1057, Sep. 2009, doi: 10.1016/j.compstruc.2009.05.007.
- [74] J. Passard and P. Perré, "A Control-Volume Procedure Compared with the Finite-Element Method for Calculating Stress and Strain During Wood Drying," *Dry. Technol.*, vol. 13, no. 3, pp. 635–660, Jan. 1995, doi: 10.1080/07373939508916978.
- [75] Q. Fang, T. Tsuchiya, and T. Yamamoto, "Finite difference, finite element and finite volume methods applied to two-point boundary value problems," *J. Comput. Appl. Math.*, vol. 139, no. 1, pp. 9–19, Feb. 2002, doi: 10.1016/S0377-0427(01)00392-2.
- [76] Y. D. Fryer, C. Bailey, M. Cross, and C. H. Lai, "A control volume procedure for solving the elastic stress-strain equations on an unstructured mesh," *Top. Catal.*, vol. 15, no. 11–12, pp. 639–645, Nov. 1991, doi: 10.1016/S0307-904X(09)81010-X.
- [77] S. N. Atluri and T. Zhu, "A new Meshless Local Petrov-Galerkin (MLPG) approach in computational mechanics," *Comput. Mech.*, vol. 22, no. 2, pp. 117–127, 1998, doi: 10.1007/s004660050346.
- [78] Ž. Tuković, A. Ivanković, and A. Karač, "Finite-volume stress analysis in multi-material linear elastic body," *Int. J. Numer. Methods Eng.*, vol. 93, no. 4, pp. 400–419, 2013, doi: 10.1002/nme.4390.
- [79] P. Cardiff, "Development of the finite volume method for hip joint stress analysis," *PhD Thesis, Sch. Mech. Mater. Eng. Univ. Coll. Dublin*, 2012.
- [80] P. Cardiff, Tuković, H. Jasak, and A. Ivanković, "A block-coupled Finite Volume methodology for linear elasticity and unstructured meshes," *Comput. Struct.*, vol. 175, pp. 100–122, 2016, doi: 10.1016/j.compstruc.2016.07.004.
- [81] P. Cardiff *et al.*, "An open-source finite volume toolbox for solid mechanics and fluid-solid interaction simulations," *arXiv*. 2018.
- [82] J. C. Simo and T. J. Hughes, *Computational inelasticity*, vol. 7. Springer Science & Business Media, 2006.

-
- [83] K. Maneeratana, "Development of the finite volume method for non-linear structural applications," *PhD thesis, Dep. Mech. Eng. Imp. Coll. London*, vol. M, p. 303, 2000.
- [84] P. Cardiff, Tuković, H. Jasak, and A. Ivanković, "A block-coupled Finite Volume methodology for linear elasticity and unstructured meshes," *Comput. Struct.*, 2016, doi: 10.1016/j.compstruc.2016.07.004.
- [85] I. Demirdžić and S. Muzaferija, "Numerical method for coupled fluid flow, heat transfer and stress analysis using unstructured moving meshes with cells of arbitrary topology," *Comput. Methods Appl. Mech. Eng.*, vol. 125, no. 1–4, pp. 235–255, 1995, doi: 10.1016/0045-7825(95)00800-G.
- [86] H. Jasak, "Error Analysis and Estimation for the Finite Volume Method with Applications to Fluid Flows," 1996.
- [87] S. MacNamara and G. Strang, "Operator Splitting," in *Splitting Methods in Communication, Imaging, Science, and Engineering. Scientific Computation*, Springer, Ed. 2016, pp. 95–114.
- [88] V. D'Ambrosi, J. M. Gatt, F. Lebon, J. Julien, C. Destouches, and D. Parrat, "Homogenization approach to model the thermal-mechanical behavior of melting fuel material," *J. Nucl. Mater.*, vol. 535, 2020, doi: 10.1016/j.jnucmat.2020.152149.
- [89] C.-H. Kang, S.-U. Lee, D.-Y. Yang, H.-C. Kim, and Y.-S. Yang, "3D finite element analysis of a nuclear fuel rod with gap elements between the pellet and the cladding," *J. Nucl. Sci. Technol.*, vol. 53, no. 2, pp. 232–239, 2016, doi: 10.1080/00223131.2015.1037374doi.org/10.1080/00223131.2015.1037374.
- [90] P. E. Farrell and J. R. Maddison, "Conservative interpolation between volume meshes by local Galerkin projection," *Comput. Methods Appl. Mech. Eng.*, vol. 200, no. 1–4, pp. 89–100, 2011, doi: 10.1016/j.cma.2010.07.015.
- [91] "OpenFOAM 2.1.0: Arbitrary Mesh Interface | OpenFOAM." <https://openfoam.org/release/2-1-0/ami/> (accessed Dec. 23, 2020).
- [92] M. Beaudoin and H. Jasak, "Development of a Generalized Grid Interface for Turbomachinery simulations with OpenFOAM," *Talk*, no. December 2008, pp. 1–11, 2008, [Online]. Available: papers3://publication/uuid/81CCD00D-DF48-4595-B591-C577955CEA06.
- [93] "The foam-extend project." <https://sourceforge.net/projects/foam-extend/> (accessed Dec. 23, 2020).
- [94] P. Wriggers, *Computational contact mechanics*. Springer, 2006.
- [95] L. De Lorenzis, P. Wriggers, and C. Weißenfels, "Computational Contact Mechanics with the Finite Element Method," in *Encyclopedia of Computational Mechanics Second Edition*, 2017, pp. 1–45.
- [96] P. Cardiff, Tuković, P. De Jaeger, M. Clancy, and A. Ivanković, "A Lagrangian cell-centred finite volume method for metal forming simulation," *Int. J. Numer. Methods Eng.*, vol. 109, no. 13, pp. 1777–1803, 2017, doi: 10.1002/nme.5345.

-
- [97] "OpenFOAM® - Selected Papers of the 11th Workshop | Joao Nobrega | Springer." <https://www.springer.com/gp/book/9783319608457> (accessed Apr. 09, 2021).
- [98] M. Rauter, A. Kofler, A. Huber, and W. Fellin, "FaSavageHutterFOAM 1.0: Depth-integrated simulation of dense snow avalanches on natural terrain with OpenFOAM," *Geosci. Model Dev.*, vol. 11, no. 7, pp. 2923–2939, Jul. 2018, doi: 10.5194/gmd-11-2923-2018.
- [99] "SALOME Platform." <https://www.salome-platform.org/> (accessed Dec. 29, 2020).
- [100] J. AHRENS, B. GEVECI, and C. LAW, "ParaView: An End-User Tool for Large-Data Visualization," in *Visualization Handbook*, Elsevier, 2005, pp. 717–731.
- [101] R. L. Williamson, G. Pastore, S. R. Novascone, B. W. Spencer, and J. D. Hales, "Modelling of LOCA Tests with the BISON Fuel Performance Code," 2016, Accessed: Jun. 08, 2018. [Online]. Available: <https://inldigitallibrary.inl.gov/sites/sti/sti/7146879.pdf>.
- [102] F. Moukalled, L. Mangani, and M. Darwish, *The finite volume method in computational fluid dynamics : An Advanced Introduction with OpenFOAM and Matlab*, vol. 113. 2016.
- [103] Geelhood K. J. and Luscher W. G., "FRAPCON-3.5: A Computer Code For The Calculation Of Steady-State, Thermal-Mechanical Behavior Of Oxide Fuel Rods For High Burnup (NUREG/CR-7022, Volume 1, Revision 1) | NRC.gov," Richland, WA 99352, 2014. Accessed: Apr. 09, 2021. [Online]. Available: <https://www.nrc.gov/reading-rm/doc-collections/nuregs/contract/cr7022/v1/r1/index.html>.
- [104] "Arbitrary polyhedral volume -- CFD-Wiki, the free CFD reference." https://www.cfd-online.com/Wiki/Arbitrary_polyhedral_volume (accessed Apr. 12, 2021).
- [105] D. Pizzocri, T. Barani, and L. Luzzi, "SCIANTIX: A new open source multi-scale code for fission gas behaviour modelling designed for nuclear fuel performance codes," *J. Nucl. Mater.*, vol. 532, 2020, doi: 10.1016/j.jnucmat.2020.152042.
- [106] K. Forsberg and A. R. Massih, "Fission gas release under time-varying conditions," *J. Nucl. Mater.*, vol. 127, no. 2–3, pp. 141–145, Jan. 1985, doi: 10.1016/0022-3115(85)90348-4.
- [107] D. Pizzocri, C. Rabiti, L. Luzzi, T. Barani, P. Van Uffelen, and G. Pastore, "PolyPole-1: An accurate numerical algorithm for intra-granular fission gas release," *J. Nucl. Mater.*, vol. 478, pp. 333–342, 2016, doi: 10.1016/j.jnucmat.2016.06.028.
- [108] O. K and I. N, "Thermal conductivity measurements of high burnup UO₂ pellet and a benchmark calculation of fuel center temperature.," *Proceedings. 1997 Int. Top. Meet. Light Water React. Fuel Perform.*, pp. 541–549, 1997, Accessed: Apr. 09, 2021. [Online]. Available: https://jglobal.jst.go.jp/en/detail?JGLOBAL_ID=200902117925917725.
- [109] M. Herbert, N. Berkow, and D. M. Berkow, "Safety Evaluation by the Office of Nuclear Reactor Regulation of Electric Power Research Institute (EPRI) Topical Report TR-1002865, "Topical Report on Reactivity Initiated Accidents: Bases for RIA Fuel Rod Failures and Core Coolability Criteria," 2006.
- [110] M. Limbäck and T. Andersson, "A Model for Analysis of the Effect of Final Annealing on the In- and Out-of-Reactor Creep Behavior of Zircaloy Cladding," in *Zirconium in the Nuclear*

Industry: Eleventh International Symposium, 2009.

- [111] W. Liu *et al.*, “Numerical method of modeling creep of zirconium-alloy cladding in a multi-physics fuel performance code,” in *LWR Fuel Performance Meeting, Top Fuel 2013*, 2013.
- [112] Y. Matsuo, “Thermal Creep of Zircaloy-4 Cladding under Internal Pressure,” *J. Nucl. Sci. Technol.*, 1987, doi: 10.3327/jnst.24.111.
- [113] B. Baurens, J. Sercombe, C. Riglet-Martial, L. Desgranges, L. Trotignon, and P. Maugis, “3D thermo-chemical-mechanical simulation of power ramps with ALCYONE fuel code,” *J. Nucl. Mater.*, vol. 452, no. 1–3, pp. 578–594, Sep. 2014, doi: 10.1016/j.jnucmat.2014.06.021.
- [114] M. Jin and M. Short, “Multiphysics modeling of two-phase film boiling within porous corrosion deposits,” *J. Comput. Phys.*, vol. 316, pp. 504–518, 2016, doi: 10.1016/j.jcp.2016.03.013.
- [115] C. Fiorina, I. Clifford, M. Aufiero, and K. Mikityuk, “GeN-Foam: a novel OpenFOAM® based multi-physics solver for 2D/3D transient analysis of nuclear reactors,” *Nucl. Eng. Des.*, vol. 294, pp. 24–37, Dec. 2015, doi: 10.1016/J.NUCENGDES.2015.05.035.
- [116] Ieee, *IEEE Standard Glossary of Software Engineering Terminology*, vol. 121990, no. 1. 1990.
- [117] J. D. Hales, S. R. Novascone, B. W. Spencer, R. L. Williamson, G. Pastore, and D. M. Perez, “Verification of the BISON fuel performance code,” *Ann. Nucl. Energy*, vol. 71, pp. 81–90, Sep. 2014, doi: 10.1016/j.anucene.2014.03.027.
- [118] A. Scolaro, I. Clifford, C. Fiorina, and A. Pautz, “First steps towards the development of a 3D nuclear fuel behavior solver with openfoam,” in *International Conference on Nuclear Engineering, Proceedings, ICONE*, 2018, vol. 3, doi: 10.1115/ICONE26-82381.
- [119] J. H. VanSant, “Conduction heat transfer solutions,” Livermore, CA (United States), 1980. doi: 10.2172/7035199.
- [120] A. V. Phan and S. Mukherjee, “The multi-domain boundary contour method for interface and dissimilar material problems,” *Eng. Anal. Bound. Elem.*, vol. 33, no. 5, pp. 668–677, 2009, doi: 10.1016/j.enganabound.2008.10.004.
- [121] G. J. Nie and R. C. Batra, “Material tailoring and analysis of functionally graded isotropic and incompressible linear elastic hollow cylinders,” *Compos. Struct.*, vol. 92, no. 2, pp. 265–274, 2010, doi: 10.1016/j.compstruct.2009.07.023.
- [122] A. W. A. Konter, “Advanced Finite Element Contact Benchmarks,” FENET-UNOTT-DLE-09, 2005.
- [123] T. De Soza, “SSNA122-Benchmark NAFEMS of validation of contact 2: punch (rounded edges),” 2016. [Online]. Available: <http://www.gnu.org/copyleft/fdl.html>.
- [124] “3D Punch NAFEMS Contact Benchmark 2 | SimScale Validation.” <https://www.simscale.com/docs/validation-cases/3d-punch-rounded-edges-nafems-contact-benchmark-2/>.
- [125] “Code Aster,” 2017. <http://www.code-aster.org>.

-
- [126] “Creo Help Center.” http://support.ptc.com/help/creo/creo_sim/usascii/index.html#page/sim/simulate/verify/s_plasticity.html (accessed Apr. 02, 2021).
- [127] A. Rohatgi, “WebPlotDigitizer - Extract data from plots, images, and maps,” *Pacifica, California, USA*, Nov. 2020. <https://automeris.io/WebPlotDigitizer>.
- [128] Geelhood K. J. and Luscher W.G., “NUREG/CR-7022 Vol 2, PNNL-19418, Vol. 2, FRAPCON-3.4: Integral Assessment,” 2011. Accessed: Apr. 11, 2021. [Online]. Available: <http://www.nrc.gov/reading-rm.html>.
- [129] P. Van Uffelen *et al.*, “The Verification of the TRANSURANUS Fuel Performance Code-an Overview,” *7th Int. Conf. WWER Fuel Performance, Model. Exp. Support*, 2007.
- [130] R. L. Williamson *et al.*, “Validating the BISON fuel performance code to integral LWR experiments,” *Nucl. Eng. Des.*, 2016, doi: 10.1016/j.nucengdes.2016.02.020.
- [131] J. A. Turnbull, “Review of Nuclear Fuel Experimental Data,” Jan. 1995.
- [132] D. D. Lanning and E. R. Bradley, “Final irradiation and postirradiation data from the NRC/PNL instrumented assembly IFA-432,” 1986. Accessed: Apr. 25, 2021. [Online]. Available: http://inis.iaea.org/Search/search.aspx?orig_q=RN:17065466.
- [133] “NUREG/CR-7022 Vol. 2 Rev 1 ‘FRAPCON-3.5: Integral Assessment.’” Accessed: Apr. 25, 2021. [Online]. Available: <http://www.nrc.gov/reading-rm.html>.
- [134] T. Barani *et al.*, “Analysis of transient fission gas behaviour in oxide fuel using BISON and TRANSURANUS,” *J. Nucl. Mater.*, vol. 486, pp. 96–110, 2017, doi: 10.1016/j.jnucmat.2016.10.051.
- [135] G. Pastore *et al.*, “Uncertainty and sensitivity analysis of fission gas behavior in engineering-scale fuel modeling,” *J. Nucl. Mater.*, vol. 456, pp. 398–408, 2015, doi: 10.1016/j.jnucmat.2014.09.077.
- [136] J. C. Killeen, J. A. Turnbulf, and E. Sartori, “Fuel modelling at extended burnup: IAEA coordinated research project FUMEX-II,” in *American Nuclear Society - 2007 LWR Fuel Performance/Top Fuel*, 2007, pp. 261–273.
- [137] B. Michel *et al.*, “Two fuel performance codes of the PLEIADES platform: ALCYONE and GERMINAL,” in *Nuclear Power Plant Design and Analysis Codes*, 2021, pp. 207–233.
- [138] B. W. Spencer, R. L. Williamson, D. S. Stafford, S. R. Novascone, J. D. Hales, and G. Pastore, “3D modeling of missing pellet surface defects in BWR fuel,” *Nucl. Eng. Des.*, vol. 307, pp. 155–171, Oct. 2016, doi: 10.1016/J.NUCENGDES.2016.07.008.
- [139] A. A. Rezwan, M. R. Tonks, and M. P. Short, “Evaluations of the performance of multi-metallic layered composite cladding for the light water reactor accident tolerant fuel,” *J. Nucl. Mater.*, vol. 535, 2020, doi: 10.1016/j.jnucmat.2020.152136.
- [140] M. D. Goldberg, “An Investigation into the Effect of Fuel Pellet Eccentricity on Fuel-Cladding Gap Heat Transfer,” Georgia Institute of Technology, 1974.

-
- [141] R. E. Williford and C. R. Hann, "Effects of fill gas composition and pellet eccentricity," *United States N. p.*, 1977, doi: 10.2172/5370475.
 - [142] S. Yanagihara, S. Shiozawa, and S. Saito, "Effect of Fuel Pellet Eccentricity with Cladding on Fuel Rod Thermal Behavior under Reactivity Initiated Accident Condition," *J. Nucl. Sci. Technol.*, vol. 19, no. 6J, pp. 469–481, 1982, doi: 10.1080/18811248.1982.9734170.
 - [143] O. McNary and T. H. Bauer, "The effect of asymmetric fuel-clad gap conductance on fuel pin thermal performance," *Nucl. Eng. Des.*, 1981, doi: 10.1016/0029-5493(81)90015-7.
 - [144] P. A. B. Desampaio, M. D. L. Moreira, and J. C. A. Gaspar, "The effect of eccentricity in the position of UO₂ pellets," *Prog. Nucl. Energy*, vol. 69, pp. 23–28, 2013, doi: 10.1016/j.pnucene.2013.06.007.
 - [145] J. D. Hales, S. R. Novascone, G. Pastore, and D. M. Pe, "BISON Theory Manual The Equations behind Nuclear Fuel," 2013. doi: 10.2172/1107264.
 - [146] J. D. Hales, D. M. Perez, R. L. Williamson, S. R. Novascone, and B. W. Spencer, "Validation of the BISON 3D Fuel Performance Code: Temperature Comparisons for Concentrically and Eccentrically Located Fuel Pellets," *United States: N. p.*, 2013. Web. .
 - [147] R. L. Williamson *et al.*, "Validating the BISON fuel performance code to integral LWR experiments," *Nucl. Eng. Des.*, vol. 301, pp. 232–244, May 2016, doi: 10.1016/J.NUCENGDES.2016.02.020.
 - [148] M. Kinoshita *et al.*, "HBRP — Final Report," (CRIEPI) Mar 2001.
 - [149] H. M. M. Kinoshita, S. Kitajima, T. Kameyama, T. Matsumura, E. Kolstad, "High Burnup Rim Project, progress of irradiation and preliminary analysis," in *Proceedings, International Topical Meeting on Light Water Reactor Fuel Performance*.
 - [150] K. Sakai, "The fuel creep test IFA-701: results after four irradiation cycles," vol. HWR-1039.
 - [151] A. Scolaro, I. Clifford, C. Fiorina, and A. Pautz, "The OFFBEAT multi-dimensional fuel behavior solver," *Nucl. Eng. Des.*, vol. 358, 2020, doi: 10.1016/j.nucengdes.2019.110416.
 - [152] K. Lassmann, A. Schubert, J. Van De Laar, and P. Van Uffelen, "The 'Fuel Rod Analysis ToolBox': A general program for preparing the input of a fuel rod performance code," *Ann. Nucl. Energy*, vol. 81, pp. 332–335, Jul. 2015, doi: 10.1016/j.anucene.2015.03.012.
 - [153] C. Győria, M. Jonsonb, G. Robertsonb, P. Blairb, A. Schubertc, and P. Van Uffelen, "Extension and validation of the TRANSURANUS code in the course of the ESSANUF project," in *12th International conference on WWER fuel performance, modelling and experimental support (INRNE, Nessebar, Bulgaria, 2017)*.
 - [154] I. Clifford, M. Pecchia, R. Mukin, C. Cozzo, H. Ferroukhi, and A. Gorzel, "Studies on the effects of local power peaking on heat transfer under dryout conditions in BWRs," *Ann. Nucl. Energy*, 2019, doi: 10.1016/j.anucene.2019.03.017.
 - [155] C. B. Lee, D. H. Kim, J. S. Song, J. G. Bang, and Y. H. Jung, "RAPID model to predict radial burnup distribution in LWR UO₂ fuel," *J. Nucl. Mater.*, vol. 282, no. 2–3, pp. 196–204, 2000,

doi: 10.1016/S0022-3115(00)00408-6.

- [156] S. Lemehov, J. Nakamura, and M. Suzuki, "PLUTON: A three-group model for the radial distribution of plutonium, burnup, and power profiles in highly irradiated LWR fuel rods," *Nucl. Technol.*, vol. 133, no. 2, pp. 153–168, 2001, doi: 10.13182/NT01-A3166.
- [157] W. Haeck, B. Verboomen, A. Schubert, and P. Van Uffelen, "Application of EPMA data for the development of the code systems TRANSURANUS and ALEPH," in *Microscopy and Microanalysis*, 2007, vol. 13, no. 3, pp. 173–178, doi: 10.1017/S1431927607070328.
- [158] C. T. Walker, V. V. Rondinella, D. Papaioannou, S. Van Winckel, W. Goll, and R. Manzel, "On the oxidation state of UO₂ nuclear fuel at a burn-up of around 100 MWd/kgHM," *J. Nucl. Mater.*, vol. 345, no. 2–3, pp. 192–205, Oct. 2005, doi: 10.1016/j.jnucmat.2005.05.010.
- [159] H. Suikkanen, V. Rintala, A. Schubert, and P. Van Uffelen, "Development of coupled neutronics and fuel performance analysis capabilities between Serpent and TRANSURANUS," *Nucl. Eng. Des.*, vol. 359, Apr. 2020, doi: 10.1016/j.nucengdes.2019.110450.
- [160] J. Leppänen, T. Viitanen, and V. Valtavirta, "Multi-physics coupling scheme in the serpent 2 Monte Carlo code," in *Transactions of the American Nuclear Society*, 2012, vol. 107, pp. 1165–1168.
- [161] J. Leppänen, V. Valtavirta, T. Viitanen, and M. Aufiero, "Unstructured Mesh Based Multi-Physics Interface for CFD Code Coupling in the Serpent 2 Monte Carlo Code," in *PHYSOR 2014 – The Role of Reactor Physics Toward a Sustainable Future*, 2014.
- [162] M. Aufiero, C. Fiorina, A. Laureau, P. Rubiolo, and V. Valtavirta, "Serpent-Openfoam coupling in transient mode: Simulation of a godiva prompt critical burst," in *Mathematics and Computations, Supercomputing in Nuclear Applications and Monte Carlo International Conference, M and C+SNA+MC 2015*, 2015, vol. 3, pp. 1995–2006.
- [163] R. Tuominen, V. Valtavirta, J. Peltola, and J. Leppänen, "Coupling serpent and openfoam for neutronics - CFD multi-physics calculations," in *Physics of Reactors 2016, PHYSOR 2016: Unifying Theory and Experiments in the 21st Century*, 2016, vol. 1, pp. 255–269.
- [164] W. Haeck and B. Verboomen, "An optimum approach to Monte Carlo burnup," *Nucl. Sci. Eng.*, vol. 156, no. 2, pp. 180–196, 2007, doi: 10.13182/NSE07-A2695.
- [165] C. Maeder, P. Wydler, P. Wydler Eir, and S. September, "International Comparison Calculations for a BWR Lattice with Adjacent Gadolinium Pins," Eidg. Institut für Reaktorforschung Würenlingen Schweiz, 1984.
- [166] K. Shirvan, "Assessment of BISON fuel performance code and its application to advanced fuels," in *International Congress on Advances in Nuclear Power Plants, ICAPP 2014*, 2014, vol. 3, pp. 2267–2278.
- [167] M. Suzuki, H. Saitou, Y. Udagawa, and F. Nagase, "Japan Atomic Energy Agency Light Water Reactor Fuel Analysis Code FEMAXI-7; Model and Structure," 2013. Accessed: Apr. 25, 2021. [Online]. Available: <http://www.jaea.go.jp>.

-
- [168] R. L. Williamson, G. Pastore, B. W. Spencer, J. D. Hales, and T. Tverberg, "BISON Validation for LOCA and PCMI Behaviour Using Measurements From the Halden Reactor Project (Conference) | OSTI.GOV." Accessed: Apr. 25, 2021. [Online]. Available: <https://www.osti.gov/biblio/1414448-bison-validation-loca-pcmi-behaviour-using-measurements-from-halden-reactor-project>.
- [169] H. C. Kim, S. K. Seo, S. U. Lee, and Y. S. Yang, "Development of NUFORM3D module with FRAPCON3.4 for simulation of pellet-cladding mechanical interaction," *Nucl. Eng. Des.*, vol. 318, pp. 61–71, Jul. 2017, doi: 10.1016/J.NUCENGDES.2017.03.035.
- [170] T. Valentine *et al.*, "OVERVIEW OF THE OECD-NEA EXPERT GROUP ON MULTI-PHYSICS EXPERIMENTAL DATA, BENCHMARKS AND VALIDATION," *EPJ Web Conf.*, vol. 247, p. 6048, 2021, doi: 10.1051/epjconf/202124706048.
- [171] D. A. Kulik *et al.*, "GEM-Selektor geochemical modeling package: Revised algorithm and GEMS3K numerical kernel for coupled simulation codes," *Comput. Geosci.*, vol. 17, no. 1, pp. 1–24, 2013, doi: 10.1007/s10596-012-9310-6.
- [172] A. Scolaro, I. Clifford, C. Fiorina, and A. Pautz, "Cladding plasticity modeling with the multidimensional fuel performance code offbeat," in *GLOBAL 2019 - International Nuclear Fuel Cycle Conference and TOP FUEL 2019 - Light Water Reactor Fuel Performance Conference*, 2020, pp. 47–55.
- [173] A. Scolaro, I. Clifford, C. Fiorina, and A. Pautz, "First steps towards the development of a 3D nuclear fuel behavior solver with OpenFOAM," in *ICONE 2018, London*, 2018.
- [174] A. Scolaro, P. Van Uffelen, C. Fiorina, A. Schubert, I. Clifford, and A. Pautz, "Investigation on the effect of eccentricity for fuel disc irradiation tests," *Nucl. Eng. Technol.*, 2020, doi: 10.1016/j.net.2020.11.003.
- [175] A. Scolaro, Y. Robert, C. Fiorina, I. Clifford, and A. Pautz, "Coupling methodology for the multidimensional fuel performance code OFFBEAT and the monte carlo neutron transport code Serpent," in *TopFuel 2019*, 2019.

Curriculum Vitae

CONTACT INFORMATION

Email: Alessandro.scolaro@epfl.ch

PERSONAL INFORMATION

Born in Palermo, Italy, on the 17/07/1989

EMPLOYMENT HISTORY

- Nuclear Engineer, Nagra, 09/2016 to 04/2017

EDUCATION

- Liceo Classico Umberto I, 09/2003 to 07/2008
- Ingegneria Energetica, Università degli studi di Palermo, 09/2011 to 07/2014
- Master in Nuclear Engineering, joint program between EPFL and ETHZ, 09/2014 to 09/2016

PUBLICATIONS

- Scolaro, A. et al., *First steps towards the development of a 3D nuclear fuel behavior solver with OpenFOAM*, Proceedings of the 26th international conference on nuclear engineering (ICONE26), 2018
- Fiorina C., Radman, S., Scolaro, A., & Pautz, A. (2018). *A reduced order accelerator for time-dependent segregated neutronic solvers*. Annals of Nuclear Energy, 121, 177-185.
- Scolaro, A. et al., *The OFFBEAT multi-dimensional fuel behavior solver*, Nuclear Engineering and Design, Volume 358, 2020
- Scolaro, A. et al., *Cladding plasticity modeling with the multidimensional fuel performance code OFFBEAT*, Global/top fuel 2019
- Scolaro, A. et al., *Coupling methodology for the multidimensional fuel performance code OFFBEAT and the Monte Carlo neutron transport code Serpent*, Global/top fuel 2019
- Scolaro, A. et al., *Multi-Dimensional Creep Analysis Using the Novel OFFBEAT Fuel Performance Code*, IAEA Technical Meeting on Progress on Pellet Cladding Interaction and Stress Corrosion Cracking
- Scolaro, A. et al., *Investigation on the effect of eccentricity for fuel disc irradiation tests*, Nuclear Engineering and Technology, 2020
- Fiorina, C., Scolaro, A. et al., *Artificial Neural Networks as Surrogate Models for Uncertainty Quantification and Data Assimilation in 2-D/3-D Fuel Performance Studies*, J. Nucl. Eng. 2020
- Ganesello, A., Scolaro, A. et al., *Simulation of fission gas release in the 3D fuel performance code OFFBEAT*, IAEA Fast Reactor Conference, 2021